Final Report

Aquafin CRC - Southern Bluefin Tuna Aquaculture Subprogram: Risk and Response – Understanding the Tuna Farming Environment

Jason E. Tanner & John K. Volkman (Editors)

March 2009

Aquafin CRC Project 4.6

FRDC Project No. 2005/059

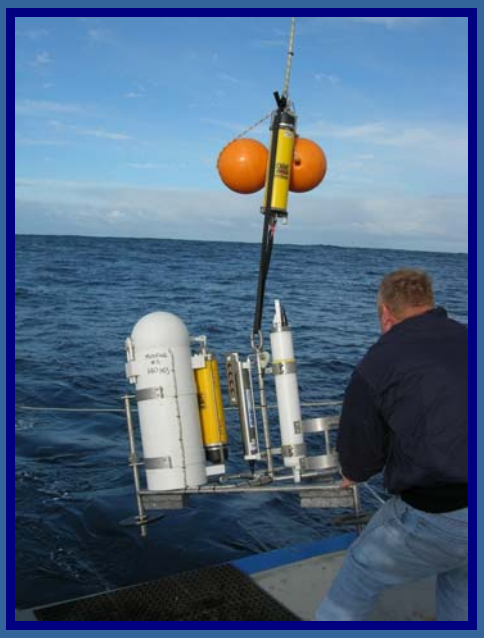

This publication may be cited as:
Tanner, J.E. and J. Volkman (Eds.) 2009. Aquafin CRC - Southern Bluefin Tuna Aquaculture Subprogram: Risk and Response – Understanding the Tuna Farming Environment. Technical report, Aquafin CRC Project 4.6, FRDC Project 2005/059. Aquafin CRC, Fisheries Research & Development Corporation and South Australian Research & Development Institute (Aquatic Sciences), Adelaide. SARDI Publication No F2008/000646-1, SARDI Research Report Series No 344, 287 pp.

Printed in Adelaide, March 2009
SARDI Aquatic Sciences
PO Box 120
Henley Beach SA 5022

SARDI Aquatic Sciences Publication Number F2008/000646-1
SARDI Research Report Series Number 344
ISBN Number 978-1-921563-13-3

Authors: Tanner, J.E., Volkman, J.
Reviewers: Charles James, Paul van Ruth, John Luick, John Middleton, Maylene Loo, Milena Fernandes, Marty Deveney, Stephen Madigan, Sunil Sharma, Sasi Nayar
Approved by: Steven Clarke

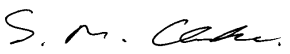

Signed:
Date: 25 March 2009
Distribution: FRDC, ASBTIA, SARDI Aquatic Sciences Library
Circulation: Public domain

Aquafin CRC - Southern Bluefin Tuna Aquaculture Subprogram: Risk and Response – Understanding the Tuna Farming Environment

Edited by

Jason E. Tanner
SARDI Aquatic Sciences
2 Hamra Ave
West Beach SA 5024

John Volkman
CSIRO Marine and Atmospheric Research
Castray Esplanade
Hobart Tas 7000

March 2009

Aquafin CRC Project 4.6

(FRDC Project No. 2005/059)

SARDI SOUTH AUSTRALIAN RESEARCH AND DEVELOPMENT INSTITUTE

Government of South Australia

CRC AUSTRALIA

CSIRO

Australian Government
Fisheries Research and Development Corporation

TABLE OF CONTENTS

Chapter 1: Hydrodynamic Modelling and Observations of the Tuna Farming Zone, Spencer Gulf 1
1.1. Introduction 2
1.2. The Hydrodynamic Models 4
1.2.1 Model Domain and Topography 4
1.2.2. Initial Temperature/Salinity Fields 5
1.2.3. Atmospheric Forcing 5
1.2.4. Boundary Forcing of the Regional Spencer Gulf Model 6
1.3. Regional Spencer Gulf Model – results and observations 7
1.3.1 Sea Level 7
1.3.2 Winter-time circulation, temperature and salinity 9
1.3.3 Summer-time circulation, temperature and salinity 11
1.4 Local Tuna Farming Zone Model – Results and Observations 16
1.4.1 Velocity - Observations 16
1.4.2 Velocity - Model Results 17
1.4.3 Temperature and Salinity 19
1.4.4 Upwelling/downwelling in the TFZ – a Local Transport Mechanism 23
1.5. Flushing Times 24
1.6. Summary and Conclusions 31
1.7. References 32

Chapter 2: The wave regime of south-west Spencer Gulf 35
2.1. Introduction 36
2.3. Methods 38
2.3.1. Wave observations 38
2.3.2 Model Description 39
2.4. Results 41
2.4.1. Model Validation 41
2.4.2. Model Results 45
2.5. Discussion 48
2.6. Conclusions 51
2.7. References 52
2.8. Appendix 54
2.8.1 The wave spectrum 54

Chapter 3: The environmental implications of sediment type distribution and resuspension for the aquaculture industry in South-West Spencer Gulf 55
3.1. Introduction 56
3.2. Methods 58
3.2.1. Mooring data 58
3.2.2. Wave Model Description 59
3.2.3. Wave analysis 60
3.2.4. Sediments 61
3.2.6. Theoretical approach to calculating the initiation of sediment movement. 63
3.3. Results 64
3.3.1. Spatial variation in observed sediment characteristics 64

3.6.2. Wave - sediment grain size interactions: 67
3.3.3. Observed sediment resuspension 69
3.4. Discussion 73
3.5. Conclusions 76
3.6. References 77
3.7 Appendix 79

Chapter 4. Numerical modelling of the sediment dynamics in the Port Lincoln region 85
4.1. Introduction 86
4.2. Model description 87
4.2.1. Hydrodynamic model 87
4.2.2. Wave model 88
4.2.3. Sediment model 88
4.3. Modelling results 89
4.3.1. Model against data 89
4.3.2. Bottom friction 91
4.3.3. Sediment dynamics 93
4.4. Discussion 94
4.5. Conclusions 98
4.6. References 99

Chapter 5: Nutrients 101
5.1. Introduction 102
5.2. Materials and Methods 102
5.2.1. Sampling 102
5.2.2. Chemical Analysis 103
5.3. Results and Discussion 104
5.3.1. Spatial and Temporal Nutrient Dynamics in the TFZ 104
5.3.2. Potentially limiting nutrients 107
5.3.3. Assessing spatial and temporal nutrient dynamics: including other data sources. 108
5.3.4. Using other data including remotely sensed data to infer nutrient dynamics 110
5.3.5. Other sources of nutrients 117
5.4. Summary 121
5.4.1. Risks 122
5.5. References 123

Chapter 6: Remote Sensing – Validation, spatial and temporal patterns in sea surface temperature and chlorophyll-*a* 127
6.1. Introduction 128
6.2. Aims 129
6.3. Methods 129
6.3.1 Remote Sensing Validation 129
6.3.2 Spatial and Temporal variability in SST and chlorophyll-*a* 130
6.4 Results 133
6.4.1 Remote Sensing Validation 133
6.5.2 Chlorophyll-*a* Spatial and Temporal Variability 134
6.5.3 Sea Surface Temperature Spatial and Temporal Variability 140
6.6 Discussion 144
6.7 Conclusions 148
6.8 References 149

Chapter 7: Temporal and spatial variability in phytoplankton abundance and community composition, and pelagic biogeochemistry in the tuna farming zone 151
7.1. Introduction 152
7.2. Methods 152
7.2.1. Phytoplankton biomass and abundance 153
7.2.2. Long term datasets 154
7.2.3. Nutrient analysis 155
7.2.4. Community connectivity with the wider region 155
7.3. Results 156
7.3.1. Monthly biomass and abundance data 156
7.3.2. Long term trends in biomass and abundance 162
7.3.3. Monthly nutrient data 167
7.3.4. Community connectivity with the wider region 167
7.3.5. Harmful algal bloom species 172
7.4. Discussion 184
7.4.1. Risk Assessment for HAB species in the TFZ 187
7.5. References 189

Chapter 8: Temporal and spatial variability in microphytobenthos, biogeochemistry and light in southern Spencer Gulf 193
8.1. Introduction 194
8.2. Methods 196
8.2.1. Sample sites and collection 196
8.2.2. Sample analysis 197
8.3. Results and Discussion 198
8.3.1. Spatial and temporal variability 198
8.3.2. MPB biomass 199
8.3.3. MPB pigment composition 201
8.3.4. MPB phaeopigment composition 203
8.3.5. Benthic algal resting stages in harmful algal blooms 205
8.3.6. Nutrient concentrations, water temperature and PAR 206
8.3.7. Sediment and wave characteristics 211
8.4. Conclusion 212
8.5. References 213

Chapter 9: Plankton Ecology: Primary Production, Zooplankton Community Composition and Grazing 217
9.1. Introduction 218
9.2. Methods 219
9.3. Results 220
9.3.1. Primary Production 220
9.3.2. Microzooplankton Grazing 222
9.3.3. Meso-zooplankton Grazing 227
9.4. Discussion 229
9.5. References 231

Chapter 10: Biogeochemical Modelling in the Southern Bluefin Tuna Farming Zone 234
10.1. Introduction 235
10.2. Model description 235
10.2.1. Physical model 235
10.2.2. Sediment model 236

10.2.3. Biogeochemical model 236
10.2.4. Model components 237
10.2.5. Primary production 238
10.2.6. Secondary production 239
10.2.7. Detritus and nutrient pools 240
10.2.8. Dissolved oxygen 242
10.2.9. Initialisation 242
10.2.10. Boundary forcing 243
10.2.11. Southern bluefin tuna farm loads 244
10.2.12. Sewerage treatment plant (STP) loads 244
10.3. Results; Model calibration 245
10.3.1. Calibration summary 255
10.4. Results: Modelled seasonal pelagic biogeochemistry 256
10.4.1. Pelagic chlorophyll and oxygen dynamics 256
10.4.2. Pelagic nutrient dynamics 259
10.4.3. Fish farm impacts on pelagic nutrients, chlorophyll and oxygen 263
10.5. Results: Seasonal epibenthos and sediment 265
10.5.1. Sediment properties 265
10.5.2. Fish farm impacts on sediment properties 265
10.5.3. Regional fish farm impacts on sediment properties 273
10.6. Conclusions 273
10.7. References 274

Chapter 11. Conclusions 277
11.1. Benefits and Adoption 277
11.2. Further Development 277
11.3. Planned Outcomes 278
11.4. Conclusions 281

Appendix 1: Intellectual Property. 286

Appendix 2: Project Staff. 286

LIST OF TABLES

Table 1.1. The four dominant tidal harmonics for Taylor's Landing 6
Table 1.2. Flushing times 25
Table 2.1. Model description. 40
Table 2.2. Summary of the swell conditions in the TFZ depending on the incident swell direction and the period of the waves at the southern boundary (T_b). Values represent the swell height in the TFZ as a percentage of the open ocean height. The highlighted column shows the direction producing the greatest swell height in the TFZ. * Limited number of observations for this direction and period. 51
Table 3.1. The location (WGS 84) and description of the instrumentation in each of the moorings used in the study. 59
Table 3.2. The results of a Kruskal-Wallis non-parametric analysis of the main groups identified by the cluster analysis. Variables with a statistically significant difference between the groups are highlighted in light-red. 66
Table 3.3. The results of a Kruskal-Wallis non-parametric analysis of the main groups identified by the cluster analysis. The variables presented in this table were not included in the cluster analysis. Variables with a statistically significant difference between the groups are highlighted in light-red. 67
Table 3.4. The results of a Kruskal-Wallis non-parametric analysis of the main groups identified by the cluster analysis of U_{sig}. Variables with a statistically significant difference between the groups are highlighted in light-red. 69
Table 3.5. The theoretical shear stress required to initiate sediment movement within erosional and depositional zones within the TFZ (see section 3.2.6). 76
Table 5.1. A summary of the statistical analyses of nutrient data from the TFZ (see map, Figure 5.1). Statistical analysis was by 3 way ANOVA followed by Bonferroni t-tests for individual differences relative to controls: January, surface and site 22 105
Table 5.2. Monthly mean nutrient concentrations at sites 22, 24, 25, 26, 44, 43, 39 at 2 depths for all sampling from August 2005 to September 2006. 105
Table 5.3. Median values for water quality parameters derived from SA EPA data sets for locations near Boston Bay, Eyre Peninsula. 110
Table 5.4. Chlorophyll-*a* concentrations (□g L^{-1}) in Spencer Gulf and around the Eyre Peninsula (median and 25^{th} & 75^{th} percentiles) from SA EPA over the period from 1996-2007. 111
Table 5.5. Benthic nutrient fluxes reported in other estuarine or marine studies 118
Table 5.6. A summary of known nitrogen pools or inputs to the Boston Bay region (model domain is specified in chapters 1 & 10). 119
Table 6.1. The co-ordinates of the stations used to assess spatial variability in chlorophyll-*a* and SST. 131
Table 7.1. List of sites from the SASQAP database used in the analysis of spatial and temporal variations in Harmful Algal Bloom species in the TFZ. 155
Table 7.2. Indicator species analysis to determine the taxa of phytoplankton contributing significantly to differences in community structure between months (probabilities (p) less than 0.05 are considered statistically significant). Mean abundance in cells L^{-1} ± standard error; n = 4, except in September 05 when n = 3. Rel. freq. = relative frequency (%), i.e. the % of samples in a given month where a given species is present. 160
Table 7.3. Indicator species analysis: Phytoplankton genera with significantly greater presence in the TFZ compared with the wider eastern Great Australian Bight region (probabilities (p) less than 0.05 are considered statistically significant). 169
Table 7.4. Comparison of phytoplankton abundance between the TFZ (RM5) and mid southern Spencer Gulf (RM3). Probabilities less than 0.05 are considered statistically significant. Statistical power < 0.80 indicates a high degree of variability in the data and that negative findings (e.g. no difference between sites) should be interpreted cautiously. 170
Table 7.5. Observations of the maximum cell densities of 6 toxic genera of phytoplankton as recorded in the SASQAP database for 5 sites: Bickers Island (BI), Boston Bay (BB), Proper Bay (PB), Louth Bay (LB), Lincoln (L) in, or near, the TFZ. A discussion of their toxicity can be found in the text 183
Table 7.6. Risk matrix – numbers in cells are the product of the consequence and the likelihood ratings = the risk (adapted from Fletcher et al. 2004). 188
Table 7.7. (a) Likelihood ratings adopted for this risk assessment 188
Table 7.7. (b) Consequence ratings. The consequences of the identified risks with specific reference to SBT. 188
Table 7.7. (c) Risk ratings. 188
Table 8.1. Reported values of MPB biomass, measured as chlorophyll-*a* in subtidal environments. 195
Table 8.2a. Percentages of chlorophyll-*a* and individual phaeopigments in samples from sites 22 and 25 (note pphytin-*a* is not in the table as it wasn't detected in any sample) 208

Table 8.2b. Percentages of chlorophyll-*a* and individual phaeopigments in samples from sites 44 and 39 (note pphytin-*a* is not in the table as it wasn't detected in any sample) 209
Table 10.1. Characteristics of primary producers included in the biogeochemical model. 239
Table 10.2. Optical parameters used in the biogeochemical model. 239
Table 10.3. Characteristics of secondary producers included in the model. 240
Table 10.4. Modelled detritus parameter values and associated remineralisation rates. 242
Table 10.5. Initial state variable concentrations. 243
Table 10.6. Successful mooring deployments within the TFZ. 249
Table 10.7. Regional classification based on annual mean pelagic chlorophyll concentration in upper 12 m of the water column after Smith et al. (1998) (SBT: Southern Bluefin Tuna). 264

LIST OF FIGURES

Figure 1.1. The Spencer Gulf / Boston Bay region. The labelled red sites denote locations of sea level data used in this study. 2
Figure 1.2. Details of moorings deployed in the TFZ. Mooring 4 was dragged during deployment #3; start and end locations are denoted 4c_start and 4c_end respectively. Mooring 4a and 4c are collectively known as mooring 4 inner, 4 d is referred to as the boundary and 4 b failed to record any data. CTD casts were made monthly from Aug 05 to Sep 06 at 6 sites along the white line. 4
Figure 1.3. Major component of daily wind stress (Units 100Pa) from Neptune Island for 2005 and 2006. The times are indicated as dd/mm for each year as well as in Julian Days (JD) since 01/01/1990. The use of Julian Days since 1990 is CSIRO standard for their modelling suite. The major component was resolved to be that along the shelf and is positive to the southeast (shelf downwelling) and negative to the northwest (shelf upwelling). 5
Figure 1.4. Sea level prediction (red) and data (blue) at Wallaroo (upper) and Whyalla (lower) for the tidal band (< 25 hr period). Note the vertical scale is in meters. 8
Figure 1.5. Sea level prediction (red) and data (blue) at Wallaroo (upper) and Whyalla (lower) for the weather- band (> 30 hr period). Note that instrument failure occurred twice in late November resulting in the absence of data. The vertical scale is in meters. 9
Figure 1.6. The time-averaged flow for July 2006 and for the depth averaged velocity. A legend vector of length 0.05 m s^{-1} is indicated. 10
Figure 1.7. Sea Surface Temperature (MODIS) for the 19th June 2006 (JD 6013). The arrows indicate the expected circulation. 10
Figure 1.8. Modelled Sea Surface Temperature (MODIS) for the 19th June 2006 (JD 6013). 11
Figure 1.9. Maximum salinity throughout the water column for 16-23 June 1986. Reproduced from Lennon et al. (1987). 12
Figure 1.10. Model bottom salinity on 29th June 2006. 13
Figure 1.11. Comparison of modelled (red) and measured (blue) temperature and salinity at mooring locations in the TFZ. See Figure 1.3 for the location of the moorings. 14
Figure 1.12. MODIS sea surface temperature for February 2006 (JD 5877). The temperature contour interval is 1ºC and the mooring sites M1, M2, M3 and M4 are indicated. 15
Figure 1.13. The time-averaged flow for January 2006 and for the depth averaged velocity. A legend vector of length 0.05 m s^{-1} is indicated. 15
Figure 1.14. Upper Panel: the (east/west) tidal-band velocity (depth-averaged) for M4 at the inner site and for September 2005 (mm/dd). Black values are data while the red values are from the fine scale numerical model. Positive values are to the east. Lower Panel: as in the upper panel but for the (north/south) tidal-band velocity. Positive values are to the north. Note the change of scale on the y- axis. 17
Figure 1.15. Upper Panel: the (east/west) weather-band velocity (depth-averaged) for M4 at the inner site. Black values are data while the red values are from the fine scale numerical model. Positive values are to the east. Lower Panel: as in the upper panel but for the (north/south) weather-band velocity. Positive values are to the north. 18
Figure 1.16. Winter depth averaged current velocity 19
Figure 1.17. Summer depth averaged current velocity 19
Figure 1.18. Upper Panel: observed temperature for Feb 11th 2006. Lower Panel: model temperature for the same day (12 noon). The vertical scale indicates depths in meters. The horizontal scale is in degrees longitude. 20
Figure 1.19. Upper Panel: observed salinity for Feb 11th 2006. Lower Panel: model salinity for the same day (12 noon). The vertical scale indicates depths in meters. The horizontal scale is in degrees longitude. 20
Figure 1.20. Upper Panel: observed temperature for April 21st 2006. Lower Panel: model temperature for the same day (12 noon). The vertical scale indicates depths in meters. The horizontal scale is in degrees longitude. 21
Figure 1.21. Upper Panel: observed salinity for April 21st 2006. Lower Panel: model salinity for the same day (12 noon). The vertical scale indicates depths in meters. The horizontal scale is in degrees longitude. 21
Figure 1.22. Upper Panel: observed temperature for June 20th, 2006 (JD 6012). Lower Panel: model temperature for the same day (12 noon). The vertical scale indicates depths in meters. The horizontal scale is in degrees longitude. 22
Figure 1.23. Upper Panel: observed salinity for June 20th, 2006 (JD 6012). Lower Panel: model salinity for the same day (12 noon). The vertical scale indicates depths in meters. The horizontal scale is in degrees longitude. 22
Figure 1.24. Progressive vector diagram of near-bottom currents at Mooring 4. The times (December 2006 - January 2006) are indicated by dd/mm. The colour gives the near-bottom temperature from the M5 mooring at the dates indicated: colour bar at top of figure. 23
Figure 1.25. Model section of temperature and currents for May 6th 2006 during strong offshore wind to the south-east. 24
Figure 1.26. Schematic of depth averaged mean flow. 25

Figure 1.27. Point source release locations for estimating removal times of pollutants. 26
Figure 1.28. Distribution of a passive tracer released at Farm #11. 27
Figure 1.29. Distribution of a passive tracer released at Peake Bay. 27
Figure 1.30. Final particle distribution from the tuna farm # 9 release site. 29
Figure 1.31. Final particle distribution from the Peake Bay release site. 29
Figure 1.32: Spring tide trajectory, 22 October 2005. 30
Figure 1.33: Dodge tide trajectory, 7 January 2006 30
Figure 1.34: Neap tide trajectory, 8 January 2006. 31
Figure 2.1. Map of study region showing the coarse scale SARWM domain, the fine scale TunaWM domain (inset) and the locations of the moorings used in the validation of the wave model (M5 to M9). The TFZ (inset) is delineated by the red border. 37
Figure 2.2. Time series of modelled (blue) and observed (red) significant wave heights (m) at M9 located 5 nautical miles off Cape de Couedic, south-west Kangaroo Island (a), and correlation between modelled and observed wave heights at this location (b). 41
Figure 2.3. Time series of modelled (blue) and observed (red) significant wave heights (m) at M8, near Thistle Island (a), and correlation between modelled and observed wave heights at this location (b). 42
Figure 2.4. Time series of modelled (blue) and observed (red) H_s (m) at Mooring 5a (a), and correlation between modelled and observed wave heights at this location (b). 43
Figure 2.5. Time series of modelled (blue) and observed (red) H_s (m) at Mooring 5b (a), and correlation between modelled and observed wave heights at this location (b). 44
Figure 2.6. Time series of observed (red) and modelled (blue) H_s (m) at M7 (a), and correlation between modelled and observed wave heights at this location (b). 44
Figure 2.7. The modelled annual mean H_s (m). The arrows indicate the direction that the waves are travelling. The circle denotes the area to the west of Point Bolingbroke that experiences elevated wave energy in comparison to other near-shore locations. 46
Figure 2.8. Modelled H_s (m) and direction for the storm event of 17/7/07. The arrows indicate the direction that the waves are travelling. 47
Figure 2.9. The modelled January (a) and July (b) mean H_s. The arrows indicate the direction that the waves are travelling. 47
Figure 2.10. a) Wind direction vs significant wave height at M7 for varying wind speeds and b) wind speed vs H_s, using the same datapoints from 2.10a. 48
Figure 2.11. The incident wave height plotted against the incident direction at the southern boundary. The data points are grouped by the period of incident waves at the southern boundary (T_b). 49
Figure 2.12. Normalised swell height (H_n) vs incident swell direction. The data points are grouped by the period of incident waves at the southern boundary (T_b). 50
Figure 3.1. Map of study region showing sampling locations (red points) and mooring locations (yellow points), water depth (m) and the extent of the fine-scale model domain (main) and the coarse-resolution model domain (inset). The TFZ is indicated by the red boundary. 56
Figure 3.2. Moorings used for the collection of temperature, salinity, pressure, turbidity and currents at locations M5a and M5b (Source: CSIRO). 58
Figure 3.3. The mooring frame used to mount the RDI Workhorse (300 kHz) ADCP in deployments M7 and M8. 59
Figure 3.4. Modified Shields Diagram (adapted from Nielsen (1992)) 63
Figure 3.5. Spatial distribution of sediment mean grain size (in μm). 64
Figure 3.6. Results of a cluster analysis displaying the locations which have similar geochemical properties. 65
Figure 3.7. Results of PCA plotting the 1st and 2nd PC's. The data points are colour-coded with respect to the group determined by the cluster analysis. The 1st principal component accounts for 48.5% of the variability within the data set and second PC accounts for 22% of the variability. 65
Figure 3.8. Spatial distribution of sediment types identified through cluster analysis of geochemical variables. 66
Figure 3.9. Results of cluster analysis displaying the locations which have similar U_{sig} properties. 68
Figure 3.10. A one dimension plot of U_{sig} highlighting the delineation between wave group 1 (blue) and wave group 2 (red). 68
Figure 3.11. Data from mooring M5a displaying (a) the distribution of EI throughout the water column and (b) the τ_w (red) and the filtered EI (blue) at 18.5 m. 70
Figure 3.12. Data from Mooring M7 showing (a) the distribution of EI throughout the water column and (b) the τ_w (red) and the filtered EI (blue) at 17 m. 71
Figure 3.13. A colour-coded time series plot of wave-induced shear vs EI at M7. 71

Figure 3.14. Data from Mooring M8 showing (a) the distribution of EI throughout the water column, and (b) the observed wave induced shear stress (red) and the EI (blue) at 3.2 m above the sea floor in a water depth of 45 m. 72
Figure 3.15. Wave shear stress vs EI at M8, just south of Thistle Island near the mouth of Spencer Gulf. 73
Figure 3.16. Seafloor classification based on U_{stg} for the entire model domain. 74
Figure 3.17. The contours in this figure show the required significant wave height (H_s in m) as a function of water depth and mean wave period (T_m) to exceed the orbital velocity of 0.07 m s^{-1}. Shading indicates the typical values of T_m for various conditions. 75
Figure 3.18. The spatial distribution of carbonate in sediments. 79
Figure 3.19. The spatial distribution of organic carbon in sediments. 80
Figure 3.20. The spatial distribution of total nitrogen in sediments. 80
Figure 3.21. The spatial distribution of total phosphorus in sediments. 81
Figure 3.22. The spatial distribution of porewater ammonium concentration in sediments. 81
Figure 3.23. The spatial distribution of porewater phosphate concentration in sediments. 82
Figure 3.24. The spatial distribution of $\delta^{13}C$ signatures in sediments. 82
Figure 3.25. The spatial distribution of $\delta^{15}N$ signatures in sediments. 83
Figure 4.1. Study area map showing the location of monthly monitoring sites. 86
Figure 4.2. Simulated suspended sediment concentrations in surface waters vs monthly data (October 2005-March 2006) along an inshore/offshore gradient east of Port Lincoln (see Figure 4.1 for site locations). The error bars show standard deviation of the data. 90
Figure 4.3. Mean (a) and maximum (b) modelled bottom shear velocity (m s^{-1}) due to waves and currents. 92
Figure 4.4. Mean (a) and maximum (b) modelled bottom shear velocity (m s^{-1}) due to currents (no waves). 92
Figure 4.5. Apparent roughness due to waves (z0_wave) and physical roughness due to small scale near bottom features (z0_ripple) at site R24. 92
Figure 4.6. Probability of apparent roughness due to waves exceeding physical roughness during the simulation period. 93
Figure 4.7. Simulated probability of resuspension for (a) fine unconsolidated sediments (critical friction velocity 0.005 m s^{-1}) and (b) fine consolidated sediments (critical friction velocity 0.014 m s^{-1}). 94
Figure 4.8. Simulated (a) probability of TSS exceeding 1 mg L^{-1} and (b) distribution of fine sediment deposits at the surface of the benthic layer (concentrations are given in kg m^{-3}; initial concentration was 72 kg m^{-3}). 94
Figure 4.9. Map of the Port Lincoln region showing seagrass distribution (after Edyvane 1999). 95
Figure 4.10 Simulated probability of resuspension of consolidated sediments for scenarios having (a) physical roughnes due to ripples increased from the baseline of 0.00033 m to 0.0033 m (b) the sediment grain size increased from the baseline of 0.2 mm to 1 mm. 96
Figure 4.11. TSS at site R24 under the baseline scenario and a scenario with increased ripple height (from 1 to 3 cm). 96
Figure 4.12. Simulated TSS at site R24 under the baseline scenario and a scenario with the reduced critical resuspension friction (from 0.014 to 0.010 m s^{-1}) 97
Figure 4.13. Simulated TSS at site R24 under the baseline scenario and a scenario with doubled wave height. 97
Figure 5.1. Left panel is a map of sites sampled previously by SARDI (+) and sites sampled from August or October 2005 to September 2006 for phytoplankton and water column characteristics. In this report this area is referred to as the TFZ. Right panel shows the locations of moorings deployed in Spencer Gulf – these sites are referred to as M1-M5. 103
Figure 5.2. The temporal dynamics of nutrients measured at locations in the TFZ and/or further afield. Figure 5.1 indicates locations. Error bars are ± 1 standard deviation. 106
Figure 5.3. Nutrient ratios from Aquafin CRC sampling of DIN (NO_3^-, NO_2^-, NH_4^+), PO_4^{3-} and SiO_2 (see Figure 5.1 for site locations, Figure 5.2 for original data). Circles indicate dates when the combination of nutrient concentrations (Figure 5.2.) and ratios suggest potential limitation by a particular nutrient (blue = Si; red = N; black =P). 108
Figure 5.4. Nitrate and ammonium concentrations from this project (detailed above) and SA EPA sampling (details at http://www.epa.sa.gov.au/nrm_map.html). Solid lines are running means. 109
Figure 5.5. Relationships between DIN inputs (calculated as winter maximum DIN concentration minus summer minimum DIN concentration) and annual mean chlorophyll-*a* concentrations. The dotted regression line refers to water bodies where *in situ* measurements of both nutrients and chlorophyll-*a* were obtained (larger symbols), the continuous regression line is from deeper more offshore water bodies where remote sensing was used to estimate mean annual chlorophyll-*a* (smaller symbols). The closely clustered pink crosses are sites 22, 24, 25, 26, 39, 43, 44 from this study (Thompson, unpublished data). 111

Figure 5.6. Temporal dynamics of remotely sensed chlorophyll-*a* and sea surface temperature for the region around the TFZ (34 to 36°S x 135 to 137°E -120 x 120 nautical miles) obtained from NASA (http://reason.gsfc.nasa.gov/Giovanni/). 112
Figure 5.7. Temporal dynamics of remotely sensed chlorophyll-*a* and sea surface temperature for the region around the TFZ (34 to 36°S x 135 to 137°E -120 x 120 nautical miles), obtained from NASA (http://reason.gsfc.nasa.gov/Giovanni/). Annual anomalies in chlorophyll-*a* were summed and plotted versus year. Years with positive anomalies (e.g. 2003) had more chlorophyll-*a* than other years (e.g. 2002 & 2006). These anomalies were significantly correlated with sea surface temperature (bottom panel). 113
Figure 5.8. Relationships between sea surface temperature in winter and surface nitrate concentrations from the 50 m coastal sites at Rottnest Island (WA), Maria Island (Tas) and Port Hacking (NSW). Lines are linear regressions through data from specific sites or overall (black). Data are available at: http://www.marine.csiro.au/warehouse/servlet/HTMLManager..... 114
Figure 5.9. Regional nutrients: Pictorial analysis of all CSIRO data for surface silicate (top panel), nitrate (middle panel) and phosphate (bottom panel) showing concentrations contours (μM); data available at: http://www.marine.csiro.au/~dunn/cars2006/. Purple indicates low concentrations, through to red which indicates high concentrations..... 116
Figure 5.10. Data for nitrogen inputs into the ecosystem from the food provided to the farmed tuna as estimated from the reported quantity of baitfish fed in 2006. Baitfish were assumed to be 3.25% N and N retention by tuna was assumed to average 9.5% (Fernandes et al. 2007)..... 118
Figure 6.1. The location of stations A to N used to investigate the seasonal chlorophyll-*a* and SST variability within and around Spencer Gulf, South Australia (co-ordinates are given in Table 6.1)..... 132
Figure 6.2. Relationship between chlorophyll-*a* determined via MODIS and collected in the field, with measurements shown in red from depths of less than or equal to 20 m and measurements in blue from water depths greater than 20 m. 133
Figure 6.3. Relationship between SST determined via MODIS and measured in the field..... 134
Figure 6.4. South Australian monthly chlorophyll-*a* climatology (μg L^{-1}) from MODIS/Aqua between 2002 and 2007. Note that values along the inshore margins are likely to be overestimated due to bottom reflectance. 135
Figure 6.5. The monthly chlorophyll-*a* concentrations at stations A, D and G from July 2002 to June 2007 (a) and the monthly climatology averaged over the 5 year period (b)..... 136
Figure 6.6. The monthly chlorophyll-*a* concentrations at stations H, D and I from July 2002 to June 2007 (a) and the monthly climatology averaged over the 5 year period (b)..... 137
Figure 6.7. The chlorophyll-*a* climatology in each month of the year at stations along the transect from A in northern Spencer Gulf to G outside the mouth of the gulf. 138
Figure 6.8. Dendrogram from hierarchical cluster analysis using Ward's method showing the similarities between stations based on chlorophyll-*a*..... 139
Figure 6.9. Results of an unsupervised classification upon 60 MODIS monthly chlorophyll-*a* images between July 2002 and June 2007. 139
Figure 6.10. South Australian monthly SST climatology (°C) from MODIS/Aqua between 2002 and 2007..... 141
Figure 6.11. Monthly average SST (a) and monthly SST climatology (b) at stations A, C, E and G highlighting the decrease in range of temperatures experienced with distance from northern Spencer Gulf..... 142
Figure 6.12. The SST climatology at stations along the transect from station A in northern Spencer Gulf and G outside the mouth of the gulf. 143
Figure 6.13. Dendrogram from hierarchical cluster analysis using Ward's method showing the similarities between stations based on SST..... 143
Figure 6.14. Results of an unsupervised classification upon 60 MODIS monthly SST images between July 2002 and June 2007. 144
Figure 6.15. (a) Monthly SST climatology during February, showing the warm gulf waters isolated from the adjacent shelf waters by the SST front during summer and (b) Monthly SST climatology during July, showing the tongue of warm GAB water extending past the mouth of Spencer Gulf during winter. Note the different scales on the colour bars..... 147
Figure 6.16. Monthly SST (a) and monthly chlorophyll-*a* (b) of March 2003 showing upwelling in the southeast of SA, on southwestern Kangaroo Island and on western Eyre Peninsula as indicated by cooler surface temperatures and increased chlorophyll-*a*. 148
Figure 7.1. Map of sites (43, 44, 39, 26, 25, 24, 22) sampled from August 2005 to September 2006 in the TFZ. .. 153
Figure 7.2. Regions used in the non-metric Multidimensional Scaling (nMDS) analysis of community composition in the TFZ and the eastern Great Australian Bight. 156
Figure 7.3. Sites outside Boston Bay (circled) used in a comparison of phytoplankton community composition between the TFZ and other regions of southern Spencer Gulf. 156

Figure 7.4. Size fractionated chlorophyll-*a* concentrations at 7 sites in the TFZ (see Figure 7.1) during part of 2005 and 2006. Circles indicate surface samples. Triangles indicate deepwater samples. Means are regional means (ie: the mean for all sites in the figure). 158
Figure 7.5. Monthly variations in phytoplankton abundance in the TFZ. Site locations shown in Figure 7.1. Circles indicate surface samples. Triangles indicate deepwater samples. Note the change in scale on the y axis for dinoflagellates and other phytoplankton. Means are regional means (ie: the mean for all sites in the figure). 159
Figure 7.6. Temporal variation in the concentration of selected marker pigments as a ratio of total chlorophyll-*a* (weight:weight) in the small size fraction (<5 μm) from samples collected in the TFZ during 2005 and 2006. Generally fucoxanthin is considered a marker for diatoms, chorophyll *b* in the absence of lutein and prasinoxanthin suggests an increased presence of certain prasinophytes, 19'-hexanoyloxyfucoxanthin of haptophytes and zeaxanthin suggests an increase in the cyanobacteria (see text for more details). Means are regional means (ie: the mean for all sites in the figure). 161
Figure 7.7. Temporal variation in the concentration of selected marker pigments as a ratio of total chlorophyll-*a* (weight:weight) in the large size fraction (>5 μm) from samples collected in the TFZ during part of 2005 and 2006. Generally fucoxanthin is considered a marker for diatoms and peridinin a marker for dinoflagellates (see text for more details). Means are regional means (ie: the mean for all sites in the figure)..... 162
Figure 7.8. The region of southern Spencer Gulf and Eyre Peninsula used to assess the temporal pattern of phytoplankton biomass using SeaWiFs chlorophyll-*a* data from 29 Aug 1997 to 13 Sept 2006. Average chlorophyll-*a* for the entire period is given in μg L^{-1} chlorophyll-*a*. 163
Figure 7.9. Eight day average SeaWiFs chlorophyll-*a* data for the region from 34°S to 36°S and 135°E to 137°E (see Figure 7.8). 163
Figure 7.10. A comparison of chlorophyll-*a* data from 6 EPA sites in Boston Bay with a single site at Port Hughes, Yorke Peninsula. 164
Figure 7.11. Top panel, time series of chlorophyll-*a* data from EPA sites in Boston Bay. Bottom panel, mean chlorophyll-*a* concentrations for Risk and Response sampling sites (2005-2006 data only) and EPA sites (1998-2007). Error bars are standard error of the mean. Analysis of EPA chlorophyll-*a* data shows that EPA1 (North Shields) is significantly different from all other EPA sites (statistics by nonparametric, paired (by time) comparisons). 165
Figure 7.12. Temporal variation in phytoplankton abundance in the TFZ from the TBOASA data. Note the change in scale on the y axis for dinoflagellates and other phytoplankton. 166
Figure 7.13. Temporal variation in nutrient concentrations in the TFZ. Circles represent surface concentrations, triangles represent deepwater samples. Means are regional means (ie: the mean for all sites in the figure).... 168
Figure 7.14. Non-metric Multidimensional Scaling (nMDS) ordination plot showing spatial variation in phytoplankton community composition in the eastern Great Australian Bight and south western Spencer Gulf. Regions are outlined in Figure 7.2. 169
Figure 7.15. Statistical analysis of the degree of similarity in toxic phytoplankton species found across 19 sites across the Spencer Gulf and Eyre Peninsula during May 2006. Site identifiers are consistent with SASQAP database. Sites that cluster together (colour groups) are similar. Sites that link with short lines are most similar. 171
Figure 7.16. A dendogram of the Bray & Curtis association matrix for phytoplankton community composition at 7 different sites in the TFZ and lower Spencer Gulf. Sites that cluster together (colour groups) are similar. Sites that link with short lines are most similar. 171
Figure 7.17. Statistical analysis of the phytoplankton species discriminating the 7 sites in the TFZ and lower Spencer Gulf. Colour indicates the degree of similarity between sites (see legend). Black indicates a high degree of similarity in species abundance while white indicates a low degree of similarity. For example the taxa *Amphora* sp. was often found at similar abundances at sites RM1, RM3, R25, R44, RM2, R39 but not R22. Site R22 was most different from site R39 in terms of species composition and abundance..... 172
Figure 7.18. TFZ Harmful Algal Bloom (HAB) species, 2005-06. Temporal variation in abundance of (a) *Karenia* spp. and (b) *Gymnodinoid* spp. Circles represent surface samples, triangles represent deepwater samples. Means are regional means (ie: the mean for all sites in the figure)..... 173
Figure 7.19. TFZ Harmful Algal Bloom (HAB) species, 2005-06: temporal variation in abundance of *Prorocentrum* spp. Circles represent surface samples, triangles represent deepwater samples. Means are regional means (ie: the mean for all sites in the figure). 174
Figure 7.20. TFZ Harmful Algal Bloom (HAB) species, 2005-06: Temporal variation in abundance of *Chrysochromulina* spp. Circles represent surface samples, triangles represent deepwater samples. Means are regional means (ie: the mean for all sites in the figure). 175
Figure 7.21. TFZ Harmful Algal Bloom (HAB) species, 2005-06: Temporal variation in abundance of *Akashiwo sanguineum* and *Chattonella* spp. Circles represent surface samples, triangles represent deepwater samples. Means are regional means (ie: the mean for all sites in the figure)..... 176

Figure 7.22. TFZ Harmful Algal Bloom (HAB) species, 2005-06: Temporal variation in abundance of *Pseudonitzschia* spp. Circles represent surface samples, triangles represent deepwater samples. Means are regional means (ie: the mean for all sites in the figure). 177
Figure 7.23. TBOASA database Harmful Algal Bloom (HAB) species: Temporal variation in abundance of *Karenia* spp. Note different scales on y axis. 178
Figure 7.24. TBOASA database Harmful Algal Bloom (HAB) species: Temporal variation in abundance of *Gymnodinium* spp. 179
Figure 7.25. TBOASA database Harmful Algal Bloom (HAB) species: Temporal variation in abundance of *Chattonella* spp. 180
Figure 7.26. TBOASA database Harmful Algal Bloom (HAB) species: Temporal variation in abundance of *Trichodesmium* spp. 181
Figure 7.27. A time series of the SASQAP data for densities of *Chattonella* (all species), *Karenia brevis* and *Karenia mikimotoi* at the 5 sites (Bickers Island, Boston Bay, Proper Bay, Louth Bay, Lincoln) in or near the TFZ. .. 182
Figure 7.28. The spatial distribution of the 3 main ichthyotoxic species *Chattonella* (all species), *Karenia brevis* and *Karenia mikimotoi* showing the mean density at 5 SASQAP sites: Bickers Island, Boston Bay, Proper Bay, Louth Bay & Port Lincoln, in or near the TFZ. (Note the relatively small number of samples from Lincoln had no observations of these species). 184
Figure 8.1. Map of southern Spencer Gulf with site locations sampled from October 2005 – October 2007 for microphytobenthos (sites 22, 25, 39, 44) and water column phytoplankton (all sites, refer chapter 7). 197
Figure 8.2. The total MV chlorophyll-*a* concentration in replicate samples collected monthly during 2005/06 from site 22. 198
Figure 8.3. The mean MV chlorophyll-*a* concentration in samples collected (a) monthly during 2005/06 and (b) quarterly during 2007 from sites 22, 25, 39 and 44. 199
Figure 8.4. The average seasonal MPB chlorophyll-*a* concentration for samples collected from October 2005 to October 2007 from sites 22, 25, 39 and 44. 200
Figure 8.5. The mean MV chlorophyll-*a* concentration in surface water (red line) and MPB (blue line) samples collected monthly during 2005/06 from (a) offshore site - 25 and (b) inshore site - 39. 201
Figure 8.6. The composition of marker pigments for MPB samples collected (a) monthly during 2005/06 and (b) quarterly during 2007 from sites 22, 25, 39 and 44. Pigments are Perid (peridinin); But-fuco (19'-*b*utanoyloxyfucoxanthin); Fuco (fucoxanthin); Pras (prasinoxanthin); Hex-fuco (19'-hexanoyloxyfucoxanthin); Astax (astaxanthin); Allo (alloxanthin); Zea (zeaxanthin); Lut (lutein); Chl *b* (chlorophyll-*b*). 202
Figure 8.7. The proportion of "living" biomass (as indicated by total MV chlorophyll-*a*) and "non-living" biomass (as indicated by the total of degradation pigments) for MPB samples collected (a) monthly during 2005/06 and (b) quarterly during 2007, from sites 22, 25, 39 and 44. 204
Figure 8.8. The proportion of different degradation pigments for MPB samples collected (a) monthly during 2005/06 and (b) quarterly during 2007 from sites 22, 25, 39 and 44. 205
Figure 8.9. Mean monthly concentrations of ammonia (left column) and phosphate (right column) in porewaters collected monthly during 2005/06 from sites 22, 25, 39 and 44. Error bars indicate standard deviation. 210
Figure 8.10. The N:P ratio in porewaters collected monthly during 2005/06 from sites 22, 25, 39 and 44. Error bars indicate standard deviation. 211
Figure 8.11. The variation of wave characteristics collected monthly during 2005/06 along the E-W transect. (a) the mean wave height (H_s) and (b) the orbital velocity at each site with ± standard deviation error bars. 212
Figure 9.1. Map of sampling sites for plankton ecology. The ADCP was moored at site 24 in July 2007. 219
Figure 9.2. Spatial variation in phytoplankton photosynthesis-irradiance characteristics in the TFZ in July 2007 (see Figure 9.1 for site locations). Circles indicate mean measured values ± standard error, n = 3. 221
Figure 9.3. Photosynthetic parameters alpha (α) the initial slope of the photosynthesis versus irradiance relationship, and P^B_{max} the maximum photosynthetic rate. 221
Figure 9.4. Daily integrated primary production (bars) for multiple sites in the TFZ from March 2007 to October 2007. Turnover times (TT) calculated as standing stock of chlorophyll-*a* /maximum photosynthetic rate (squares), the inverse (1/TT) as the gross phytoplankton growth rate (circles). 222
Figure 9.5. A single example of the experimental results showing the apparent growth rates of phytoplankton for the 12 incubated bottles plotted against the fraction of unfiltered seawater. 223
Figure 9.6. Summary of phytoplankton gross growth rates (μ_g) at sites 25 and 44 during 2007. Error bars indicate standard error. 223
Figure 9.7. Summary of grazing rate (g) of microhetertrophs on phytoplankton at sites 25 and 44 during 2007. Error bars indicate standard error. 224
Figure 9.8. Net growth rates of phytoplankton (μ_n) at sites 25 and 44 during 2007. Error bars indicate standard error. 224

Figure 9.9. (a) Net growth rates for fucoxanthin in microzooplankton grazing experiments during 2007. **(b)** Net growth rates for prasinoxanthin in microzooplankton grazing experiments during 2007. Error bars indicate standard error. 225
Figure 9.11. Net growth rates (μ_n) for sites in the TFZ (SA) in 2007, Huon Estuary (Tasmania) in 2003-04, 2005 & 2007, and the Great Australian Bight (GAB), 2006. 226
Figure 9.12. Composition of the large and small zooplankton community averaged over all times and all dates. 227
Figure 9.13. The echo intensity from an ADCP mounted on a mooring at site 24 (see Figure 9.1) deployed from 12/7/07 to the 19/7/07. 228
Figure 9.14. Estimated grazing rates by meso and microzooplankton as a percentage of phytoplankton standing stock per day. 229
Figure 10.1. Satellite image (Google Earth™) showing embayments of model domain. 236
Figure 10.2. Schematic diagram of the biogeochemical model compartments, links and vertical layers. Green compartments have fixed nutrient content at Redfield ratio (106C:16N:1P); brown compartments are fixed at Atkinson ratio (550C:30N:1P). 237
Figure 10.3. Upstream open boundary condition for nutrient concentration. 244
Figure 10.4. Upstream open boundary condition for phytoplankton biomass. 244
Figure 10.5. Southern Bluefin Tuna farm locations for 2006. 245
Figure 10.6. Southern bluefin tuna farm cumulative feed input. Different colours reporesent feed inputs to different leases (leases not identified due to confidentiality) Source: TBOASA. 245
Figure 10.7. CTD and in-situ sampling site locations (22 – 44). Mooring locations shown as M4 – M6, with letters corresponding to n deployment periods (a–f). Monthly sampling procedures and analysis protocols are described in chapter 7. 246
Figure 10.8. Surface (left) and bottom (right) chlorophyll-*a* concentrations from biogeochemical model simulation (red) and in-situ observations (blue) at sites throughout the TFZ. 247
Figure 10.9. Surface (left) and bottom (right) dissolved inorganic phosphate concentrations from biogeochemical model simulation (red) and in-situ observations (blue) at sites throughout the TFZ. 247
Figure 10.10. Surface (left) and bottom (right) dissolved inorganic nitrate concentrations from biogeochemical model simulation (red) and in-situ observations (blue) at sites throughout the TFZ. 248
Figure 10.11. Surface (left) and bottom (right) ammonia concentrations from biogeochemical model simulation (red) and in-situ observations (blue) at sites throughout the TFZ. 249
Figure 10.12(a). Moorings 4 and 6 were configured with an acoustic release, a bottom–mounted ADCP, a weight and a mid–water Seabird multi-sensor. 250
Figure 10.12(b). Mooring 5 was configured with an acoustic release, a bottom–mounted ADCP, a Seabird multi-sensor and transmissometer. 250
Figure 10.13. Mooring data from M4 showing fluorescence quenching during the daytime. 251
Figure 10.14. Uncalibrated moored fluorometer chlorophyll (with daytime values removed) and modelled chlorophyll for the same locations (M4, M5 & M6) and depths. 251
Figure 10.15. Uncalibrated moored dissolved oxygen concentration (mg L^{-1}) and modelled dissolved oxygen concentration for the same locations (M4, M5 & M6) and depths. 253
Figure 10.16. Uncalibrated moored PAR data ($\mu E\ m^{-2}\ s^{-1}$) and modelled PAR ($W\ m^{-2}$) for the same locations (M4, M5 & M6) and depths. 254
Figure 10.17. Uncalibrated turbidity from the moored transmissometer and modelled attenuation coefficient (m^{-1}) for the same locations (M4, M5 & M6) and depths. 255
Figure 10.18. Monthly mean surface chlorophyll-*a* 256
Figure 10.19. Monthly mean bottom water chlorophyll-*a* concentration. 257
Figure 10.20. Monthly mean chlorophyll-*a* concentration along CTD transect (Figure 10.7) from west (left) to east (right). 257
Figure 10.21. Monthly mean bottom water dissolved oxygen (DO) saturation. 258
Figure 10.22. Monthly mean dissolved oxygen (DO) saturation along CTD transect (Figure 10.7) from west (left) to east (right). 259
Figure 10.23. Monthly mean surface dissolved inorganic nitrogen (DIN). 260
Figure 10.24. Monthly mean bottom water dissolved inorganic nitrogen (DIN). 260
Figure 10.25. Monthly mean dissolved inorganic nitrogen (DIN) concentration along CTD transect (Figure 10.7) from west (left) to east (right). 261
Figure 10.26. Monthly mean surface dissolved inorganic phosphorus (DIP). 261
Figure 10.27. Monthly mean dissolved inorganic phosphorus (DIP) concentration along CTD transect (Figure 10.7) from west (left) to east (right). 262
Figure 10.28. Monthly mean bottom water ammonium (NH_x). 262

Figure 10.29. Monthly mean ammonium (NH_x) concentration along CTD transect (Figure 10.7) from west (left) to east (right). 263
Figure 10.30. Fish farm impact on pelagic depth integrated DIN, DIP and chlorophyll, and bottom water dissolved oxygen saturation. XS – increase in nutrient above what the model predicts without farm inputs. The table at the bottom of each panel indicates the percentage of the year for which levels are at least y % (y = 10, 20, 30, 50 except for DO where y= 1, 5, 10, 20) above abient for at least x months (x = 1, 3, 6)..... 264
Figure 10.31. Monthly mean seagrass nitrogen. 265
Figure 10.32. Monthly snapshots of microphytobenthos nitrogen in the surface sediment (correct units are mgN m^{-2}). 266
Figure 10.33. Monthly snapshots of dissolved oxygen (DO) concentration in the surface sediment..... 266
Figure 10.34. Monthly snapshots of ammonia (NHx) in surface sediment. 267
Figure 10.35. Monthly snapshots of dissolved inorganic nitrogen (DIN) in surface sediments..... 268
Figure 10.36. Monthly snapshots of dissolved inorganic phosphorus (DIP) in surface sediment..... 268
Figure 10.37. Excess monthly mean depth integrated dissolved inorganic nitrogen (DIN) due to fish farm waste loads..... 269
Figure 10.38. Excess monthly mean depth integrated dissolved inorganic phosphorus (DIP) due to fish farm waste loads..... 269
Figure 10.39. Excess monthly mean depth integrated chlorophyll due to fish farm waste loads. 270
Figure 10.40. Reduction in monthly mean bottom water dissolved oxygen (DO) due to fish farm loads..... 270
Figure 10.41. Monthly snapshots of excess dissolved inorganic nitrogen (DIN) in surface sediment due to fish farm waste loads. 271
Figure 10.42. Monthly snapshots of excess dissolved inorganic phosphorus (DIP) in surface sediment due to fish farm waste loads..... 271
Figure 10.43. Monthly snapshots of excess chlorophyll in surface sediment due to fish farm waste loads. Note contoured areas in purple have reduced chlorophyll due to fish farm waste loads. 272
Figure 10.44. Monthly snapshots of reduced dissolved oxygen (DO) in surface sediment due to fish farm waste loads..... 272
Figure 10.45. Fish farm impact on regional surface sediment properties..... 273

Non Technical Summary

2005/059 Aquafin CRC – Southern Bluefin Tuna aquaculture subprogram: Risk and Response – Understanding the Tuna Farming Environment

PRINCIPAL INVESTIGATOR: Dr J.E. Tanner
ADDRESS: SARDI Aquatic Sciences
PO Box 120,
Henley Beach, S.A. 5022
Telephone: 08 8207 5489
Fax: 08 8207 5481
Email: tanner.jason@saugov.sa.gov.au

OBJECTIVES:

1. Characterisation of the main oceanographic features of the tuna grow-out region at Port Lincoln through field studies and calibration of the three dimensional hydrodynamic model previously developed for salmonid farming in Tasmania.
2. Identification and description of dynamics of phytoplankton and benthic microalgal species, the factors causing algal blooms and the role, if any, of nutrients released from tuna farming.
3. Integration of phytoplankton and nutrient data into a 3D biogeochemical model for the Port Lincoln farming area that will allow movement of blooms etc to be predicted.
4. Refine description of variations in sediment type and assimilative capacity for organic matter including an assessment of the role of microbial and faunal communities in carbon remineralisation and nutrient release.
5. Application of sediment models to identify likelihood of sediments being resuspended and identification of factors affecting this together with an assessment of their role in algal blooms.
6. Further development of the near real-time telemetered environmental observation system with web access.
7. The above all lead to the primary objective, which is to develop an integrated hydrodynamic and biogeochemical model of the Port Lincoln tuna farming area, that will assist managers and farmers to assess how external and internal disturbances are likely to move through the area, and thus allow them to make informed decisions on how to best mitigate the risks associated with any given disturbance, and to develop pre-prepared emergency management protocols for particular events. Establish a steering committee of stakeholders and hold a Steering Committee for Fisheries and Aquaculture Environmental Sustainable Development reporting workshop to develop a set of operational parameters for regional scale environmentally sustainable development (ESD) assessment.

Outcomes Achieved to Date:

This project has produced an integrated hydrodynamic, sediment and biogeochemical model of the tuna farming zone (TFZ) and surrounds that encapsulates most of our knowledge about the relevant processes acting in this region. In developing this suite of models, a substantial effort was also made to improve our understanding of the processes operating in the TFZ. As a consequence, we now understand the hydrodynamics, nutrient cycling, sediment dynamics and phytoplankton ecology much better than previously. As an example, it was previously considered that the farming zone was hydrodynamically well connected to southern Spencer Gulf, and that nutrients would likely be flushed out into the gulf itself. However, we have demonstrated that this is not correct, and that not only is the farming zone relatively poorly connected to the rest of the gulf, but that nutrients tend to be advected inshore, and particularly to the north-west, where they accumulate in Louth and Peake bays.

The hydrodynamics of the tuna farming zone (TFZ) were examined through the deployment of oceanographic moorings and the development of a high resolution model of the zone and all inshore areas from Cape Donnington in the south to Point Bolingbroke in the north. This model was nested in a lower resolution model of Spencer Gulf, and while the low resolution model displayed some discrepancies with known current patterns, the high resolution model appeared to have good predictive ability. The model showed that mean currents were relatively weak, although tidal currents could reach speeds of up to 20 cm s^{-1}, and that flushing of the entire model domain took around 20 days. Particles introduced into the TFZ tended to move into inshore areas, especially in Louth Bay, before being eventually flushed from the region.

A wave model of the same domain showed that the area south of Point Bolingbroke and east of Cape Donnington was subject to both locally generated wind waves and oceanic swell, while inshore areas were relatively protected. There was, however, an area in Louth Bay that experienced relatively energetic conditions near-shore. The greatest swell height in the TFZ occurs when oceanic swells come from due south, with swell height being 8-10% of that found on the continental shelf. The more westerly the swell direction, the lower the swell height in the TFZ. The highest wind waves are generated by winds from the east and south-east, which have the greatest fetch.

Sediments in the central TFZ are distinct from those found elsewhere in the region, being enriched in nutrients and having a higher percentage of fine silts. Much of the TFZ is depositional in nature, with a high percentage of fine sediments. The greatest risk of sediment resuspension is associated with incoming swell from the southern ocean. Field measurements suggest that only weak sediment resuspension is occurring during routine storm events, although major storms could cause problems.

Sediment modelling also indicates that sediment resuspension is primarily only likely to be a problem during acute storm events, as wave action is insufficient to resuspend fine sediments in most of the region once they have had a chance to settle for a few days and become consolidated. However, during acute events, those with return times > 1 year, there is a substantial amount of fine sediment that can become resuspended, and which might pose a risk to the industry.

There were no differences in nutrient concentrations between surface and bottom samples, and few spatial differences within the TFZ. There was substantial temporal variability, however, and as a consequence of this, different nutrients became limiting at different times of year. Nitrogen tended to be limiting through most of the farming season (February-August), while silica was limiting in December and phosphorus in September. These patterns suggest a regular injection of dissolved inorganic nitrogen into the area in autumn, probably from waters on the continental shelf, as the spatial scale of this phenomenon is too large to be due to anthropogenic activities. However, tuna farming provides an important augmentation to this natural nitrogen source. The inshore data from the EPA showed that nutrient levels were relatively low in Boston Bay when compared to other sites in Spencer Gulf and on the west coast of SA. The remotely sensed data showed a strong and consistent peak in chlorophyll-*a* in May, with a low in December.

MODIS remote sensing was used to examine larger spatial and temporal scale patterns in sea surface temperature and chlorophyll-*a*. Waters within Spencer Gulf showed higher summer and lower winter temperatures than outside the gulf, with the TFZ being located just north of the transition between oceanic and gulf waters from a temperature perspective. The timing

and magnitude of peaks in chlorophyll-*a* levels varied with location, with areas in the northern gulf having putatively higher values (although this may be due to bottom reflectance), and the largest seasonal differences. MODIS estimations made in the TFZ appeared to be relatively good when water depth was > 20 m, but poor in shallower areas, and as discussed above, values peaked in autumn.

Concordant with the remotely sensed imagery, in situ sampling indicated a peak in phytoplankton abundance in May 2006, which is driven by an increase in diatoms. Analysis of long term datasets suggest that predominately diatom peaks have been consistent phenomena in the TFZ during late autumn or early winter. The May peak in diatoms appears to be made possible, in part, by a February peak in silica concentrations (>3.5 μmol L^{-1}). A range of Harmful Algal Bloom (HAB) species were detected, but there is little evidence of a HAB having occurred in the region. However, abundances of known ichthyotoxic phytoplankton species are sufficiently dense to warrant monitoring and caution. There is evidence that ichthyotoxic species are more prevalent in some locations than others (e.g. Bickers Island and Boston Bay), which suggests that local populations of harmful algae may be developing in the vicinity of the TFZ. A risk assessment of the potential for HABs in the TFZ suggests that the risk is currently low, although this could change under several scenarios, including if nutrient inputs increase or climate change causes waters to become stratified.

Similar to the phytoplankton, the microphytobenthos (MPB) were dominated by diatoms. There was significant variation in biomass between the inshore and offshore sites, with the deeper offshore sites tending to have higher biomass. The dominance of diatoms suggests silica availability from porewaters was not limiting. Photosynthetically active radiation (PAR) measurements showed light not to be limiting either, with between 4-28% of incident irradiance calculated at the sediment surface. High concentrations of chlorophyll degradation products and the pigment astaxanthin in the MPB samples suggest grazing of the MPB by benthic copepods. No evidence of dinoflagellates, which include most of the potentially harmful microalgal species, was found in the samples, although the methods used were not suited to detecting cysts. Previous studies have found high cyst densities of some potentially harmful species in areas inshore of the current TFZ.

The highest rates of primary production in the TFZ in 2007 occurred in March, in the lead up to the autumn phytoplankton peak that has been identified as a regular occurrence in the region. Highest phytoplankton growth rates occurred during May, at the height of the autumn phytoplankton peak. Peak micro-zooplankton abundance and biomass also occurred during May, with micro-zooplankton grazing ~70% of phytoplankton standing stock per day during this period. Peak meso-zooplankton abundance and biomass occurred during March, with ~300% of phytoplankton standing stock grazed by meso-zooplankton per day at this time. Meso-zooplankton grazing impact fell to ~30% of standing stock per day in May. The increase in phytoplankton growth rate in May is most likely due to a decrease in meso-zooplankton grazing impact from the March peak.

The biogeochemical model was initialised for September 2005 with spatially uniform pelagic and sediment concentrations of dissolved nutrients, plankton biomass, macrophytes and detritus. The model was able to reproduce the major features of the observed seasonal cycles of chlorophyll and dissolved inorganic phosphorus (DIP) when compared with observations. It successfully represented the timing and the nature of the autumn diatom peak. Preliminary model results suggest that phytoplankton productivity is seasonally limited by phosphorus during the summer months. However, uncertainty remains in the observed nutrient

biogeochemistry of the region. At inshore sites the model underestimated the observed concentration of DIP, possibly due in part to the omission of coastal sewerage loads. The impacts of farm discharge on the regional biogeochemistry were investigated by comparing scenario simulations with and without farm loads. Nutrient levels increased near fish farms and these form observable nutrient hotspots in the model results. Fish farm inputs may also lead to environmental effects distant from the farming zone. Modification to the seasonal timing of feed inputs may have an effect on the regions biogeochemistry and could be included in future modelling studies. More observations in the embayments and near shore areas would help model calibration as the model is not yet well constrained in these areas, and these results must be viewed as preliminary.

The results of this research have strong implications for aquaculture managers, in particular with respect to setting maximum farmed biomass in the TFZ, the design of regional environmental monitoring programs, and associated policy development. They provide the foundation and direction for further research and development necessary to ensure the sustainable development and equitable allocation of marine resources managed in the TFZ. Such goals can only be achieved through the integrated efforts of multi-disciplinary research teams, as presented in this report.

Keywords

Aquaculture, Remote sensing, Environmental sustainability, Tuna farming, Oceanography, Environmental risks, Hydrodynamics, Biogeochemistry, Sediment model, Sediment resuspension, Phytoplankton, Harmful algal bloom

Acknowledgements

This work formed part of a project of Aquafin CRC, and received funds from the Australian Government's CRCs Program, the Fisheries R&D Corporation and other CRC Participants. SARDI Aquatic Sciences, CSIRO Marine Research, Adelaide University, Flinders University and the Tuna Boat Owners Association of South Australia (now Australian Southern Bluefin Tuna Industry Association) provided additional support. The authors would like to thank the Tuna Boat Owners Association of South Australia, and particularly David Ellis, for their support in achieving the outcomes of this project, and their input into various chapters of this report.

Thank you to all those who have been involved in the project. The primary contributors are listed in Appendix 2, although many volunteers have also contributed to various aspects of the project. Kathryn Wiltshire formatted each of the chapters and combined them into this single report.

Special thanks go to those who have reviewed this report, or sections thereof, especially Marty Deveney, Milena Fernandes, Charles James, Maylene Loo, John Luick, Stephen Madigan, John Middleton, Sasi Mayar, Sunil Sharma and Paul van Ruth.

Background

The broad concept of this project was initially developed in the planning phase for the Aquafin CRC, and it is identified in the Aquafin CRC Commonwealth Agreement under both the strategies and deliverables. The concept for this proposal was further developed at a meeting attended by J. Volkman, A. Cheshire, J. Tanner and D. Ellis at SARDI, May 7-8th, 2003 to directly address industry concerns about potential environmental risks to the tuna farming zone. In particular, interest was expressed by industry in being able to identify risks, forecast their likely movement in space over time (e.g. spread of a phytoplankton bloom), and develop risk mitigation procedures such as identifying safe sites to which pontoons could be moved. At the same time, both industry and the regulators are keen to maintain and enhance the industry's current high environmental standards. These ideas were further refined through informal discussions with industry and Government representatives over the next year and formalised at a research workshop at SARDI on May 11th, 2004 and CSIRO on August 23rd and 24th, 2004. An outline of the project proposal was presented to the SBT Aquaculture Subprogram Steering Committee in Port Lincoln on October 27th, 2004, and received support from the industry representatives present. The project amalgamates work currently being done in 2001-103 (waste mitigation and partitioning) and 2001-104 (regional environmental sustainability analysis), and picks up issues that have been identified in each project. The general approach follows that developed by CSIRO in project 2001/097, with the modeling protocols developed for Tasmania being directly transferred to South Australia. Further discussions were held with industry representatives prior to the submission of this revised proposal in April 2005, and comments from industry specifically addressed in this revision.

Need

Representatives of the tuna industry have expressed a clear need to understand the oceanography of the Port Lincoln tuna farming zone (TFZ) so that they could predict likely trajectories and effects of phytoplankton blooms and any instances of dirty water on tuna farming, enabling them to develop emergency management protocols for such events. They also need to identify the range of variation in environmental conditions in both the water

column and sediments within the farming zone and how this might impact on farming practices, particularly if fish are to be kept for longer periods and if stocking numbers increase. In the event of an emergency (e.g. algal bloom, oil spill, disease outbreak), the industry needs to identify areas likely to be impacted and safer areas where pontoons might be relocated. Industry would also benefit from real-time weather and oceanographic information being available at the farm site to optimize visits to the farms for feeding, maintenance etc.

To meet this need, we have developed an integrated hydrodynamic and biogeochemical model of the tuna farming area, based on that which CSIRO have developed for the Huon Estuary. Based on the knowledge that CSIRO have gained from this previous study, and our knowledge of the data available for the Port Lincoln area, a number of knowledge gaps were identified that needed to be addressed before we could have confidence in the outputs of the model. These gaps included the extent and nature of benthic-pelagic coupling in the area (ie how do nutrients move between the water column and the sediments), the nature and role of phytoplankton in the system, the nature of the hydrodynamic regime in the area, and how prone the sediments are to resuspension under different wind and wave regimes. While it will still be possible to develop a basic modelling framework without addressing these knowledge gaps, we felt that doing this would result in the development of a poorly calibrated and inadequately verified model that could provide misleading results, possibly resulting in decisions by farmers and managers that are detrimental to the industry.

The industry depends on a healthy marine environment to maintain production and profitability. Tuna farms are a significant point source of nutrients into the marine environment (most of the nitrogen in the feed is excreted as ammonia), but this needs to be put into the context of natural nutrient levels and their seasonal variations. It is important to establish the carrying capacity of the farming region that both maintains a healthy and productive industry and protects marine environmental values. Phytoplankton blooms, including potentially harmful species such as *Chatonella*, are known in the Port Lincoln area but the causative factors are poorly understood and the influence of advection from regions further off-shore (e.g. upwelling cells) is unknown. Thus the risk they pose to the industry is unknown, and needs to be assessed.

Sediments are a key site for regeneration of nutrients back into the water column, but their quantitative importance in nutrient recycling in the Port Lincoln area is presently poorly known. Also, sediments are resuspended by waves and tide presenting an additional threat to penned tuna through gill damage, reduced feeding and as a possible source of harmful algal species from released cysts. The consequences of sediment resuspension can be dramatic as seen in the high mortality associated with the April 1996 event when tuna were held in pens located in shallow water inside Boston Island. While this is less likely with current farming practices, it would still be wise to properly assess the threat of a repeat event. Alternatively, during milder resuspension events, organic wastes may be dispersed over a larger area, allowing them to be assimilated more rapidly. The dropping of the nets to the seafloor at the end of the farming season may also act to disperse wastes and increase their assimilation.

This combination of issues and risks constitutes a significant scientific challenge. While we must continue to guard against any major environmental changes due to eutrophication, it is clear that more subtle environmental effects (phytoplankton bloom frequency and composition, zooplankton and jellyfish swarms, sediment resuspension) may affect industry production and profitability. Equally, regulators need assurance that marine ecosystems will not undergo unacceptable environmental change as industry develops. Industry and managers

not only require knowledge of environmental changes, but a capability to resolve and predict the environmental response to changes in the offshore ocean regime, changes in catchment loads, and effects of the industry itself. Advances in observation technologies, in scientific understanding, and in modelling capability, together make it possible for scientists to develop the knowledge, understanding and prediction needed to underpin both long-term planning and short-term operational decisions. The goal here is for the Aquafin CRC to work with industry and managers to provide an environmental information and prediction system that allows industry and regulators to manage environmental risk.

Objectives

1. Characterisation of the main oceanographic features of the tuna grow-out region at Port Lincoln through field studies and calibration of the three dimensional hydrodynamic model previously developed for salmonid farming in Tasmania.
2. Identification and description of dynamics of phytoplankton and benthic microalgal species, the factors causing algal blooms and the role, if any, of nutrients released from tuna farming.
3. Integration of phytoplankton and nutrient data into a 3D biogeochemical model for the Port Lincoln farming area that will allow movement of blooms etc to be predicted.
4. Refine description of variations in sediment type and assimilative capacity for organic matter including an assessment of the role of microbial and faunal communities in carbon remineralisation and nutrient release.
5. Application of sediment models to identify likelihood of sediments being resuspended and identification of factors affecting this together with an assessment of their role in algal blooms.
6. Further development of the near real-time telemetered environmental observation system with web access.
7. The above all lead to the primary objective, which is to develop an integrated hydrodynamic and biogeochemical model of the Port Lincoln tuna farming area, that will assist managers and farmers to assess how external and internal disturbances are likely to move through the area, and thus allow them to make informed decisions on how to best mitigate the risks associated with any given disturbance, and to develop pre-prepared emergency management protocols for particular events.

Chapter 1: Hydrodynamic Modelling and Observations of the Tuna Farming Zone, Spencer Gulf

Mike Herzfeld[1,3*], John F. Middleton[2,3], John R. Andrewartha[1,3], John Luick[2,3], Leeying Wu[2,3]

[1]CSIRO Division of Marine and Atmospheric Research
[2] South Australian Research and Development Institute (Aquatic Sciences)
[3] Aquafin CRC

*corresponding author: CSIRO Division of Marine and Atmospheric Research, GPO Box 1538, Hobart, Tas, 7001
Phone: +61 (3) 6232 5222, E-mail: mike.herzfeld@csiro.au

Abstract

A numerical hydrodynamic model was developed for the tuna farming zone (TFZ) region in south-western Spencer Gulf in order to investigate the circulation, flushing and connectivity. The model was forced with measured meteorological fields at the sea surface and sea surface elevation, temperature and salinity at the offshore boundary. The offshore boundary forcing was obtained using a nesting strategy involving a larger scale model of the gulf. Simulations using the model were performed for the period August 2005 – August 2006, providing output of currents, sea level and temperature and salinity distributions. The gulf-scale model reproduces the clockwise circulation expected for winter. During summer, a similar pattern is found and opposite that expected from other studies. Nonetheless, the model does show predictive ability in the TFZ region. Indeed, the data from this region show there to be strong (~20 cm s^{-1}) tidal currents that are very well reproduced by the model and that may be implicated in bottom stirring but not transport: particle displacements due to the tides were small and less than 1.4 km over a 3 hr period. Results for the weather-band currents (periods 3-20 days) are reasonably well produced by the model and show smaller currents (< 5 cm s^{-1}). However, due to the longer periods these can be important to the transport and flushing of the region: a 5 cm s^{-1} current with period 10 days will transport a fluid parcel 7 km over a 2.5 day period. Both data and model indicate the mean currents to be weak (~ 1 cm s^{1}) and to the north/north east during both summer and winter: transport here over a 3-month period is around 80 km. The currents were also found to be strongly sheared in the vertical and so may be important to shear enhanced diffusion and dispersal. However, estimates of the flushing times based on tracers and Lagrangian tracking show flushing time scales of 10 days (Boston Bay) to 2 days for the TFZ. During summer, the model and data also show a degree of connectivity between the coastal zone and the TFZ that can be caused by local upwelling during summer, whereby offshore (eastward) winds force surface waters offshore creating an onshore bottom flow. In addition, the higher evaporation that occurs near the coast leads to dense water formation and bottom plumes that flow to the TFZ. During winter, similar plumes result from coastal cooling rather than evaporation.

1.1. Introduction

Boston Bay is situated in the lower western side of Spencer Gulf adjacent to Port Lincoln (Figure 1.1) on the southern coast of Australia, and is the base for a large tuna aquaculture industry that operates just outside the bay. Studies of the tidal circulation of the gulf (eg. Easton 1978; Nixon and Noye 1999) show it to be a ¾ wave resonator whereby the semi-diurnal tidal constituents are amplified with current speeds of up to 50 cm s^{-1}, mid-gulf. Additionally, because both the M2 and S2 tides have almost equal amplitude, (but different frequency), these constituents interfere destructively leading to a 4-5 day period, every 14.8 days when the tidal velocities are small – the "dodge tide".

The gulf circulation driven by both local meteorology and remote forcing (eg., tides, coastal trapped waves) is strongly seasonal. During winter, the westerly winds and atmospheric cooling combine to drive a westerly shelf circulation with water downwelled to depths of 300 m. Shelf current speeds of up to 1 m s^{-1} have been recorded on the shelf (Middleton and Bye 2007). Within the gulf, the atmospheric cooling is known to drive a clockwise circulation that appears to be modulated by the fortnightly dodge tide when the otherwise large (~50 cm s^{-1}) currents relax to near zero. Water is drawn in along the western side of the gulf and expelled past Kangaroo Island on the eastern side of the gulf.

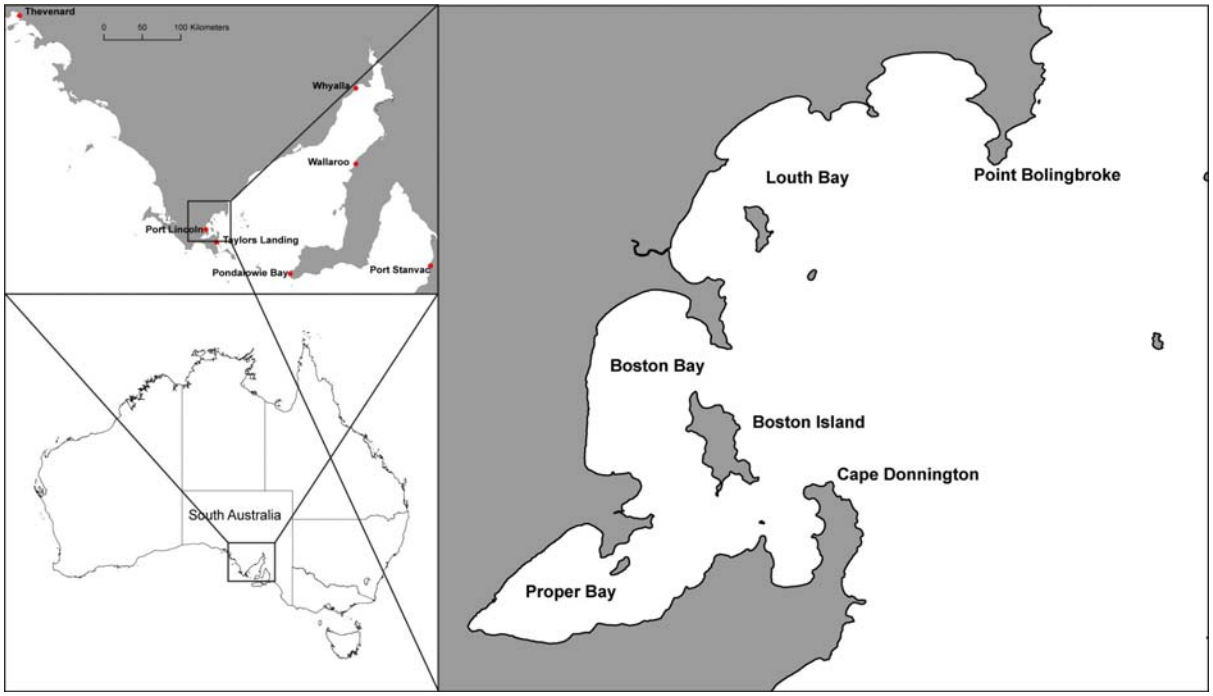

Figure 1.1. The Spencer Gulf / Boston Bay region. The labelled red sites denote locations of sea level data used in this study.

During summer, evaporation is sufficient to make the gulf water denser than that found during winter, although significant gulf-shelf exchange is not observed. The reason for this appears related to the reversal of winds and resultant upwelling to the south-east of Kangaroo Island. Indeed, the analyses of Nunes Vaz et al. (1990), Petrusivics (1993) and McClatchie et al. (2006) suggest that the upwelled water forms a pool of sub-surface, nutrient rich water across the mouth of the gulf. This water is denser than that found in the gulf and may block its passage onto the shelf (Petrusivics 1993). Some penetration of upwelled water into the eastern side of the gulf is indicated from sea surface temperature data (see the review by

Middleton and Bye 2007). However, it may be possible that sub-surface intrusions do occur: little data has been collected to answer these questions.

The circulation driven by local winds and by the circulation on the adjacent shelf has received little attention. Most recently, Middleton and Teixeira (2008) have shown that the gulf circulation driven by strong winds (10 m s^{-1}) is quite weak (< 5 cm s^{-1}) where the water depth is 10-20 m or more. The reason for this is that the conditions of zero normal flow at coastal boundaries penetrate over a distance of the external deformation radius, that is of order the width and length of the gulf. A similar result is found for the gulf circulation that is driven by shelf circulation. As we will see from the study below, weak currents (< 5 cm s^{-1}) are found for the weather-band (3-20 days) and both in the data and model. In shallow water (< 5 m), the study of Middleton and Teixiera (2008) indicates that currents can be significantly larger (~15 cm s^{-1}) since the deformation radius is smaller.

During winter, the south-eastward winds are expected to drive a clockwise circulation near the mouth of the gulf with water drawn in along the western side of the gulf and expelled along the Yorke Peninsula (Middleton and Teixeira 2008). This circulation should enhance that driven by dense water formation.

During summer, the winds and gulf circulation are expected to reverse, albeit with a weaker anticlockwise circulation near the gulf mouth (Middleton and Platov 2003; Middleton and Teixeira 2008). Consistent with this pattern, observations show cold, dense, nutrient rich water to be drawn in along the eastern gulf mouth. The origin of this water arises from the summertime upwelling onto the shelf and to the south of Kangaroo Island. As noted above, this dense water appears to prevent the strong gulf-shelf exchange that is found in winter (Lennon et al. 1987).

The numerical results below will support the above conceptual model but with two additional complexities. The first is that when the waters are stratified, the model results and data indicate that localized upwelling (downwelling) can occur for the TFZ region in the presence of eastward (westward) winds. Eastward winds drive surface gulf waters offshore that can drive a compensatory deeper onshore flow. On the adjacent shelf, eastward (westward) winds lead to downwelling (upwelling). The second complexity arises from the prediction of an clockwise circulation pattern in the southern half of the gulf during summer. This result was not expected, but notably, the model does have predictive ability in the TFZ region.

While the wind-forced circulation (~ 5 cm s^{-1}) is smaller in magnitude than that of the 12 hourly tides (30-50 cm s^{-1}), we note here that the former persist for longer times (3 –20 days) and can be more important in terms of flushing of the region and in nutrient transport. Thus, both tidal and wind-driven motions are modelled in the study below, as are density currents that arise from atmospheric cooling and evaporation.

The purpose of the model development and associated observational program is to develop a predictive capacity for currents and mixing. Insight into current regimes, flushing times, tracer dispersal distributions and residual flows can be gained from application of the model. The hydrodynamic model also forms the basis for the sediment transport and biogeochemical numerical investigations that form part of the current project (chapters 4 & 10).

In section 2, the models are described. In sections 3 and 4, output from the gulf-scale and regional model of the TFZ are discussed and a comparison with observations made. In

section 5, flushing times of regions around the TFZ are presented and a summary and discussion is made in section 6. More details are presented in Herzfeld et al. (2008).

1.2. The Hydrodynamic Models

The hydrodynamic model used to simulate the flow and mixing of the TFZ region is SHOC (Sparse Hydrodynamic Ocean Code; Herzfeld, 2006). Outputs from the model include three-dimensional distributions of velocity, temperature, salinity, density, passive tracers, mixing coefficients and sea level. The equations forming the basis of the model are similar to those described by Blumberg and Herring (1987). In the following, we describe the models and forcing fields adopted.

1.2.1 Model Domain and Topography

The simulation of the physics of the TFZ region required the construction of two models. The regional Spencer Gulf model supplied the initial and open boundary conditions for a smaller, higher-resolution local Boston Bay model. The southern extent of the domain for the TFZ model is illustrated in Figure 1.2.

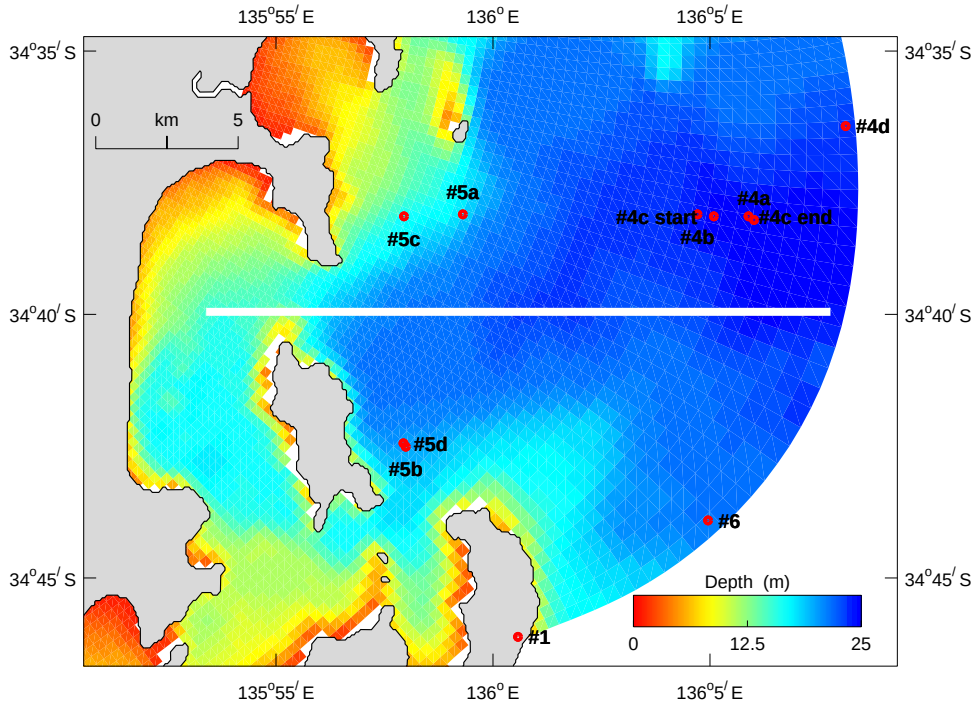

Figure 1.2. Details of moorings deployed in the TFZ. Mooring 4 was dragged during deployment #3; start and end locations are denoted 4c_start and 4c_end respectively. Mooring 4a and 4c are collectively known as mooring 4 inner, 4 d is referred to as the boundary and 4 b failed to record any data. CTD casts were made monthly from Aug 05 to Sep 06 at 6 sites along the white line.

The regional Spencer Gulf grid has a variable resolution from 1.5 km to 6 km on the eastern side of the gulf. The model uses 23 layers in the vertical with 0.5 m resolution at the surface and ~8 m resolution near the maximum depth of 60 m. The grid size is 55 x 95 x 23. The TFZ model has a grid spacing seaward from Boston Island of ~330 m and a maximum resolution of ~1 km at the offshore open boundary. The grid dimensions are 134 x 17 x19, with 0.5 m resolution in the vertical at the surface and ~4 m resolution at the bottom with a maximum depth of 30 m.

The bathymetry for the regional model was interpolated from Geoscience Australia's 1 km bathymetric product (Petkovic and Buchanan, 2002). The bathymetry for the TFZ region was initially interpolated from Geoscience Australia's 2005 product at 250 m resolution and supplemented with digitized bathymetry from the AUS134 navigational charts. The final bathymetry used for the TFZ is displayed in Figure 1.2.

1.2.2. Initial Temperature/Salinity Fields

The initial conditions for temperature and salinity for both regional and local grids were derived from the product synTS (Ridgway et al., 2006). This product uses satellite altimetry to prescribe surface temperature and sea level distributions and correlations (based on a climatological data set) to project the surface distributions through depth. The resolution of this synthetic data is 0.25 degrees.

1.2.3. Atmospheric Forcing

Wind speed and direction data were obtained from the Bureau of Meteorology at seven Automatic Weather Station (AWS) sites around Spencer Gulf and interpolated onto the regional model domain to provide a temporally and spatially varying wind-field. The wind stress was then obtained following Smith (1980) and the alongshore component for Neptune Island is shown in Figure 1.3.

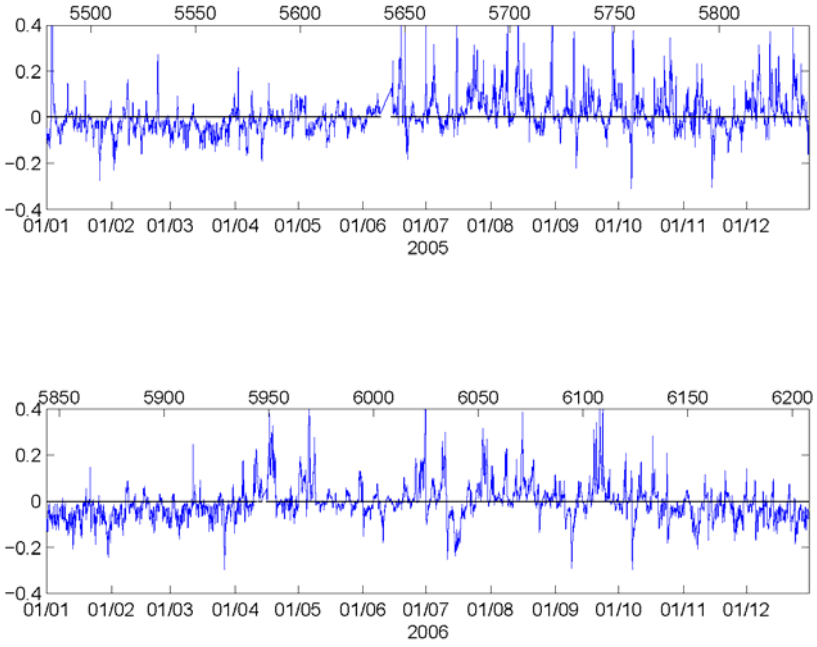

Figure 1.3. Major component of daily wind stress (Units 100Pa) from Neptune Island for 2005 and 2006. The times are indicated as dd/mm for each year as well as in Julian Days (JD) since 01/01/1990. The use of Julian Days since 1990 is CSIRO standard for their modelling suite. The major component was resolved to be that along the shelf and is positive to the southeast (shelf downwelling) and negative to the northwest (shelf upwelling).

For the July 2005-July 2006 period of interest, the winds were generally downwelling favourable along the shelf until January 1st 2006, and were then upwelling favourable until April 2006.

Surface fluxes of salt and heat were also determined from the AWS data, and model sea surface temperature. These fluxes are somewhat uncertain as they depend on the nature of the marine atmospheric boundary layer that can differ from that over land. The monthly averaged net heat fluxes are of around 300 W m^{-2} during summer and act to warm the gulf waters. Monthly averaged evaporation exceeds precipitation all year round with values of 2-8 mm d^{-1}.

1.2.4. Boundary Forcing of the Regional Spencer Gulf Model

The open boundary forcing for temperature and salinity was derived from measurements obtained from the moored instruments across the mouth of Spencer Gulf (Figure 1.12). These instruments provided temperature and salinity at the surface on the eastern and western sides of the gulf, and at the deepest location mid-gulf. These surface and bottom data were used as endpoints of a profile of temperature and salinity (T/S); the depth distribution of T/S between these endpoints was scaled to a time dependent density profile obtained from the model during its simulation and at a location 10 grid cells into the interior of the domain from the open boundary.

The prescription of sea level (and normal velocities) along the mouth of the Spencer Gulf model was determined using a relaxation to a gravity wave radiation condition with a time-scale of 30 minutes following the methodology of Blumberg and Kantha (1985). This condition was applied to a combination of a tidal and low-frequency weather-band sea level data.

Tidal-band Forcing

The open boundary of the regional Spencer Gulf model fortuitously corresponds to a linear transect between Taylor's Landing and Pondalowie Bay where the tidal harmonics are known from previous observational studies (http://www.flaterco.com/xtide/): the four dominant harmonics are listed in Table 1.1. These and the next 10 harmonics were then linearly interpolated across the gulf mouth boundary to provide forcing of tidal motion within the gulf model.

Table 1.1. The four dominant tidal harmonics for Taylor's Landing

Constituent	Amplitude (m)	Phase (Deg)
M2	0.2013	17.75
S2	0.2109	67.80
K1	0.2105	24.49
O1	0.1528	358.26

We note from Table 1.1. that the dominant constituents in the region are those due to M2, S2, O1 and K1, all of which have approximately the same amplitude. It is the similarity between the amplitude of the semi-diurnal components that allows the unique phenomena of the dodge tide to occur in Spencer Gulf; this occurs when M2 and S2 are exactly out of phase, therefore cancelling and resulting in no tidal movement (and hence no currents) every 14 days or so.

Weather-band Forcing

Here sea level signals across the gulf mouth need to be prescribed that correspond to forcing by local winds and which might arise from the wind-forced shelf circulation. Unfortunately, the sea level records from M1 and M2 at the gulf mouth were found to have datum shifts of 10 – 20 cm brought about by re-deployment of the instruments at slightly different depths after servicing. The elimination of these data shifts proved problematic due to strong seasonal and inter-annual variability of sea level height for the region.

As an alternative, continuous time series of sea level were also obtained for Thevenard and Port Stanvac (Figure 1.2) from the National Tidal Centre and used to extract the low frequency signal. This signal propagates anti-clockwise around the Australian coast, and a lag of 7.68 hours was computed between Thevenard and Port Stanvac. The lag between any open boundary node and Thevenard could then be computed as a fraction of this lag. The amplitude of the low frequency signal at each open boundary node was calculated using a weighted interpolation in time and space between the Thevenard and Port Stanvac data, and applied at the correctly lagged time relative to Thevenard. The sea level was then linearly interpolated across the gulf mouth. We note that a relaxation condition to sea level is adopted: the strict application of linearity formally precludes simultaneous inflow/outflows on either side of the gulf mouth that are expected for wind-forced motion (eg., Middleton and Platov 2003; Middleton and Teixeira 2008). We will discuss this further below.

1.3. Regional Spencer Gulf Model – results and observations

We examine here some larger scale circulation features associated with the Spencer Gulf model and find them to be in qualitative agreement with the limited observations available. This model also provides the boundary conditions for the local TFZ model that has a higher resolution and more accurate topography: the latter is important for the accurate prediction of ocean currents and as we will see the comparison with data is very encouraging.

1.3.1 Sea Level

A brief comparison is first made with model sea level in the tidal band (< 25 hr period) and weather-band (> 30 hr period) with observations from Wallaroo (Figures 1.4 and 1.5, data from Flinders Ports) that lies far from the prescribed boundary at the gulf mouth. As is evident from Figure 1.4 the ¾ wave tidal resonance (where the tidal displacements exceed that at the gulf mouth), and dodge tide, are both well predicted.

For the weather-band, the sea level variations are smaller than for the tides since resonance is no longer applicable. Sea level fluctuations are generally well produced (Figure 1.5) although errors of just a few centimetres can lead to significant errors in weather-band ocean currents.

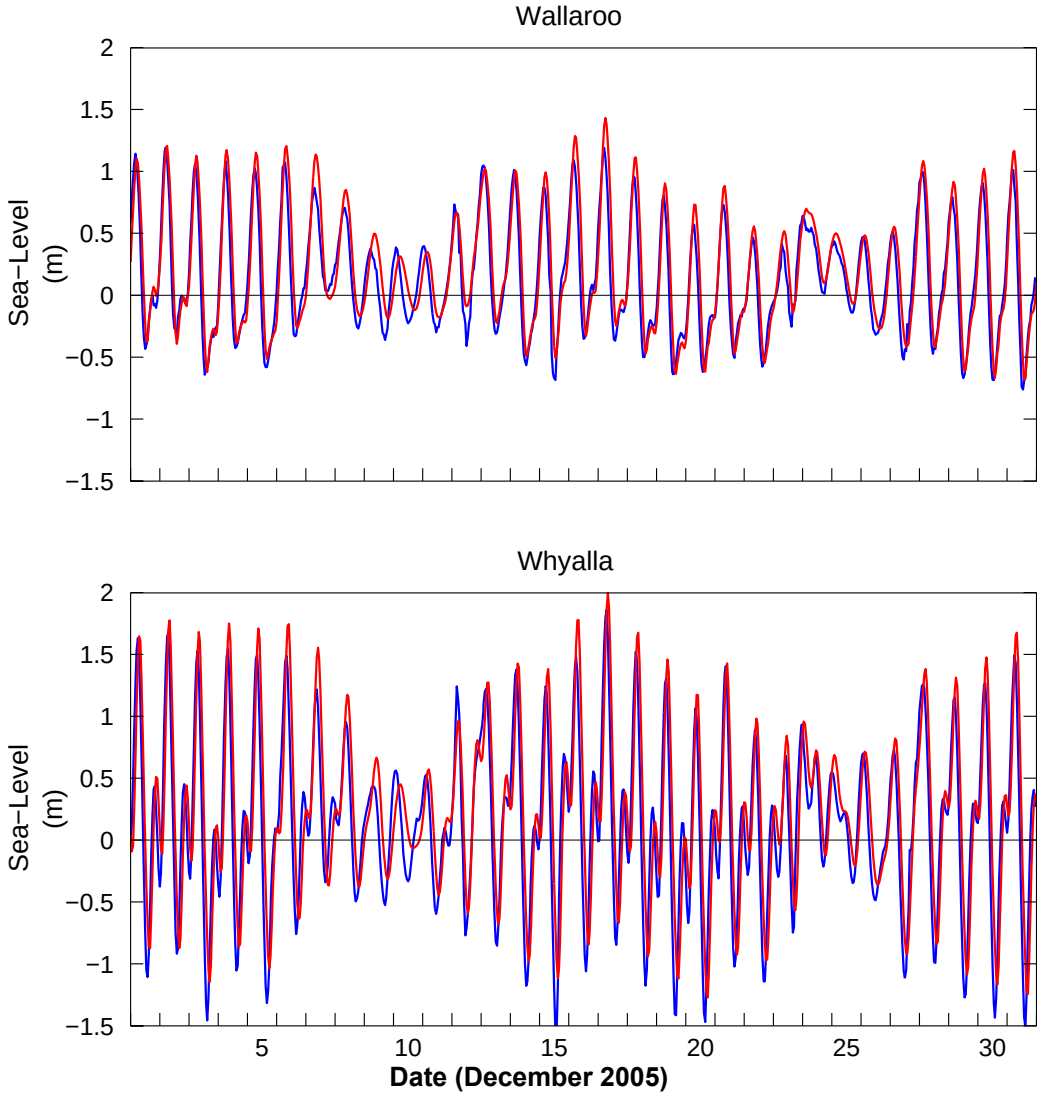

Figure 1.4. Sea level prediction (red) and data (blue) at Wallaroo (upper) and Whyalla (lower) for the tidal band (< 25 hr period). Note the vertical scale is in meters.

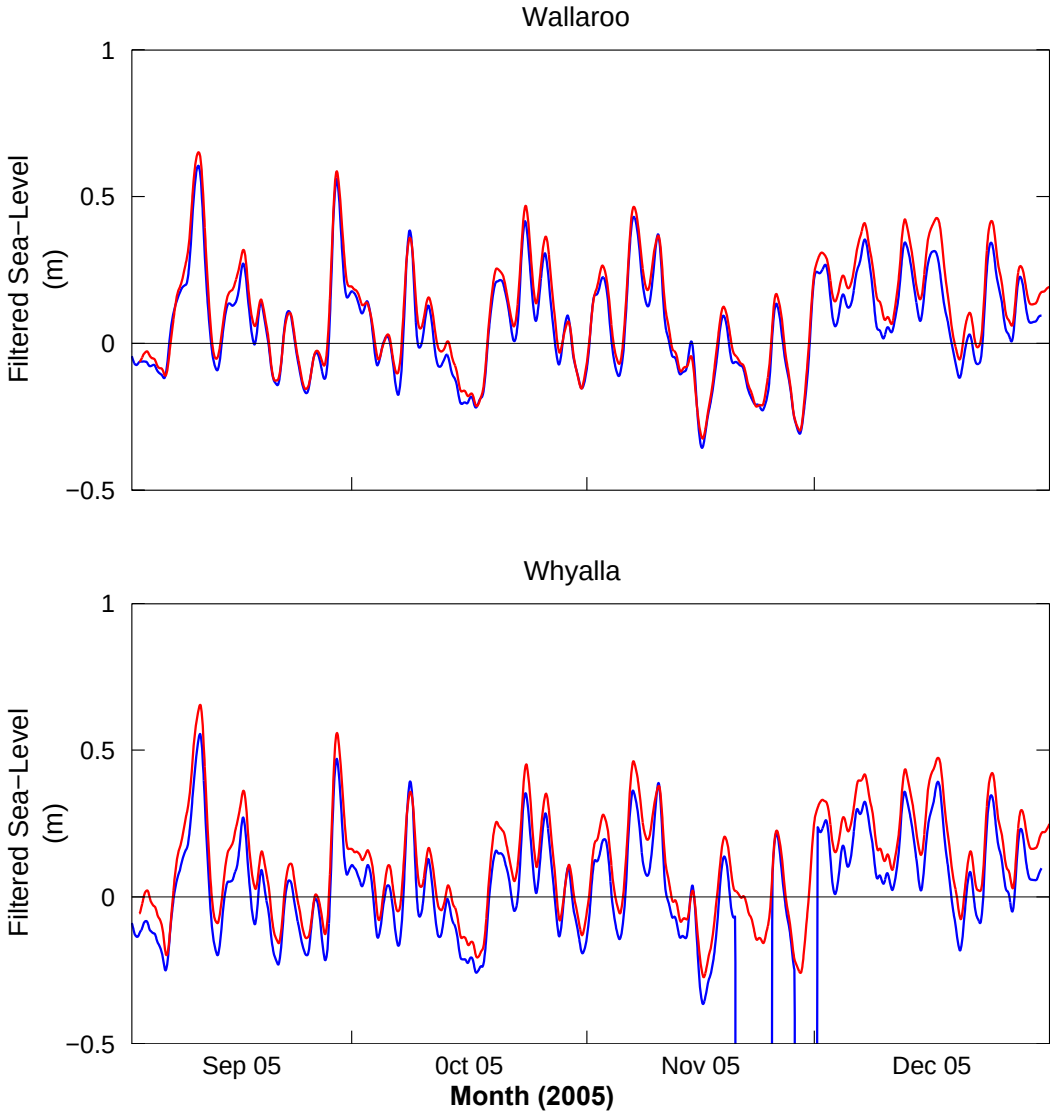

Figure 1.5. Sea level prediction (red) and data (blue) at Wallaroo (upper) and Whyalla (lower) for the weather-band (> 30 hr period). Note that instrument failure occurred twice in late November resulting in the absence of data. The vertical scale is in meters.

1.3.2 Winter-time circulation, temperature and salinity

The July 2006 depth averaged circulation for the lower gulf region is presented in Figure 1.6. As is evident, the mean circulation is weak (< 5 cm s^{-1}) and indicates a clockwise gyre with water drawn in from the adjacent shelf along the western gulf boundary and expelled on the eastern boundary. Such a circulation is expected (eg. Middleton and Texeira 2008) and also reflects the inward excursion of the average south-eastward currents on the adjacent shelf that are driven by the predominant south-eastward winds during winter.

Associated with this gyre is another forced by the formation of cold, dense water in the shallow northern extremities of the gulf. Cold, dense water formation here occurs due to winter-time cooling that is most pronounced where the water is shallowest and in the north and eastern side of the gulf (Figure 1.7). The model predicts this cooling (Figure 1.8) although the water temperature is generally 1ºC higher than that obtained from satellite observations (Figure 1.7).

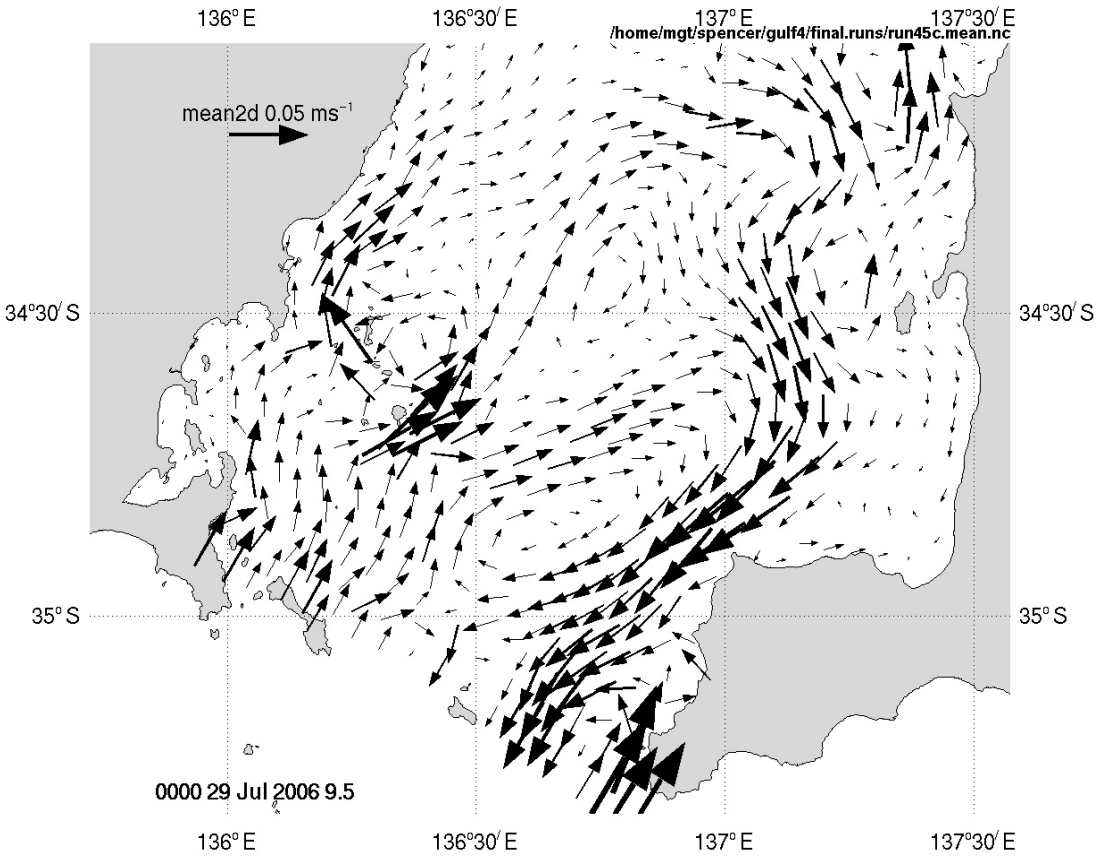

Figure 1.6. The time-averaged flow for July 2006 and for the depth averaged velocity. A legend vector of length 0.05 m s^{-1} is indicated.

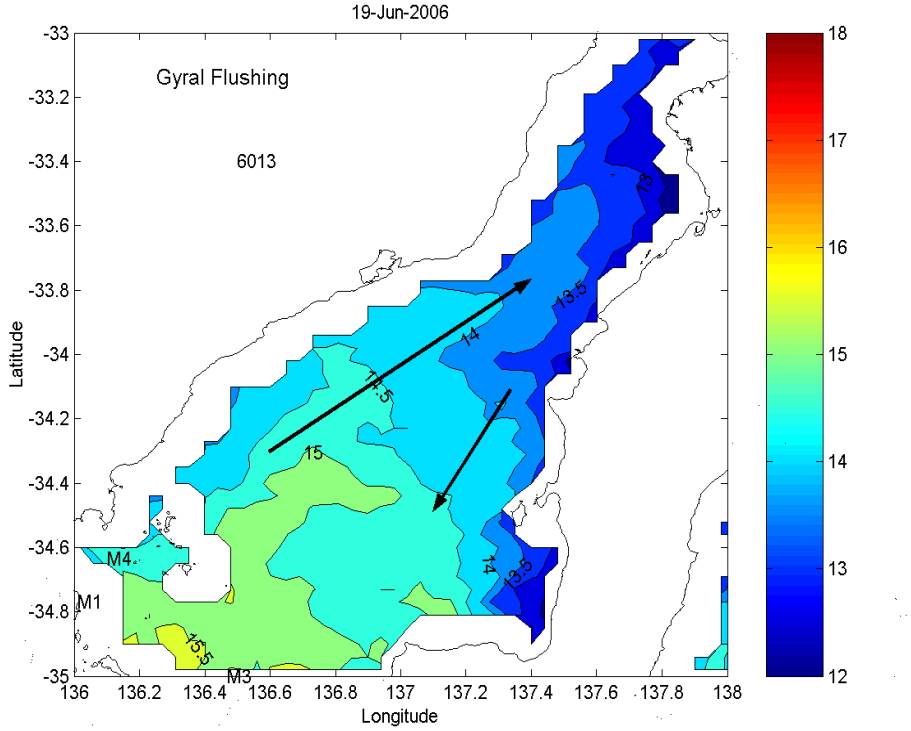

Figure 1.7. Sea Surface Temperature (MODIS) for the 19th June 2006 (JD 6013). The arrows indicate the expected circulation.

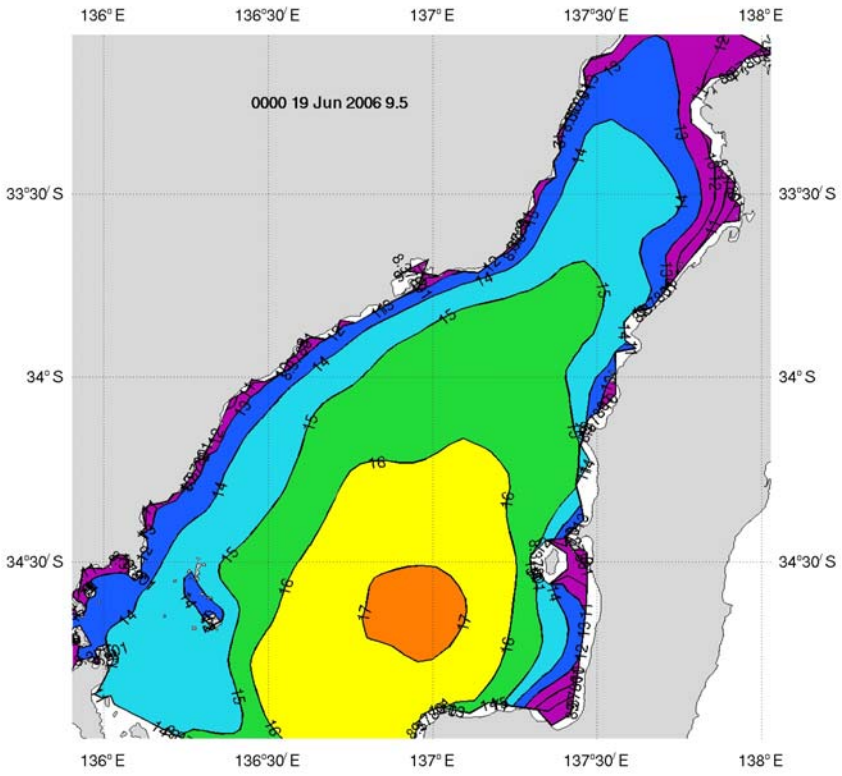

Figure 1.8. Modelled Sea Surface Temperature (MODIS) for the 19th June 2006 (JD 6013).

We also compare bottom salinity of the model (Figure 1.10) with the data obtained by Lennon et al. (1987) for June 1986 (Figure 1.9). While spaced years apart, the 2006 model salinities are generally within 0.1 psu of the 1986 data and illustrate the expected clockwise gyre again.

1.3.3 Summer-time circulation, temperature and salinity

Following winter, the heat and evaporation fluxes increase leading to higher temperature and salinities as illustrated by Figure 1.11. The annual variability is well captured by the model both in terms of temperature and salinity. Model temperature is however, cooler than the observations towards the end of the simulation. Results show that up to 50% of the observed temperature variations are determined by the local heat flux, (computed from available meteorological data), rather than by the transport of warm/cold water into the mooring sites (Herzfeld et al. 2008). The over-prediction of temperature in winter is most likely the result of excessive heat input due to inaccurate prescription of the heat flux.

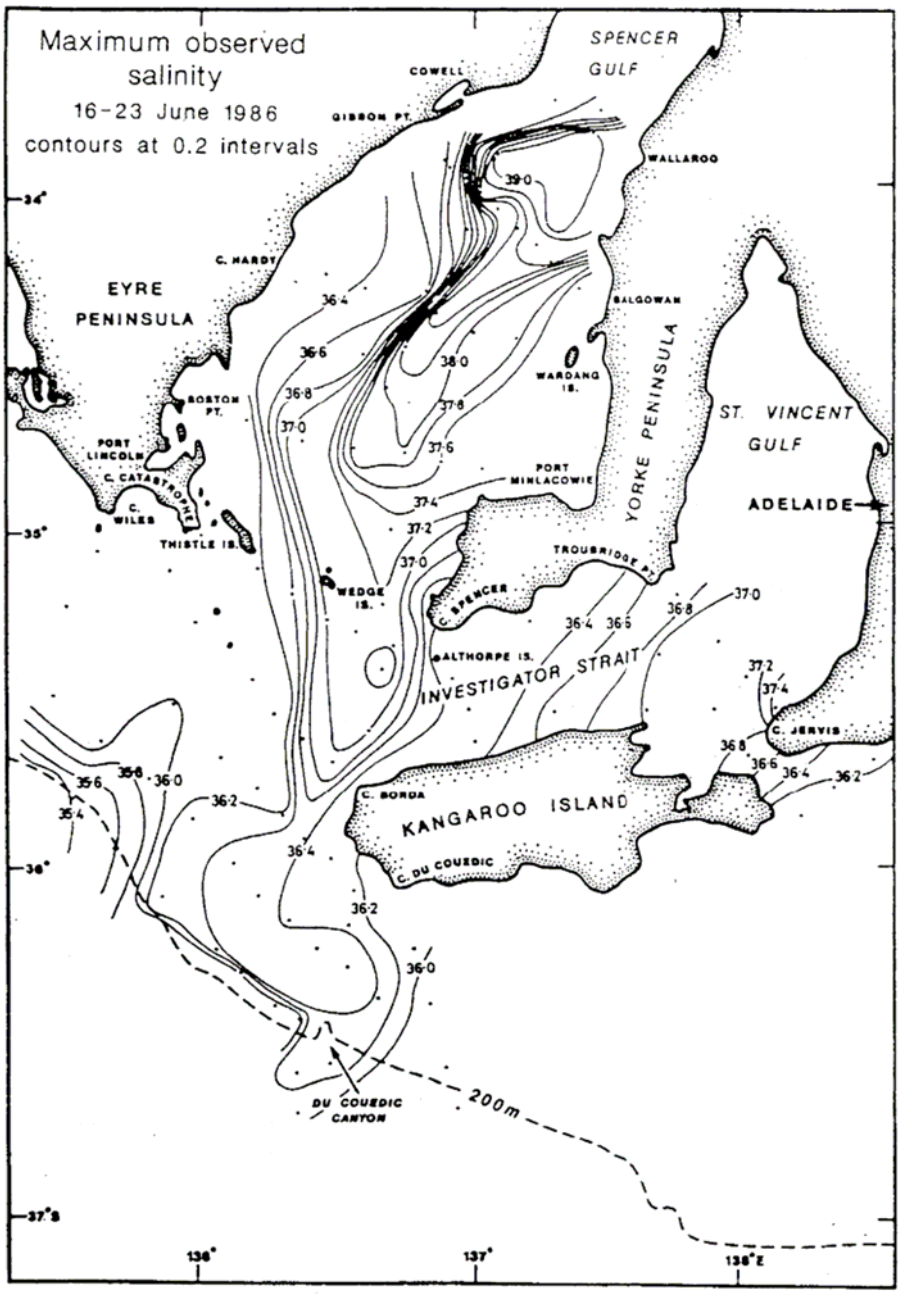

Figure 1.9. Maximum salinity throughout the water column for 16-23 June 1986. Reproduced from Lennon et al. (1987).

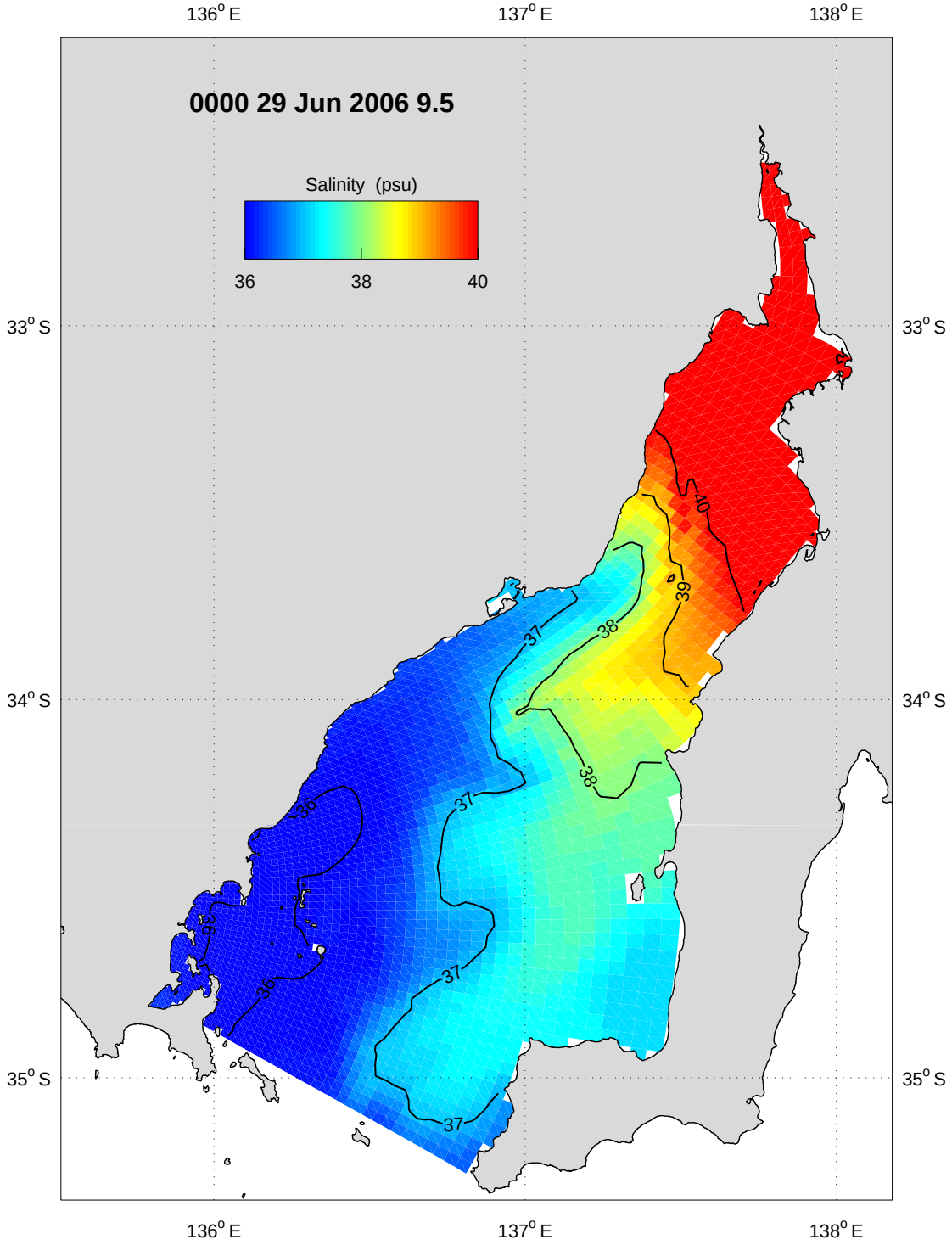

Figure 1.10. Model bottom salinity on 29th June 2006.

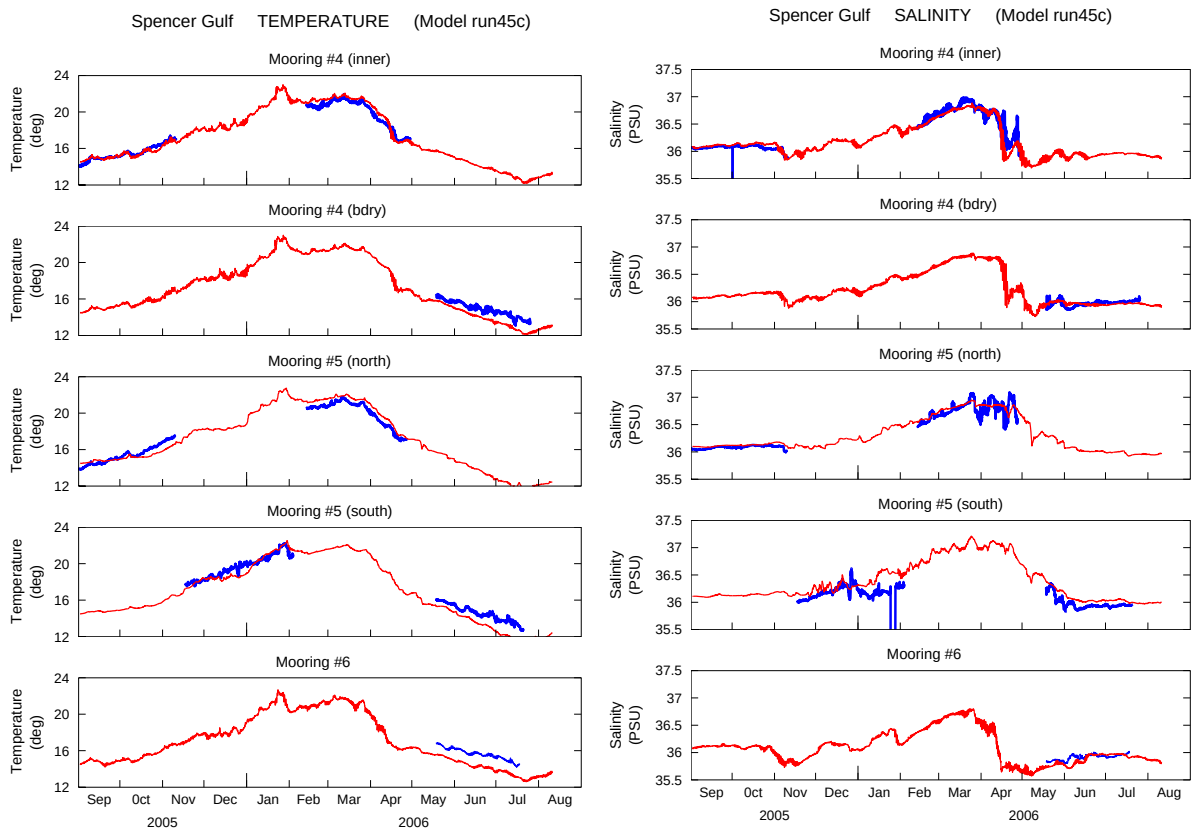

Figure 1.11. Comparison of modelled (red) and measured (blue) temperature and salinity at mooring locations in the TFZ. See Figure 1.3 for the location of the moorings.

While the above results are encouraging, the model fails to reproduce the upwelling of cold, salty water into the eastern side of the gulf mouth. Such water is upwelled off Kangaroo Island during summer (eg. Middleton and Bye 2007), follows isobaths and from most satellite imagery, extends into the eastern side of the gulf mouth as illustrated by the SST image for February 2006 (Figure 1.12).

Indeed, the results for summer (Figure 1.13) again show a clockwise circulation near the mouth of the gulf and opposite to that expected from numerical studies (eg. Middleton and Platov 2003; 2005, Middleton and Teixeira 2008) and observations of cold water intrusions into the eastern gulf mouth (eg. Figure 1.12). Moreover, in Herzfeld et al. (2008), we show that an anti-clockwise (clockwise) circulation is consistent with the gulf-mouth sea level data when alongshelf winds are upwelling (downwelling) favourable.

The explanation for this anomalous result may involve the boundary condition adopted for weather-band sea level variability. This necessarily assumed a linear relation across the gulf mouth and implies that the model is relaxed towards a (geostrophic) velocity field that is directed either into or out of the gulf but not both at the same time. This precludes the inflow/outflow needed for a clockwise or anticlockwise gyre. Inspection of Figure 1.13 suggests that the boundary condition at the gulf mouth acts to “block” the inflow/outflow of the evident clockwise gyre. On the other hand, the results for winter in Figure 1.6 suggest the boundary condition is “well behaved”.

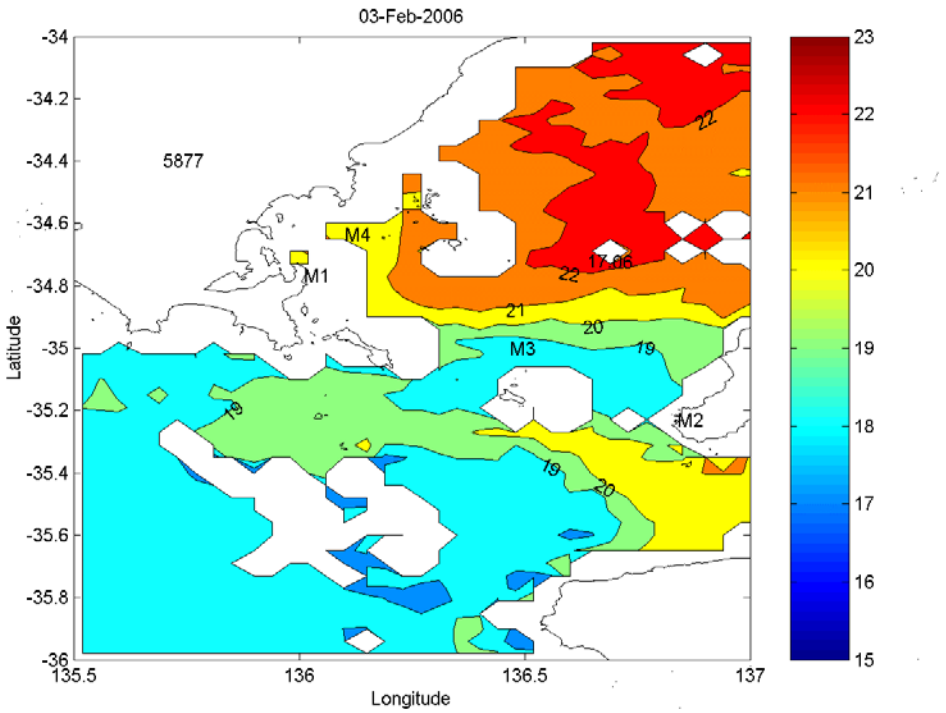

Figure 1.12. MODIS sea surface temperature for February 2006 (JD 5877). The temperature contour interval is 1ºC and the mooring sites M1, M2, M3 and M4 are indicated.

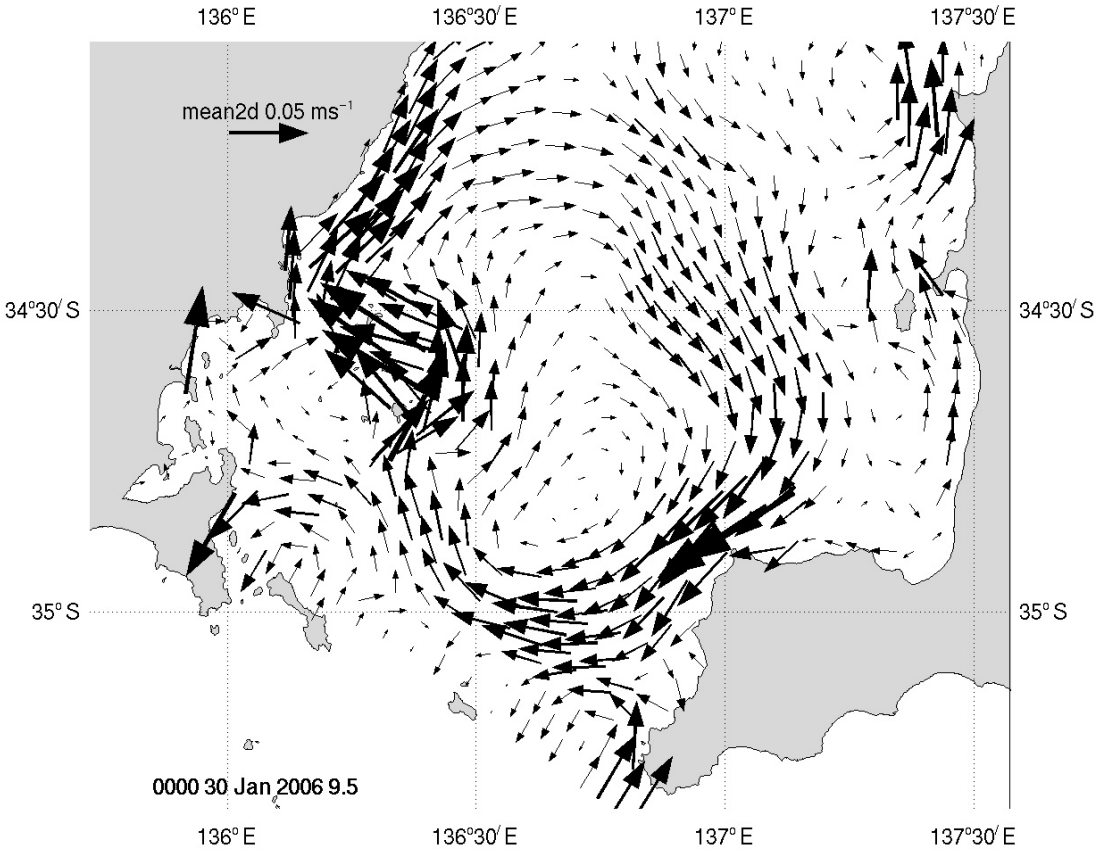

Figure 1.13. The time-averaged flow for January 2006 and for the depth averaged velocity. A legend vector of length 0.05 m s^{-1} is indicated.

As noted, the model does have predictive ability for temperature and salinity and we show below that it also has reasonable predictive ability for the TFZ region and for both the mean, tidal and weather-band flow.

1.4 Local Tuna Farming Zone Model – Results and Observations

Here the output of the local TFZ model is examined and compared to data collected for the region during 2006-2007. Since the model is driven along its open boundaries by the large scale Spencer Gulf model, this comparison also serves to validate the results of the latter (at least for the TFZ region. We begin with a comparison of the model and observed velocity and then compare predictions for temperature and salinity. As will be shown, the local TFZ model has reasonable predictive ability for currents and events in localized upwelling and coastal cooling/heating and dense water formation. A comparison of predicted and observed sea level was also made and good agreement found. As noted, a more stringent test is a comparison of velocities which are driven by gradients in sea level.

1.4.1 Velocity - Observations

Hourly averages of velocity data from moorings M4 and M5 were extracted, and as a first step, the data was averaged in the vertical. The low-pass Thompson (1983) filter was applied, and with the filtered weather-band data so determined, residual (tidal band) time series were then obtained.

Plots of the tidal band signals are presented in Figure 1.14 for M4 at the inner site. Results for M4 at the boundary site are similar. Results for M5 (not shown) are similar but reduced in magnitude to 5-10 cm s^{-1}. For the east/west and north/south components presented in Figure 1.14, it is evident that the latter dominate with speeds of 30 cm s^{-1}. The fortnightly dodge tide is also evident.

The filtered depth-averaged velocity field is shown in Figure 1.15 and again for the inner sites. The data for the two inner deployment sites is shown in black. The model output that will be discussed below is shown in red. As is evident, there is again variability in the 2-30 day band. Strikingly, the current speeds of the filtered (weather-band) data are much smaller (< 5 cm s^{-1}) than those of the tides (~ 30 cm s^{-1}) shown in Figure 1.14. The small current speeds are however consistent with geostrophic currents estimated from the M4 and M5 sea level data in Herzfeld et al. (2008).

Results were also obtained for the other sites and also M5 and were similar in character to those shown in Figures 1.14 and 1.15 with amplitudes 5 cm s^{-1} or less.

The weather-band currents within the gulf are much smaller than those typically found on the shelf (~ 25 cm s^{-1}), and for the reasons outlined in the introduction.

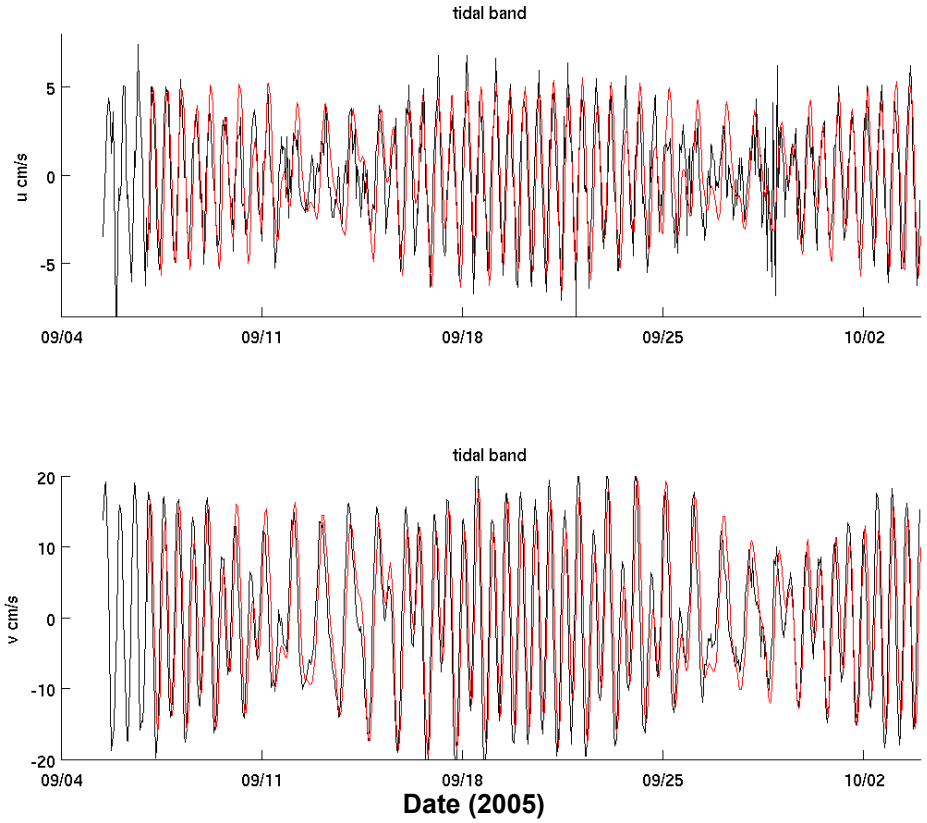

Figure 1.14. Upper Panel: the (east/west) tidal-band velocity (depth-averaged) for M4 at the inner site and for September 2005 (mm/dd). Black values are data while the red values are from the fine scale numerical model. Positive values are to the east. Lower Panel: as in the upper panel but for the (north/south) tidal-band velocity. Positive values are to the north. Note the change of scale on the y- axis.

The stronger semi-diurnal tidal currents shown above may be implicated in bottom stirring, particularly when wave action is included. A useful measure of their importance to flushing is the net displacement a water parcel would undergo after ¼ period (3 hrs). For the dominant semi-diurnal tide this distance is 1.4 km. For the weaker weather-band currents, the displacements will generally be larger since they persist over a longer time. For example, a 5 cm s^{-1} current with a 10 day period will displace a water parcel by 7 km over a 2.5 day period: five times that of the tide. Thus, the successful modelling of the low-frequency circulation may be more important to predicting cage flushing and nutrient transport.

1.4.2 Velocity - Model Results

A comparison of the local model tidal currents with data is shown in Figure 1.14 and for the M4 inner site. The model is able to reproduce both the timing and amplitude of the observed tide extremely well at this site. We note that the comparison (not shown) is less favourable at the M4 site that lies adjacent to the local model open boundary. The explanation here is that the open boundary condition adopted does not locally require that both the normal and tangential velocities exactly match. Rather, mass transport between the regional and local models is conserved through the open boundary so that results from the local model farther from the boundary are in good agreement with the data. The model tidal band results for M5 are also in good agreement with the data.

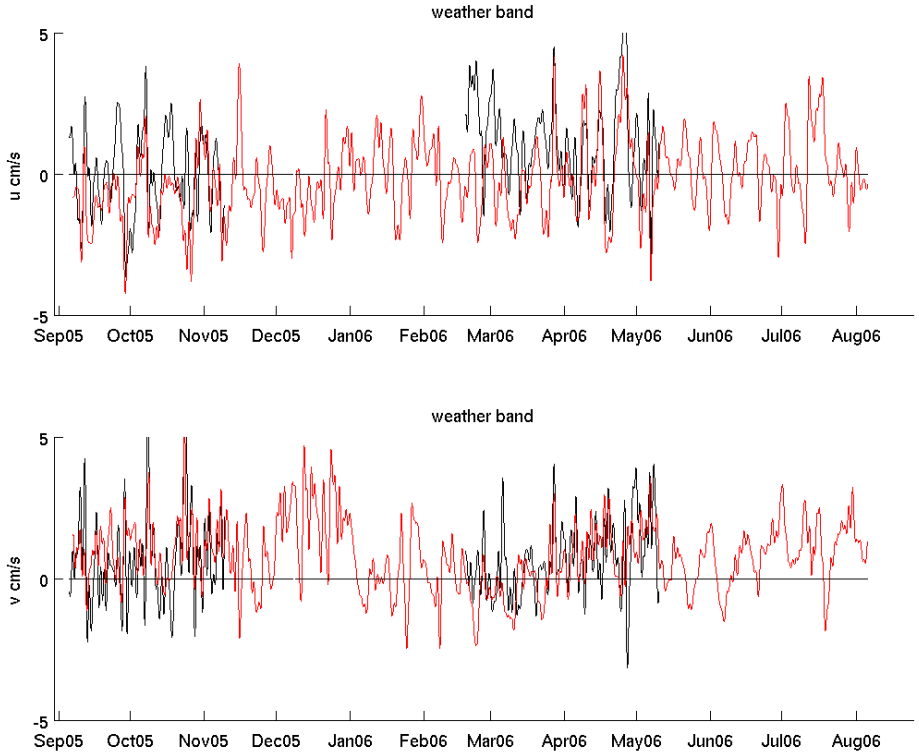

Figure 1.15. Upper Panel: the (east/west) weather-band velocity (depth-averaged) for M4 at the inner site. Black values are data while the red values are from the fine scale numerical model. Positive values are to the east. Lower Panel: as in the upper panel but for the (north/south) weather-band velocity. Positive values are to the north.

A comparison of the local model results for the M4 inner site and for the weather-band signals is made in Figure 1.15. The results show the model to have reasonable predictive skill. As noted, errors here can arise simply from inaccuracies in the adopted topography and this may be the cause of the poor predictive skill found for the weather-band at the M5 sites. Moreover, errors in the open boundary condition of the Spencer Gulf model and for weather-band sea level and velocity will lead to loss of predictive skill.

The mean depth averaged currents estimated from the model are also in reasonable agreement with the data as shown in the report. At the M4 sites a north-east circulation of 2 cm s^{-1} is generally found in the data and this is in qualitative agreement with the model (see Figures 1.16 and 1.17 below). At the M5 sites, the data indicates a west to southward mean flow of 2-3 cm s^{-1} that again is consistent with the model results.

With some slight differences, the averaged summer (December-March) and winter (June-August) velocity fields are similar as shown by the model output in Figure 1.16 and 1.17 below. A generally weak northward flow of ~ 1 cm s^{-1} (~ 78 km/3 month season) is found along the sea-ward boundary of the TFZ. A second notable feature of the season-averaged solutions is that the circulation and thus flushing of Boston Bay proper and the coastal regions is almost zero. This will be reflected in the long flushing time-scales estimates in section 5 below.

1.4.3 Temperature and Salinity

Results for temperature and salinity at the mooring sites are similar to those obtained from the regional Spencer Gulf model. During the winter of 2005 the increased solar heating acted to warm the gulf and shelf waters. The winds were, until late December, downwelling favourable and the gulf circulation would tend to draw water in along the western side as indicated by the model results in Figure 1.6.

After December 28th, 2005 (JD 5840), the winds reverse (Figure 1.3) to become upwelling favourable for the shelf and remained so until the end of March 2006 (JD 5935). There was no dramatic drop in mooring temperatures following the onset of shelf upwelling, although the cooler temperatures observed (Figure 1.11) resulted from a combination of solar heating and inflow of cool upwelled water. The strong upwelling winds around the 1st February 2006 (JD 5875) coincide with the marked drop in temperature at all moorings and the local heating model adopted in the report is only able to account for half of the 1.5ºC drop in temperature at this time (Figure 1.11) indicating the transport of colder, and likely upwelled water, into the TFZ region.

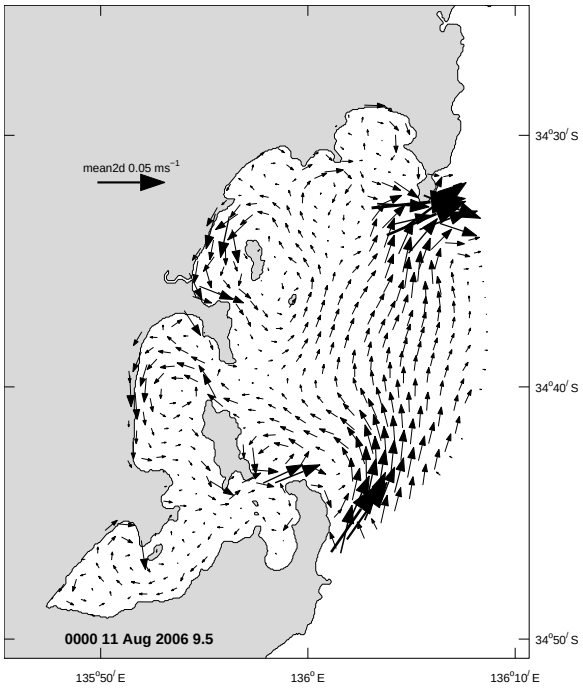

Figure 1.16. Winter depth averaged current velocity

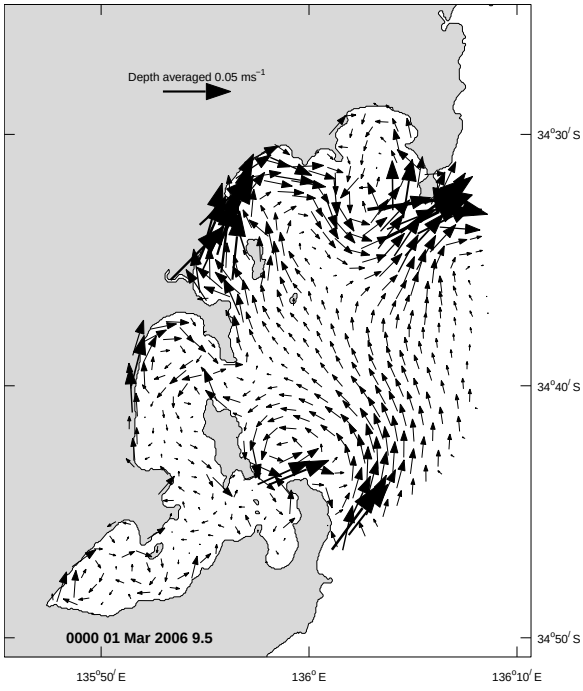

Figure 1.17. Summer depth averaged current velocity

There is evidence that some of the shelf upwelled water is reaching the eastern side of the TFZ. In Figure 1.12, we present SST for February 3rd 2006 (JD 5877). As can be seen, the gulf waters (warmed by solar heating) are cooler on the eastern side of the gulf. The path of the upwelled plume follows that from previous studies (eg. Middleton and Bye 2007) and it is possible some upwelled water moves into the TFZ as a sub-surface plume.

Transects of temperature and salinity were obtained for the TFZ region and along the white line indicated in Figure 1.2. The data for February 11th 2006 are presented in Figure 1.18 and 1.19.The transects for temperature provide marginal evidence of upwelling at this time with cooler, fresher water at the bottom and at the eastern side of the transect and close to M4 (boundary) mooring site. Evidence of evaporation comes from the denser water found on the

western side of the transect that lies in shallower water. There is also evidence of stratification with a 15 m deep surface mixed layer. The model results are broadly similar to the data in that warmer saltier water is found nearer the coast: the model does not indicate any near bottom upwelling at this time. We discuss this further below.

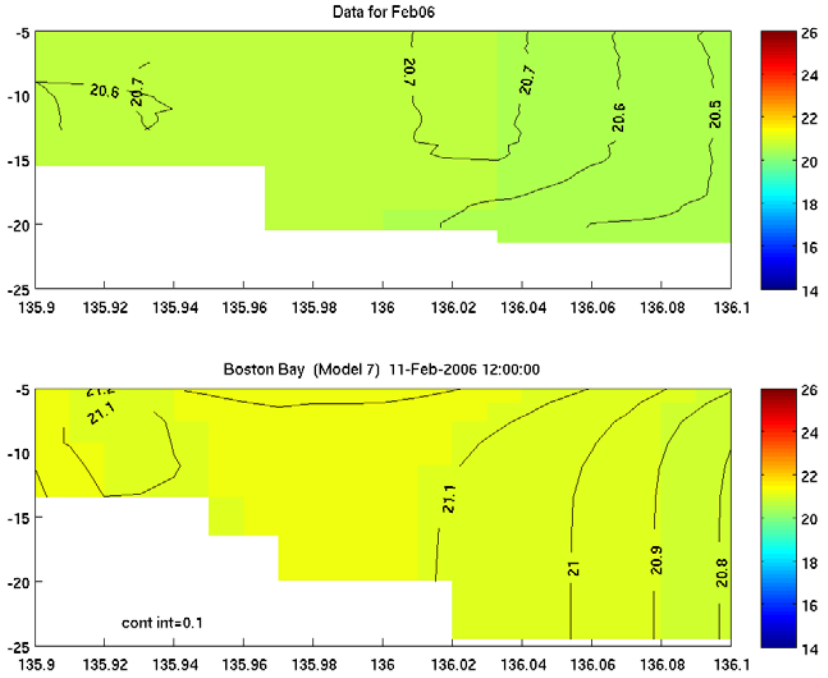

Figure 1.18. Upper Panel: observed temperature for Feb 11th 2006. Lower Panel: model temperature for the same day (12 noon). The vertical scale indicates depths in meters. The horizontal scale is in degrees longitude.

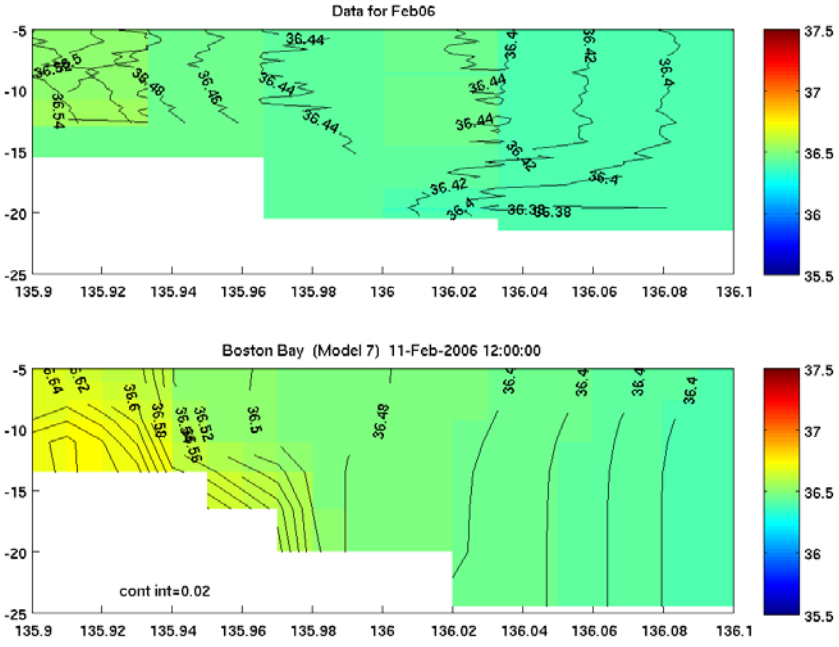

Figure 1.19. Upper Panel: observed salinity for Feb 11th 2006. Lower Panel: model salinity for the same day (12 noon). The vertical scale indicates depths in meters. The horizontal scale is in degrees longitude.

The coastal heating and brine water formation is well illustrated in the April 21st 2006 transect shown in Figure 1.20 and 1.21. The additional salt (0.9 psu) makes the water denser than that offshore with an offshore sub-surface plume structure: the warmest water is at the bottom. The model is able to reproduce these features.

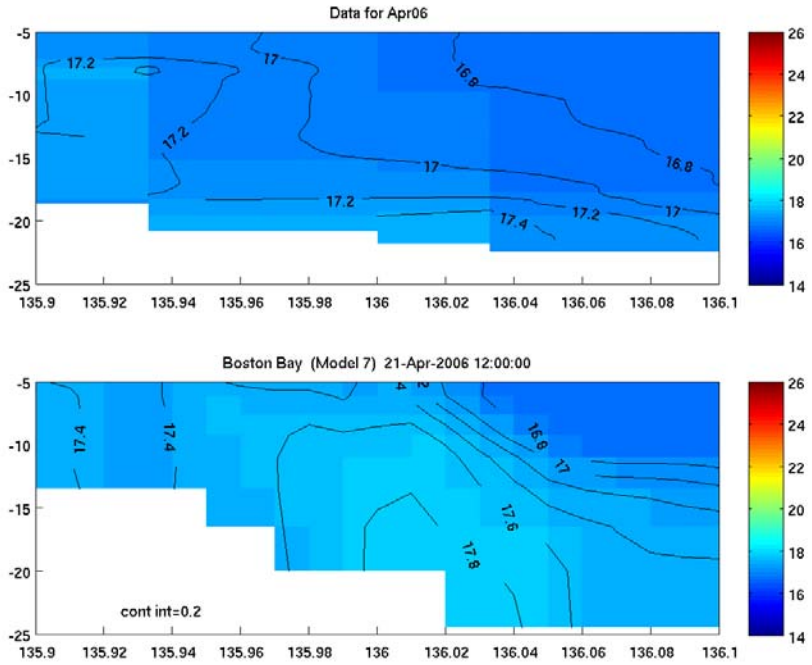

Figure 1.20. Upper Panel: observed temperature for April 21st 2006. Lower Panel: model temperature for the same day (12 noon). The vertical scale indicates depths in meters. The horizontal scale is in degrees longitude.

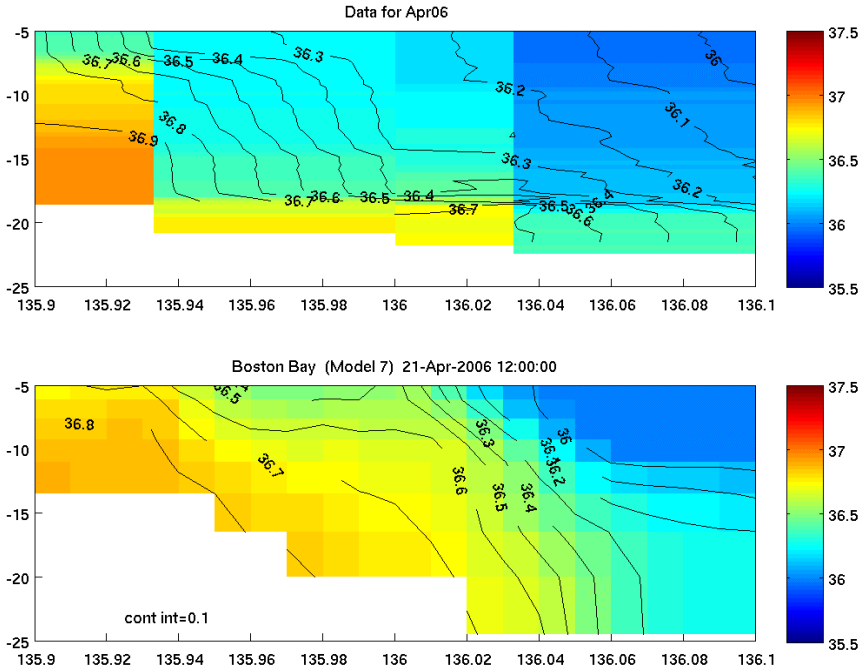

Figure 1.21. Upper Panel: observed salinity for April 21st 2006. Lower Panel: model salinity for the same day (12 noon). The vertical scale indicates depths in meters. The horizontal scale is in degrees longitude.

After April, the atmospheric cooling begins to dominate. The transect data for June 20th 2006 are presented in Figures 1.22 and 1.23 and indicate cold dense water formation at the coast that flows to the east as a 2-3 m deep bottom plume. Isotherms near the coast are vertical indicating convective over-turning. Salinity is largely homogeneous. The model is able to reproduce these features although the temperature is generally 2ºC cooler than the data. The spatial extent of this coastal cooling is illustrated by the SST image (Figure 1.7).

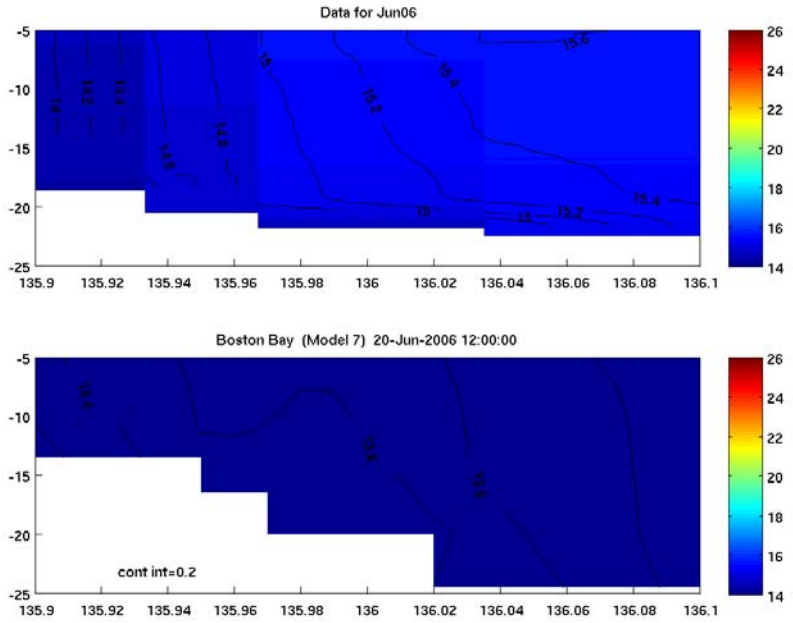

Figure 1.22. Upper Panel: observed temperature for June 20th, 2006 (JD 6012). Lower Panel: model temperature for the same day (12 noon). The vertical scale indicates depths in meters. The horizontal scale is in degrees longitude.

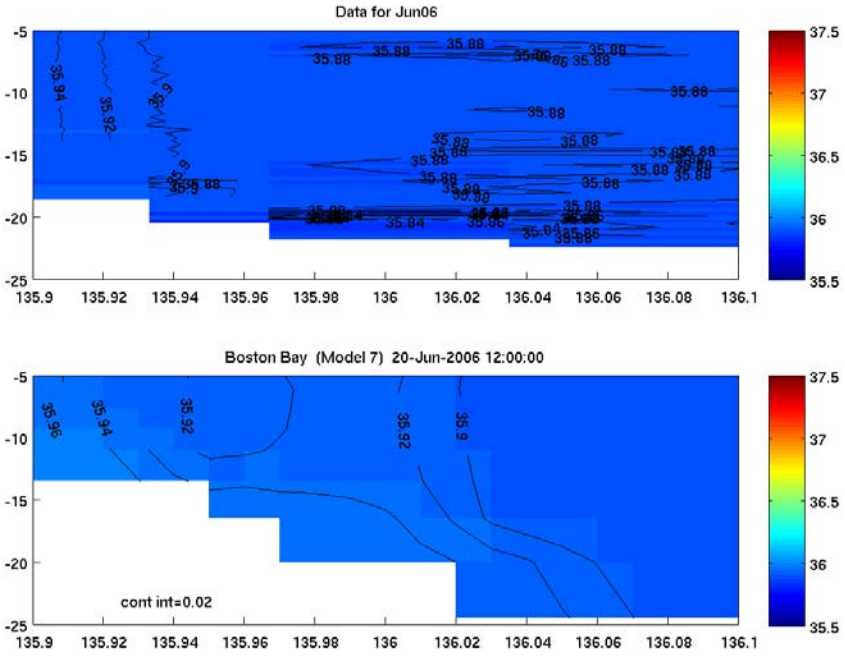

Figure 1.23. Upper Panel: observed salinity for June 20th, 2006 (JD 6012). Lower Panel: model salinity for the same day (12 noon). The vertical scale indicates depths in meters. The horizontal scale is in degrees longitude.

1.4.4 Upwelling/downwelling in the TFZ – a Local Transport Mechanism

Finally we note that upwelling of nutrients into the TFZ may be determined by local winds and a "two-layer" circulation. Evidence for this comes from the current meter data at M4 whereby bottom currents are on average directed in the opposite direction to the surface current and surface winds. This is illustrated by a progressive vector diagram of bottom currents obtained from the M4 current data. The progressive vector represents the position a fluid parcel would have if it always moved with the M4 mooring current velocity. As shown in Figure 1.24, between 6th and 26th December 2005, the net displacement of water near the bottom at M4 is directed to the N.W. and towards the shallower waters of the coast.

The winds at this time are directed to the southeast and for the shelf these winds are downwelling favourable. For the TFZ, they appear to be upwelling favourable. After the 26th December, the winds reverse and so does the direction of bottom water displacement. The winds are now to the north-west/west, but the vector displacement is to the east.

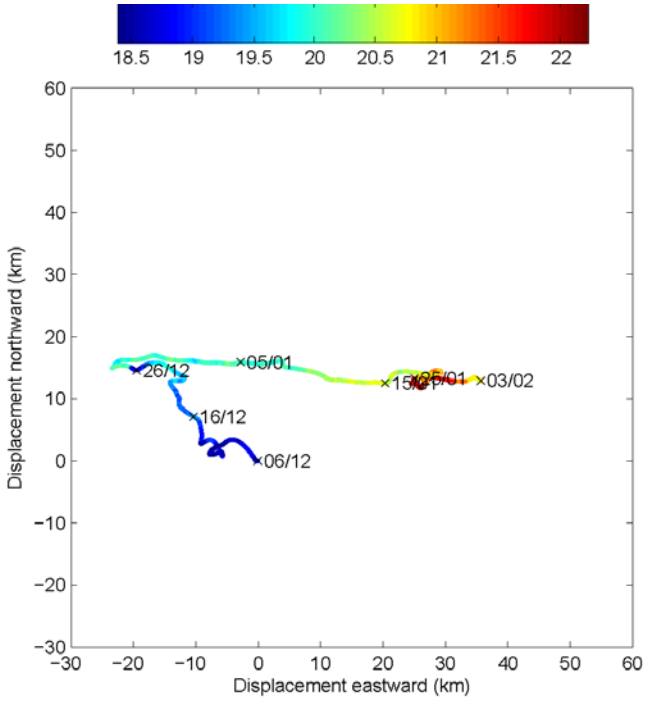

Figure 1.24. Progressive vector diagram of near-bottom currents at Mooring 4. The times (December 2006 - January 2006) are indicated by dd/mm. The colour gives the near-bottom temperature from the M5 mooring at the dates indicated: colour bar at top of figure.

This two-layer upwelling is reproduced by the model for May 6th 2006 when the winds were strongly to the south-east. As shown in Figure 1.25, near bottom water along the transects indicated is drawn towards the coast while surface water is driven offshore. The dynamics of this flow correspond to those in a channel. Such a channel may be effectively set by the Sir Joseph Banks Islands to the north and Thistle Island to the south.

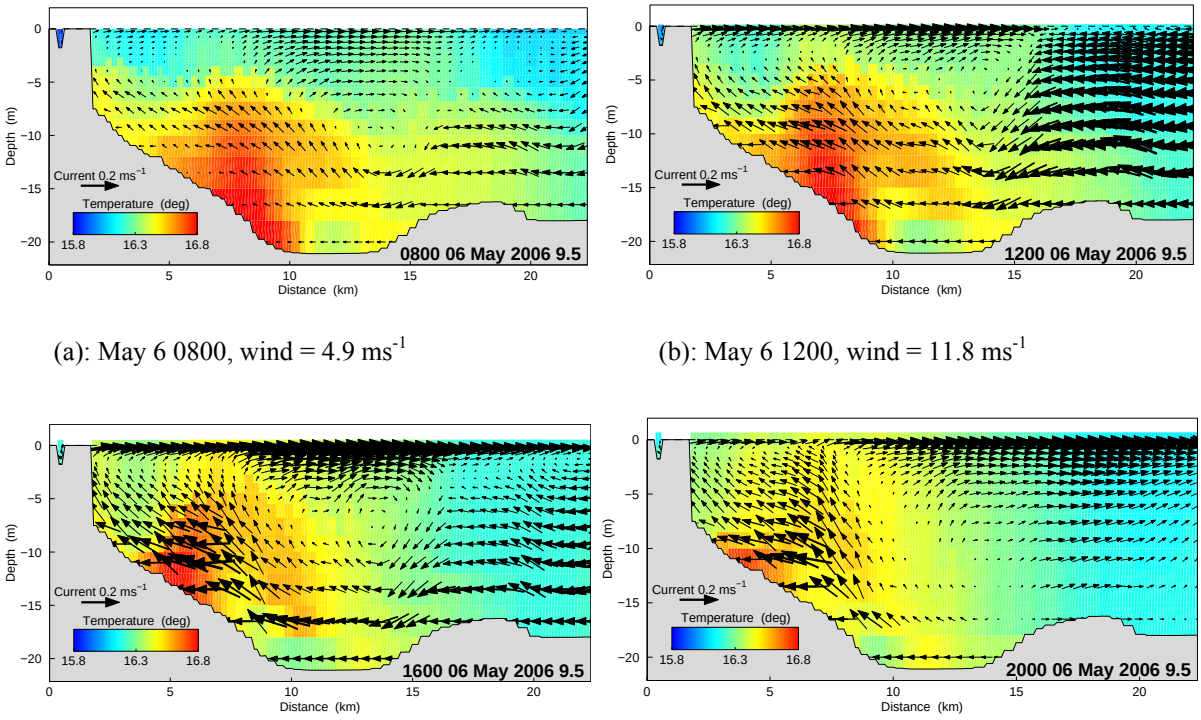

(a): May 6 0800, wind = 4.9 ms^{-1}

(b): May 6 1200, wind = 11.8 ms^{-1}

(c): May 6 1600, wind = 15.2 ms^{-1}

(d): May 6 2000, wind = 10.9 ms^{-1}

Figure 1.25. Model section of temperature and currents for May 6th 2006 during strong offshore wind to the south-east.

1.5. Flushing Times

The long term mean currents are of interest from the perspective of diagnosing the flushing characteristics of the region, hence the residence time of pollutants. As mentioned above, the tidal currents are oscillatory in nature, and are associated with little net displacement. It is the low frequency weather band component of the currents that are more relevant for moving parcels of water long distances, and these flow patterns reflect the distribution tracers are expected to follow in the long term. These currents may be separated from the tidal component by calculating an average of the model velocity components over 90 day (i.e. seasonal) periods. An example of the depth average residual flow for summer and winter are displayed in Figures 4.3 and 4.4 respectively.

An analysis of the seasonal depth averaged flow reveals that three main sub-regions within the domain may be characterised. Firstly offshore of Boston Island flow enters the domain in the south and exits in the north, with little penetration into the coastal margins. Secondly the Boston Bay / Proper Bay area can be treated as a separate system, with flow generally entering north of Boston Island, flowing south to loop through Proper Bay and exiting to the east of Boston Island, where a persistent anti-clockwise gyre exists off Cape Donnington. Thirdly Louth and Peake Bays exhibit northwards flow along the coast, fed by water seaward of Point Boston, and seasonally exhibiting gyres within Peake Bay and off Louth Island. This circulation is schematically illustrated in Figure 1.26. Additionally, surface seasonal currents generally exhibit onshore flow during summer and autumn and offshore flow during winter and spring; the local upwelling referred to in Section 4.4.

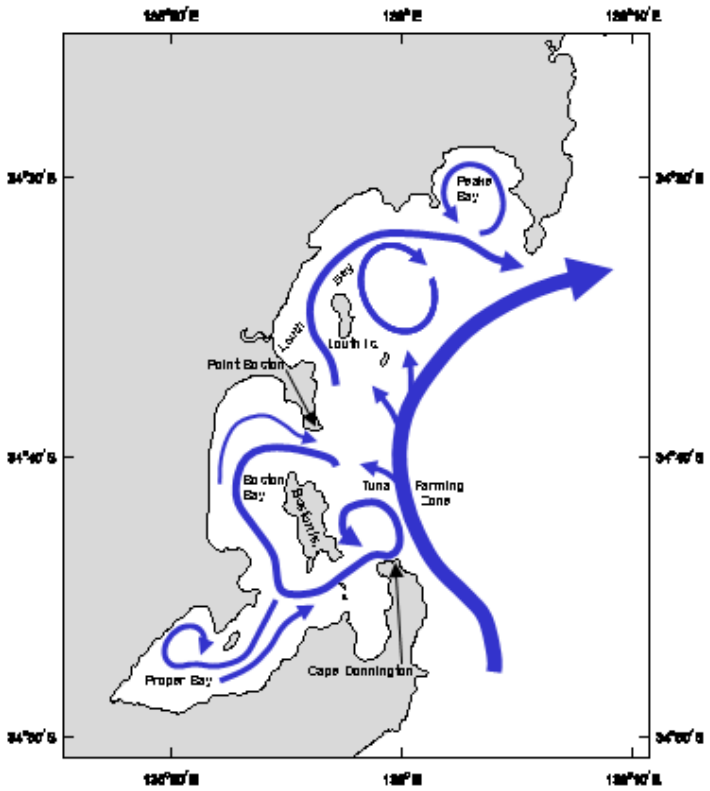

Figure 1.26. Schematic of depth averaged mean flow.

The flushing time of the various sub-regions identified above may be inferred by observing the reduction in total mass of an idealized tracer initialized to unity in the respective sub-region. The flushing time is diagnosed when total mass in the sub-region is reduced to ~38% of the initial mass (Tartinville et al. 1997). Flushing times for various sub-regions during summer and winter are displayed in Table 1.2.

Table 1.2. Flushing times

Region	Flushing time (days)
Whole domain	13.9
Boston Bay	8.2
Proper Bay	10.8
Louth Bay	1.5
Peake Bay	2.7
Tuna farming zone	2.0

Table 1.2 indicates that there exists a wide range of flushing times depending on the region. The computed flushing estimates are a somewhat subjective measure of exchange, since there are various methods of computing flushing which may potentially yield different results, and the assumptions made in deriving flushing times are often violated. The forcing in effect at the time the flushing was estimated also has a large impact on the flushing rate; flushing times computed for a different time period under the influence of differing wind, heatflux and tidal conditions are expected to produce different flushing times. Therefore the flushing times presented in Table 1.2 should be treated with caution, and should not be assumed to be a definitive measure. They are, however, a useful indication of the relative flushing rates of various regions within the domain.

Proper Bay appears to have poor connectivity with the remainder of the domain and consequently also is associated with relatively slow flushing. Boston Island diminishes the connectivity of the bay westwards of the island with open water to the east, resulting in longer flushing times than Louth and Peake Bays. The TFZ is also flushed relatively quickly, however, the tracer in this region has not exited the domain completely but rather has been re-distributed to other areas within the domain. This highlights one of the limitations of the application of these flushing estimates; the region in question may be flushed, but the material flushed quite often is relocated to another area within the system and hence not completely removed. If tracer is distributed throughout the whole region then this is not possible, and a reduction in total mass is only possible via transport through the open boundary resulting in the longest flushing estimate of ~14 days. This estimate is again dependent on the forcing in effect; using particle tracking provides a more accurate estime of ~20 days for flushing the entire region (see below).

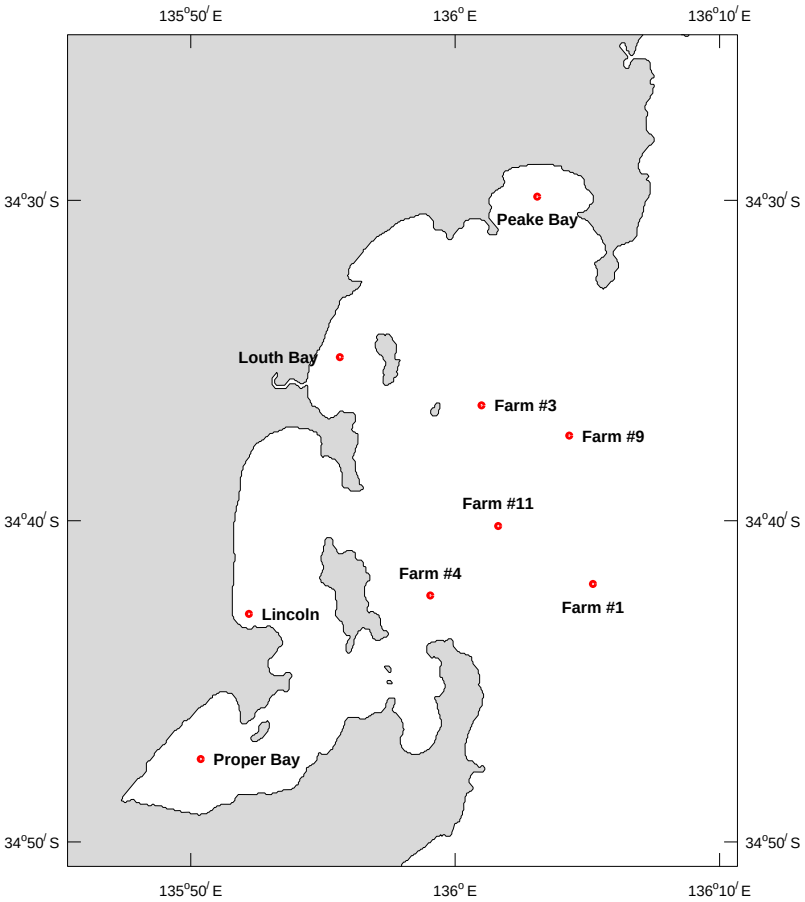

Figure 1.27. Point source release locations for estimating removal times of pollutants.

A more useful measure of the circulation's ability to remove unwanted pollutants, or conversely retain material within the domain, is via the use of passive tracers. Using point source inputs of unit loads, a statistical description of the resultant concentration distribution can be obtained. These concentrations vary according to the input location of the point source; i.e. the connectivity of the region with respect to the point source input location may be inferred. The statistical measures used are the 5, 50 and 95 percentile concentration distributions for the whole model simulation. These outputs are therefore applicable to the full annual cycle, and not a short period as is the case with the flushing estimates. Note that

the response of the tracers to the interaction of the point source input with the system dynamics is linear, so that if the load were scaled by some arbitrary factor then the corresponding concentrations can be scaled accordingly. Point source releases were performed at the locations marked in Figure 1.27. Examples of the statistical distributions are displayed as Figure 1.28 for a release in the TFZ (farm #11), and Figure 1.29 for a release in Peake Bay. Results are interpreted thus: given that a continuous unit load is input at farm #11 and its distribution throughout the domain allowed to reach quasi-steady state, at any given location in the domain one would expect to find the concentrations less than those shown in Figure 1.28 (a) for 5% of the time, less than those in Figure 1.28 (b) for 50% of the time and less than those in Figure 1.28 (c) for 95% of the time.

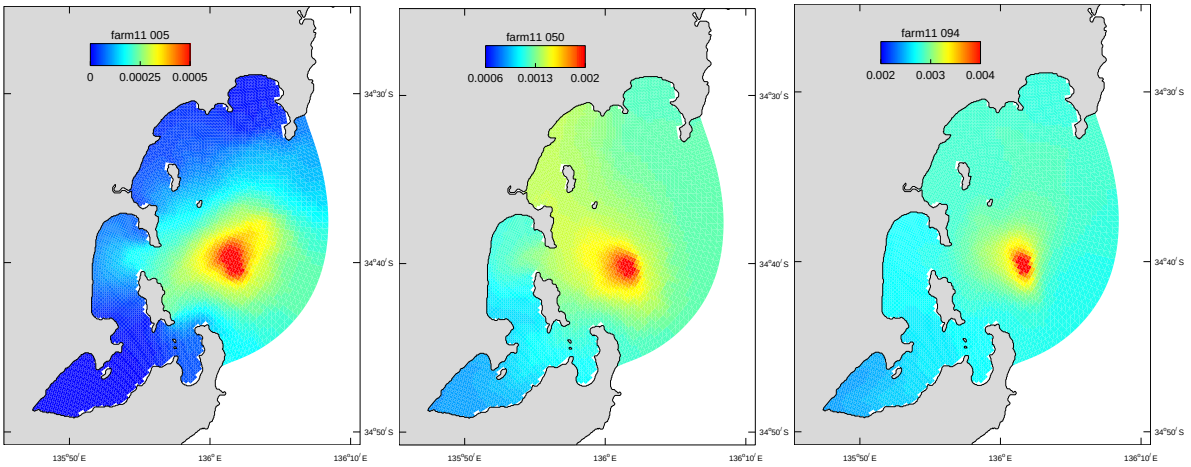

(a) 5 percentile (b) Median (c) 95 percentile

Figure 1.28. Distribution of a passive tracer released at Farm #11.

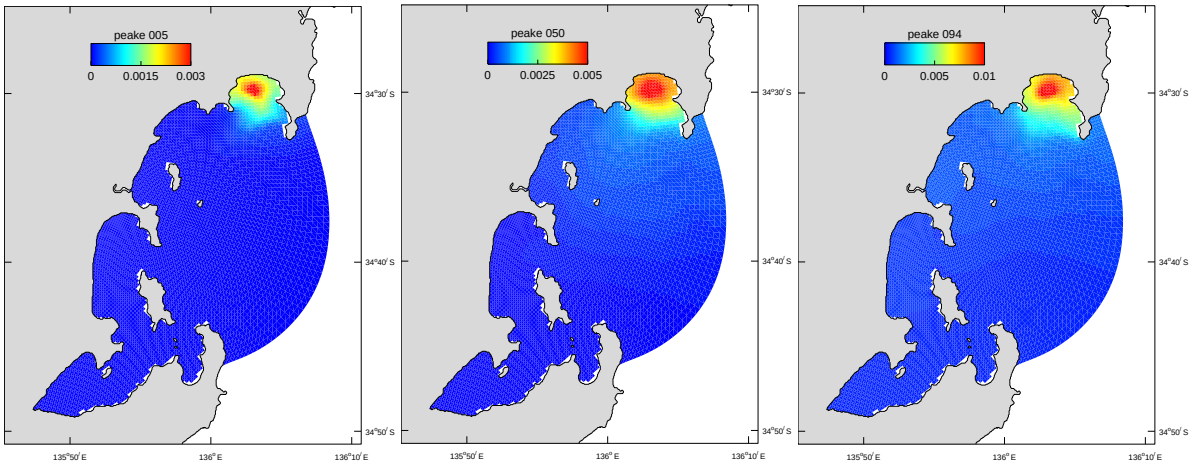

(a) 5 percentile (b) Median (c) 95 percentile

Figure 1.29. Distribution of a passive tracer released at Peake Bay.

Analysis of the distribution of concentrations due to tracer release from the sites in Figure 1.27 indicates that tracer released in the Proper Bay / Port Lincoln area tends to remain in that area; similarly tracer released in Louth or Peake Bays remains restricted to those areas. Tracer released offshore of Boston Island is distributed throughout most of the domain,

although concentrations are lower indicating a larger amount of tracer is removed from the system. Connectivity therefore appears to be divided into three separate regions:

1. Proper Bay and the region landward of Boston Island, having poor connectivity with the rest of the domain,
2. Louth and Peake bays, with moderate connectivity with the rest of the domain,
3. Regions outside these bays and offshore of Boston Island with good connectivity with the remainder of the domain, and subject to greater flushing.

The farm sites offshore of Boston Island but close to the bay regions tend to assume the character of those respective regions; e.g. farm #3 release near Louth / Peake bays is less well connected with Proper Bay than tracer released closer to that region (farm #4). Tracer input along the open boundary rapidly finds its way throughout the whole domain, with Proper Bay being the least accessible region. The connectivity of the domain as diagnosed from the point source releases is consistent with the mean depth averaged flow schematic of 1.26, where circulation cells are established in Boston / Proper and Louth / Peake bays, fed by south to north throughflow in the deeper parts of the domain seaward of Boston Island. The circulation cells are of a closed nature and do not promote good connectivity with the reminder of the region.

The connectivity of the domain can also be examined by observing the behaviour of neutrally buoyant particles released from the same locations and depths as the point source releases above. The particles were released at a rate of 2 particles hour^{-1} from an initial pool of 10,000 particles. These particles were subsequently advected with the circulation to provide insight into how various regions of the domain are connected. The particles are also subjected to random motion representing the effect of diffusion (i.e. sub-grid scale effects). Therefore, any two particles released from the same place at the same time are expected to undergo different trajectories due to this random motion. When a particle crosses the offshore open boundary it is placed in the initial pool for subsequent re-release. The particle distributions after 12 months of simulation are displayed in Figures 1.30 and 1.31 for the TFZ and Peake Bay releases respectively. This distribution is the projection of particles at all depths onto the surface. Particles are colour coded according to their age since being released over the range 0 to 30 days (i.e. blue particles are 0 days old, red particles are > 30 days old).

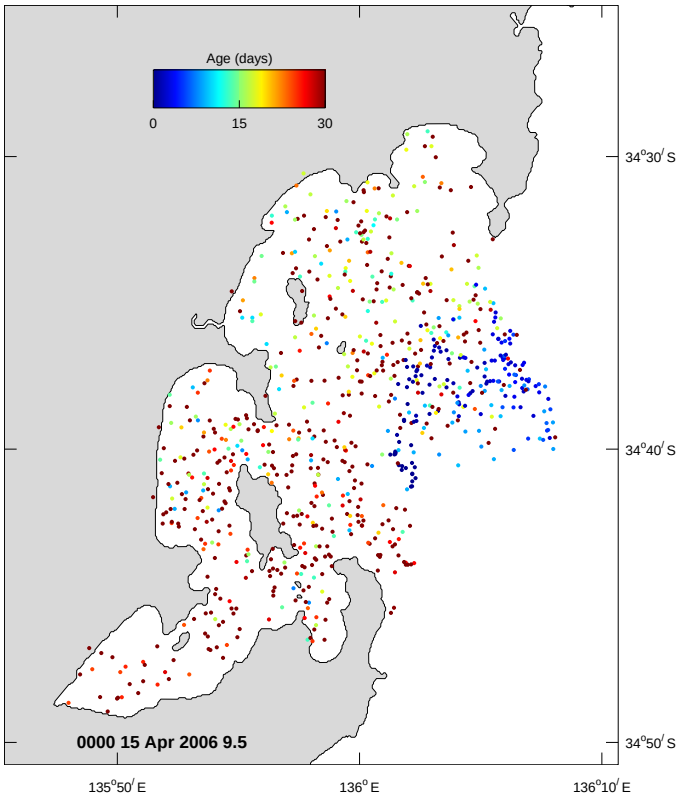

Figure 1.30. Final particle distribution from the tuna farm # 9 release site.

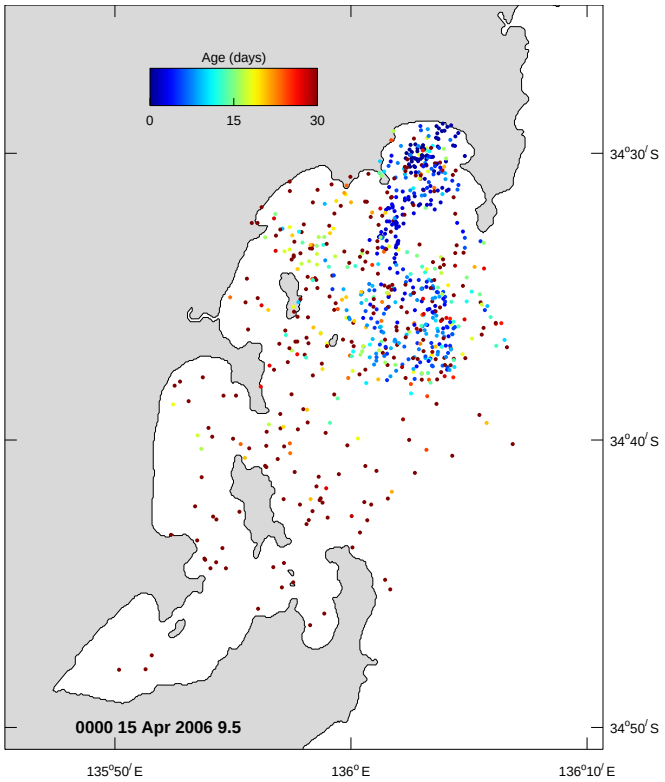

Figure 1.31. Final particle distribution from the Peake Bay release site.

Overall, the connectivity of the domain inferred from the particle distributions is in agreement with the point source distributions. Particles released in Boston Bay are confined to that area, whereas those released in Louth / Peake bays remain in the northern vicinity of the domain. Those released near the open boundary (Farm #1 and #9) are rapidly removed, with few particles distributed throughout the domain. Particles within the domain for these release sites are associated with an older age. These distributions are consistent with the depth averaged net flow conceptualized in Figure 1.26. The average age of the 122,428 particles that exited the domain was 19.9 days, which is indicative of the flushing time for the whole domain.

Note that these images represent a snapshot of the particle distributions, and will vary in accordance with the forcing in effect. An animation of the particle motion over time best conveys the connectivity of the region, although observation of isolated particle trajectories does supply insight into the dynamics of the system. Trajectories were plotted during spring and neap tides for one tidal cycle (low water to low water). Note that circles correspond to the start of the trajectory and squares to the end in these figures, with the net displacement of start and end locations being indicative of the residual flow. Particles trajectories are superimposed on the surface from all depth levels.

Trajectories under the influence of spring tides show oscillatory nature of the tide (Figure 1.32), especially near the offshore boundary. Gross displacements may be large, over 8 km, but small net displacements are observed, consistent with analysis of the ADCP velocity measurements. Neap tide trajectories exhibit little tidal motion, with particle displacement dominated by the wind (Figure 1.33 on 7 January 2006 for an easterly wind, showing net westward motion). Dodge tides reveal a similar situation to neap tides (Figure 1.34), highlighting the poor flushing of the region during these periods. As stated in Section 4.1, it is the low frequency weather band flows that predominantly contribute to flushing the region, rather than tidal circulation.

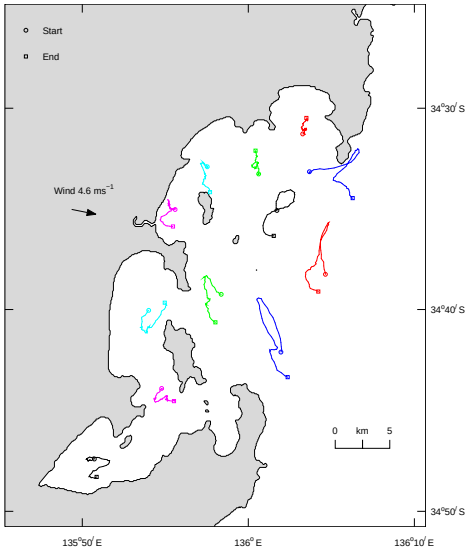

Figure 1.32: Spring tide trajectory, 22 October 2005

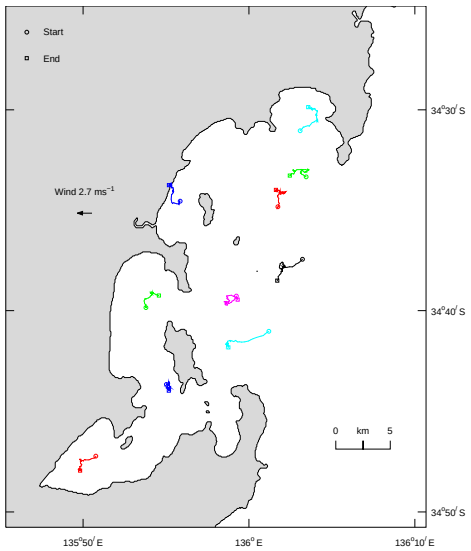

Figure 1.33: Dodge tide trajectory, 7 January 2006

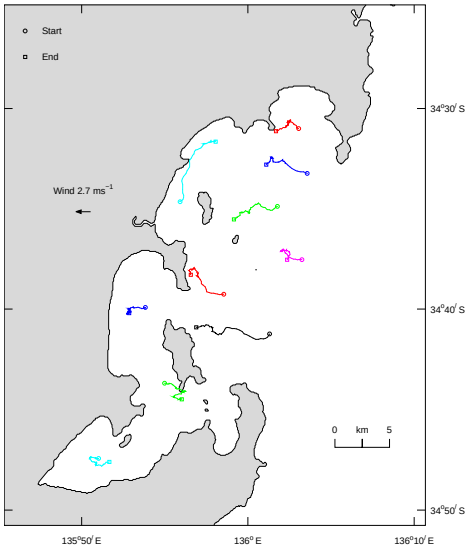

Figure 1.34: Neap tide trajectory, 8 January 2006

1.6. Summary and Conclusions

A 3D primitive equation model was applied to the TFZ region to examine the hydrodynamics of the region. Using a nesting process the region was represented with high resolution while incorporating forcing due to wind stress, tides, low frequency sea level oscillations and pressure gradients due to temperature and salinity distributions. The open boundaries of this model were supplied from a larger scale regional model that encompassed the whole of Spencer Gulf. This model was in turn forced with data collected in the field. The model was simulated for 12 months for the period September 2005 – August 2006 and calibrated to sea level measurements at Port Lincoln, Whyalla and Wallaroo, and temperature, salinity and velocity at numerous locations in the TFZ region obtained from a dedicated field program. The model was able to successfully reproduce tidal and low frequency sea level oscillations in both regional and TFZ models. Temperature, salinity and currents corresponding to tidal (diurnal) and weather band (periods 3-20 days) frequencies were also successfully reproduced by the model.

Both the data and model results showed there to be strong (~20 cm s^{-1}) tidal currents that may be implicated in bottom stirring. Although the tide may be responsible for trajectories of over 8 km, the net displacements due to these currents are small (less than 1.4 km over a 3 hr period). Magnitudes of the weather-band currents are smaller than the tidal currents (< 5 cm s^{-1}), however, due to their longer periods they are the dominant contributor to residual flow and hence primarily responsible for transport and flushing of the region. Both data and model indicate the residual currents eastward of Boston Island (in the TFZ) to be weak (~ 1 cm s^{-1}) and to the north/north east during both summer and winter, contrary to previous studies. The transport due to these flows over a 3-month period is around 80 km. The currents were also found to be strongly sheared in the vertical and so may be important to shear enhanced diffusion and dispersal. However, estimates of the flushing times based on tracers and Lagrangian tracking show flushing time scales of 10 days (Boston Bay) to 2 days for the TFZ. The flushing time for the whole domain based on particle tracking is ~20 days.

The tide in the region is classified as semi-diurnal mixed and is dominated by the semi-diurnal constituents M2 and S2, and the diurnal constituents K1 and O1. Coincidentally, all these constituents have approximately the same amplitude of ~0.18 m, and when they are out of phase they destructively combine to produce very little tidal variation for several days.

During these periods, called the 'dodge tide', the tidal currents are small and transport is primarily wind driven. If wind-speed is low, then it is possible that the region is very poorly flushed. The model was able to reproduce the occurrence of the dodge tide, allowing predictive capability of the timing of these events.

There exists a degree of connectivity between the coastal zone and the TFZ in summer that can be caused by local upwelling. Offshore (eastward) winds force surface waters offshore, resulting in compensatory onshore interior or bottom flow. In addition, the larger evaporation that occurs near the coast leads to dense water formation and bottom plumes that flow to the TFZ. During winter, similar plumes result from coastal cooling rather than evaporation. The annual temperature cycle in the TFZ region is largely driven by atmospheric heating and cooling. Salinity is also controlled by atmospheric exchanges, but to a lesser extent, with advective processes playing a more dominant role. Large decreases in salinity in autumn occur, coincident with the flushing of Spencer Gulf when fresher compensatory oceanic flows enter western Spencer Gulf. Due to the atmospheric exchanges, the TFZ region was also found to be stratified during summer and well mixed during winter.

The depth averaged seasonal flow can be characterised into three main sub-regions within the domain (Figure 1.26). Firstly offshore of Boston Island flow enters the TFZ in the south and exits in the north, with little penetration into the coastal margins. Secondly the Boston Bay / Proper Bay area can be treated as a separate system, with flow generally entering north of Boston Island, flowing south to loop through Proper Bay and exiting to the south-east of Boston Island, where a persistent anti-clockwise gyre exists off Cape Donnington. Thirdly Louth and Peake bays exhibit northwards flow along the coast, fed by water seaward of Point Boston, and seasonally exhibiting gyres within Peake Bay and off Louth Island.

This residual flow determines the connectivity of the region, which consequently can be categorised into three main regions, consistent with passive tracer and particle tracking analyses;

1. A region encompassing Proper Bay and the area landward of Boston Island, which has poor connectivity with the rest of the domain,
2. Louth and Peake Bay regions, which also have moderate connectivity with the rest of the domain,
3. Regions outside these bays and offshore of Boston Island with good connectivity with the remainder of the domain, and subject to greater flushing.

The TFZ numerical model was found to have satisfactory predictive skill, and as such is a suitable tool to couple sediment transport and biogeochemical models to for transport purposes.

Acknowledgements

The authors thank Phillip Adams and all who assisted in collecting data for the project.

1.7. References

Atkinson, I., Ford, P., Noble, R., Oubelkheir, K., Radke, L., Robson, B., Tindall, C., verwey, P. and Webster, I. (2004) Field report on the second survey of dry season water column and sediment properties in the Fitzroy Estuary and Keppel Bay, Rockhampton Queensland, August 15 – September 1, 2004. Coastal CRC, Contaminants dynamics sub-project. Milestones AC09, AC11, AC43 and AC44.

Blanc, T.V. (1985) Variation of bulk-derived surface flux, stability, and roughness results due to the use of different transfer coefficient schemes. J. Phys. Oceanogr. 15, 650-669.

Blumberg, A.F. and Herring, J. (1987) Circulation modelling using orthogonal curvilinear coordinates, in Three-Dimensional Models of marine and Estuarine Dynamics, eds. Nihoul, J.C.J and Jamart, B.M., Elsevier.

Blumberg, A.F. and Kantha, L.H. (1985) Open boundary condition for circulation models, Journal of Hydraulic Engineering, 111, 237-255.

Eanes, R. and Bettadpur, S. (1995) The CSR 3.0 global ocean tide model. Center for Space Research, Technical Memorandum, CST-TM-95-06.

Easton, A. K. (1970) The tides of the continent of Australia. Horace Lamb Centre for Oceanographical Research, Res. Paper 37, Flinders University, South Australia.

Easton, A. K. (1978) A Reappraisal of the Tides in Spencer Gulf, South Australia. Aust. J. Mar. Freshw. Res. 29, 467-477.

Griffes, S.M. and Hallberg, R. W. (2000) Biharmonic friction with a Smagorinsky viscosity for use in large-scale eddy-permitting ocean models. Mon. Weath. Rev. 128, 2935-2946.

Herzfeld, M. (2005) SHOC, sparse hydrodynamic ocean code, scientific manual. CSIRO Marine and Atmospheric Research.

Herzfeld, M. (2006) An alternative coordinate system for solving finite difference ocean models. Ocean Modelling, 14, 174–196.

Herzfeld, M., Middleton, J.F., Andrewartha, J.R., Luick, J. and Wu, L. (2008) Numerical Hydrodynamic Modelling of the tuna farming zone, Spencer Gulf. Technical report, Aquafin CRC Project 4.6, FRDC Project 2005/059. Aquafin CRC, Fisheries Research & Development Corporation and South Australian Research & Development Institute (Aquatic Sciences), Adelaide. SARDI Publication No F2008/000745-1, SARDI Research Report Series No 342, 100 pp.

Kitaigorodskii, S.A., Kuznetsov, O.A. and Panin, G.N. (1973) Coefficients of drag, sensible heat and evaporation in the atmosphere over the surface of the sea. Izv. Acad. Sci. USSR.

Kondo, J. (1975) Air-sea bulk transfer coefficients in diabatic conditions. Boundary-Layer Meteorology, 9, 91-112.

Large, W.G., and Pond, S. (1981) Open ocean momentum flux measurements in moderate to strong winds, J. Phys. Oceanogr. 11, 324-336.

Lennon, G.W., Bowers, D.G., Nunes, R.A., Scott, B.D., Ali, M., Boyle, J., Wenju, C., Herzfeld, M., Johansson, G., Nield, S., Petrusevics, P., Stephenson, P., Suskin A.A. and Wijffles S.E.A. (1987) Gravity currents and the release of salt from an inverse estuary. Nature, 327, 695-697.

Leonard, B.P. (1979) A stable and accurate convective modelling procedure based on quadratic upstream interpolation. Computer methods in applied Mech. and Eng. 19, 59–98.

Leonard, B.P. (1991) The ULTIMATE conservative difference scheme applied to unsteady one-dimensional advection. Comp. Methods in Appl. Mech. and Eng. 19, 17–74.

Masagutov, T.F. (1981) Calculation of the vertical turbulent fluxes in the near-water atmospheric layer over the ocean in tropical latitudes. Meteor. Gidrol. 12, 61-68.

McClatchie, S., Middleton, J.F. and Ward, T. 2006: Water mass analysis and alongshore variation in upwelling intensity in the eastern Great Australian Bight. J. Geophys. Res. 111, C08007

Mellor, G.L. and Yamada, T. (1982) Development of a turbulence closure model for geophysical fluid problems. Rev. Geophysics and Space Phys. 20, 851-875.

Middleton, J. F. and Platov, G. (2003) The Mean Summertime Circulation along Australia's Southern Shelves: a numerical study. J. Phys. Oceanogr. 33, 2270-2287.

Middleton J. F. and Platov, G. (2005) Hydrodynamic model of the Great Australian Bight. Ward T., Goldsworthy S. D. and B. C. Page, Eds, In Tropho-dynamics of the GAB: Assessing the Need for an Ecological Allocation in the SA Pilchard Fishery. Report to the Fisheries Res. Develop. Corp., Proj. Number 2003/072, SARDI Aquatic Sciences Publication Number RD03/0166-2, pp 51-99.

Middleton, J. F., and J.T Bye, (2007) The Physical Oceanography of Australia's Southern Shelves: a review. Progress in Oceanography, 75, 1-41.

Middleton, J. F. and Teixeira, C. (2009) Low frequency circulation in a gulf: wind and remote forcing. In preparation.

Miller, M.J. and Thorpe, A.J. (1981) Radiation conditions for the lateral boundaries of limited-area numerical models. Q. J. R. Meteorol. Soc. 107, 615-628.

Nixon, J. B. and Noye, B. J. (1999) Prawn Larvae Advection-Diffusion Modelling in Spencer Gulf. In Noye, B.J., ed., Modelling Coastal Sea Processes, pp 189-218.

Noye, B. J., Matthews, K. and Grzechnik, M. P. (1999a) A three dimensional model of tides and surges in the Great Australian Bight. In Noye, B.J., Ed., Modelling Coastal Sea Processes, pp 107-134.

Noye, B. J., Grzechnik, M. and Stevens, J. M. (1999b) Modelling Currents and Dispersion in Boston Bay, South Australia. In Noye, B.J., ed., Modelling Coastal Sea Processes, 1, 247-272.

Nunes Vaz, R.A., Lennon, G. W. and Bowers, D. G. (1990) Physical Behaviour of a large inverse estuary. Cont. Shelf Res. 10, 277-304.

Nunes, R.A. and Lennon, G. W. (1987) Episodic Stratification and Gravity Currents in a Marine Environment of Modulated Turbulence. J. Geophys. Res. 92, 5465-5480.

Petrusevics. P.M. (1993) SST fronts in inverse estuaries, South Australia – indicators of reduced gulf-shelf exchange. Aust. J. Mar. Freshwater Res. 44, 305-323.

Petkovic, P. and Buchanan, C. (2002) January 2002 edition of the AGSO bathymetry. Geographic projection WGS84 Datum. Australian bathymetry and topography grid. Canberra: Geoscience Australia.

Ridgway, K. J., Dunn, J., Griffin, D. and Cahill, M. (2006) SynTS – a 3D ocean observational analysis for the Australian region, Second Argo Science Workshop, Venice, Italy.

Ridgway K. R., Dunn, J. R. and Wilkin, J. L. (2002) Ocean interpolation by four-dimensional least squares -Application to the waters around Australia, J. Atmos. Ocean. Tech. 19, 1357-1375.

Simons, T.J., (1974) verification of numerical models of lake Ontario. Part I, circulation in spring and early summer. J. Phys. Oceanog. 4, 507 – 523.

Simpson, J.J. and Dickey, T.D. (1981) The relationship between downward irradiance and upper ocean structure. J. Phys. Oceanog. 11, 309-323.

Smagorinsky, J. (1963) General circulation experiments with the primitive equations, I. The basic experiment. Mon. Wea. Rev. 91, 99 – 164.

Smith, S. D., (1980) wind stress and heat flux over the ocean in gale force winds. J. Phys. Oceanogr. 10, 709-726

Tartinville, B., Deleersnijder, E. and Rancher, J. (1997) The water residence time in the Mururoa atoll lagoon: sensitivity analysis of a three-dimensional model. Coral Reefs, 16, 193–203.

Walker, S.J. and Waring, J.R. (1998) A multiple grid, 3-dimensional, non-linear, variable-density hydrodynamic model with curvilinear horizontal coordinates and level (z) vertical coordinates, CSIRO Marine Research, Report OMR-118/120.

Chapter 2: The wave regime of south-west Spencer Gulf

Emlyn Jones[1,2,3*], Jochen Kampf[2,3], Milena Fernandes[1,3]

[1]SARDI Aquatic Sciences, PO Box 120, Henley Beach SA 5022
[2]Flinders University of South Australia, GPO Box 2100, Adelaide SA 5001
[3] Aquafin CRC

*corresponding author: School of Chemistry, Physics and Earth Sciences, Flinders University GPO Box 2100, Adelaide 5001 Australia.
Current address: CSIRO Marine Labs, Castray Esplanade, GPO Box 1538, Hobart TAS 7001
Phone: +61 (3) 6232 5483, E-mail: emlyn.jones@csiro.au

Abstract

This chapter details the numerical modelling of surface gravity waves within Spencer Gulf and the Tuna Farming Zone (TFZ). Details of the field observations, model description, model validation and modelling results are presented.

The numerical model SWAN (Simulating WAves Nearshore) is used to predict the spatial and temporal wave fields within the study region. SWAN is a finite-difference spectral wave model that is forced with open ocean waves and local winds. Two numerical grids are used in the study, a coarse grid covering Spencer Gulf, Gulf St Vincent and the adjacent continental shelf, in which a fine resolution grid is nested that covers the region of south-west Spencer Gulf, where the TFZ is located.

The wave model is validated against five datasets, collected between August 2005 and November 2007. There is good agreement between observed significant wave height (H_s) and modelled H_s in all but the very near-shore sites. The model is used to predict the annual mean H_s for the TFZ and also investigate the seasonal mean H_s for the region.

Model results show that the region to the south of Point Bolingbroke and to the east of Cape Donnington is subjected to a mixture of locally generated wind waves and oceanic swell that is refracted into the area. Proper Bay, Boston Bay and the area to the west of Louth Island are well protected. There is a region in central Louth Bay that experiences moderately energetic conditions near shore.

January conditions are less energetic than those found during winter. This is due to the westerly storm track being blocked during January by a high pressure ridge that extends over much of the Great Australian Bight. During energetic synoptic scale wind events, the H_s for the TFZ reaches heights of up to 1.2m, and the maximum wave height can be up to twice this value.

The swell height within the TFZ is highly dependent upon the swell direction as it enters the model domain. Swell that propagates into the region from due south causes the highest swell height within the TFZ, with swell heights between 8 and 10% of values found on the adjacent shelf. As the offshore swell direction moves more westerly, the swell height in the TFZ drops to around 2-3% of the offshore swell height. Winds from the east and south-east generate the highest wind waves in the area.

2.1. Introduction

More than 95% of the Australian quota of southern bluefin tuna is farmed in South Australia in the waters of south-west Spencer Gulf. The gulf is triangular in shape, with a length of ~ 300 km, and at its southern end a width of ~ 80 km (Figure 2.1). Spencer Gulf is an inverse estuary, with a salinity gradient that increases towards the head of the estuary (Nunes and Lennon, 1986). Southern Spencer Gulf is classified as micro-tidal (< 2m range) (Harris, 1994). The hydrodynamic regime of the area is complex in nature. During the summer months (December – April), upwelling generated by the predominant south-easterly winds drives cool nutrient rich water on to the shelf adjacent to Spencer Gulf (Middleton and Platov, 2003). During this period the mouth of Spencer Gulf is dominated by a seasonal density front that forms due to the heating of shallow gulf waters. This front limits the cross-shelf exchange with oceanic waters to the winter months of April - November (Petrusevics, 1993). Evidence suggests that the seasonal density front inhibits cross-shelf exchange, thus limiting the inflow of nutrient rich upwelled water. Therefore the release of porewater nutrients during wave generated sediment resuspension could play an important role in the nutrient dynamics of the area.

The sediments found in lower Spencer Gulf share properties of those found both in northern Spencer Gulf and those of the adjacent shelf (Fuller et al., 1994). The continental shelf forms part of one of the largest cool-water carbonate facies in the world. Porter-Smith et al. (2004) suggest that sediment transport in Spencer Gulf is dominated by tidal currents rather than storm induced transport, which dominates the shelf region. The sediments and geochemistry of south-west Spencer Gulf are discussed in Fernandes et al. (2006). These findings differ from those of Porter-Smith et al. (2004) in that Fernandes et al. (2006) propose that sediments within this region are mobilised by wind waves and swell as well as tidal currents. Synoptic scale (3-7 days) weather events in this region have previously caused significant sediment resuspension events that have impacted the region's aquaculture industry. In April of 1996, a sediment resuspension event led to mass mortalities of southern bluefin tuna resulting in the loss of millions of dollars to the industry. Since this event there have been significant changes in management practices and the Tuna Farming Zone (TFZ) was relocated to the east of Boston Island. The new area is subject to stronger water flows beneath the pens and as such there is less accumulation of detritus beneath them.

A key objective identified in the current project was:

" 5.) Application of sediment models to identify likelihood of sediments being resuspended and identification of factors affecting this together with an assessment of their role in algal blooms."

The physical mechanisms behind wave and current-induced sediment resuspension are associated with an increase in the bed-shear in the bottom boundary layer (Guillen et al., 2002; Graber et al., 1989; Jing and Ridd, 1996; Cheng et al., 1999; Paphitis and Collins, 2005). Waves in coastal zones can have periods (the time taken for successive crests to pass a fixed location) ranging from minutes (seiches and infra-gravity waves) to less than one second (capillary waves). Only waves with a period of between 1 and 20 seconds (surface-gravity waves) are considered in this study. Surface-gravity waves can be the result of locally generated wind-waves, swell or a combination of both (Holthuijsen, 2007). The modeling of waves in these coastal environments provides an effective means to quantify not only the spatial distribution of wave characteristics, but also to hindcast events that have not been measured. Freely available wave models, such as Simulating WAves Nearshore (SWAN)

(Booij et al., 1999; Ris et al., 1999; Lin et al., 2002; Moghimi et al., 2005), have been used for many different coastal applications. SWAN is a third generation spectral wave model that can be applied to coastal environments, from large, coarse-resolution shelf-wide scales, to fine-resolution small area scales. Fine scale grids can be located within coarse scale grids (nesting) so that topographically complex regions can be resolved while retaining reasonable run times. The process of nesting uses the coarse scale model to force the boundary conditions of the fine scale model. The application of such a model in coastal regions allows one to model the spatial and temporal wave fields during storm events.

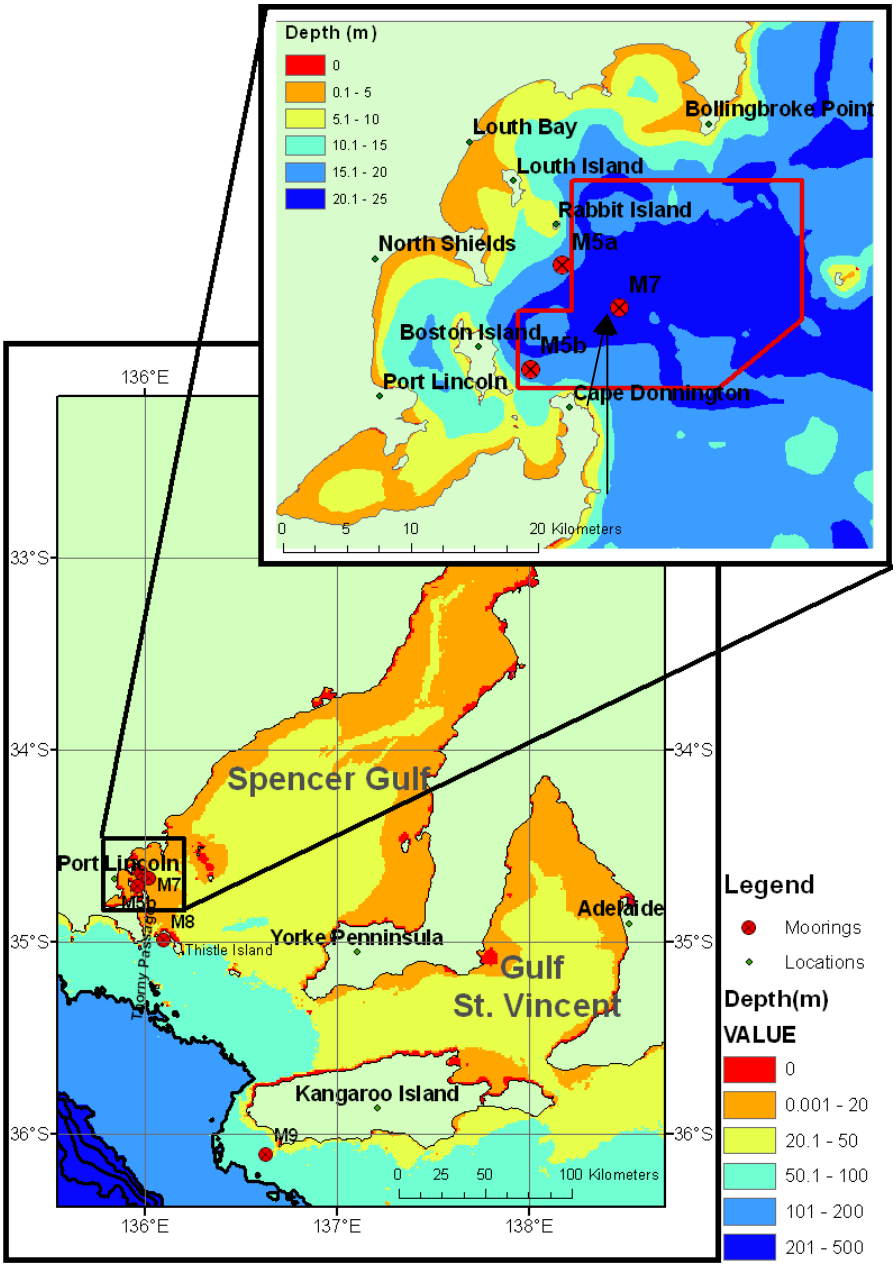

Figure 2.1. Map of study region showing the coarse scale SARWM domain, the fine scale TunaWM domain (inset) and the locations of the moorings used in the validation of the wave model (M5 to M9). The TFZ (inset) is delineated by the red border.

Previous studies into the swell height (H_{swell}) and wave characteristics of Spencer Gulf have found that little or no swell (H_{swell} < ~5cm) is present in its upper reaches. Waves with a

period of >6.5 s are present for less than 1% of the time in the central regions of the gulf (Noye, 1984). In the southern section of Spencer Gulf the wave field is a combination of locally generated wind waves and incoming swell from the Southern Ocean. Hemer and Bye (1999) present the first wave modeling study on this area, in which only the incident swell is used to force the model. H_{swell} within Spencer Gulf and Gulf St Vincent is highly sensitive to the approaching incident swell direction to the west of Kangaroo Island. A wave model has been applied to Gulf St Vincent, to the east of the present study area, as part of the Adelaide Coastal Waters Study (ACWS) (Pattiaratchi et al., 2007). The model used for the ACWS was SWAN, running in default mode and forced by a homogenous wind field over the entire model domain. When compared with field data it was found to over-predict the significant wave-height (H_s) by up to 50% during periods of low wave height, it also under-predicted the wave height during peak events by ~20%. These discrepancies were attributed to the use of a homogenous wind field over the model domain. There have been no studies that have investigated the combined swell and wind-wave characteristics in the region of the TFZ in south-west Spencer Gulf. The aim of this study was to ascertain the seasonal and storm-associated wave heights for the area and their implications for sediment resuspension, which is discussed in Chapter 3, within the TFZ.

2.3. Methods

2.3.1. Wave observations

Wave observations in areas with high amounts of shipping activity are a trade-off between the accuracy gained by using a wave-rider buoy and the safety of using a bottom mounted Acoustic Doppler Current Profiler (ADCP). A bottom mounted ADCP was chosen due to it being less likely to be damaged by shipping and availability of instrumentation. Four deployments were successfully undertaken at different locations. Three deployments were within the area of interest in south-west Spencer Gulf in approximately 20 m of water, and a fourth was in the vicinity of the southern entrance to Thorny Passage in 45 m of water (Figure 2.1).

A relocatable mooring was located in south-west Spencer Gulf from September 2005 to August 2006 (M5a and M5b in Figure 2.1). During this period, the first two successful deployments were made. The first deployment, M5a, was situated 4 km south-east of Rabbit Island lasting from 30/08/2005 to 11/11/2005. The second deployment, M5b, was made 2 km east of Boston Island from 12/11/2005 to 2/02/2006. Two further deployments were made, however no wave data was recovered from the instrument. A Nortek Aquadopp Profiler was configured to record wave parameters along with current profiles. The Aquadopp uses the pressure sensor set to sample at 2 Hz to derive the wave spectra, and orbital velocities to derive the 2-D direction spectra.

The third deployment was again in the TFZ, from 12/07/07 until 19/07/07 using a 300 kHz RDI Workhorse Sentinel ADCP with a wave package (M7). This instrument has the ability to derive wave spectra using three different techniques. Like the Aquadopp, the Workhorse can use pressure (1) and velocity (2) to derive the wave spectra, but unlike the Aquadopp, the Workhorse can acoustically measure (3) the instantaneous free surface elevation from the acoustic signal in each of the four beams. This deployment was aimed at capturing wind induced wave events. The instrument was set to continuously sample at 2 Hz until the memory was filled, resulting in a high-resolution record. This differs from the other deployments in that the instrument mounted on M5a and M5b sampled for waves every 8 hours for a duration of 512 seconds (burst mode). The advantage of using burst mode is that it

allows the instrument to conserve battery power and memory, resulting in a deployment that can last months instead of weeks.

The fourth deployment positioned the RDI ADCP near the southern entrance of Thorny Passage, near Thistle Island, from 1/10/07 until 15/12/07 (M8). The instrument was set to burst sample for waves every 2 h.

Data from a non-directional wave-rider buoy (M9) operated by the Bureau of Meteorology (BOM) located south-west of Kangaroo Island was also used for model verification near the southern boundary of the SARWM domain.

2.3.2 Model Description

The temporal and spatial dynamics of the wave field were investigated using the freely available SWAN model. A description of the SWAN model is contained in Booij et al. (1999) and Holthuijsen (2007). Waves can be characterized by their frequency and the direction they propagate from. This concept is called the directional wave spectra. The energy (E) contained at a particular frequency and direction is called the energy density. SWAN is a third generation spectral wave model that solves the spectral energy balance equation whereby the wave spectra is characterised by a number of discreet frequencies (Δf) and directions ($\Delta\theta$) (Holthuijsen, 2007). SWAN uses an implicit numerical scheme to allow for shallow water depths and give greater numerical stability. The model uses the energy balance equation:

$$\frac{\partial}{\partial t}E + \frac{\partial}{\partial x}c_x E + \frac{\partial}{\partial y}c_y E + \frac{\partial}{\partial \vartheta}c_\vartheta E = S \qquad (2.1)$$

where $E(f,\theta;x,y,t)$ is the energy density (See Appendix, section 2.8.) as a function of frequency f and direction θ, referenced to the coordinate system whereby x is orthogonal to y, and t is time. The first term of equation 2.1 represents the local rate of change of the energy density in time. The second and third terms relate to the propagation of the energy density in space with propagation velocities given by c_x and c_y, where c is defined as:

$$c = \sqrt{\frac{g}{k}\tanh(kd)} \qquad (2.2)$$

where g is the acceleration due to gravity (9.8 ms^{-2}), k is the wave number and d is the water depth. The fourth term of equation 2.1, where c_θ is the rate of change which represents the directional (θ) rate of change of c due to the effects of varying bottom topography, essentially topographic refraction. There has been no attempt to incorporate the effect of time varying water depths (e.g. tidal range) or currents (e.g. tidal and wind driven currents). It is possible that in shallow near-shore regions and Thorny Passage, such tidal effects may cause significant errors within the model, but throughout the majority of the model domain, these tidal effects will be negligible. S in equation 2.1 represents the source terms that account for generation (wind), dissipation (white capping, bottom-friction and depth-induced breaking) and non-linear wave-wave interactions (triads and quadruplets).

Two grids are used in this study. A coarse resolution grid, referred to as the South Australian Regional Wave Model (SARWM) and, nested within this, a fine-resolution grid covering the Tuna Farming Zone, referred to as the Tuna Wave Model (TunaWM) (Table 2.1). The open boundary of the TunaWM is forced from output obtained from SARWM. The southern and

western open-sea boundary of the SARWM domain is forced by the Meso-WAM output obtained from the Australian Bureau of Meteorology (BOM). Wave data is read into the model every 3 h. Wind forcing data is taken from Meso-LAPS, also obtained from BOM, which gives a spatial varying wind field with a 12.5 min latitude (~23km) resolution. Wind data is read into the model at hourly intervals. Observational data exists from automatic weather stations (AWS) throughout the region, however such data is subject to errors caused by local topography and is therefore not representative of regional scale processes. The AWS located to the north of Port Lincoln was found to be contaminated with numerous local effects caused by the range of hills to the west and also locally generated sea-breezes. For the purpose of this modeling study, the use of Meso-LAPS data gives the highest resolution wind-data available. At all land boundaries, i.e. the coastline, it is assumed that all the wave energy is dissipated in near-shore processes such as depth induced breaking. SWAN allows for reflective boundary conditions, however there has been no attempt to incorporate such influences in this application. Observational data from the southern side of Thistle Island (M8) show no swell reflection in the directional spectra.

Table 2.1. Model description.

	SARWM	**TunaWM**
Latitude Extent	32.157˚S – 36.378˚S	34.463˚S - 34.835˚S
Longitude Extent	135.544˚E – 138.708˚E	135.786˚E – 136.208˚E
Bathymetry	GA Bathytopo 0.01	CSIRO
Resolution	2.2 km	0.4 km
Surface Forcing	MesoLAPS Winds	MesoLAPS Winds
Boundary Forcing	MesoWAM	Nested within SARWM

A sensitivity analysis investigating the effects of varying the physics schemes that represent the source terms in Equation 2.1 was performed to find the best combination. The default physics scheme in the SWAN model, run in third generation mode, uses the formulations of Komen et al. (1984). However there are options to use the methods of Jansenn (1991) or a saturation based white capping method using the wind formulation of Yan (1987) presented in van der Westhuysen et al. (2007). All three physics schemes were tested to determine the best scheme for this application. The physics scheme using the method of Jansenn (1991) provided the best agreement between observations and modelled output.

Southern Spencer Gulf is littered with islands and reef systems that combine to form a topographically complex bathymetry. To this end the choice of bottom friction schemes seemed critical. The default used by SWAN is the JONSWAP scheme (Hasselmann et al. 1973). The other options available are the COLLINS (Collins, 1972) and MADSEN (Madsen et al. 1988) schemes. In this study it was found that results were not sensitive to the type of scheme used if the parameters were tuned accordingly. For this study, we used the MADSEN option for all reported simulations, which will allow us to input a spatially variable roughness-length (a measure of the “roughness” of the bottom e.g. a reef will have a much greater roughness than fine-sand) in the future if this information becomes available.

2.4. Results

2.4.1. Model Validation

A number of datasets were used to validate both the SARWM coarse resolution model and the TunaWM fine resolution model. In the following section we present a time-series comparison and scatter plot showing the correlation coefficient between the observed and modelled Hs at various locations within the model domain. The Cape de Couedic wave rider buoy (M9) is sufficiently close to the southern boundary to be used to validate the forcing data used in this study. Figure 2.2 shows a time-series plot comparing the modelled significant wave height (H_s) with the observed H_s taken from the wave rider. Generally there is fairly good agreement between the observed and modelled results. There is a slight bias in the model to under-predict the significant wave height by up to 15% during high wave events. During times of low wave heights, the model has a tendency to over-predict H_s by up to 20%.

A comparison of the modelled and observed data from M8 near Thistle Island (Figure 2.3), also shows good agreement. On some occasions, during peak events such as on 29/10/07, the model under-predicts H_s by approximately 20%. The high frequency variations seen in the observed H_s are not reproduced by the model, as it was forced with both modelled winds (Meso-LAPS) and modelled wave heights on the boundaries (Meso-WAM). Modelled wind fields tend to lack short time scale variability associated with gusts. If observational data were used to force the model, some of the higher frequency variation would be accounted for, however local effects such as sea-breezes would affect the entire model domain.

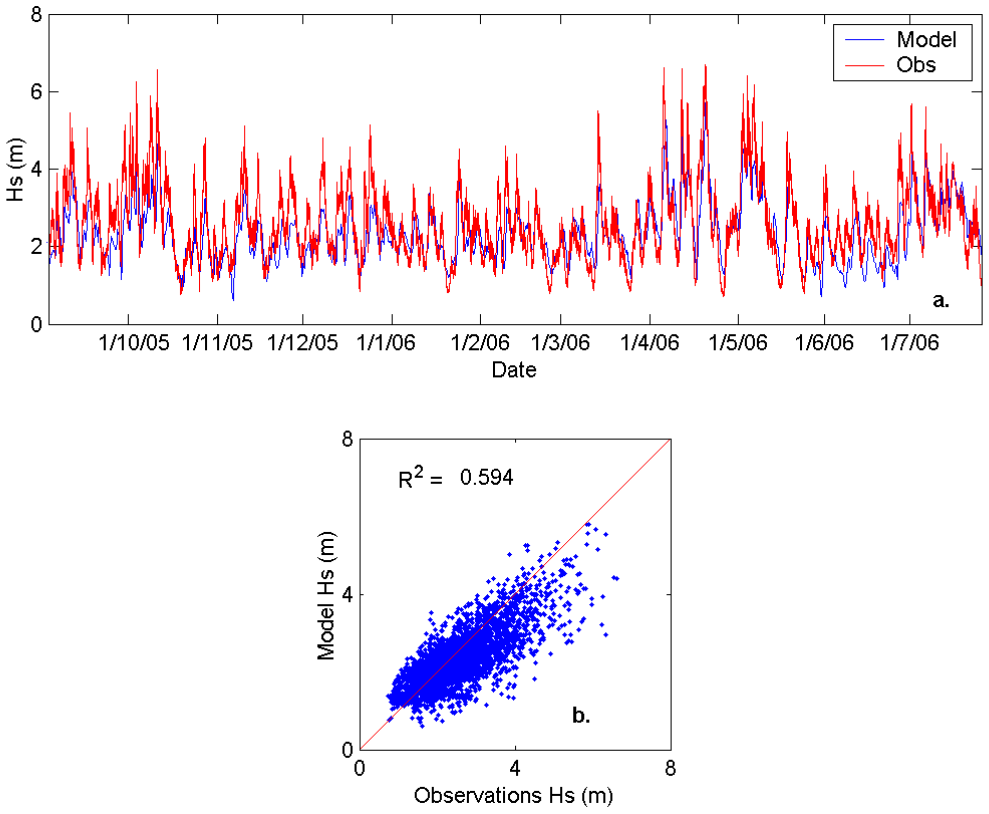

Figure 2.2. Time series of modelled (blue) and observed (red) significant wave heights (m) at M9 located 5 nautical miles off Cape de Couedic, south-west Kangaroo Island (a), and correlation between modelled and observed wave heights at this location (b).

The comparison between the modelled and observed H_s at location M5a shows reasonable agreement throughout the deployment (Figure 2.4), with a bias towards under-prediction during peak events. However, during the deployment at location M5b (Figure 2.5), the model over-predicts H_s. The observed Hs signal at M5b is the smallest of any of the sites, the poor agreement between the modelled H_s and observed H_s at this location is likely to be due to three factors:

1. Proximity to Boston Island and the nature of the wind field. The Meso-LAPS wind fields do not include the effects of locally generated sea-breezes as the model grid is too coarse. Meso-LAPS may not predict the actual wind direction accurately, which will lead to erroneous predictions in wave height in topographically complex areas. If the (model, coarse grid) wind directions differ from reality by more than a few degrees, the associated fetch may be significantly different as shown by the arrows in figure 2.1 inset. The discrepancy in fetch will lead to the incorrect prediction of wave heights.

2. Bathymetry may not be well represented in this near-shore area, thus impacting on the accuracy of the modelled wave fields.

3. The instrument cannot resolve waves with periods of less than 5 seconds, leading to under-prediction of the observed H_s. This is due to the way the wave spectra are derived on this mooring. The Nortek Aquadopp Profiler uses the pressure sensor to derive the wave spectra. In 20 m of water, the dynamic pressure generated from high-frequency wind waves doesn't penetrate to the depth of the pressure sensor.

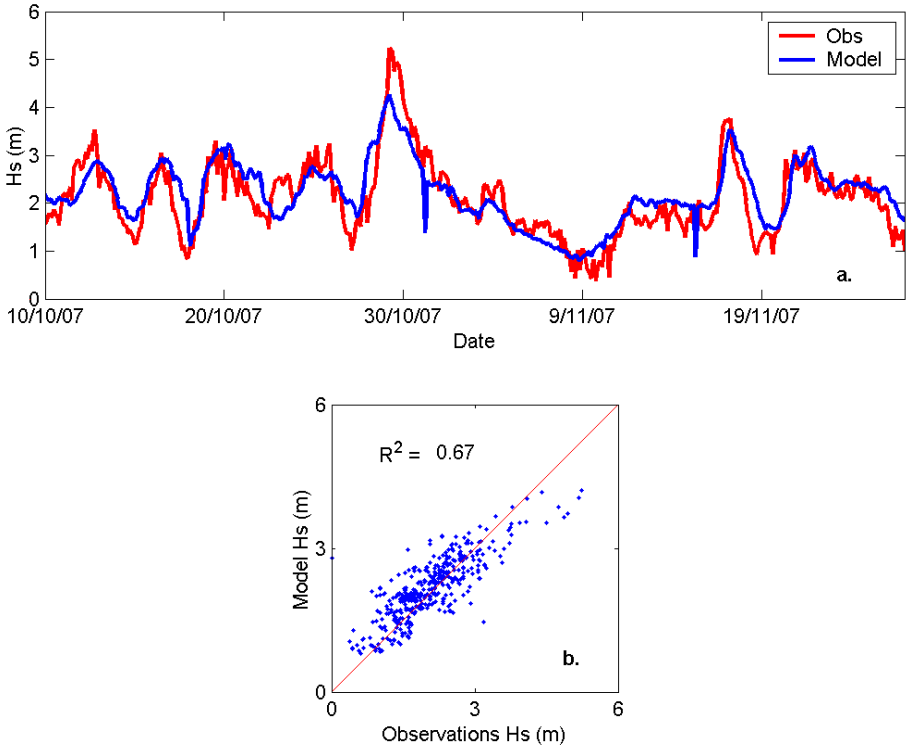

Figure 2.3. Time series of modelled (blue) and observed (red) significant wave heights (m) at M8, near Thistle Island (a), and correlation between modelled and observed wave heights at this location (b).

The observational datasets collected at M5a and M5b did not capture the higher frequency wind waves and therefore does not provide a rigorous dataset with which to validate the

model. A third deployment (M7) using a different instrument was therefore used for model validation in the TFZ.

When mooring M7 was deployed, it was hoped that it would record a storm event. The instrument was configured to record data continuously at 2 Hz until the memory filled, which was approximately seven days. While not capturing a severe storm event, a moderately energetic event did occur on 17/07/2007. Once again, although the model does not reproduce the higher frequency variability seen in the observations, it does predict the overall trend (Figure 2.6). When the modelled wave heights are compared to the observed wave heights, there is very good agreement. The velocity measurements from the closest three layers to the surface were used to derive the wave spectra. The RDI Workhorse can also use the spectra derived from the instantaneous free surface elevation, measured acoustically by the four beams. However, we found that the signal was severely contaminated by infra-gravity waves in this deployment. This phenomenon has been observed before (Hoitink et al., 2007), therefore the velocity spectrum was used. While the instrument was set to sample at 2 Hz, it is not possible to include frequencies above 0.3 Hz due to the limitations imposed by the error associated with acoustic measurements. This limits the amount of energy that is used to derive the significant wave height. We have no way to verify the model at frequencies above 0.3 Hz in this location. Nonetheless, overall there is a good agreement between the observed and modelled wave heights.

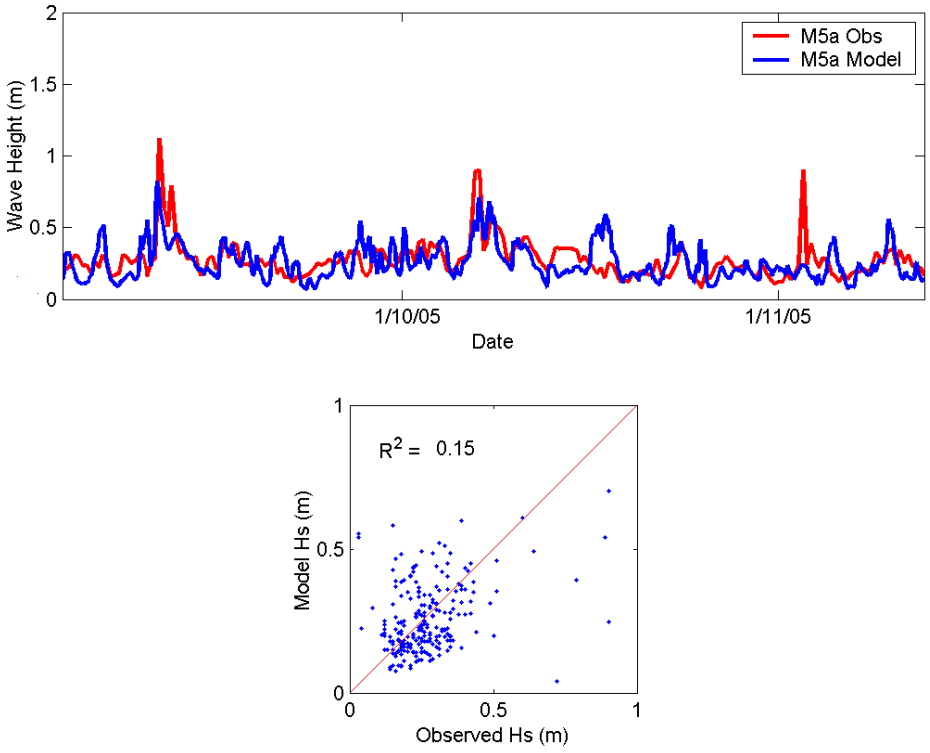

Figure 2.4. Time series of modelled (blue) and observed (red) H_s (m) at Mooring 5a (a), and correlation between modelled and observed wave heights at this location (b).

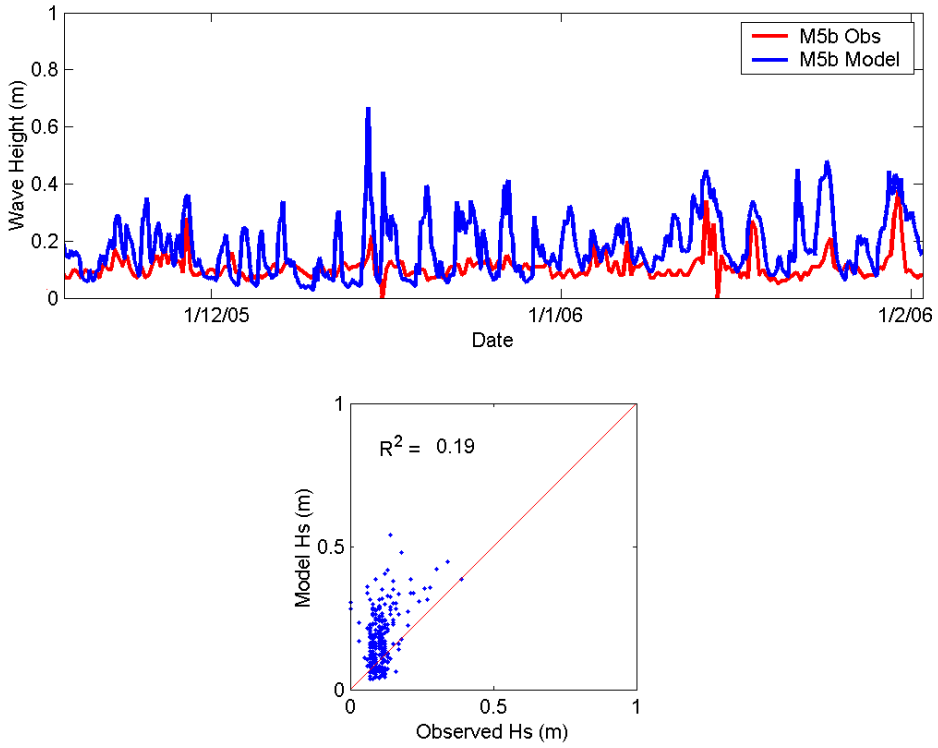

Figure 2.5. Time series of modelled (blue) and observed (red) H_s (m) at Mooring 5b (a), and correlation between modelled and observed wave heights at this location (b).

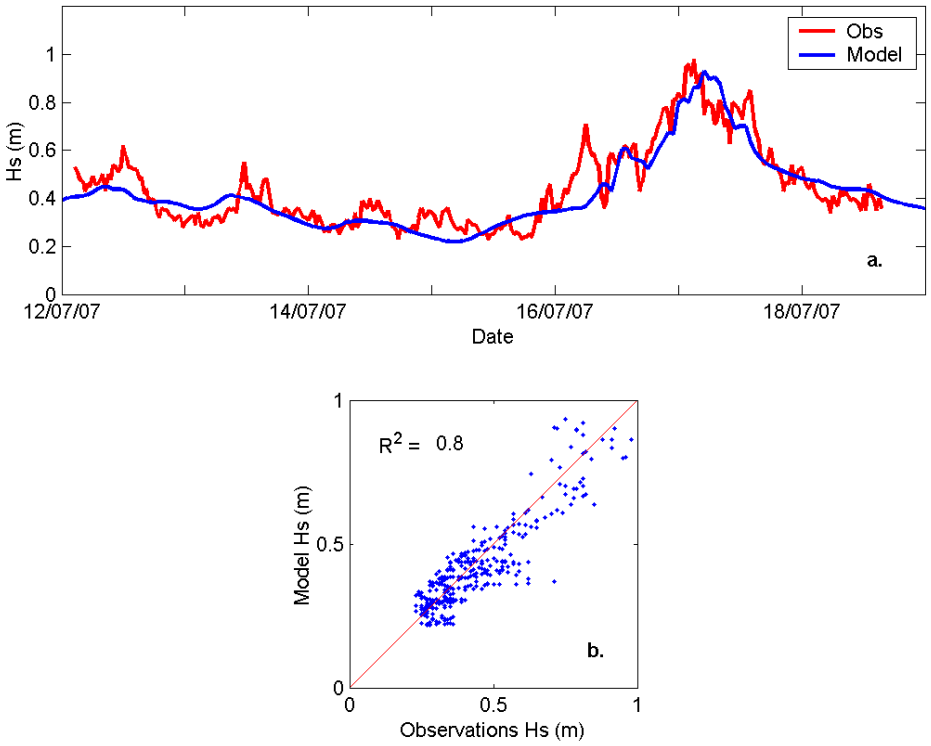

Figure 2.6. Time series of observed (red) and modelled (blue) H_s (m) at M7 (a), and correlation between modelled and observed wave heights at this location (b).

2.4.2. Model Results

The annual mean H_s varies from 0.1 m in the sheltered coastal embayments, up to 0.7 m in the more exposed offshore regions (Figure 2.7). The incoming wave direction is generally from the south, and is refracted by the bottom topography into the more sheltered regions. The wave height diminishes significantly as the depth decreases, as the interaction of the waves with the bottom dissipates much of the wave energy. The region to the east of Cape Donnington is the most energetic, with an annual mean H_s of 0.6 m near-shore. For most of the TFZ the annual mean H_s is between 0.3 and 0.5 m.

During the storm event of 17/7/07, the observed H_s at M7 in the middle of the TFZ peaked at 1.0 m and the modelled wave height reached 0.95 m (Figure 2.6). This event is probably representative of many of the energetic events that occur throughout the year. The spatial variation in the modelled wave fields during this event (Figure 2.8), shows that the sheltered areas west and south of Boston Island had H_s up to 0.3 m, whereas the exposed areas to the east of Cape Donnington ranged between 0.8 and 1.2 m. The offshore wave direction was from the south, but in areas protected from the incident swell, the waves had a south-westerly direction closely aligned with the wind direction.

We assessed the seasonal variability in H_s by comparing the modelled mean wave heights in January to those in July. The January mean H_s (Figure 2.9a) differs only slightly to that of July (Figure 2.9b). During January the mean wave direction in the TFZ is from the south through to the south-east. During July this alters only slightly to a more southerly direction. The mean wave heights in July are slightly higher, ~0.4 – 0.6 m compared to 0.3 – 0.4 m during January. The variations in H_s between January and July are likely due to the lack of energetic storm events during summer, which are typically blocked by a high pressure system centered over the Great Australian Bight. During winter the high pressure system is located over continental Australia, allowing cold fronts and strong winter storms to pass closer to the southern margin of the Australian landmass. Figure 2.8 shows the spatial variation in wave height and direction for a typical storm event for the region.

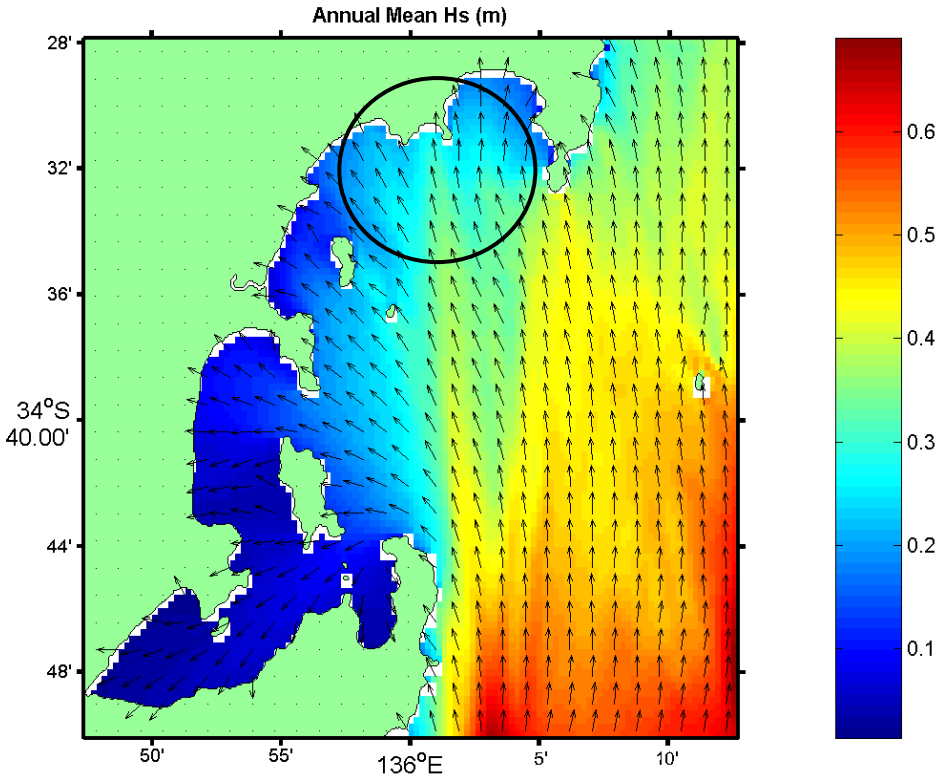

Figure 2.7. The modelled annual mean H_s (m). The arrows indicate the direction that the waves are travelling. The circle denotes the area to the west of Point Bolingbroke that experiences elevated wave energy in comparison to other near-shore locations.

The main source of wave energy, apparent in the annual mean, January mean and July mean H_s, is the propagation of waves into the TFZ from the south. This is supported by the mean wave direction coming from the south. Only a small proportion of the wave energy is able to propagate into the area through Thorny Passage. Thistle Island blocks the incoming swell from directly south, therefore a majority of the incoming wave energy is refracted by the bottom topography into the TFZ from between Thistle Island and Yorke Penninsula. The source of this wave energy is dependent upon the period of the waves. For waves with a period greater than 6-7 seconds, i.e. swell and longer period wind waves, the southern ocean is the dominant source. However, waves with periods of less than 6 seconds, are generated by the local wind field within the model domain. There appears to be a concentration of wave energy near the shore-line to the west of Point Bolingbroke, once again it is likely that this is due to the refraction effects of the bottom topography.

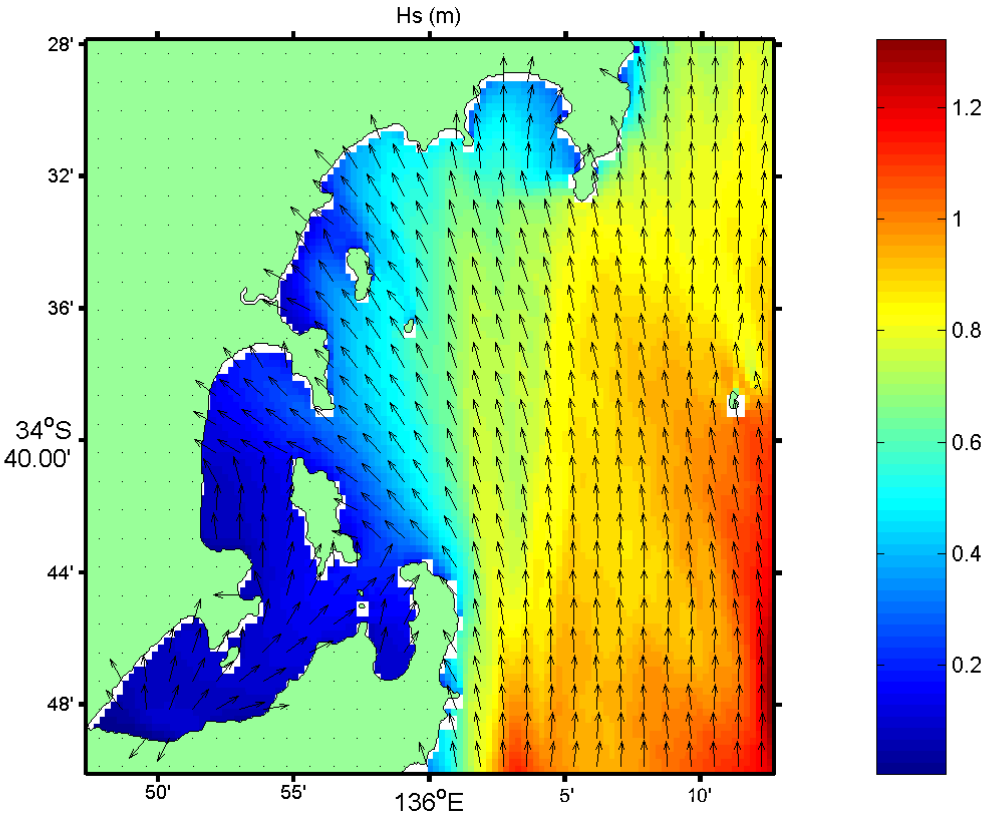

Figure 2.8. Modelled H_s (m) and direction for the storm event of 17/7/07. The arrows indicate the direction that the waves are travelling.

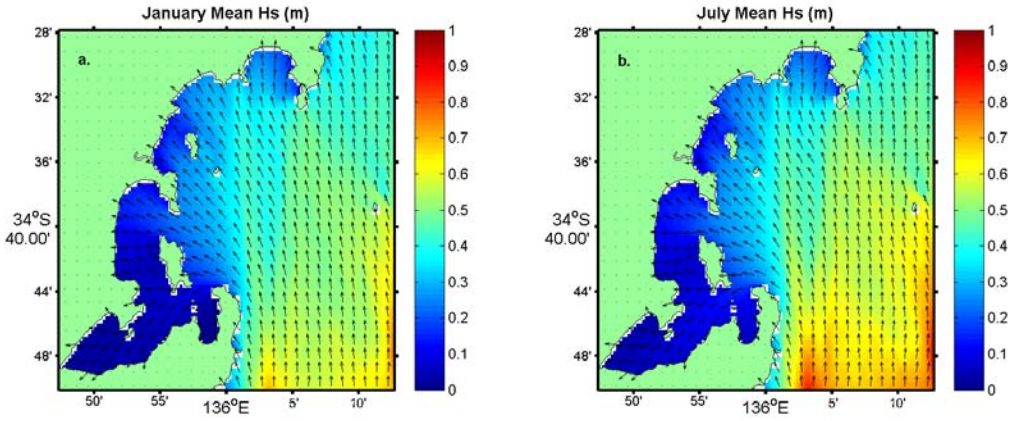

Figure 2.9. The modelled January (a) and July (b) mean H_s. The arrows indicate the direction that the waves are travelling.

2.5. Discussion

The prevalent wave conditions within the TFZ are a combination of locally generated wind waves and incoming swell from the Southern Ocean. The effects of locally generated wind waves are often masked by the influence of the incoming swell from the Southern Ocean, except in the sheltered areas to the west of Boston Island. To investigate the role of wind waves, a process study using only homogenous wind forcing across the model domain was used to identify the wind direction capable of generating the greatest wave energy in the TFZ (Figure 2.10).

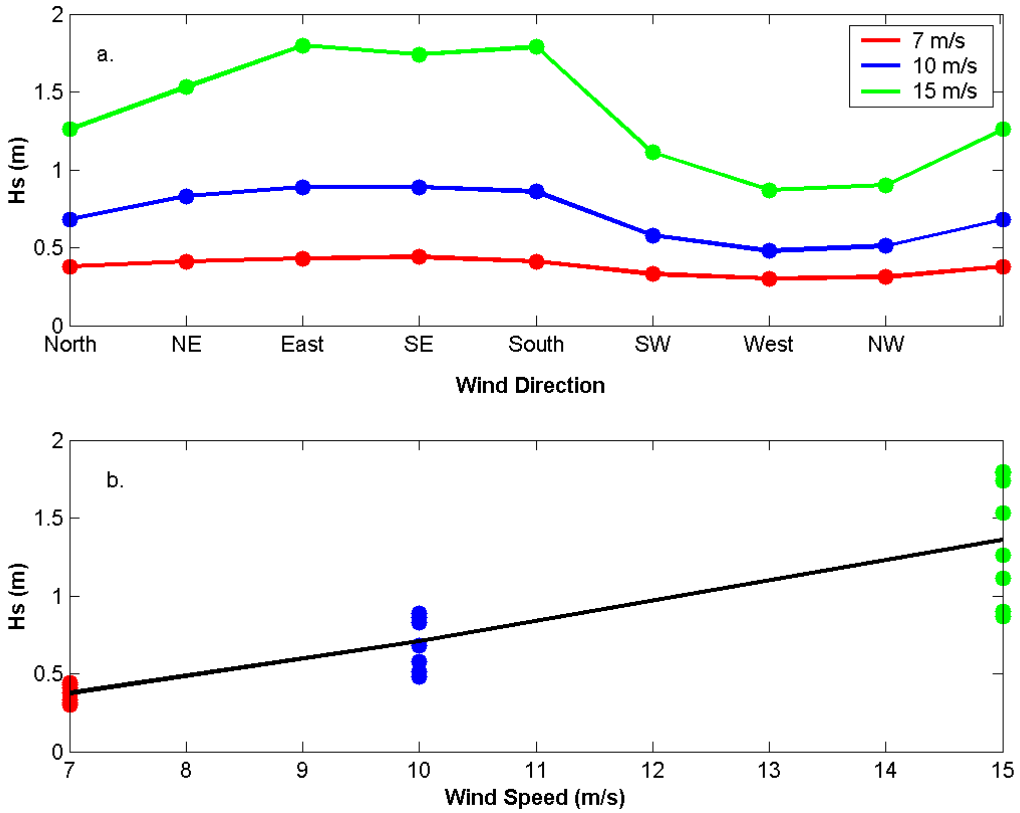

Figure 2.10. a) Wind direction vs significant wave height at M7 for varying wind speeds and b) wind speed vs $H_{s,}$ using the same datapoints from 2.10a.

Within the TFZ, the wave height associated with wind waves is highly sensitive to the wind direction and strength. Winds from the north through east to the south generate the greatest wave heights. This is directly related to the fetch available for these wind directions. There is a linear response to an increase in wind speed between $7ms^{-1}$ and $15\ ms^{-1}$, however as previously stated, the wind direction does cause significant variation at higher wind speeds. Winds from the east through to south cause the greatest wind wave heights in the middle of the TFZ at M7.

Swell waves are considered to be waves with a period of greater than 10 seconds. To investigate the effect of the incident swell angle on the swell height within the TFZ, the normalised height (H_n) is used to identify which incident angle allows the greatest amount of swell energy to reach a typical location within the TFZ (M7). The angle at which the swell approaches the model boundary is defined as the direction the waves are propagating from, e.g. swell coming from the south, has an incident angle of 180º.

$$H_n = \frac{H_{swell,M7}}{H_{incident}} \tag{2.3}$$

where $H_{swell,M7}$ is the swell height at M7 and $H_{incident}$ is the significant wave height at the southern boundary.

The normalized height at M7 is used rather than the actual height as this removes any bias associated with waves propagating from different directions having significantly different heights. At the southern boundary, waves propagating from the south-west are responsible for the greatest heights (Figure 2.11), but due to the effects of refraction, the energy associated with this wave direction may not reach the TFZ.

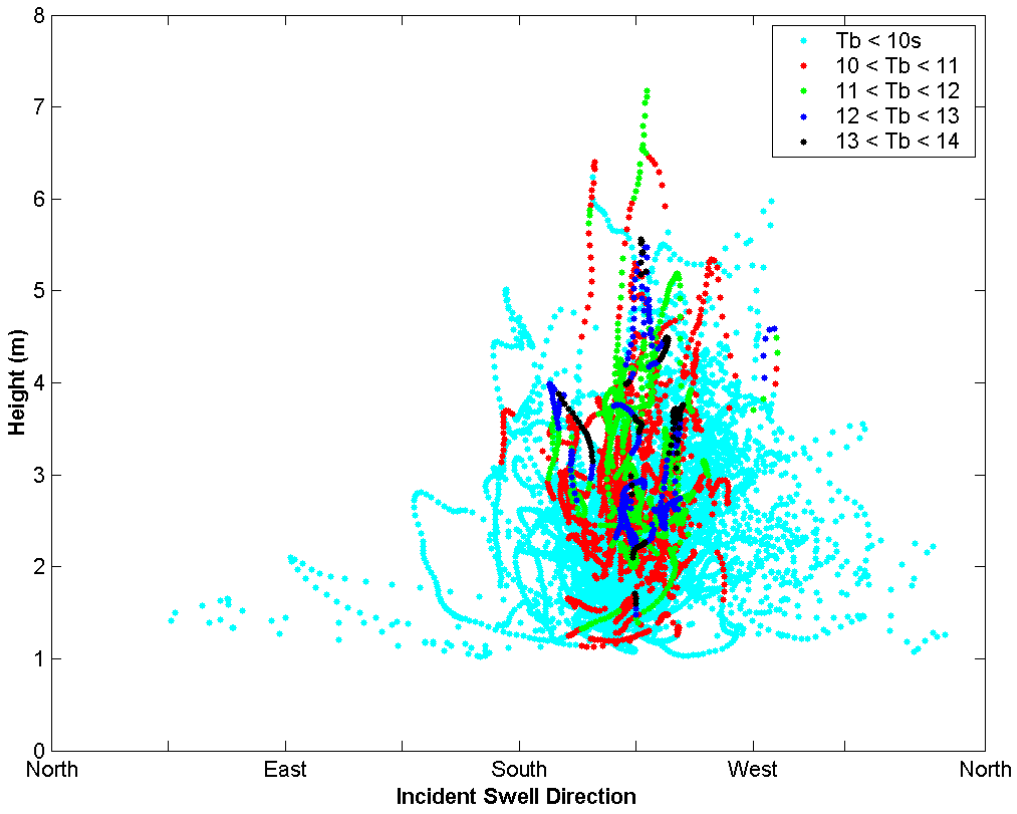

Figure 2.11. The incident wave height plotted against the incident direction at the southern boundary. The data points are grouped by the period of incident waves at the southern boundary (T_b).

A plot of normalized height vs incident swell direction for the period 1/9/05 – 30/8/06 was constructed to identify the incident swell direction that generates the greatest swell heights at site M7. It was found that the swell component of the spectra within the TFZ is highly dependent upon the incident angle of the swell (Figure 2.12). This result agrees with the findings of Hemer and Bye (1999), in that as swell approaches the entrance to Spencer Gulf from the south, it is refracted by the bathymetry such that it is able to propagate into the TFZ.

The relationship between the incident swell direction and the peak period is an important consideration. The incident swell was grouped into five categories, depending on the peak period of the incoming waves at the southern boundary (Figure 2.12). Wave directions greater than 270˚ and less than 90˚ originate from the coastline and are not associated with swell waves, due to the fact that these waves are propagating from the coastline and are

therefore not originating from the Southern Ocean. For waves with a period of less than 10 s, the incoming waves are not considered to be swell waves as they have a period of less than 10 seconds. As the period exceeds 10 s, the incident direction is confined between 180˚ to 270˚, approaching the coastline from the open ocean.

The greatest normalized height is reached when the incident swell direction is ~200˚ (SSW) with a period between 11 and 13 s, with swell height at site M7 reaching 8-11% of the height at the southern boundary. As the incident swell direction progressively shifts to the west, the normalized height decreases linearly to 2-3% of the height found on the southern boundary. As the period exceeds 13 s, the normalized height decreases for most incident directions. This is due to the longer period waves being subjected to higher dissipation or enhanced refraction, caused by interactions with the sea-floor at greater depths.

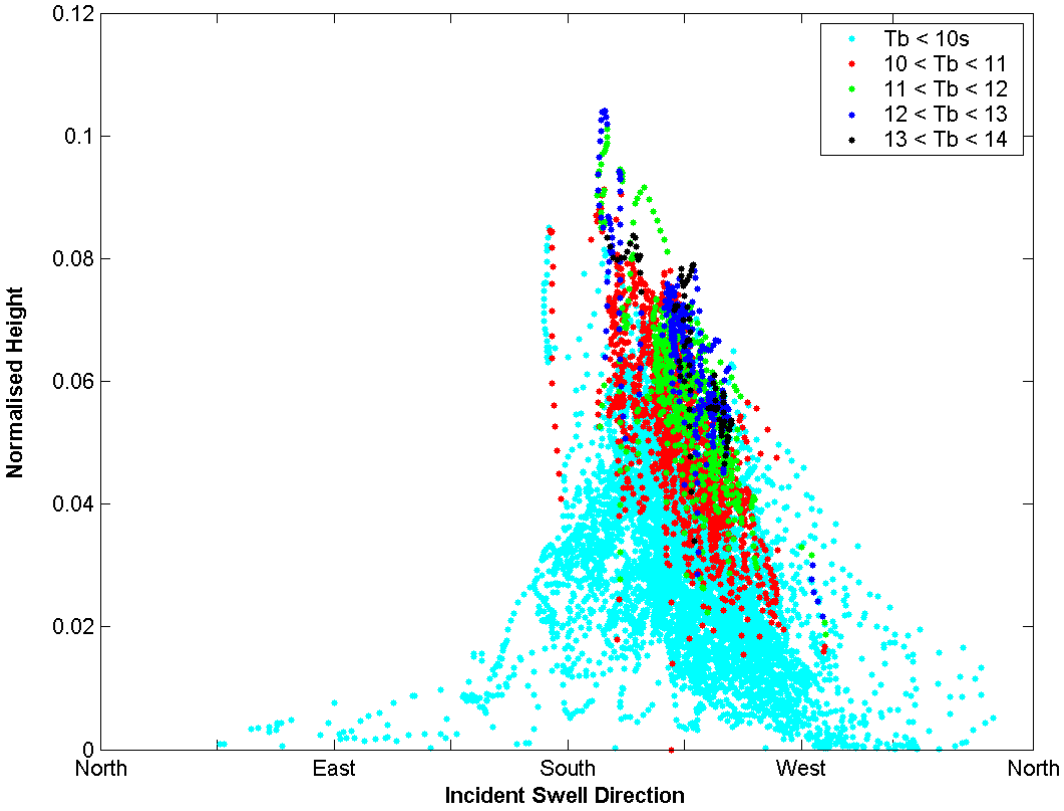

Figure 2.12. Normalised swell height (H_n) vs incident swell direction. The data points are grouped by the period of incident waves at the southern boundary (T_b).

The relationship between normalized swell height and direction provides an estimate for swell height within the TFZ. The observed period and wave height at Cape de Couedic are publicly available from the BOM website (www.bom.gov.au), and directional information is also easily accessible from websites such as www.bouyweather.com. The amount of swell that will penetrate into the TFZ is summarized in Table 2.2. The combination of wind direction and incoming swell that will cause the most energetic conditions within the TFZ is a swell propagating from the south-south-west at the southern boundary with winds from the north-east through to the south.

Table 2.2. Summary of the swell conditions in the TFZ depending on the incident swell direction and the period of the waves at the southern boundary (T_b). Values represent the swell height in the TFZ as a percentage of the open ocean height. The highlighted column shows the direction producing the greatest swell height in the TFZ. * Limited number of observations for this direction and period.

T_b	Incident Swell Direction				
	S	SSW	SW	WSW	W
<10	0% – 4%	4% - 6%	2% - 4%	1% - 4%	0% - 2%
10-11	4% - 9%*	4% - 8%	4% – 7%	3% – 5%	-
11-12	-	6% - 10%	5% – 8%	4% – 6%	-
12-13	-	8% - 10%	6% – 8%	4% – 6%	2%
13-14	-	8%	6% - 8%	6%	-

To investigate the main source of wave energy within the TFZ, the energy ratio (ER) between the swell height (H_{swell}) and the significant wave height (H_s) is used (eq. 2.4)

$$ER = \frac{H_{swell,M7}}{H_{s,M7}} \tag{2.4}$$

The ER at M7 was calculated for the period 1/9/05 – 30/8/06 and the mean value was 0.37 with a standard deviation of 0.16. The mean ER value of 0.37 indicates that 37% of the wave energy present in the TFZ is contained within the swell band of the wave spectrum. Swell waves propagating into the TFZ from the Southern Ocean cannot be generated within the model domain by any wind forcing. This result shows that the wave energy derived from wind forcing is slightly larger than the energy propagating into the region from the southern ocean.

2.6. Conclusions

The modelling of wave heights and directions in the TFZ is an important tool for predicting physical conditions prevalent in this area, and is crucial for a better understanding of the parameters driving sediment resuspension and ultimately water quality (see Chapter 4). The wave modelling can be summarised as follows:

- The two wave model grids used in this study have been validated against five datasets throughout the model domains. There is good agreement between field observations and modelled wave characteristics in the region of the TFZ.
- There are sheltered regions to the north and west of Louth Island and in the embayments of Boston Bay and Proper Bay. These areas are largely affected by locally generated wind waves, with an annual mean H_s of less than 0.3 m. The regions to the south of Point Bolingbroke and east of Cape Donnington are far more exposed, with an annual mean H_s of 0.4-0.8 m.
- Waves within the TFZ are a mixture of incident swell originating from the Southern Ocean and locally generated wind waves. The swell from the Southern Ocean is

refracted by the bottom topography into the region. The swell height in the TFZ varies between 3% and 10% of the oceanic swell height, with the highest values generated by swell entering the area from the south-south-west. The highest wind waves are generated by winds from the east through to the south due to the fetch associated with these directions. The swell propagating into the TFZ contributes ~37% of the energy found in the wind wave spectrum.

Acknowledgements
We wish to thank Sonja Venema, Kate Rodda and Brenton Ebert (SARDI Aquatic Sciences) for their help in deploying and retrieving instruments, the South Australian Partnership for Advanced Computing (SAPAC) for the use of their facilities to run the wave models. We also wish to thank Graham Warren, Aihong Zhong and Bruce Brooks from the Australian Bureau of Meteorology for supplying meteorological data.

2.7. References

Booij, N., Ris, R. C. and Holthuijsen, L. H. (1999). "A third-generation wave model for coastal regions - 1. Model description and validation." Journal of Geophysical Research-Oceans 104: 7649-7666.

Cheng, R. T., Ling, C. H., Gartner, J. W. and Wang, P. F. (1999). "Estimates of bottom roughness length and bottom shear stress in South San Francisco Bay, California." Journal of Geophysical Research-Oceans 104: 7715-7728.

Collins, J. I. (1972). "Prediction of shallow-water spectra." Journal of Geophysical Research 77: 2693-2707.

Fernandes, M., Cheshire, A. and Doonan, A. (2006). "Sediment geochemistry in lower Spencer Gulf, South Australia: implications for southern bluefin tuna farming." Australian Journal of Earth Sciences 53: 421-432.

Fuller, M. K., Bone, Y., Gostin, V. A. and Von Der Borch, C. C. (1994). "Holocene cool-water carbonate and terrigenous sediements from southern Spencer Gulf, South Australia." Australian Journal of Earth Sciences 41: 353-363.

Graber, H. C., Beardsley, R. C. and Grant, W. D. (1989). "Storm-Generated Surface-Waves And Sediment Resuspension In The East China And Yellow Seas." Journal of Physical Oceanography 19: 1039-1059.

Guillen, J., Jimenez, J. A., Palanques, A., Gracia, V., Puig, P. and Sanchez-Arcilla, A. (2002). "Sediment resuspension across a microtidal, low-energy inner shelf." Continental Shelf Research 22: 305-325.

Harris, P. T. (1994). "Comparison of tropical, carbonate and temperate, siliciclastic tidally dominated sedimentary deposits: Examples from the Australian continental shelf." Australian Journal of Earth Sciences 41: 241-254.

Hasselmann, K., T. P. Barnett, et al. (1973). "Measurements of wind-wave growth and swell decay during the Joint North Sea Wave Project (JONSWAP)." Ergnzungsheft zur Deutschen Hydrographischen Zeitschrift Reihe A(8)(12): 95.

Hemer, M. A. and Bye, J. A. T. (1999). "The swell climate of the South Australian Sea." Transactions of the Royal Society of South Australia 123: 107-113.

Hoitink, A. J. F., Peters, H. C. and Schroevers, M. (2007). "Field verification of ADCP surface gravity wave elevation spectra." Journal of Atmospheric tnd Oceanic Technology 24: 912-922.

Holthuijsen, L. H. (2007). Waves in Oceanic and Coastal Waters. New York, USA, Cambridge University Press.

Jansenn, P. A. E. M. (1991). "Quais-linear theory of wind-wave generation applied to wave forecasting." Journal of Physical Oceanography 21: 1631-1642.

Jing, L. and Ridd, P. V. (1996). "Wave-current bottom shear stresses and sediment resuspension in Cleveland Bay, Australia." Coastal Engineering 29: 169.

Komen, G. J., Hasselmann, S. and Hasselman, K. (1984). "On the existence of a fully developed wind-sea spectrum." Journal of Physical Oceanography 14: 1271-1285.

Lin, W. Q., Sanford, L. P. and Suttles, S. E. (2002). "Wave measurement and modeling in Chesapeake Bay." Continental Shelf Research 22: 2673-2686.

Madsen, O. S., Poon, Y. K. and Graber, H. C. (1988). Spectral wave attenuation by bottom friction: theory. 21st International Conference of Coastal Engineering, (Malaga), New York, ASCE.

Middleton, J. F. and Platov, G. (2003). "The mean summertime circulation along Australia's southern shelves: A numerical study." Journal of Physical Oceanography 33: 2270-2287.

Moghimi, S., Gayer, G., Gunther, H. and Shafieefar, M. (2005). "Application of third generation shallow water wave models in a tidal environment." Ocean Dynamics 55: 10-27.

Noye, J. (1984). "Physical processes and pollution in the waters of Spencer Gulf." Marine Geology 61: 197-220.

Nunes, R. A. and Lennon, G. W. (1986). "Physical property distributions and seasonal trends in Spencer Gulf, South Australia: an inverse estuary." Australian Journal of Marine and Freshwater Research 37: 39-53.

Paphitis, D. and Collins, M. B. (2005). "Sediment resuspension events within the (microtidal) coastal waters of Thermaikos Gulf, northern Greece." Continental Shelf Research 25: 2350-2365.

Pattiaratchi, C., Newgard, J. and Hollings, B. (2007). Physical oceanographic studies of Adelaide coastal waters using high-resolution modelling, in-situ observations and satellite techniques. ACWS Technical Report No. 20 prepared for the Adelaide Coastal Waters Study Steering Committee., School of Environmental Systems Engineering, The University of Western Australia.

Petrusevics, P. M. (1993). "SST Fronts in inverse estuaries, South Australia - Indicators of reduced gulf - shelf exchange." Australian Journal of Marine and Freshwater Research 44: 305-323.

Porter-Smith, R., Harris, P. T., Andersen, O. B., Coleman, R., Greenslade, D. and Jenkins, C. J. (2004). "Classification of the Australian continental shelf based on predicted sediment threshold exceedence from tidal currents and swell waves." Marine Geology 211: 1-20.

Ris, R. C., Holthuijsen, L. H. and Booij, N. (1999). "A third-generation wave model for coastal regions - 2. Verification." Journal of Geophysical Research-Oceans 104: 7667-7681.

van der Westhuysen, A. J., Zijlema, M. and Battjes, J. A. (2007). "Nonlinear saturation-based whitecapping dissipation in SWAN for deep and shallow water." Coastal Engineering 54: 151-170.

Yan, L. (1987). An improved wind input source term for third generation ocean wave modelling. Scientific Report WR-No 87-8, Royal Netherlands Meteorological Institute (KNMI).

2.8. Appendix

2.8.1 The wave spectrum

The instantaneous free-surface elevation η(t) can be approximated by the sum of a large number of harmonic waves at discrete frequencies (f_i), each with a constant amplitude (a) and phase(α) called the amplitude spectrum $E\{a_i\}$. Rather than use the amplitude spectrum $E\{a_i\}$, the variance spectrum $E\{(1/2)a^2_i\}$ is used so that all the statistical measures of the wave field can be expressed. To take into account all the frequencies present at sea, the variance spectrum at a particular frequency f_i, is distributed over the frequency interval Δf_i. This results in the discontinuous form of the variance density spectrum:

$$E_{dis}(f_i) = \frac{1}{\Delta f_i} E\left\{\frac{1}{2} a^2{}_i\right\} \tag{2.4}$$

By allowing the frequency interval to vary such that Δf_i approaches zero, the variance density spectrum becomes continuous and is now referred to as the energy density spectrum:

$$E(f) \equiv \lim_{\Delta f \to 0} \frac{1}{\Delta f} E\left\{\frac{1}{2} a^2\right\} \tag{2.5}$$

The energy density function *E(f)* is a key concept in the observation and modelling of oceanic waves. An extension of this concept is the introduction of the two-dimensional energy density function to not only include the frequency (*f*) but also the direction (θ).

$$E(f,\theta) \equiv \lim_{\Delta f \to 0} \lim_{\Delta\theta \to 0} \frac{1}{\Delta f \Delta\theta} E\left\{\frac{1}{2} a^2\right\} \tag{2.6}$$

The one-dimensional frequency spectrum *E(f)* can be obtained from Eqn. 2.6 by integrating over all directions for each frequency:

$$E(f) = \int_0^{2\pi} E(f,\theta) d\theta \tag{2.7}$$

Wave characteristics such as the significant wave height (H_s) and inverse mean frequency (T_{m01}), can be described by the "moments" of the wave spectra:

$$m_n = \int_0^{\infty} f^n E(f) df \tag{2.8}$$

The moment m_n is the defined as the *n*th moment of the energy density spectra *E(f)*. H_s can be calculated from the 0^{th}- order moment by the following equation

$$H_s = 4\sqrt{m_0} \tag{2.9}$$

The mean period can be found by:

$$T_{m01} = \frac{m_0}{m_1} \tag{2.10}$$

Chapter 3: The environmental implications of sediment type distribution and resuspension for the aquaculture industry in South-West Spencer Gulf

Emlyn Jones[1,2,3]*, Milena Fernandes[1,3], Jochen Kampf[2,3]

[1]SARDI Aquatic Sciences, PO Box 120, Henley Beach SA 5022
[2]Flinders University of South Australia, GPO Box 2100, Adelaide SA 5001
[3] Aquafin CRC

*corresponding author: School of Chemistry, Physics and Earth Sciences, Flinders University GPO Box 2100, Adelaide 5001 Australia.
Current address: CSIRO Marine Labs, Castray Esplanade, GPO Box 1538, Hobart TAS 7001
Phone: +61 (3) 6232 5483, E-mail: emlyn.jones@csiro.au

Abstract

In this study we present the results of a combination of field and modeling research, that aims to identify the major sediment types and wave regimes affecting the tuna farming zone (TFZ) in south-west Spencer Gulf. The sediments within the region fall within two major geochemical provinces. Sediments in the central TFZ contain significantly more nutrients (organic carbon, total nitrogen and porewater ammonium and phosphate) than those found elsewhere in the study region. The nutrient rich sediments also have a higher percentage of fine silts and a heavier isotopic signature for nitrogen, suggesting increased microbial activity in these locations. A wave model was used to classify the seafloor in this region into erosional and depositional zones. To this end, a large proportion of the current TFZ is located within a depositional area characterized by fine-grained sediments. Acoustic Doppler Current Profiler (ADCP) data suggests that these sediments may be resuspended if the wave induced bed shear stress exceeds 0.1 N m^{-2}. This agrees with the theoretical thresholds calculated using the Shields parameter. Based on modeling results, incoming swell from the Southern Ocean poses the greatest risk for sediment resuspension in the TFZ.

3.1. Introduction

The south-west corner of Spencer Gulf in South Australia supports a large aquaculture industry deriving most of its value from the farming of southern bluefin tuna. Approximately 5,000 tonnes of this species are fattened over autumn and winter in the 172 km^2 of the tuna farming zone (TFZ). The Gulf has the shape of an inverted 'V' with a length of ~ 300 km and a width of ~ 110 km at its southern end (Figure 3.1). It behaves as an inverse estuary (Nunes and Lennon, 1986), with flushing by shelf waters restricted to the austral winter, and a seasonal density front forming during summer, during which gulf-shelf exchange is limited (Petrusevics, 1993).

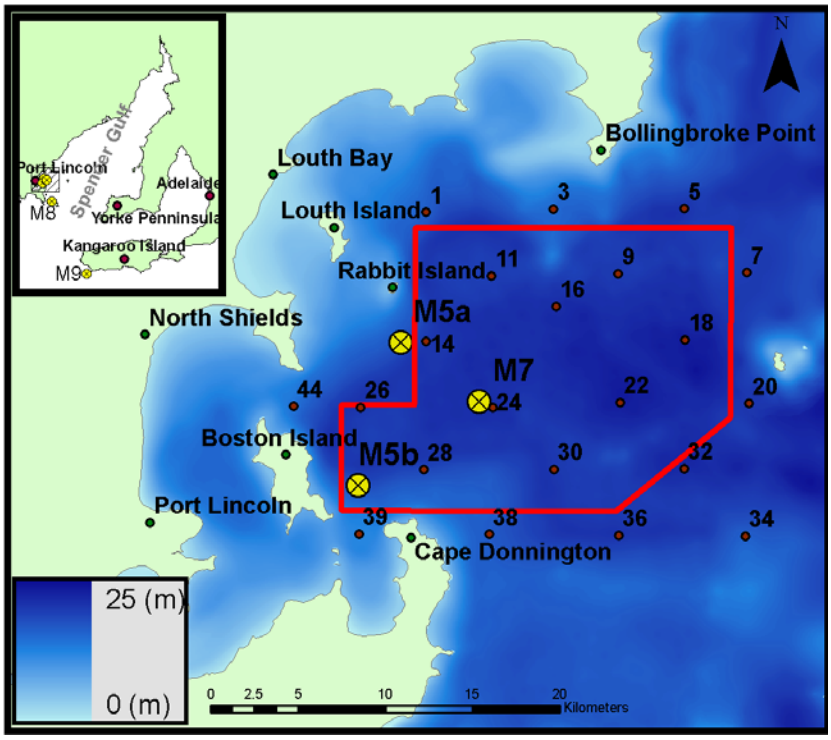

Figure 3.1. Map of study region showing sampling locations (red points) and mooring locations (yellow points), water depth (m) and the extent of the fine-scale model domain (main) and the coarse-resolution model domain (inset). The TFZ is indicated by the red boundary.

As southern Spencer Gulf is a micro-tidal system (< 2 m range) (Harris, 1994), near-bottom currents in the region of the TFZ rarely exceed 0.1 m s^{-1} (see Chapter 1). However, tidal currents across the mouth of the gulf are relatively strong, often reaching 0.5 m s^{-1}. Previous studies using tidal and wave models suggest that sand transport in Spencer Gulf is dominated by tidal currents rather than storm induced transport, which dominates the adjacent shelf region (Porter-Smith et al., 2004).

The sediments found in lower Spencer Gulf share properties of those found both in northern Spencer Gulf and the adjacent shelf (Fuller et al., 1994). The continental shelf in this region forms part of one of the largest cool-water carbonate facies in the world. The sediments and geochemistry of south-west Spencer Gulf are discussed in Fernandes et al. (2006). These findings compliment those of Porter-Smith et al., (2004) in that Fernandes et al. (2006) proposed that sediments within this region are mobilised by wind waves and swell as well as

tidal currents. Evidence suggests that waves in the region of the TFZ interact with the bottom, winnowing out the fine-grained sediments in the more exposed locations.

Before the TFZ was relocated to its current position, a resuspension event in 1996 severely impacted upon the regional aquaculture industry by causing up to 75% mortality in some tuna pens. Resuspension events have also been shown to increase the concentration of nutrients in the water column (Lawrence et al., 2004). Under commercial tuna pens, the concentrations of ammonium and phosphate in sediment porewaters are significantly higher than values at control sites located at least 1 km from any tuna lease (Lauer, 2005). When resuspended, these sediments are likely to increase nutrient inputs to the water column, potentially fuelling phytoplankton blooms, and/or toxic responses in the fish.

The physical mechanisms behind wave and current induced sediment resuspension and transport are associated with an increase in the bed-shear stress in the bottom boundary layer (Guillen et al., 2002). Previous studies into the swell and wave characteristics of Spencer Gulf have found that little or no swell is present in the upper (wave heights typically < 5 cm) and central regions of the gulf (wave periods typically < 6.5 s) (Noye, 1984). In the southern section of Spencer Gulf, the wave field is a combination of locally generated wind waves and incoming swell from the Southern Ocean. However, in a previous wave modeling study of this area, the only parameter used was incident swell (Hemer and Bye, 1999). Another wave model applied to Gulf St Vincent, to the east of our study area, indicated that fine and medium-grained sands in the near-shore region are mobilised by wave-induced currents for between 50% and 90% of the time (Pattiaratchi et al., 2007). When tidal currents were included, this increased to 70-90% of the time.

The most common parameter used to assess sediment resuspension in the field is Suspended Particulate Matter (SPM) concentration. SPM can be measured either directly or indirectly. Direct methods involve the collection of water samples whereby SPM is measured gravimetrically after filtration. Indirect methods use a turbidity sensor calibrated against direct SPM measurements. Although the indirect method has the advantage of producing a continuous datastream, it requires validation from field measurements. Indirect measurements of SPM usually rely on Optical Backscatter Sensors (OBS), light transmissometers or Echo Intensity (EI) acoustic measurements.

OBS measure the intensity of the reflected light, which is then converted into a turbidity measurement (Hamblin et al., 2000). During long deployments in the photic zone, OBS measurements are highly susceptible to marine fouling unless a cleaning mechanism is installed on the sensor (You, 2005). Many studies have used OBS measurements to investigate the link between tidal currents, wave action, or a combination of both, to the SPM concentration in the water column (Paphitis and Collins, 2005; Tragou et al., 2005).

The use of acoustic devices such as Acoustic Doppler Current Profilers (ADCPs) provides information on EI throughout the entire profile of the water column. As the concentration of particles in the water column increases so too does the EI. To quantitatively measure SPM using EI, a calibration dataset of direct measurements must be taken. If direct measurements of SPM are not available to calibrate the EI, the technique can still be used to qualitatively identify periods of elevated SPM (Klein, 2003). Acoustic measurements assume that particles in the water column are moving at the same rate as the ambient current, however if there are small particles in the water column that move independently of the ambient current, e.g.

zooplankton, then the velocity measurements can be biased (Smyth et al., 2006). Not only can the velocity measurements be biased by such a phenomena, but also the measurements of the SPM.

In this study, we investigated the geochemical characteristics of sediments, and the wave regime leading to resuspension episodes, in the region to the east of Boston Island, encompassing the TFZ, in lower south-west Spencer Gulf. Our primary objectives were to determine:

- the spatial distribution of sediment types, expanding on the previous work of Fernandes et al. (2006), to include a much larger area with a higher density of sampling sites,
- the relationship between the modeled wave regime and the observed distribution of sediment characteristics,
- the mechanism and critical shear stress produced by waves affecting the area, and the thresholds necessary for sediment resuspension.

3.2. Methods

3.2.1. Mooring data

Three moorings were deployed in four locations in south-west Spencer Gulf and on the adjacent shelf (Figure 3.1; Table 3.1). The moorings were equipped with an ADCP capable of measuring currents and waves (Figures 3.2 and 3.3). Moorings M5 and M7 also collected salinity and turbidity data.

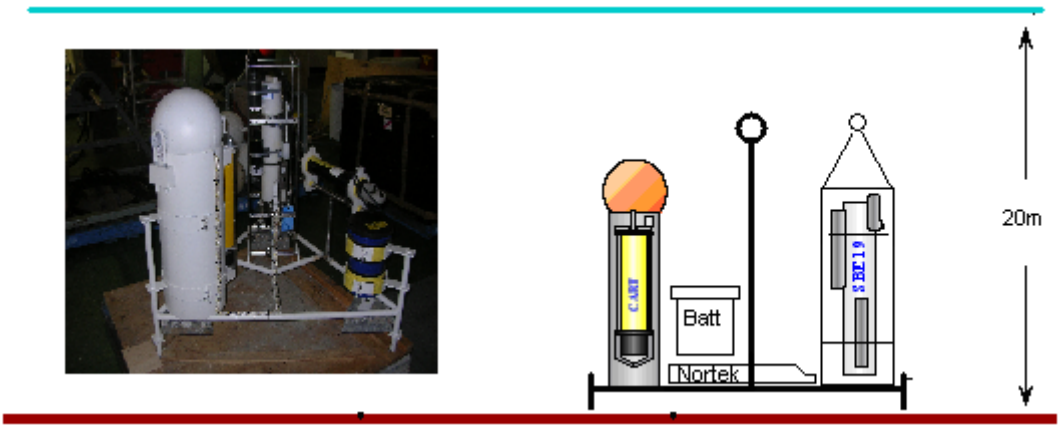

Figure 3.2. Moorings used for the collection of temperature, salinity, pressure, turbidity and currents at locations M5a and M5b (Source: CSIRO).

Figure 3.3. The mooring frame used to mount the RDI Workhorse (300 kHz) ADCP in deployments M7 and M8.

Table 3.1. The location (WGS 84) and description of the instrumentation in each of the moorings used in the study.

	M5a	M5b	M7	M8
Latitude (S)	34.635	34.708	34.666	34.992
Longitude (E)	135.988	135.967	136.033	136.099
Depth (m)	21	19	22	44
Location Description	South of Rabbit Island	East of Boston Island	Central Tuna Farming Zone	Southern Thorny Passage near Thistle Island
Variables measured	Temperature, Conductivity, Pressure, Turbidity, Fluorescence, Oxygen	Temperature, Conductivity, Pressure, Turbidity, Fluorescence, Oxygen	Temperature, Conductivity, Pressure, Turbidity,	Temperature, Pressure
Instrumentation	Seabird SBE 19 Nortek 600 kHz ADCP	Same as M5a	Aanderraa RCM-9 RDI 300kHz ADCP	RDI 300kHz ADCP

3.2.2. Wave Model Description

The temporal and spatial dynamics of the wave field were investigated using the freely available SWAN model. SWAN is a third generation spectral wave model that characterises wave spectra by a number of discreet frequencies and directions (Booij et al., 1999; Ris et al., 1999). Two grids were used in this study. A fine grid (TunaWM) with a resolution of 0.4 km

covering the TFZ was nested within a coarser grid (SARWM) with a resolution of 2 km covering the gulfs of South Australia (Figure 3.1). The open-sea boundary of SARWM was forced with the output from the regional Meso-WAM wave model obtained from the Bureau of Meteorology (BOM). The surface wind fields were forced with BOM MesoLAPS wind fields. The open boundary of the fine-scale model was forced with data obtained from the coarse-scale model. The comparison of modeled significant wave height and observed significant wave height at five locations showed good agreement. A detailed discussion of the wave model is presented in Chapter 2 of this report.

3.2.3. Wave analysis

Wave-induced orbital velocities generate a shear force that the sediments experience. The combined presence of ambient currents and wave-induced orbital velocities lead to a non-linear interaction between the two processes in the bottom boundary layer (Grant and Madsen, 1979). This study exclusively focused on the wave-induced bed-shear stress, τ_w, which is related to the maximum orbital velocity, U_b, according to:

$$\tau_w = 0.5\rho f_w U_b^{\,2} \tag{3.1}$$

where ρ is the density and f_w is the wave friction factor (Fredsoe and Deigaard, 1992; Nielsen, 1992). Linear wave theory relates significant wave height (H_s) and average wave period (T_m) to U_b according to:

$$U_b = \frac{\pi H_s}{T_m \sinh(kh)} \tag{3.2}$$

where h is the water depth and k is the wave number. k is approximated using the method of Fentona and McKee (1990):

$$k \approx \frac{4\pi^2}{gT_m^{\,2}}\left(\coth\left(\frac{2\pi}{T_m}\sqrt{\frac{h}{g}}\right)^{\frac{3}{2}}\right)^{\frac{2}{3}} \tag{3.3}$$

where g is the acceleration due to gravity.

The values of U_b were obtained from the output of SWAN in 1 h intervals for the Austral winter (June – August 2006) at each of the sites used in the sediment survey (see next section). Winter was chosen for the simulation period as this is the time of year when strong south-west swells are generated (see Chapter 2). The mean of the highest third of U_b at each site was used to calculate a parameter called the "significant orbital speed", which is analogous to the concept of significant wave height (Holthuijsen, 2007):

$$U_{sig} = \frac{1}{N/3}\sum_{j=1}^{N/3} U_b \tag{3.4}$$

In a record of bottom orbital speeds, U_b, with N records, U_{sig} is defined as the significant orbital speed, j is not the sequence number (i.e. sequence in time) but rather the rank number

based on orbital speeds where j=1 is the highest orbital speed, j=2 is the second highest orbital speed etc.

A hierarchical-cluster analysis using the complete Euclidean distance between points was used to identify areas with significantly different wave characteristics. The parameter U_{sig}^2 was used in the cluster analysis, as τ_w is proportional to U_b^2. We did not calculate the actual value of τ_w as there were insufficient data on sediment grain-size characteristics to calculate f_w. A Kruskal-Wallace non-parametric one-way ANOVA (Hollander, 1973) was performed to test whether there was a statistically significant difference between the sediment characteristics found in the wave groups identified in the cluster analysis.

3.2.4. Sediments

Sediment cores were collected at each of 21 sites (Figure 3.1) for mineral grain size analysis, the determination of porewater ammonium ($NH_4^+ + NH_3$) and phosphate, and sediment carbonate, organic carbon, total nitrogen, and total phosphorus contents, and the isotopic composition of organic carbon and total nitrogen. The cores were collected using a ship-deployed HAPS Corer (KC Denmark). Cores were 6.7 cm in diameter and 10-15 cm in length. Upon retrieval, the overlying water in the tube was carefully discarded to minimise surface disturbance and the sediment extruded onto a clean stainless steel table.

Grain size

Two replicate cores were collected, the top 1 cm transferred into pre-combusted alfoil trays, and stored on ice before transfer to the laboratory and long-term storage at -20ºC. The analysis method is detailed in Fernandes et al. (2006), whereby clay was analysed with a hydrometer and larger grain sizes were separated using a series of stacked sieves of 2000, 1000, 500, 250, 125 and 63 μm mesh sizes. Silt was calculated as the difference between the total weight of sediment, and the sum of the clay and sand fractions. Each grain size was then presented as a percentage of the total weight. The statistics of particle size distributions (mean grain size, sorting, skewness and kurtosis) were calculated using the GRADISTAT software developed by Blott and Pye (2001). The Folk and Ward method was used to analyse the data due to it being relatively insensitive to large variations in the tails of the sediment distribution.

Porewaters

Two replicate cores were collected, the top 2 cm transferred into 50 mL centrifuge tubes, and stored on ice before transfer to the laboratory. The tubes were then centrifuged at 1400 g for 10 min. The overlying water was filtered through a 0.45 μm filter and stored at -20ºC. Ammonium ($NH_4^+ + NH_3$) and phosphate were determined by the Water Studies Centre (Monash University, Melbourne, VIC) using a QuickChem 8000 Automated Ion Analyser (APHA-AWWA-WPCF, 1998a; APHA-AWWA-WPCF, 1998b).

Other geochemical variables

Two replicate cores were collected, the top 1 cm transferred into pre-combusted glass jars, and stored on ice before transfer to the laboratory and long-term storage at -20˚C. Samples were freeze-dried and sieved through a 500 μm sieve to remove large shell fragments and homogenized with a mortar and pestle.

Carbonate content was determined by CSBP (Perth, WA) with a pressure transducer (RS Components, part 348-8065, Iso-Tech voltameter IDM 91) by measuring the increase in pressure generated by the CO_2 released after acidification of aliquots with 5.5 N HCl at room temperature.

Organic carbon and total nitrogen contents, and their isotopic signatures, were analysed by the Isotope Analysis Service at CSIRO Land and Water (Adelaide, SA) using a Europa Scientific ANCA-SL elemental analyser coupled to a Geo 20-20 Mass Spectrometer. Aliquots for organic carbon analysis were pre-treated with 1 N hydrochloric acid to remove carbonates, rinsed with MilliQ water to remove hygroscopic salts and oven-dried at 40^{o}C using a method modified from Hedges and Stern (1984). Organic carbon concentrations were corrected for the loss of carbonate during pre-treatment. Natural isotopic abundances for organic carbon and nitrogen are reported as $\delta^{13}C$ and $\delta^{15}N$, which correspond to the deviation (in ‰) of the isotopic composition of a sample from an internationally accepted standard (std) (Pee Dee Belemnite limestone for $\delta^{13}C$ and nitrogen in air for $\delta^{15}N$):

$$\delta^{13}C \text{ or } \delta^{15}N = \left(\frac{R_{sample}}{R_{std}} - 1 \right) x\, 10^{3} \tag{3.5}$$

where

$$R = \frac{^{13}C}{^{12}C} \quad or \quad \frac{^{15}N}{^{14}N} \tag{3.6}$$

Total phosphorus content was determined by the Marine and Freshwater Research Laboratory (Murdoch University, Perth, WA) using a Varian Vista Axial Inductively Coupled Plasma-Atomic Emission Spectrometer (ICP-AES) after digestion with nitric acid, hydrogen peroxide, and hydrochloric acid (US Environmental Protection Agency, 1991).

The statistical analysis of the geochemical data set was carried out using Matlab 6.0. A hierarchical-cluster analysis using the complete Euclidean distance between the sediment nutrient contents of organic carbon, total phosphorus, total nitrogen, and porewater nutrient concentrations (ammonium and phosphate) was used to identify the major geochemical groupings within the study region. Principal component analysis (PCA) using the variables in the cluster analysis was also performed to validate the groupings identified in the cluster analysis. A multi-variate analysis of variance (MANOVA) using the variables previously mentioned was used to test whether there was a significant difference in the means between the two groups identified in the cluster analysis. Univariate tests using a Kruskal-Wallis non-parametric one-way ANOVA, were then conducted to investigate the differences in individual variables between the two geochemical groups

To investigate the spatial distributions of various sediment characteristics, ArcMAP GIS 9.2 software was used. Two interpolation schemes were used. For all geochemical variables other than mean grain size and porewaters, we used Krigging. For mean grain size and porewater distributions, we used Radial Basis Functions (RBF's), which are exact, deterministic, interpolators. RBF's were used instead of Krigging for these variables as Krigging produced a surface that contained an unacceptable amount of error. RBFs make no assumption about the data and provide prediction surfaces that are comparable to exact forms of Krigging.

3.2.6. Theoretical approach to calculating the initiation of sediment movement.

Sediment mobility under the combined effects of waves and currents has long been of interest in engineering problems. Many theories have developed dimensionless measures to identify when the initiation of sediment motion takes place. One of the most commonly used parameters is the Shields parameter, in which the balance between disturbing and stabilising forces is taken into account (Nielsen, 1992). The critical Shields parameter (ψ_c) used in this study was estimated from empirical data, using the sediment-fluid parameter S^* (Madsen and Grant, 1979):

$$S^* = \frac{d}{4\nu}\sqrt{(s-1)gd} \tag{3.7}$$

where s = 2.65 for sand, g is the acceleration due to gravity, d is particle diameter, and ν is the kinematic viscosity (1.6 x 10^{-6} m^2 s^{-1}). ψ_c is then related to S^* using the following relationship:

$$\psi_c = \begin{cases} 0.1S^{*\frac{2}{7}} \rightarrow S < 0.8 \\ 0.06 \rightarrow S > 300 \end{cases} \tag{3.8}$$

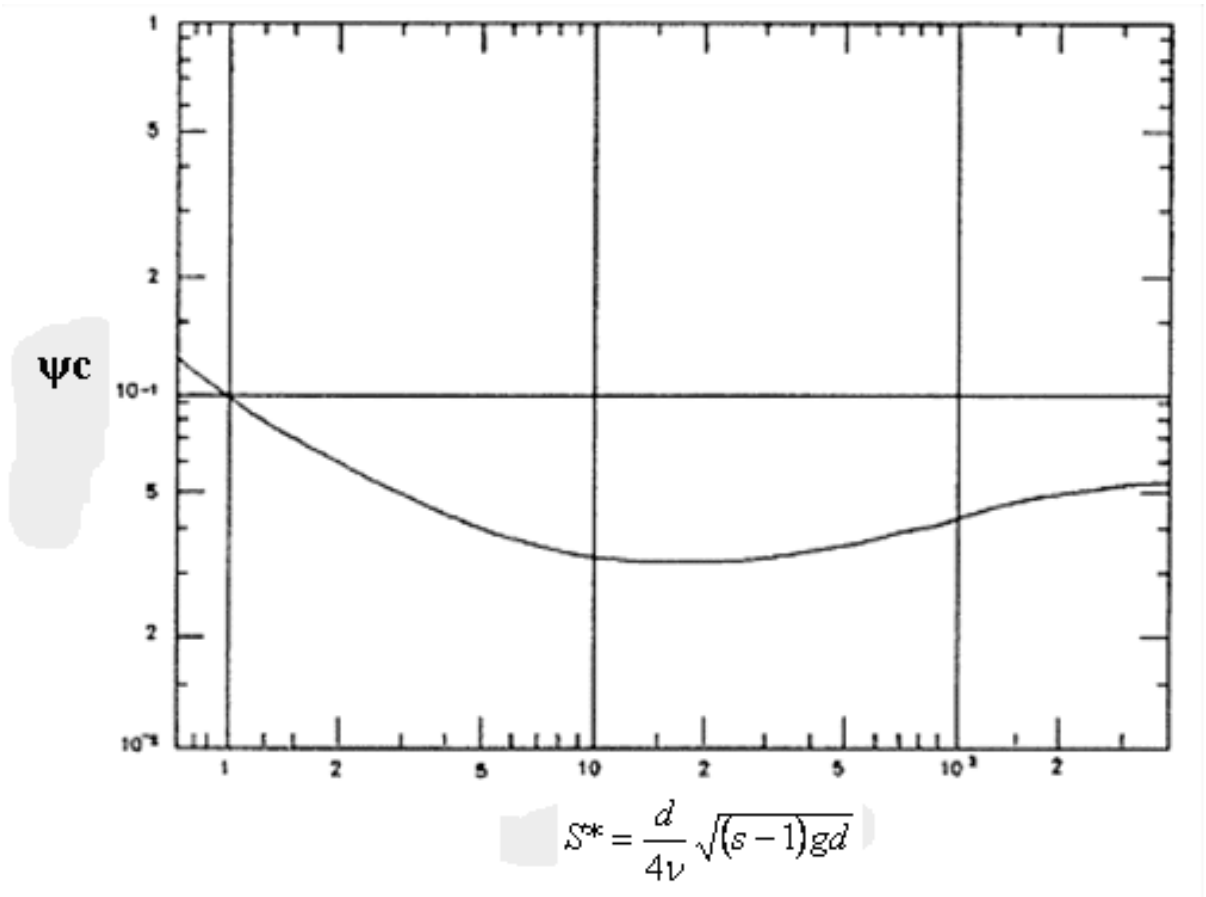

Figure 3.4. Modified Shields Diagram (adapted from Nielsen (1992))

For $0.8 > S > 300$, ψ_c can be found using the modified Shields diagram of Madsen and Grant (1976) (Figure 3.4). In this work, typical values for ψ_c ranged between 0.050 and 0.055. The critical Shields parameter is related to the critical shear stress (τ_c) by the following equation:

$$\tau_c = \rho(s-1)gd\psi_c \qquad (3.9)$$

where ρ is the density of the fluid, $s = 2.65$ for sand, g is the acceleration due to gravity, and d is particle diameter. In this study, we only consider the shear stress due to waves in the bottom boundary layer and make no attempt to include the effect of ambient currents.

3.3. Results

3.3.1. Spatial variation in observed sediment characteristics

The sediments within south-west Spencer Gulf can be classified as a mixture of very fine to fine sands (mean diameter 50-130 μm). The silt:clay ratio is approximately 2 or greater for the majority of the region. Regions of fine sediments are located to the north of Cape Donnington and east of Boston Island, which join a band of fine sediments from east of Louth Island extending in a south-easterly direction for ~35 km (Figure 3.5). There are regions of coarse-grained sediments south of Louth Island and to the south-west of Rabbit Island, to the east of Cape Donnington and also south of Point Bolingbroke.

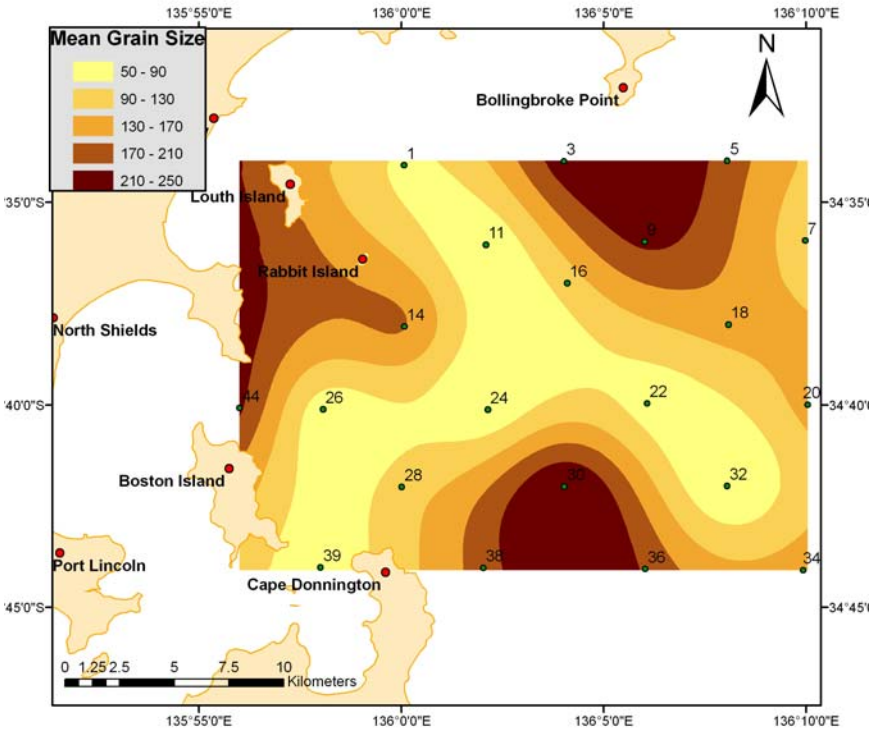

Figure 3.5. Spatial distribution of sediment mean grain size (in μm).

The geochemical composition of the sediments followed a complex spatial distribution; maps of individual variables can be found in the Appendix (Section 3.7) Cluster analysis using sediment nutrient contents (organic carbon, total nitrogen, and total phosphorus), as well as the porewater nutrient concentrations (ammonium and phosphate), was used to identify the

major geochemical provinces in the study area (Figure 3.6). The results of PCA confirm the groupings identified in the cluster analysis (Figure 3.7). The first principal component clearly shows a difference between type 1 and type 2 sediments. A map detailing the geographical locations of these sediment types was constructed to help visualize their spatial distribution (Figure 3.8).

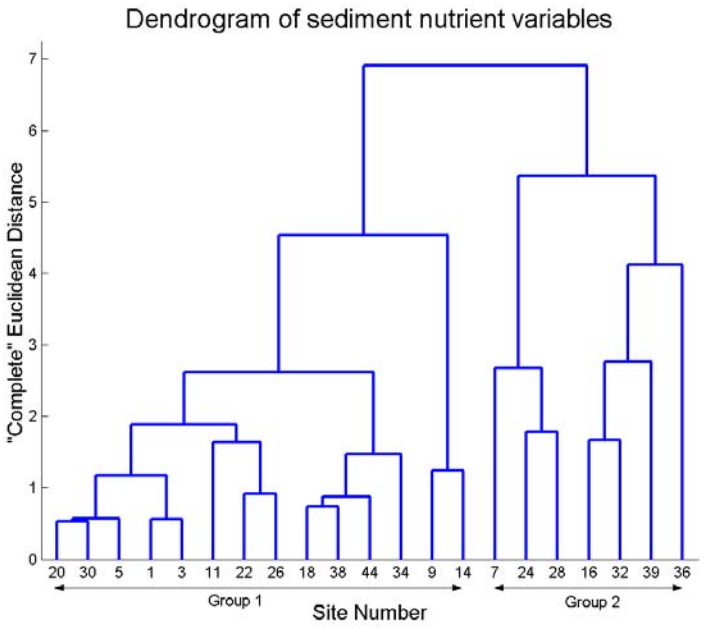

Figure 3.6. Results of a cluster analysis displaying the locations which have similar geochemical properties.

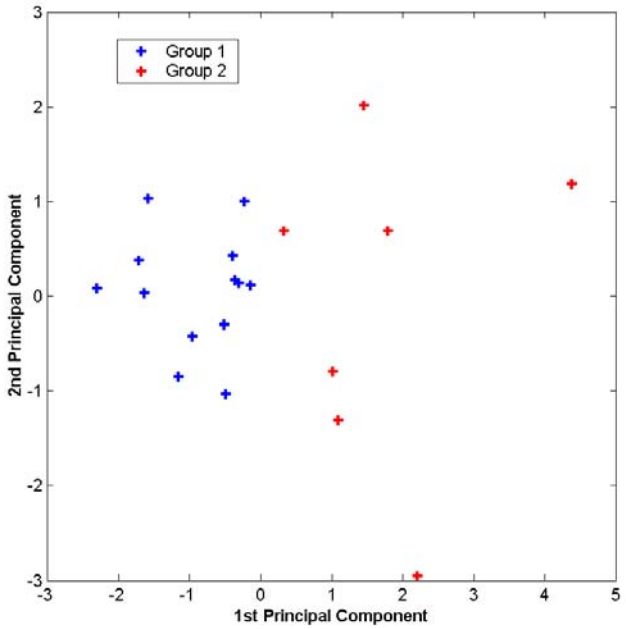

Figure 3.7. Results of PCA plotting the 1st and 2nd PC's. The data points are colour-coded with respect to the group determined by the cluster analysis. The 1st principal component accounts for 48.5% of the variability within the data set and second PC accounts for 22% of the variability.

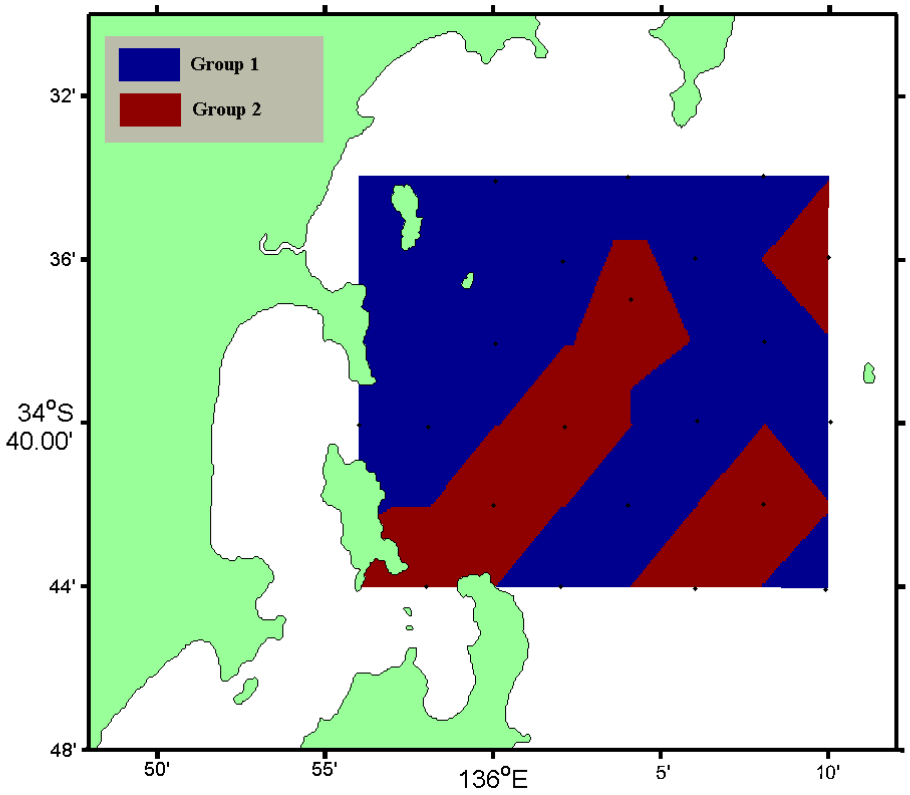

Figure 3.8. Spatial distribution of sediment types identified through cluster analysis of geochemical variables.

Two broad groupings are identified in the cluster analysis. Group 1 sediments form the largest group and cover much of the study region. The sediments forming Group 2 fall on an axis oriented in the south-west to north-east direction running through the central TFZ. There are two other separate locations classed as Group 2, they are located in the far north-east corner of the study region and also in the south-east of the study region.

The results of MANOVA confirm sediments from the two groups are significantly different ($p = 0.0021$), analysis of the univariate statistics highlighted the major differences between the two groups. The results of the Kruskal-Wallis test showed Group 2 sediments are significantly more nutrient rich in all variables except total phosphorus (Table 3.2). Nutrient concentrations for Group 2 sediments are typically 2-3 times those from Group 1.

Table 3.2. The results of a Kruskal-Wallis non-parametric analysis of the main groups identified by the cluster analysis. Variables with a statistically significant difference between the groups are highlighted in light-red.

Geochemical Variable	Sediment type 1 (n=14)	Sediment type 2 (n=7)	p-value
Organic Carbon (%)	0.48	1.38	0.0138
Total Phosphorus (%)	0.05	0.04	0.6813
Total Nitrogen (%)	0.08	0.12	0.0128
Porewater: NH4 (μmol/L)	0.026	0.055	0.0112
Porewater: PO4 (μmol/L)	0.004	0.011	<0.001

To investigate the difference between the two sediment groups in more detail, a second statistical analysis using variables not included in the cluster analysis was also performed

(Table 3.3). Group 2 sediments have a heavier $\delta^{15}N$ signature, a higher percentage of silts (4-63 μm), and a lower percentage of fine sands (125-250 μm), than the sediments in Group 1.

Table 3.3. The results of a Kruskal-Wallis non-parametric analysis of the main groups identified by the cluster analysis. The variables presented in this table were not included in the cluster analysis. Variables with a statistically significant difference between the groups are highlighted in light-red.

Geochemical/Grain size Variable	Sediment type 1 (n=14)	Sediment type 2 (n=7)	p-value
$\delta^{15}N$	2.46	3.27	0.0072
$\delta^{13}C$	-19.35	-19.60	0.5506
Carbonate (%)	72.87	77.79	0.4118
Clay (%)	5.3	6.2	0.2963
Silt (%)	12.3	20.3	0.0300
Very Fine Sand (%)	15.26	20.19	0.1172
Fine Sand (%)	28.4	21.2	0.0170
Medium Sand (%)	21.8	14.6	0.0524
Coarse Sand (%)	9.7	7.1	0.1007
Very Coarse Sand (%)	4.4	3.1	0.2631
Granule (%)	3.0	7.2	0.2631
Mean Grain Size (μm)	192.9	150.9	0.1793
U_{sig} (m s^{-1})	0.07	0.05	0.3321

3.6.2. Wave - sediment grain size interactions:

The modeled values of U_{sig} range from 0.01 m s^{-1} at the sheltered site 39 to 0.11 m s^{-1} at the far more exposed site 36. During storm events U_b can reach up to twice U_{sig}, peaking between 0.20 m s^{-1} and 0.22 m s^{-1} at exposed locations. A comparison between the modeled U_{sig} and the bathymetry shows a vague relationship between depth and U_{sig}, with areas of shallow water depth experiencing high values of U_{sig}. Besides depth, other parameters such as exposure to fetch, shoaling, and wave refraction will combine to create a complex set of non-linear interactions responsible for the spatial distribution of the U_{sig} observed.

The results of a separate cluster analysis based only on U_{sig} identified two major groupings (Figure 3.9 and 3.10). Sites forming Wave Group 1 were less energetic with $U_{sig} < 0.070$ m s^{-1}, whereas those from Wave Group 2 had $U_{sig} > 0.074$ m s^{-1}. To test the relationship between U_{sig} and the observed sediment characteristics, a Kruskal-Wallis test was performed to identify any significant differences between the 2 wave groups (Table 3.4). The test was performed using the values at the actual sites not from the interpolated data. The only sediment variable that had a statistically significant difference between the two groups was the mean grain size. Statistically, there was no significant difference between the two groups for the other geochemical characteristics.

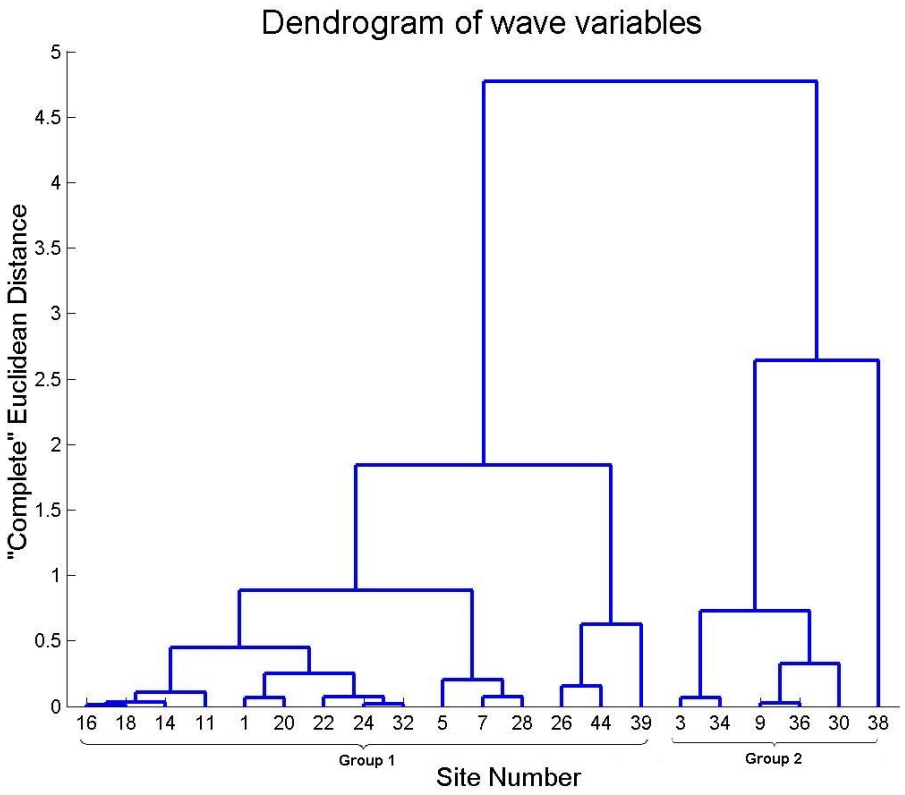

Figure 3.9. Results of cluster analysis displaying the locations which have similar U_{sig} properties.

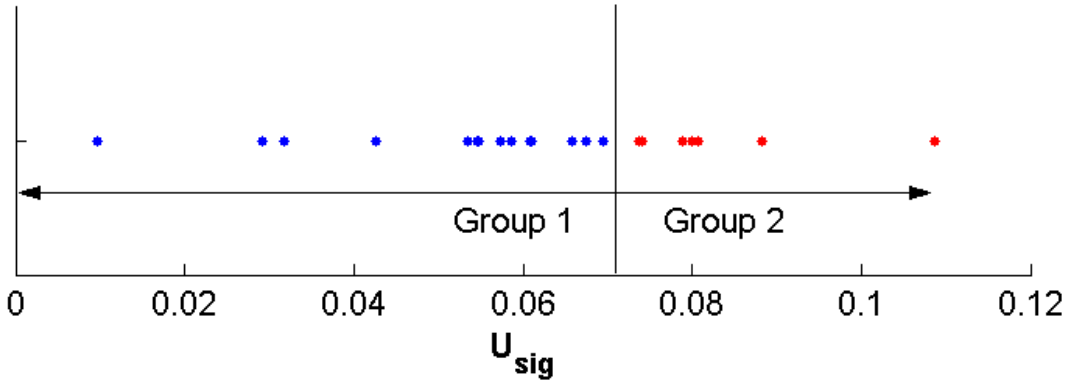

Figure 3.10. A one dimension plot of U_{sig} highlighting the delineation between wave group 1 (blue) and wave group 2 (red).

With the exception of site 44, the mean grain size in Wave Group 1 was less than 200 μm. Site 44 lies within the channel at the northern entrance of Boston Bay, which is subject to significant tidal flows (Grzechnik, 2000), therefore fine sediments may be eroded due to high current speeds as opposed to wave action. In Wave Group 1 areas, sediments consisted of ~45% fine material (63 – 125 μm), in contrast to Wave Group 2 areas, which contained < 18% of this size fraction. This suggests that the finer-grained sediments are winnowed-out where U_{sig} exceeds 0.074 m s^{-1}. With the exception of site 36, the mean grain size in Wave Group 2 sites was greater than 240 μm.

Table 3.4. The results of a Kruskal-Wallis non-parametric analysis of the main groups identified by the cluster analysis of U_{sig}. Variables with a statistically significant difference between the groups are highlighted in light-red.

	Wave type 1 (n=14)	Wave type 2 (n=7)	p-value
Wave Parameters			
U_{sig} (m s^{-1})	0.054	0.084	0.0005
Grain Size Variables			
Mean Grain Size (μm)	138.6	259.4	0.0112
Clay (%)	5.5	5.7	0.4118
Silt (%)	17.6	9.7	0.0734
Very Fine Sand (%)	19.7	11.2	0.0013
Fine Sand (%)	25.8	26.6	0.2963
Medium Sand (%)	18.4	21.0	0.6015
Coarse Sand (%)	8.1	10.3	0.2326
Very Coarse Sand (%)	2.8	6.0	0.0036
Granule (%)	1.9	9.3	0.0090
Geochemical Variables			
Carbonate (%)	72.5	78.5	0.1357
Organic Carbon (%)	0.72	0.90	1.0000
Total Phosphorous (%)	0.045	0.051	0.6274
Total Nitrogen (%)	0.096	0.086	0.1516
Pore-water: NH4 (μmol/L)	0.037	0.034	0.7370
Pore-water: PO4 (μmol/L)	0.0071	0.0050	0.1355
$\delta^{15}N$	2.74	2.72	0.9702
$\delta^{13}C$	-19.5	-19.3	0.9405

3.3.3. Observed sediment resuspension

Sediment resuspension in coastal waters can be difficult to measure. Traditional optical sensors are highly susceptible to marine fouling. In this study a number of these sensors were mounted on various moorings (M5, M7), but the signal recorded showed significant amounts of contamination due to bio-fouling. An alternative to optical sensors is the use of echo intensity (EI) obtained from acoustic instruments. EI was measured at moorings M5, M7 and M9 with an ADCP. EI was used as a qualitative tool for signaling an increase of SPM concentrations in the water column, bearing in mind that the signal can be biased by particles other than suspended sediments, such as living organisms capable of reflecting sound waves.

The mooring M5a was located in a relatively sheltered environment to the south of Rabbit Island where $U_{sig} < 0.070$ m s^{-1}. The EI time series extracted from M5a describes a complex signal (Figure 3.11a). Periods when high EI extends throughout the water column coincide with the hours of darkness and are likely to be migrating zooplankton that feed at night. This signal is especially evident between the 1/9/05 and the 10/9/05. However, wave events occurring on the 2/9/05, 11/9/05 and the 8/10/05 led to the wave-induced shear stress (τ_w) peaking at over 0.1 N m^{-2}, and were also accompanied by an increase in the EI throughout the water column (Figure 3.11a).

To investigate the signal close to the seafloor at 18.5 m, we removed the effects of the diel vertical migrators by calculating the 24 h moving average (Figure 3.11b). This approach

removed the signal associated with the zooplankton, so that any increase in signal intensity was not likely to be biological in nature. Figure 3.11b clearly indicates that wave events generating a $\tau_w > 0.1$ N m^{-2} always led to sediment resuspension in the region of M5a. The resuspension appears to be largely confined to the bottom 10 m of the water column (Figure 3.11a). However, Figure 3.11b also suggests that the EI signal is not always explained by τ_w alone. Tidal currents, which are not considered here, may also enhance the bed-shear on occasion. Mooring M5 sampled for waves every 8 h. This resolution is too coarse for a detailed insight into the physical conditions that may generate a resuspension event.

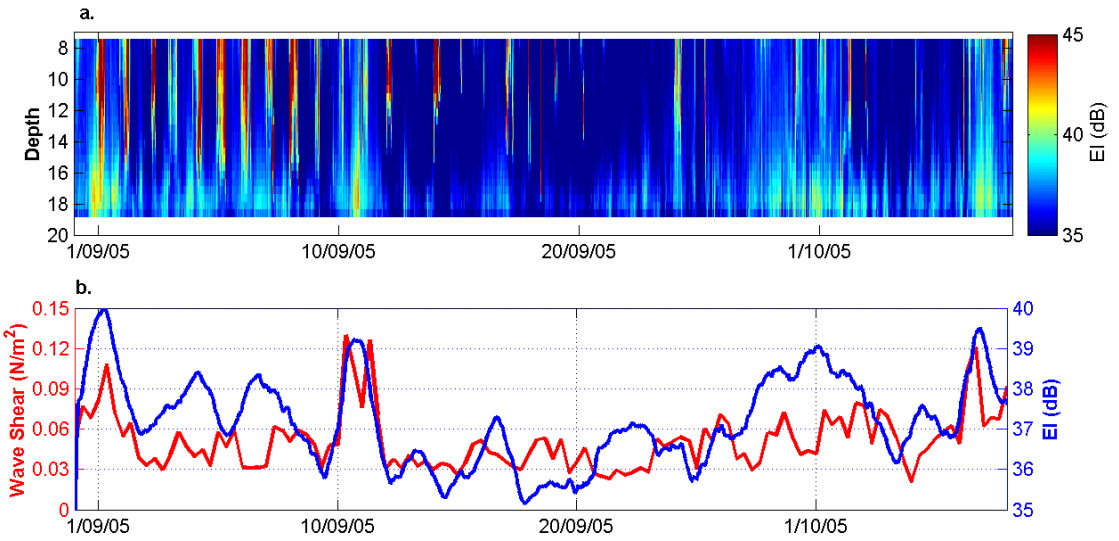

Figure 3.11. Data from mooring M5a displaying (a) the distribution of EI throughout the water column and (b) the τ_w (red) and the filtered EI (blue) at 18.5 m.

Mooring M7 was set to continuously sample at 2 Hz for almost a week, resulting in a more detailed picture of a resuspension event than mooring M5. Data obtained from mooring M7 again showed the diel vertical migration of zooplankton, with a strong signal at night (Figure 3.12a). To filter this biological signal, a 24 h moving average was applied to the EI signal close to the seafloor at 17 m (Figure 3.12b). With the onset of a wave event generating a $\tau_w > 0.1$ N m^{-2}, the EI close to the seafloor increased by 3.5 db, reaching a maximum value of 66.5 dB. This time series is depicted in Figure 3.13, with the EI abruptly increasing over a period of 8 h, and remaining high for up to two days even though the τ_w began to decrease. Sediments at M7 are fine-grained, with a mean diameter of ~70 µm, and will remain in suspension as τ_w decreases due to their low settling velocities and residual turbulence. The increase in EI as τ_w exceeded 0.1 N m^{-2} suggests that this is the critical shear (τ_c) required for the initiation of sediment resuspension in this area.

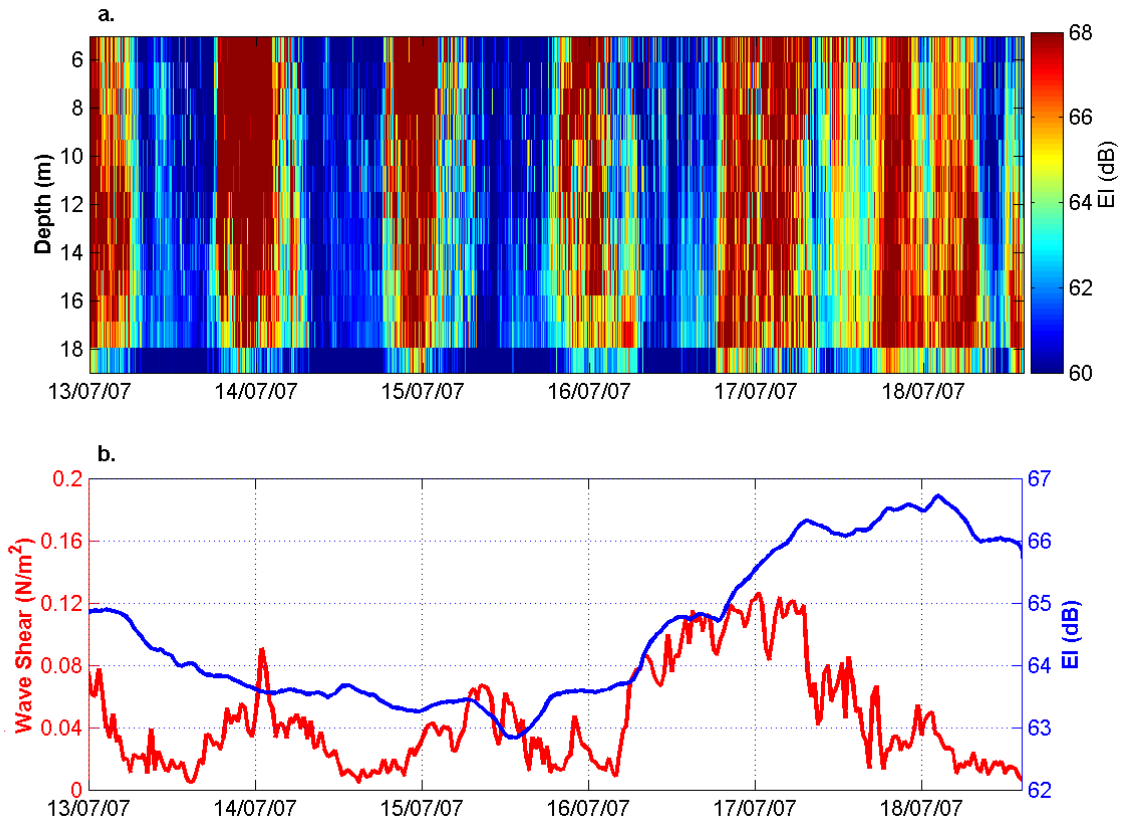

Figure 3.12. Data from Mooring M7 showing (a) the distribution of EI throughout the water column and (b) the τ_w (red) and the filtered EI (blue) at 17 m.

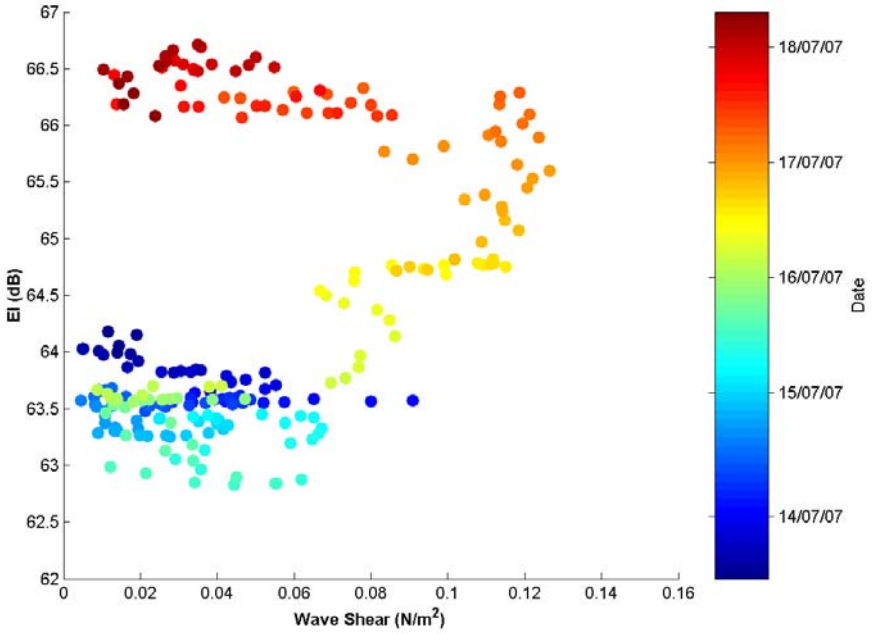

Figure 3.13. A colour-coded time series plot of wave-induced shear vs EI at M7.

Mooring M8 used the same instrument as mooring M7, configured to burst sample at 2 Hz for 15 min every 2 h. M8 was moored outside the TFZ near the southern entrance to Thorny Passage, in the vicinity of Thistle Island. At this site, there was only a weak signal from vertical diel migrators (Figure 3.14a), perhaps a consequence of the energetic nature of the area, characterized by strong tidal flows (>0.5 m s^{-1}) and a τ_w rarely below 0.15 N m^{-2}. EI and τ_w were highly correlated at this location, with EI increasing throughout the water column in response to increased τ_w (Figure 3.14b). There was no clear threshold values for τ_c to initiate resuspension, and no delay between the decrease in τ_w and decrease in EI, resulting in a near linear relationship between EI and τ_w (Figure 3.15).

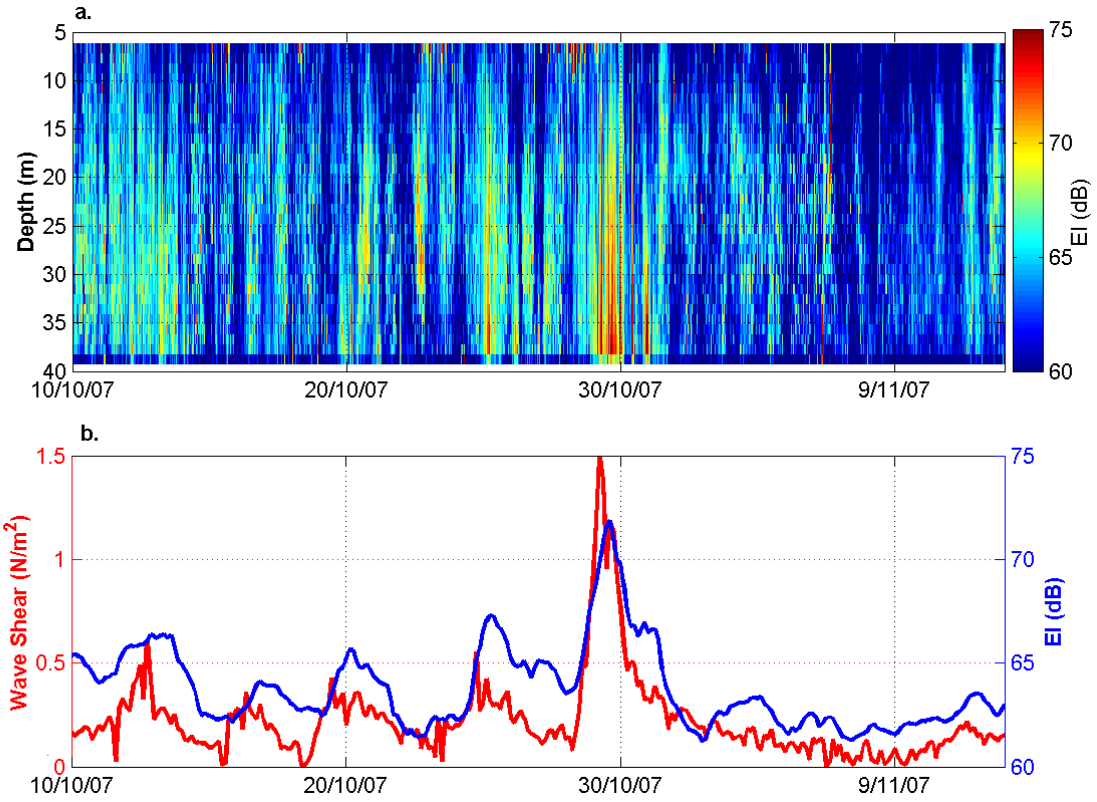

Figure 3.14. Data from Mooring M8 showing (a) the distribution of EI throughout the water column, and (b) the observed wave induced shear stress (red) and the EI (blue) at 3.2 m above the sea floor in a water depth of 45 m.

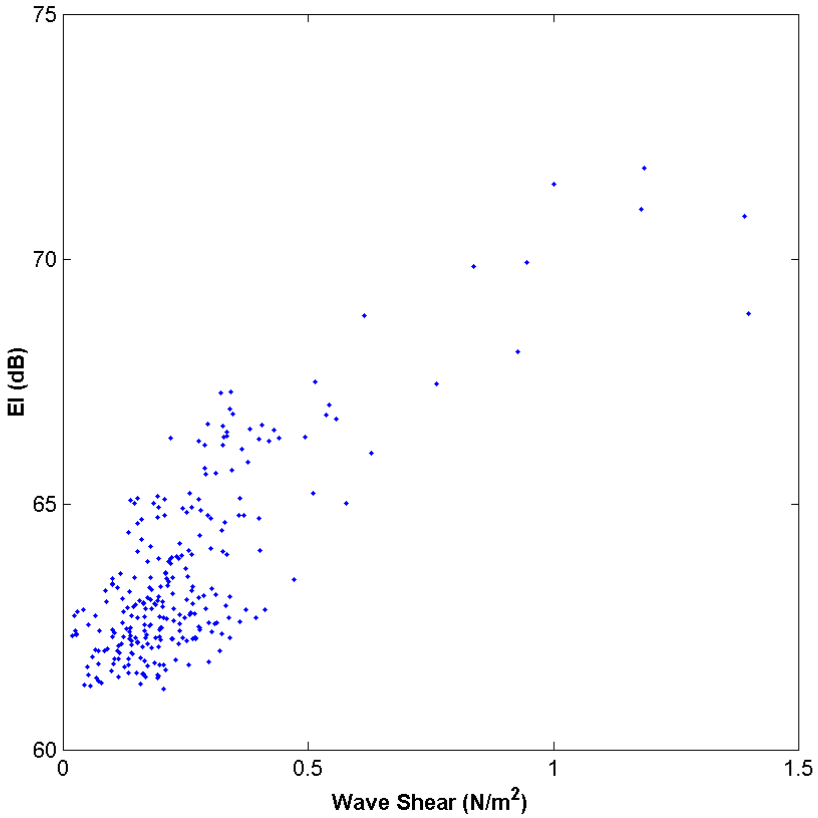

Figure 3.15. Wave shear stress vs EI at M8, just south of Thistle Island near the mouth of Spencer Gulf.

3.4. Discussion

The two major sediment types identified in the cluster analysis of geochemical variables (Figures 3.6, 3.7 and 3.8) differ significantly in their nutrient concentrations. The sediments forming Group 2, generally found in the central TFZ, are much richer in nutrients, typically with double the concentrations found in Group 1, confirming the earlier work of Fernandes et al. (2006). The distribution of the sediment types is not directly related to either the wave regime or the mean sediment grain size, with no statistically significant difference in either U_{sig} or mean grain size between the two regions. While there is no difference in mean grain size between the two regions, certain sediment grain size fractions do show significant differences. The nutrient-rich region contains a much higher percentage of silt (4-63 μm) than elsewhere. The accumulation of such fine particles in this region is not surprising given that U_{sig} is < 0.07 m s^{-1} for all sites (with the exception of site 36). The increase in silts is accompanied by a decrease in fine-sands (125-250 μm), typically the dominant size fraction.

The nutrient-rich region also has a characteristically heavier $\delta^{15}N$ isotopic signature. The high nutrient concentrations and heavier isotopic signature suggest that nutrients accumulating in the area are subject to higher microbial activity within the sediments. The observed spatial distribution of the geochemical variables indicates that not only physical mechanisms will play a role in defining distributions, but possibly distance to sources of organic inputs (e.g. seagrass beds, aquaculture activities) and changes in sediment metabolism with organic matter supply and depth. Despite a clear delineation between sediment types, it is difficult to separate natural versus anthropogenic factors driving the observed differences.

Sediment particle mean grain size does not show the same disparity to the physical setting as the other geochemical parameters. Sediments subject to U_{sig} < 0.070 m s^{-1} were finer, indicating that these areas are depositional in nature, whereas those subject to U_{sig} > 0.074 m s^{-1} were coarser and erosional in nature. By extending this principle, with intermediate values assigned to a transportational regime, a map covering the entire TFZ was developed (Figure 3.16). This seafloor classification reflects exposure to fetch, shoaling, and wave refraction, which combine to create a complex set of non-linear interactions.

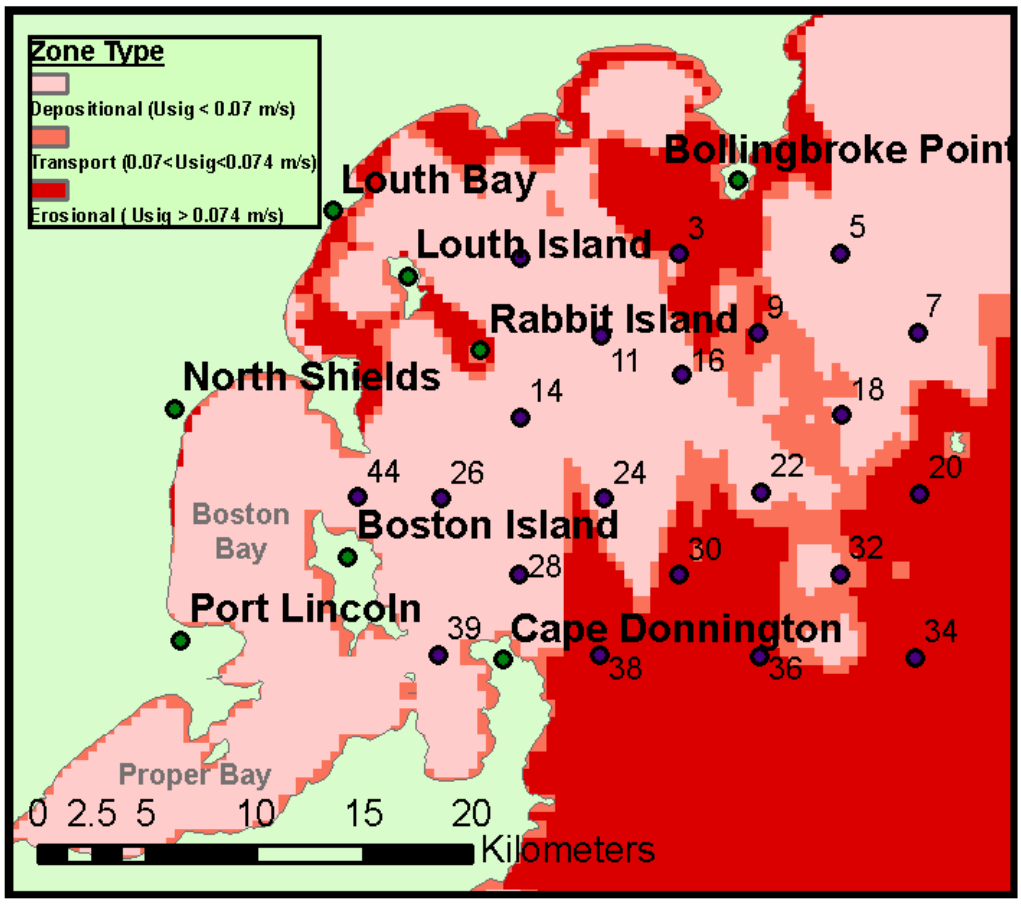

Figure 3.16. Seafloor classification based on U_{sig} for the entire model domain.

The mapping of U_{sig} suggests that depositional areas exist in the sheltered embayments of Proper and Boston Bay to the west of Boston Island. The region directly east of Boston Island was also classified as depositional. The region to the east of Cape Donnington was classified as erosional with U_{sig} peaking at over 0.2 m s^{-1}. This area is subject to significant amounts of bottom dissipation due to the shoaling of incoming swell as the water depth decreases from ~60 m to ~30 m. Of particular interest are the erosional zones in the northern embayments of Louth Bay and south of Point Bolingbroke. These regions are generally quite shallow (<15 m) and it is in these zones that shorter period wind waves will dissipate most of their energy.

The risk of resuspension in the TFZ, an area classified as depositional, can be estimated from the modeled H_s and T_m. Using linear wave theory (equations 3.2 and 3.3), it is possible to derive relationships between H_s, T_m and total water depth, to find the required combination to exceed a certain critical threshold of U_b, which in the depositional zones is 0.07 m s^{-1} (Figure 3.17).

The wave conditions in the TFZ are presented in Chapter 2. Normal conditions for the TFZ (Figure 3.17; green shading), have T_m ranging from 2 to 4 seconds, with a typical H_s of <0.5 m. These conditions are not energetic enough to generate sediment resuspension in water deeper than 5-8 m. Therefore under normal conditions there is no possibility of sediment resuspension in the current TFZ.

Typical wave conditions during storm events (Figure 3.17; red shading), generate T_m's between 4 and 6 seconds with H_s reaching 0.8-1.2 meters. During storm events, if waves with a period of 5-6 s and height of 1 m propagate into the TFZ, orbital velocities may exceed 0.07 m s^{-1} in regions shallower than 20-22 m deep, in which case sediment resuspension may occur.

The relationship between oceanic swell and the conditions in the TFZ is discussed in detail in Chapter 2. The swell height in the TFZ typically ranges between 1% and 10% of the value at Cape de Couedic. The swell height in the TFZ is sensitive to the incident direction, with swell entering from between 180˚ and 200˚ generating the greatest heights. Figure 3.17 (blue shading) suggests that swell has the greatest potential to cause sediment resuspension, as it requires a wave height of >0.45 m to generate U_b in excess of 0.07 m s^{-1}. Such conditions are most likely to occur if swell enters the region from S-SSW with an oceanic significant wave height of > 5 m.

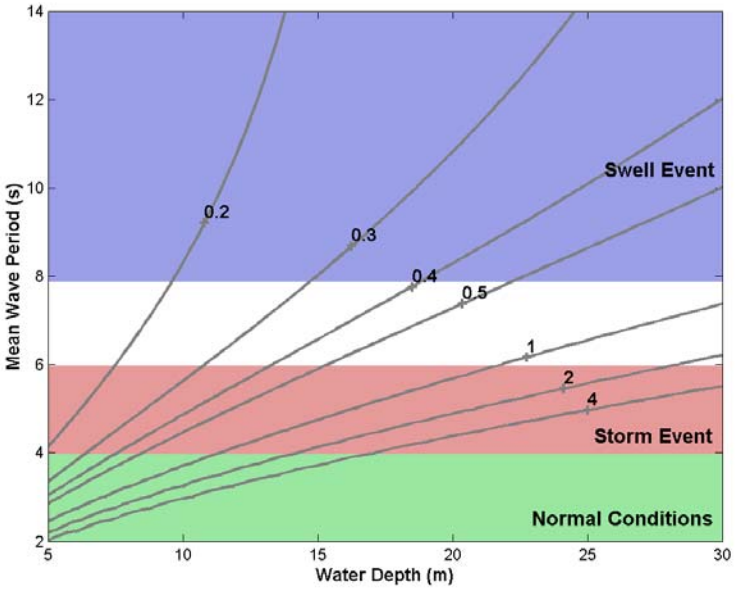

Figure 3.17. The contours in this figure show the required significant wave height (H_s in m) as a function of water depth and mean wave period (T_m) to exceed the orbital velocity of 0.07 m s^{-1}. Shading indicates the typical values of T_m for various conditions.

Observations of EI both in the TFZ (M5 and M7) and from the far more energetic Thistle Island (M8) show a distinct relationship between the wave induced bed-shear and resuspension events. The relationship between EI and τ_w is more complex in the TFZ, potentially a consequence of differing sediment types between the two locations. The linear relationship at M8 suggests that as τ_w increases, the sediment is rapidly resuspended. There appears to be no lag between the decrease in τ_w and a decrease in EI. This suggests that the sediments in this area have a much larger grain size and therefore the suspended sediment

rapidly settles after τ_w decreases. The relationship between EI and τ_w at M7 suggests that once τ_c is exceeded in the TFZ, sediments are resuspended and remain in suspension for some time after the event due to the low settling velocities of the finer grained particles inherent to this location. The observed value of τ_c for the TFZ is ~ 0.1 N m^{-2}, based on EI data.

The theoretical τ_w thresholds for the initiation of sediment motion (Table 3.5) for the major groups identified by the cluster analysis of U_{sig} is 0.199 N m^{-2} in erosional zones, and 0.08-0.179 N m^{-2} in depositional areas largely made up of silts and fine sands. These theoretical resuspension thresholds agree remarkably well with the observed sediment resuspension thresholds of 0.1 N m^{-2}.

Table 3.5. The theoretical shear stress required to initiate sediment movement within erosional and depositional zones within the TFZ (see section 3.2.6).

	Depositional Zones	**Erosional Zones**
d	<180 μm	>250 μm
s	2.43	2.8
θ_c	0.06	0.05
τ_c (N m^{-2})	0.08 - 0.1788	> 0.1987

3.5. Conclusions

Separate cluster analyses of sediment geochemical variables and the modeled U_{sig} have identified two significantly different geochemical provinces and two different physical regimes. There appears to be little relationship between the two, suggesting that the distribution of geochemical provinces is influenced by other variables in addition to the physical conditions inherent to the area.

The implications of the sediment geochemistry and the seafloor classification derived in this work for the tuna industry are dependent upon the locations of individual operators. When T_m exceeds 8 s during swell events, there is the potential for sediment resuspension at a 20 m water depth typical of that under tuna farms if the swell height is over 0.45 m. In the case of a storm event, when T_m = 4-6 s, and if the significant wave height exceeds 1-2 m, there is an increased risk of sediment resuspension. During storm events the wave height rarely exceeds 1 m in the central TFZ (see Chapter 2), therefore swell events pose the greatest risk for sediment resuspension.

Lease sites located within depositional areas may be subject to decreases in water quality during high-energy storm or swell events. During such events, fine sediments such as silts and fine-sands can become resuspended. It is these size fractions that were found in abundance in the mucus contained in the gills of the tuna during the 1996 mortality event. Once these fine sediments come into suspension, the turbulence associated with such storm events will keep them in suspension for many days. Ambient currents are then able to transport the resuspended sediments over large areas, moving them from the regions where the resuspension was initiated.

Field observations show that there are weak sediment resuspension events occurring within the current TFZ. However the measured events do not persist for longer than 1-3 days and are typically confined to the lower 10 m of the water column. Tuna pens typically have a wall depth of 10 m, although the center of the bottom net is lower, so that the fish are generally able to avoid these events. Tthe wave events that were recorded during this study would not be considered highly-energetic storm events that may occur with a frequency of 1 every 5-10

years, but rather typical wave events associated with the passage of synoptic scale weather events that occur 5 – 10 times per year depending on the location.

Acknowledgements
Sonja Venema, Kate Rodda, Brenton Ebert, Bruce Miller-Smith, Yvette Eglington, Mandee Theil and Jeremy Barnett are acknowledged for sample collection, and Gen Mount for sample preparation and database entry (SARDI Aquatic Sciences). We also wish to thank Tina Hines for porewater nutrient analyses (Water Studies Centre, Monash University), Stuart McClure (CSIRO Land & Water) for elemental and isotopic analyses, and Jamie Woodward (MAFRL, Murdoch University) for phosphorus analyses.

3.6. References

APHA-AWWA-WPCF (1998a). Method 4500-NH3-I. Standard methods for the examination of water and wastewater, 20th edition. L. S. Clesceri, A. E. Greenberg and A. D. Eaton. Washington, American Public Health Association: 4-111.

APHA-AWWA-WPCF (1998b). Method 4500-PG. Standard methods for the examination of water and wastewater. L. S. Clesceri, A. E. Greenberg and A. D. Eaton. Washington, American Public Health Association: 4-149.

Blott, S. J. and Pye, K. (2001). "Gradistat: a grain size distribution and statistics package for the analysis of unconsolidated sediments." Earth Surface Processes and Landforms 26: 1237-1248.

Booij, N., Ris, R. C. and Holthuijsen, L. H. (1999). "A third-generation wave model for coastal regions - 1. Model description and validation." Journal of Geophysical Research-Oceans 104: 7649-7666.

Clarke, S. F. (1996). Tuna Mortalities: April - May 1996. Adelaide, South Australian Research and Development Institute.

Fernandes, M., A. Cheshire, and A. Doonan (2006). "Sediment geochemistry in lower Spencer Gulf, South Australia: implications for southern bluefin tuna farming." Australian Journal of Earth Sciences 53: 421-432.

Fenton, J. D. and McKee, W. D. (1990). "On Calculating The Lengths Of Water-Waves." Coastal Engineering 14: 499-513.

Fredsoe, J. and Deigaard, R. (1992). Mechanics of Coastal Sediment Transport. Singapore, World Scientific Publishing.

Fuller, M. K., Bone, Y., Gostin, V. A. and Von Der Borch, C. C. (1994). "Holocene cool-water carbonate and terrigenous sediements from southern Spencer Gulf, South Australia." Australian Journal of Earth Sciences 41: 353-363.

Grant, W. D. and Madsen, O. S. (1979). "Combined wave and current interaction with a rough bottom." Journal of Geophysical Research 84: 1797-1808.

Grzechnik, M. P. (2000). Three dimensional tide and surge modelling and layered particle tracking techniques applied to southern Australian coastal seas. Adelaide, Adelaide Universtiy. PhD.

Guillen, J., Jimenez, J. A., Palanques, A., Gracia, V., Puig, P. and Sanchez-Arcilla, A. (2002). "Sediment resuspension across a microtidal, low-energy inner shelf." Continental Shelf Research 22: 305-325.

Hamblin, P. F., Zhu, D. Z., Chiocchio, F., He, C. and Charlton, M. N. (2000). "Monitoring suspended sediment plumes by optical and acoustical methods with application to sand capping." Canadian Journal of Civil Engineering 27: 125-137.

Harris, P. T. (1994). "Comparison of tropical, carbonate and temperate, siliciclastic tidally dominated sedimentary deposits: Examples from the Australian continental shelf." Australian Journal of Earth Sciences 41: 241-254.

Hedges, J. I. and Stern, J. H. (1984). "Carbon and nitrogen determinations of carbonate-containing solids." Limnology and Oceanography 29: 657-663.
Hemer, M. A. and Bye, J. A. T. (1999). "The swell climate of the South Australian Sea." Transactions of the Royal Society of South Australia 123: 107-113.
Hollander, M. (1973). Nonparametric Statistical Methods. New York, Wiley.
Holthuijsen, L. H. (2007). Waves in Oceanic and Coastal Waters. New York, USA, Cambridge University Press.
Klein, H. (2003). "Investigating sediment re-mobilisation due to wave action by means of ADCP echo intensity data Field data from the Tromper Wiek, western Baltic Sea." Estuarine Coastal And Shelf Science 58: 467-474.
Lauer, P. (2005). Benthic metabolism addjacent to southern bluefin tuna (*Thunnus maccoyii*) pontoons in South Australia. School of Biological Sciences, Faculty of Science and Engineering. Adelaide, Flinders University. PhD: 210.
Lawrence, D., Dagg, M. J., Liu, H. B., Cummings, S. R., Ortner, P. B. and Kelble, C. (2004). "Wind events and benthic-pelagic coupling in a shallow subtropical bay in Florida." Marine Ecology-Progress Series 266: 1-13.
Nielsen, P. (1992). Coastal Bottom Boundary Layers and Sediment Transport. Singapore, World Scientific Publishing.
Noye, J. (1984). "Physical processes and pollution in the waters of Spencer Gulf." Marine Geology 61: 197-220.
Nunes, R. A. and Lennon, G. W. (1986). "Physical property distributions and seasonal trends in Spencer Gulf, South Australia: an inverse estuary." Australian Journal of Marine and Freshwater Research 37: 39-53.
Paphitis, D. and Collins, M. B. (2005). "Sediment resuspension events wihtin the (microtidal) coastal waters of Thermaikos Gulf, northern Greece." Continental Shelf Research 25: 2350-2365.
Pattiaratchi, C., Newgard, J. and Hollings, B. (2007). Physical oceanographic studies of Adelaide coastal waters using high-resolution modelling, in-situ observations and satellite techniques. ACWS Technical Report No. 20 prepared for the Adelaide Coastal Waters Study Steering Committee., School of Environmental Systems Engineering, The University of Western Australia.
Petrusevics, P. M. (1993). "SST Fronts in inverse estuaries, South Australia - Indicators of reduced gulf - shelf exchange." Australian Journal of Marine and Freshwater Research 44: 305-323.
Porter-Smith, R., Harris, P. T., Andersen, O. B., Coleman, R., Greenslade, D. and Jenkins, C. J. (2004). "Classification of the Australian continental shelf based on predicted sediment threshold exceedence from tidal currents and swell waves." Marine Geology 211: 1-20.
Ris, R. C., Holthuijsen, L. H. and Booij, N. (1999). "A third-generation wave model for coastal regions - 2. Verification." Journal of Geophysical Research-Oceans 104: 7667-7681.
Smyth, C., Hay, A. E., Hill, P. S. and Schillinger, D. (2006). "Acoustic observations of vertical and horizontal swimming velocities of a diel migrator." Journal of Marine Research 64: 723-743.
Tragou, E., Zervakis, V., Papageogiou, E., Stavrakis, S. and Lykousis, V. (2005). "Monitoring the physical forcing of resuspension events in the Thermaikos Gulf - NW Aegean during 2001-2002." Continental Shelf Research 25: 2315-2331.
US Environmental Protection Agency (1991). Method 200.3. Sample preparation procedure for spectrochemical determination of total recoverable elements in biological tissues. Methods for the Determination of Metals in Environmental Samples. EPA/600/4-

91/010. Cincinnati, Ohio, Office of Research and Development, US Environmental Protection Agency: 23-30.
You, Z. J. (2005). "Fine sediment resuspension dynamics in a large semi-enclosed bay." Ocean Engineering 32: 1982-1993.

3.7 Appendix

The following appendix contains the spatial maps outlining the distribution of the various geochemical properties in south-west Spencer Gulf.

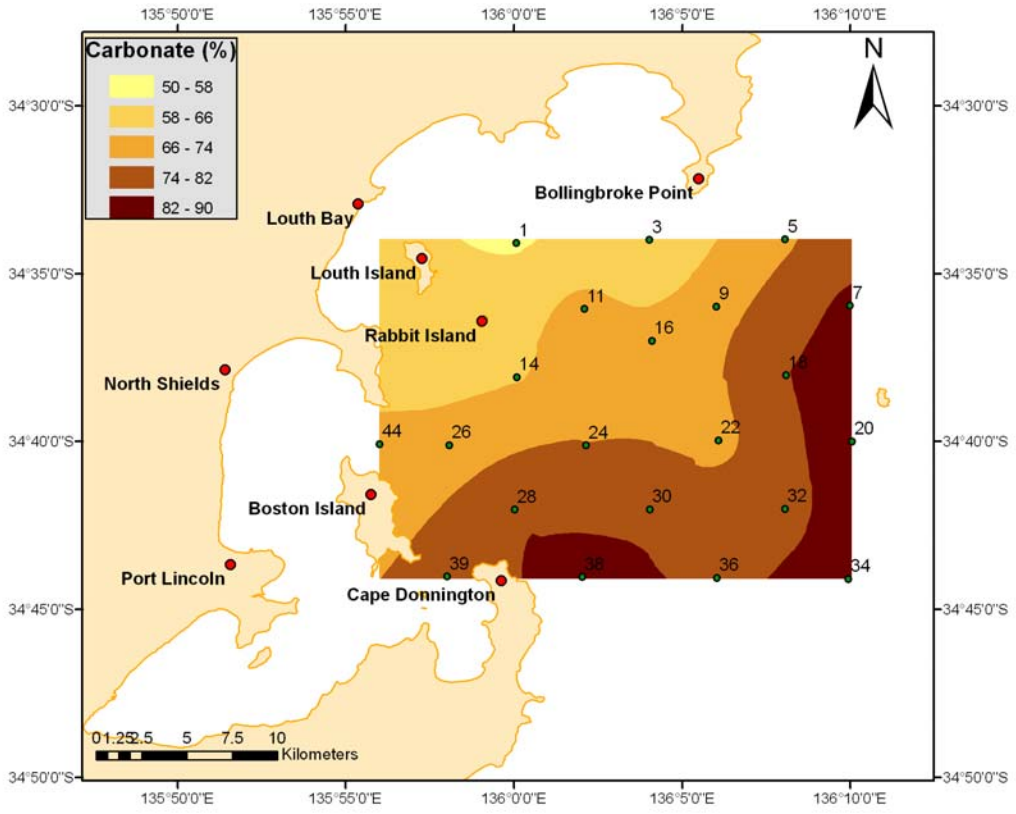

Figure 3.18. The spatial distribution of carbonate in sediments.

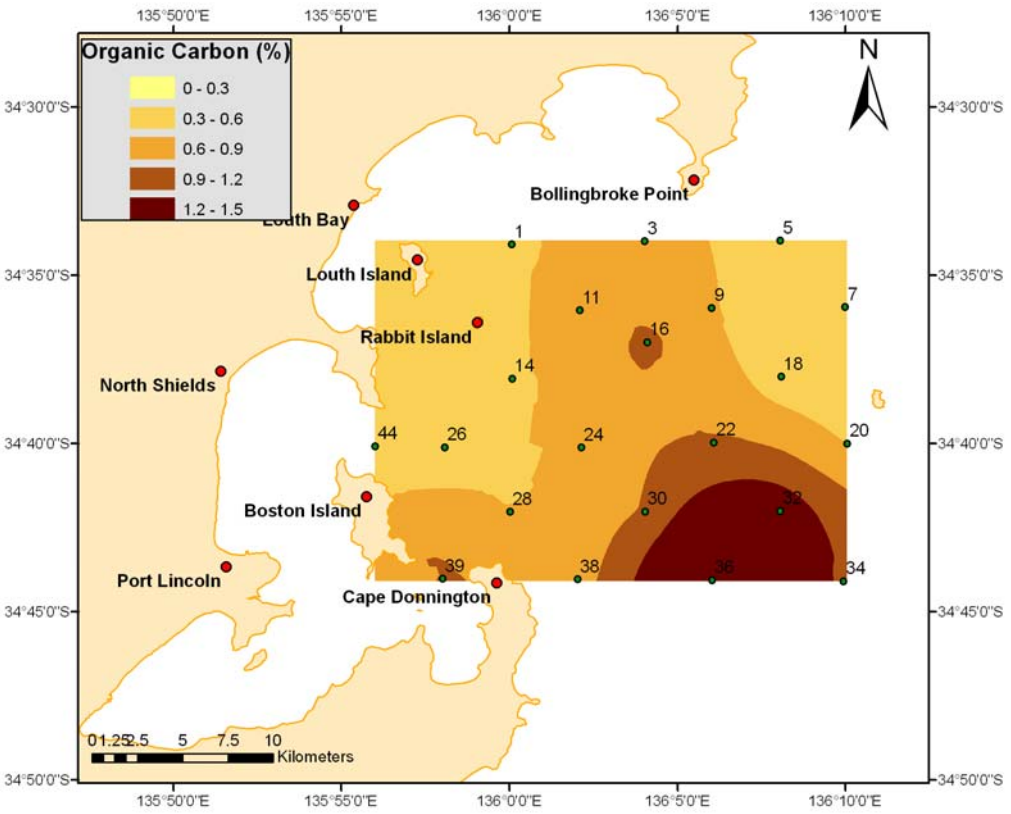

Figure 3.19. The spatial distribution of organic carbon in sediments.

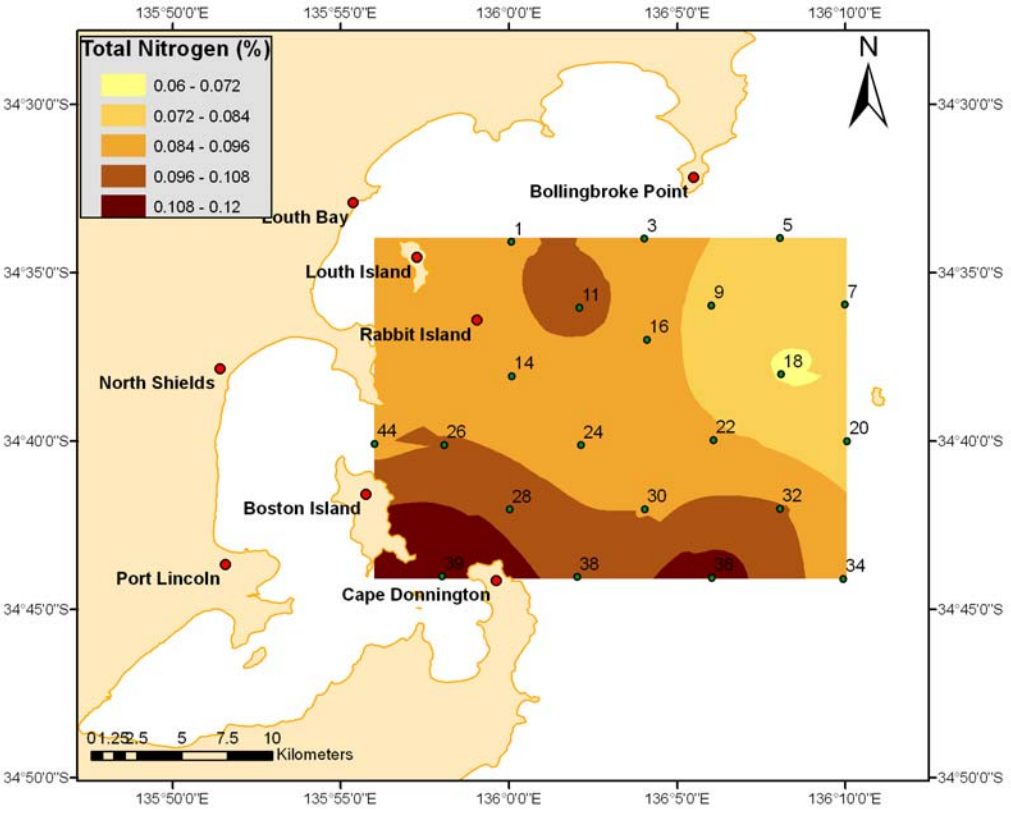

Figure 3.20. The spatial distribution of total nitrogen in sediments.

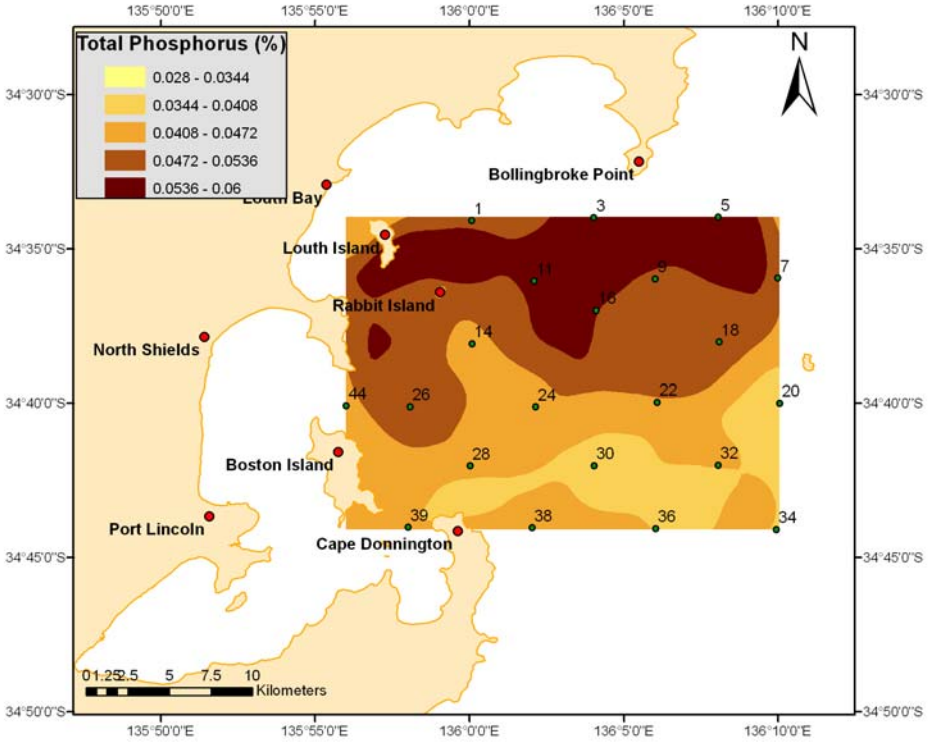

Figure 3.21. The spatial distribution of total phosphorus in sediments.

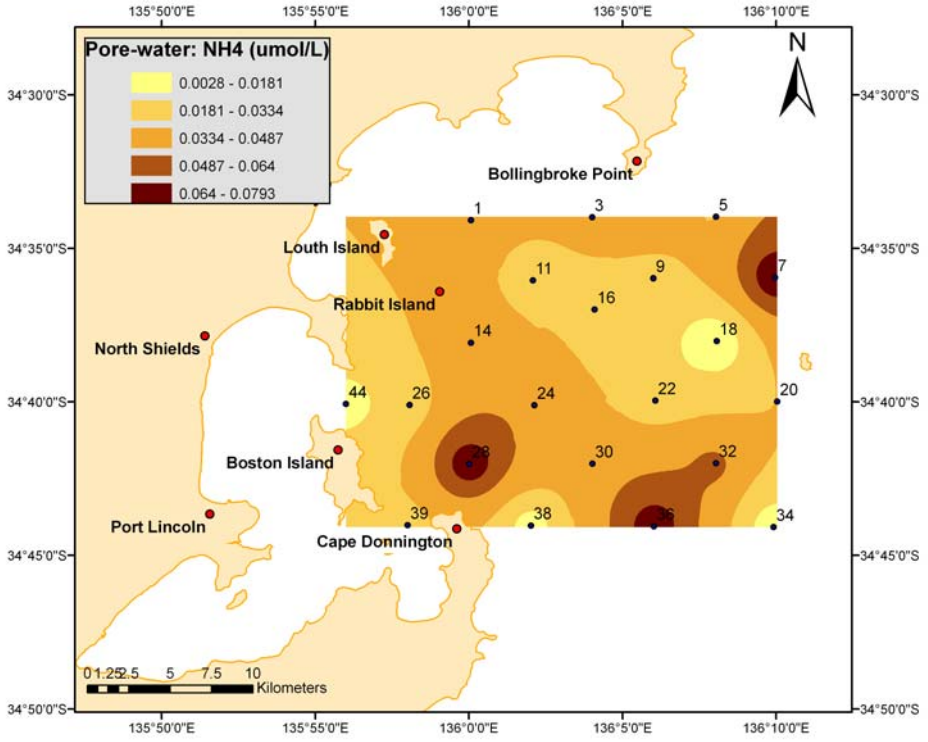

Figure 3.22. The spatial distribution of porewater ammonium concentration in sediments.

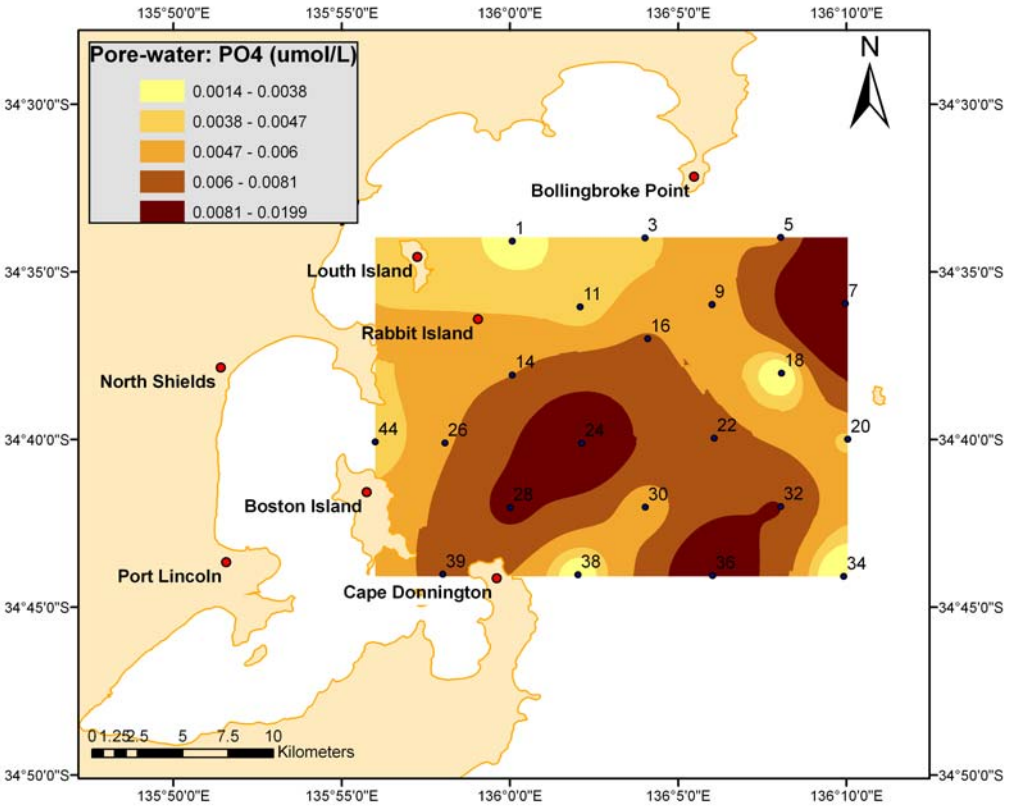

Figure 3.23. The spatial distribution of porewater phosphate concentration in sediments.

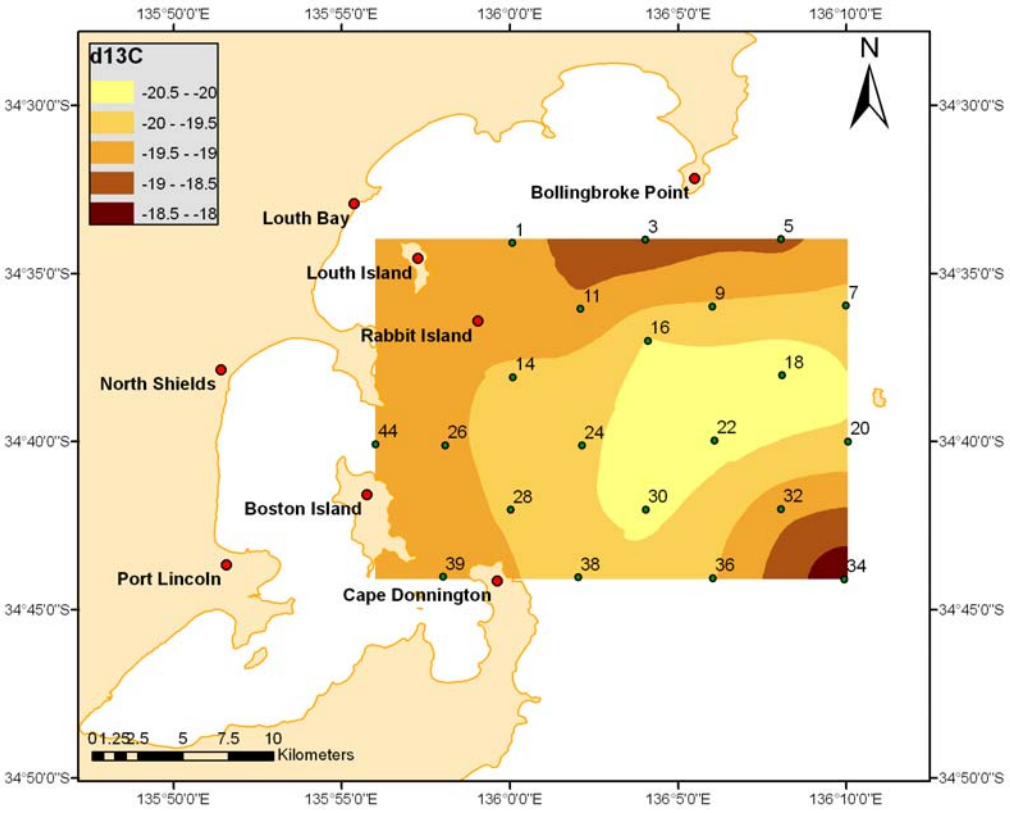

Figure 3.24. The spatial distribution of $\delta^{13}C$ signatures in sediments.

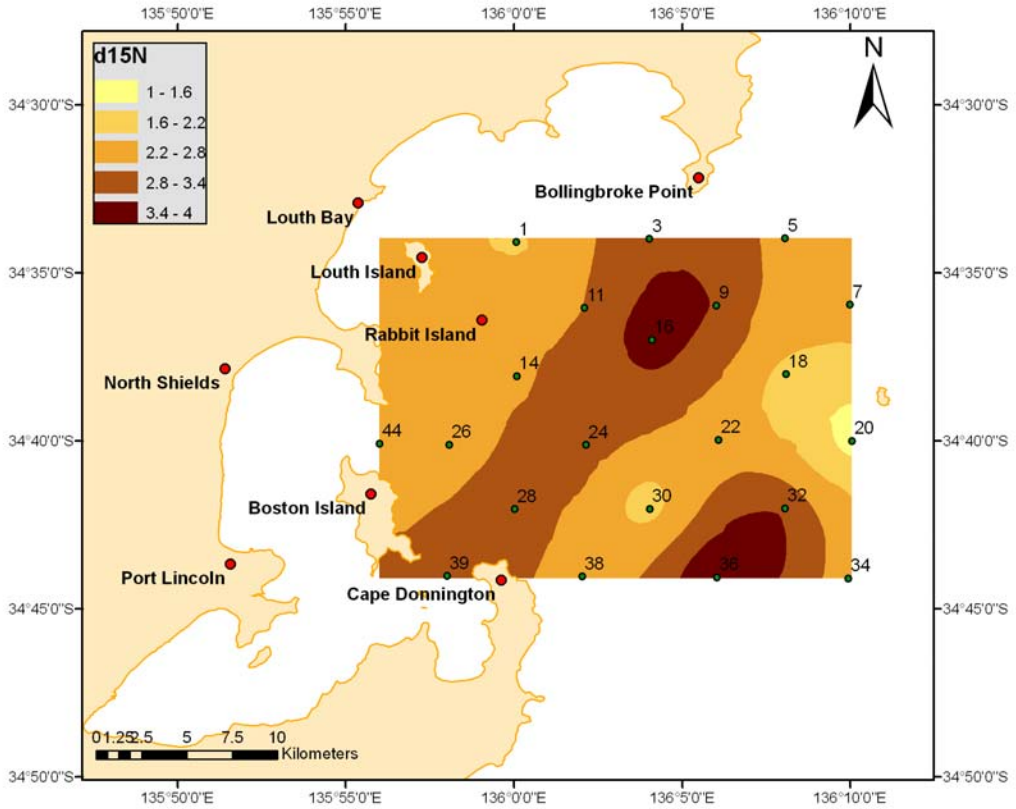

Figure 3.25. The spatial distribution of $\delta^{15}N$ signatures in sediments.

Chapter 4. Numerical modelling of the sediment dynamics in the Port Lincoln region

Nugzar Margvelashvili

CSIRO Division of Marine and Atmospheric Research, GPO Box 1538, Hobart, Tas, 7001
Phone +61 (3) 6232 5222, E-mail: nugzar.margvelashvili@csiro.au

and Aquafin CRC

Abstract

A 3-D fine resolution model of fine sediment transport in the Port Lincoln coastal waters has been developed. The model is driven by simulated waves and currents, and predicts bottom friction and suspended sediment concentrations. The model was calibrated against monthly monitoring data and applied to the study area to simulate transport of fine sediments over a one-year period (September 2005 – August 2006). The main objectives of the modelling were to improve our understanding of fine sediment dynamics in the Port Lincoln region and to provide physical settings for biogeochemical simulations.

The analysis of the predicted bottom friction maps suggests regular resuspension of fine sediment fractions, having low critical shear velocity of resuspension (0.005 m s^{-1}) typical of fresh sediment deposits, microflocs or fluff layer sediments. These fine particles do not create a cohesive network in sediments and can be easily resuspended by waves and currents. The lowest probability of resuspension is predicted around Boston Island and in Proper Bay. Eastward from Rabbit Island, in the middle section of the modelling domain, the simulated sediments are resuspended about 30 % of the time. The probability of resuspension of the bulk mass of cohesive consolidated sediments having higher critical shear velocity of resuspension (0.014 m s^{-1}) does not exceed 20 %, and erosion zones for these sediments are limited to a few isolated areas north-east from Cape Donnington and around Point Bolingbroke.

The sediment transport model predicts accumulation of fines in sheltered coastal embayments and northwest from Cape Donnington, consistent with the field measurements. The model does not reproduce winnowing of fines south from Rabbit Island. Sensitivity tests with varying model parameters suggest that uncertainties in the sea-bed roughness and critical shear stress distribution translate into uncertainty in the predicted total suspended sediment (TSS) concentrations of factor 3. Numerical experiments with doubled wave height predict elevated levels of TSS in the fish-farm area persisting for up to 10 days.

Based on observations and modelling results we conclude that while the deeper waters off Boston Island, which are exposed to the open sea, have better flushing characteristics compared to the sheltered coastal embayments, the energy of the prevailing waves and currents over the greater part of this region is not sufficient to resuspend and disperse cohesive consolidated sediments. When waves and currents are sufficiently strong to break cohesive networks of sediments, these sediments can provide an abundant source of fines suspended into the water column. Given the large amount of fine sediment deposits in the Port Lincoln region, the risk of extremely high turbidity levels is acute if another extreme weather event, such as that in April 1996, were to occur. To quantify this risk, numerical experiments with sediment resuspension during persistent northeasterly winds (which have the potential to bring extremely energetic waves into the region) are needed.

4.1. Introduction

Farming of Southern Bluefin Tuna (SBT) is a well established aquaculture industry in the Port Lincoln region, offshore from Boston Island (see Figure 4.1). Intensive fish farm operations result in the leakage of liquid and solid wastes into the surrounding environment. The ability of the environment to assimilate these by-product materials depends on many factors including the rate of physical dispersal of the waste and biogeochemical transformations of the organic and mineral substances in the water column and sediments.

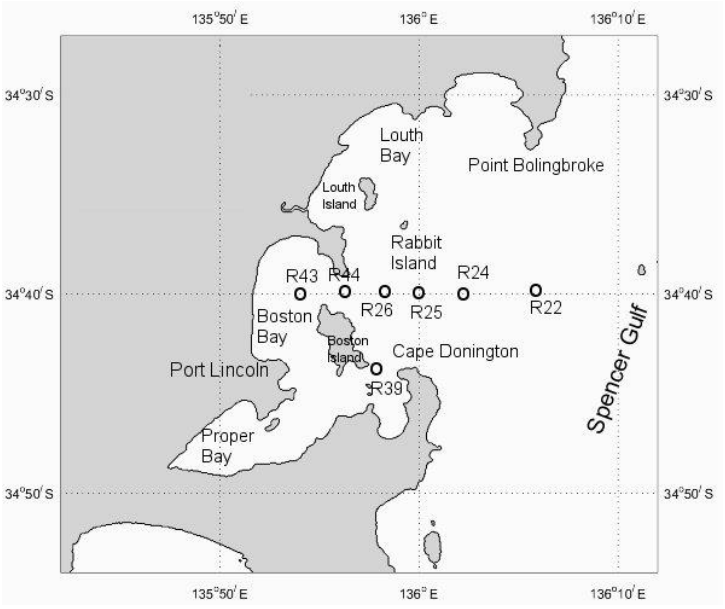

Figure 4.1. Study area map showing the location of monthly monitoring sites.

Sediments are instrumental to the ecology of the Port Lincoln area in many ways. The benthic layer acts as a deposition zone for fine particles, and may increase the residence time of solid and liquid substances accumulating in the region. Resuspension and deposition of sediments enhances cycling of materials between benthic and pelagic layers. High turbidity levels driven by occasional resuspension of particles can inhibit access to light for benthic organisms.

In April 1996, a severe storm in the Port Lincoln region caused extremely high turbidity levels in the water column, leading to up to 60% mortality of stock (Clarke, 1996). High mortality rates were attributed to irritation of SBT gills by the suspended particles, leading to respiratory difficulties and increased infestation by sediment dwelling parasites (Clarke, 1996). Partly to reduce the risk of high turbidity, the industry has moved fish farms from the shallow protected waters of Boston Bay to the deeper areas exposed to the open sea off Boston Island. Higher flushing rates at these locations are expected to reduce the accumulation of fines in the sediments and lower the risk of high turbidity levels. However, our current understanding of the sediment dynamics in this area is poor.

Past studies of the sedimentary setting in the SBT farming area show a heterogeneous distribution of sediment deposits, with extensive areas having a high content of fines. Fernandes et al. (2006) hypothesised that given winds and swell of sufficient energy, these fine particles may be resuspended from the seafloor, affecting the farm sites. To improve the understanding of sediment dynamics in the area, a limited number of modelling studies have been carried out in the past. Noye (1997) and Grzechnik (2000) employed a Lagrangian

particle tracking model to simulate dispersion of fine particles in Boston Bay during the storm event of April 1996. The transport was driven by a 3D tide-surge model, which utilised a simplified heuristic formulation for sediment resuspension and deposition. Particles were released from five point sources, and sediment settling was accounted for by halving the number of particles every 24 hours. The spread of simulated particles was compared to mortalities of tuna caged in farms, and generally a good match between cumulative tuna losses and the concentration of particles was reported. Porter-Smith et al. (2004) studied the role of waves and tides in sediment resuspension around the Australian coast. The study involved modelling waves and tidal currents in the Spencer Gulf region, with the subsequent assessment of the probability of sediment resuspension. The Spencer Gulf region was ranked as an environment with tidally dominated transport of sediments, however, the tuna farming zone (TFZ) was not properly resolved during these simulations.

This chapter presents results of the sediment modelling undertaken within the framework of an integrated multidisciplinary modelling study of the Port Lincoln region. The integrated study involved the development and application of 3D coupled hydrodynamic, sediment transport and biogeochemical models. The main objectives of the sediment modelling were to improve our understanding of fine sediment dynamics in the Port Lincoln region, and to provide physical settings for biogeochemical simulations.

4.2. Model description

The sediment transport model is driven by the hydrodynamic (chapter 1) and wave (chapter 2) models. The hydrodynamic model provides three-dimensional fields of currents and turbulence characteristics, while the wave model (SWAN) predicts the near-bottom wave orbital velocities, which may greatly enhance sediment resuspension during storm or high swell events.

4.2.1. Hydrodynamic model

A comprehensive description of the theory underlying the 3D hydrodynamic model is available in Herzfeld (2006) and its application to the Port Lincoln region is described in detail in Herzfeld and Middleton (2008), with a summary in chapter 1 of this report. Only a brief general description of the model will be given here. The model has been developed by the Environmental Modelling group at CSIRO (Commonwealth Scientific and Industrial Research Organization) Division of Marine and Atmospheric Research over the last decade. It is intended to be a general purpose model applicable to scales ranging from estuaries to regional ocean domains, and has been successfully applied to a variety of applications around the Australian coast. The hydrodynamic model solves Reynolds' equations with a free surface boundary condition, using the Boussinesq approximation and the hydrostatic assumption. The governing equations include equations for momentum, continuity, and transport of salinity and temperature. The model can invoke several turbulence closure schemes, including k-epsilon, Mellor-Yamada 2.0 and Csanady type parameterisations. A variety of advection schemes may be used on tracers and 1st or 2nd order can be used for momentum. The model uses a curvilinear orthogonal grid in the horizontal and fixed 'z' coordinates in the vertical. In this study the vertical resolution followed a logarithmic distribution, with z-layer height expanding from 0.5 m near the surface to a maximum of 3 m at its maximum depth of 30 m.

4.2.2. Wave model

Surface wave forcing was included into the sediment model to improve bottom friction estimates. The wave data were obtained from the Spectral Wave Model Simulations (SWAN). A detailed description of the wave model application to the Port Lincoln region is given in chapter 2 of this report. SWAN solves equations for the directional wave spectrum on a regular grid based on local wind input, wave dissipation, nonlinear wave-wave interactions and propagation of waves from non-local sources. The model predicts significant wave height, period and direction of the surface gravity waves (locally generated wind waves and swell with a period of 1-20 seconds). To provide boundary conditions for the fine resolution wave model of the Port Lincoln region, the model was nested into a larger-scale modelling domain covering the whole of Spencer Gulf. The wind fields for the wave model are derived from the Bureau of Meteorology (BOM) MesoLAPS model. The open ocean boundary of the large-scale wave model is forced with output from the BOM global wave model, WAM. The simulation period covered one year (from 1/08/05 to 1/08/06) and the model output was stored at 3-hour intervals. The wave model was tested against measurements (Jones et al., 2008 – see chapter 2 of this report), showing generally good agreement with data.

4.2.3. Sediment model

The sediment model solves advection-diffusion equations for the mass conservation of suspended and bottom sediments, taking into account bottom exchanges due to resuspension and deposition (Condie and Sherwood 2006, Margvelashvili et al, 2008). The resuspension and deposition of cohesive sediment is parameterised by the Ariathurai and Krone (1976) formula. Bottom friction under combined waves and currents is calculated using the Grant and Madsen (GM) model (Grant and Madsen, 1986; Madsen, 1994).

One of the limitations of the GM model is that it is not applicable when the scale of physical roughness elements exceeds the thickness of the wave-current turbulent boundary layer. In the Port Lincoln region, a typically low wave energy environment, one can expect weak or no turbulent wave bottom boundary layer over extended periods of time. During these periods the bottom friction will be dominated by physical roughness associated with ripples, biological mounds, and other small scale near bottom features. A turbulent wave-current bottom boundary layer will be fully developed during storm and high swell events. To accommodate these varying regimes of bottom friction development, the model employs several different formulations for the bottom boundary layer processes. The GM model is applied to predict bottom stresses when the apparent roughness associated with waves exceeds the physical roughness. Conversely, when the apparent roughness due to waves is lower than the physical roughness of the seabed, the bottom friction is estimated from the log profile approximation of the velocity field. The physical roughness of the seabed and the sediment grain size are two key parameters required by the bottom boundary layer model. The median grain size of the sediment particles (0.2 mm) was estimated from the observed grain size distribution (Fernandes et al., 2006). The physical roughness has been inferred from the model calibration study.

The modelled sediments were represented by non-cohesive sand, cohesive silt and clay fractions. The initial concentrations of sediment deposits were specified from the observed grain size distribution (Fernandes et al., 2006) assuming that all bottom sediments initially are evenly distributed throughout the modelling domain, and there are no particles suspended into the water column. Because of limitations of the z-coordinate numerical grid, only fine

(cohesive) sediment transport has been simulated during this study. The coarse sand particles were kept immobilised within the benthic layer. There were no interactions between sediment fractions in the water column. In the benthic layer, when fine sediments were eroded from the top layer, coarser immobilised particles sheltered the underlying fine sediments from further resuspension.

Apart from resuspension and deposition, the model also simulates background exchange of fine particles between the benthic and pelagic layers. This exchange represents a lump sum of the processes not simulated explicitly, including bioresuspension and biodeposition (Graf and Rosenberg, 1997), resuspension of fines due to unresolved variability of the near bottom currents, critical shear velocity and grain size, among others.

At the open sea boundaries, where sediments were carried out of the modelling domain, the sediment model utilised a free-flow boundary condition. During inflow events, constant sediment concentrations of 0.1 mg L^{-1} were applied. There was no flux of sediments through the solid coastal boundaries or through the water surface.

The numerical grid for sediment variables in the water column coincided with the numerical grid for the hydrodynamic model. Within the bottom sediments, the model utilised a time-varying sediment-thickness adapted grid, with the active upper sediment layer having constant thickness (0.5 cm), while the thickness of deeper layers varied to accommodate the deposited sediment. The top 30 cm of sediment was divided into three layers with the resolution gradually becoming finer towards the sediment-water interface. Horizontal resolution of the seabed followed the resolution of the water column grid.

The model simulation was run for the period September 2005 to August 2006. This corresponds to the period for which the hydrodynamic model was run, and to when the oceanographic moorings were deployed and the monthly biogeochemical sampling took place.

4.3. Modelling results

4.3.1. Model against data

The sediment model was tested against monthly total suspended solids (TSS) data collected at the 7 sites shown in Figure 4.1. The calibration parameters were settling velocities of fine particles, the sediment background exchange coefficient between benthic and pelagic layers, critical shear stress for resuspension, and bottom physical roughness. The best match between model and data (Figure 4.2) was achieved with the following set of parameters: settling velocity of silt - 0.001 m s^{-1}, settling velocity of clay - 0.00003 m s^{-1}; critical friction velocity - 0.014 m s^{-1}, bottom physical roughness - 0.00033 m; sediment-water exchange coefficient – 1 x 10^{-13} m^2 s^{-1}. The calibrated model reproduces typical concentrations of the suspended sediments observed during the monthly monitoring program, as well as the observed decline of the suspended solids towards the open sea (Figure 4.2). The one exception was for site R26, which had substantially lower observed suspended sediment concentrations than predicted by the model, probably related to an unmeasured characteristic of the physical environment. Note that, because of sparse spatial and temporal resolution of monthly data, the results based on this modelling should be treated with care. Significant uncertainties in the model predictions are likely to occur in areas with substantially altered seabed characteristics (e.g. areas with extensive seagrass cover or regions having substantially varying ripple characteristics).

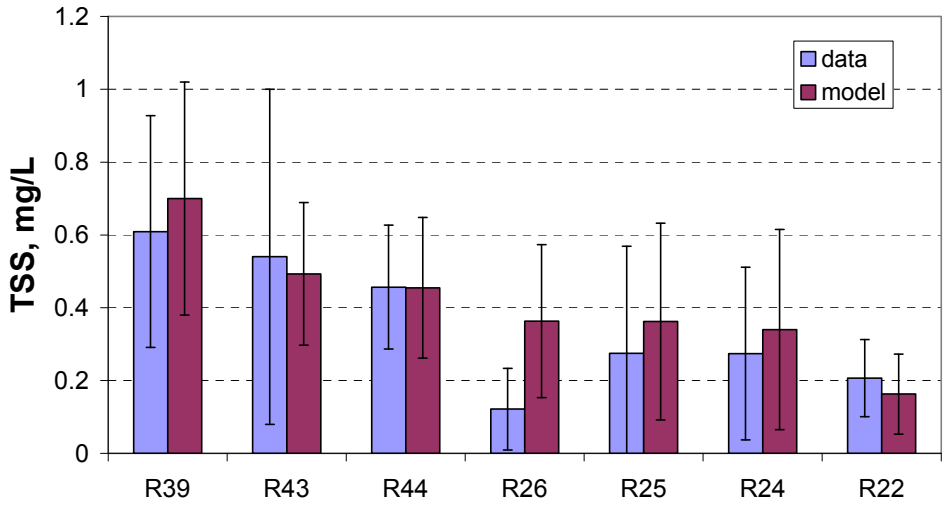

Figure 4.2. Simulated suspended sediment concentrations in surface waters vs monthly data (October 2005-March 2006) along an inshore/offshore gradient east of Port Lincoln (see Figure 4.1 for site locations). The error bars show standard deviation of the data.

The estimated parameters for the model lie within the range of published values and can be given physical interpretation. In the water column, cohesive sediment particles tend to stick together forming aggregates known as flocs, whose size and settling velocity are much larger than those of the individual grains. The high settling velocity of the silt fraction of sediments (0.001 m s^{-1}) is in accordance with published values of the settling rates for flocculated sediments in coastal waters (van Leussen, 1998). The low settling velocity of the clay fraction (0.00003 m s^{-1}) can be thought of as a representative velocity for settling of microflocs and unflocculated fine particles.

The degree of cohesion of fine particles in sediments increases with the proportion of clay minerals in the benthic layer (Mitchener and Torfs, 1996). Fresh mud deposits have a very loose texture, and erosion can occur easily. If newly settled deposits are not eroded again, their density gradually increases as interstitial water is pressed out of the fresh sediment by the weight of the deposit itself. With the compaction of the sediments, their resistance to erosion rapidly increases. The critical shear velocity of resuspension obtained through the model calibration (0.014 m s^{-1}) is within the range of values reported in the literature, and corresponds to the critical friction of cohesive sediments that have been undisturbed and allowed to consolidate for several days (from 1 to 7 days, according to van Rijn, 1993).

The predicted physical roughness value (0.00033 m) is consistent with an independent estimate inferred from the hydrodynamic model calibration (0.0004 m). This estimated value is within the range of typical values for the roughness length of mud or unrippled sand measured in the field (from 0.0002 m to 0.0004 m, see Mitchener and Torfs, 1996). Using a formula for the roughness length over a rippled seabed (Grant and Madsen, 1982), this estimated roughness can also be interpreted as a roughness introduced by ripples having 1 cm height and 30 cm wavelength. This corresponds broadly to observations of the bottom made using remote video in 2003, when most of the farming zone was classified as having low undulations. The exception was some sites in the south, which were classified as having medium undulations, typically due to biologically created mounds up to ~ 10 cm high and 40-50 cm in diameter (M. Loo pers. comm.).

The sediment-water exchange parameter was specified by fitting the model to data. The calibrated value (1×10^{-13} m^2 s^{-1}) is orders of magnitude lower than typical bioturbation rates in sediments (Berg et al., 2001), and represents a conservative estimate of unresolved sediment exchange between water and sediments.

4.3.2. Bottom friction

Simulated mean and maximum bottom friction maps (Figure 4.3) indicate that the highest friction velocities in the study area tend to develop near the open sea boundary (north-east from Cape Donnington, and in the vicinity of Point Bolingbroke) and in shallow areas of Louth Bay. The mean shear velocities are well below the critical threshold value for sediment resuspension (0.014 m s^{-1}), while the maximum values of the bottom friction tend to exceed the critical friction in a number of isolated areas.

To assess the impact of waves on the bottom friction, an additional scenario has been simulated with no impact of surface gravity waves on the bottom friction (Figure 4.4). The model suggests that the gravity waves in general tend to enhance the bottom friction in shallow coastal waters of Louth Bay and eastward from Rabbit Island. Near the sea boundary, and in particular north-east from Cape Donnington and around Point Bolingbroke, the impact of waves was relatively small for the simulated period, and the key patterns in the shear velocity distribution were well captured by stationary currents.

The role of gravity waves in driving bottom friction has been further explored through the comparison of the apparent roughness introduced by waves and the physical roughness attributed to bottom features. As discussed above, the later is a model calibration parameter, while the former was obtained from the model. Figure 4.5 shows that under low wave energy conditions during a typical period in September 2005, the bottom roughness at site R24 tended to be dominated by the near bottom physical roughness elements. The peaks in bottom roughness corresponded to short periods of higher wave energy, with a peak wave height of 0.95 m near the open boundary of the model. The probability (calculated on an hourly basis) of the apparent roughness due to waves exceeding physical roughness due to ripples (Figure 4.6) suggests that for the simulation period waves dominated bottom roughness in shallow areas of Louth Bay, while over the rest of the model domain the bottom roughness was predominantly represented by the near bottom features (ripples, bioturbated mounds, seagrass etc). Note that neither the hydrodynamic nor the wave or sediment models take into account seagrass distribution in shallow coastal areas, which may alter the model predictions for these areas.

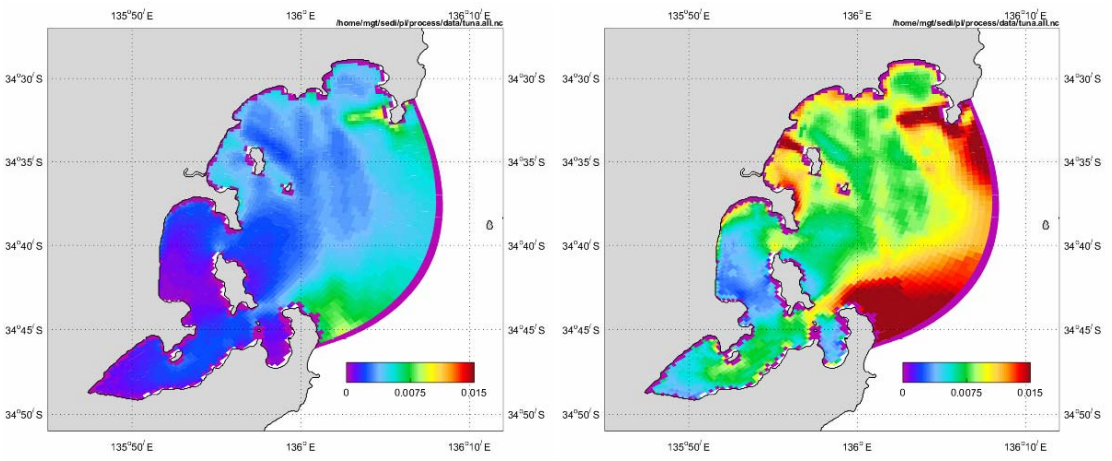

Figure 4.3. Mean (a) and maximum (b) modelled bottom shear velocity (m s^{-1}) due to waves and currents.

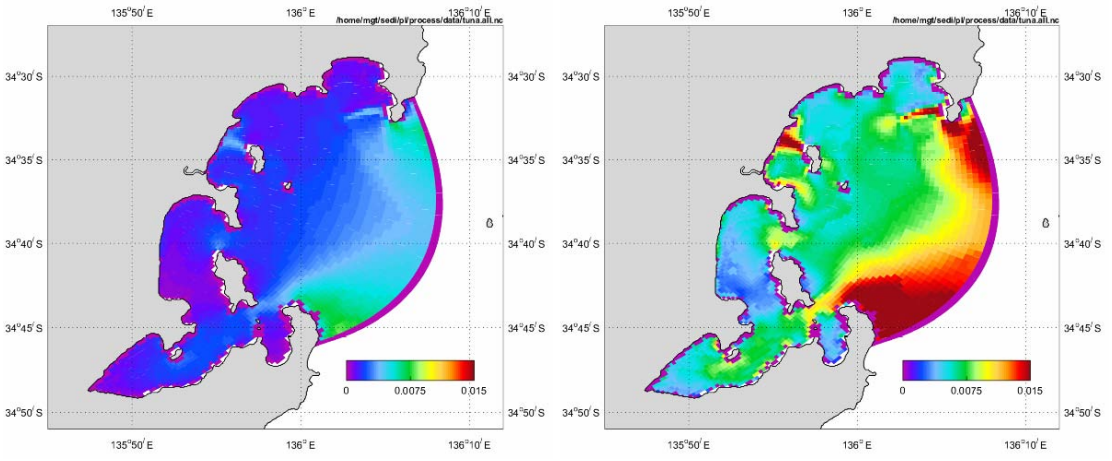

Figure 4.4. Mean (a) and maximum (b) modelled bottom shear velocity (m s^{-1}) due to currents (no waves).

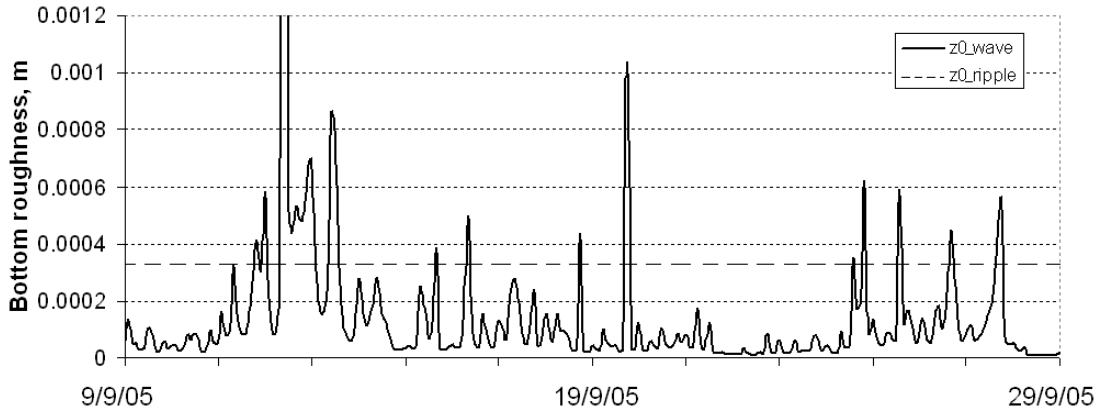

Figure 4.5. Apparent roughness due to waves (z0_wave) and physical roughness due to small scale near bottom features (z0_ripple) at site R24.

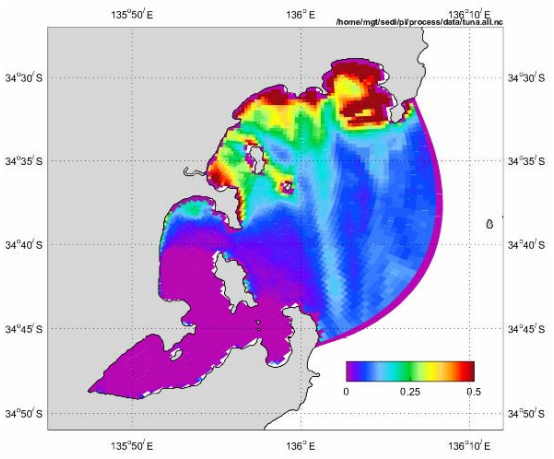

Figure 4.6. Probability of apparent roughness due to waves exceeding physical roughness during the simulation period.

4.3.3. Sediment dynamics

The probability of sediment resuspension was calculated on an hourly basis as the number of times the bottom friction exceeded a critical level for resuspension normalised by the total number of simulated hours. For instance, the probability of 0.5 would indicate that the bottom friction exceeded the critical level for about half the time of the simulation period. Large variability in the sediment characteristics implies critical friction of resuspension varying in space and time. To account for this variability, the resuspension maps have been developed for two values of the critical friction of resuspension. The first critical value of 0.014 m s^{-1} corresponds to cohesive sediments, which have consolidated over a few days. Another critical value of 0.005 m s^{-1} represents fresh sediment deposits or microflocs, which in a low energy environment tend to settle on the seabed but do not create a cohesive network and could easily be resuspended by waves and currents (Maa et al., 1998; Ganaoui et al., 2004).

As illustrated in Figure 4.7, the probability of resuspension of fine unconsolidated sediments tends to exceed 0.5 near the open sea boundary and in shallow areas along the coastline of Louth Bay. In the middle section of the model domain, eastward from Rabbit Island, these sediments are resuspended about 30 % of the time. The lowest probability of resuspension is predicted around Boston Island and in Proper Bay.

The largest probability of resuspension of consolidated fine sediments for the modelled period tends to be lower then 0.2, and is predicted for north-east of Cape Donnington, and around Point Bolingbroke (Figure 4.7b). The probability of resuspension is close to zero in the sheltered areas of Boston Bay and Proper Bay, and in the middle section of the study area, eastward from Rabbit Island.

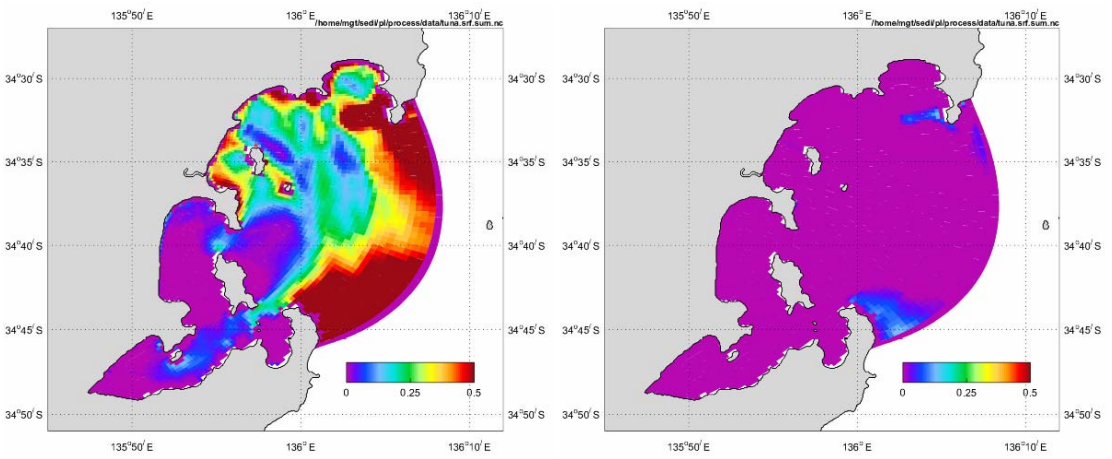

Figure 4.7. Simulated probability of resuspension for (a) fine unconsolidated sediments (critical friction velocity 0.005 m s^{-1}) and (b) fine consolidated sediments (critical friction velocity 0.014 m s^{-1}).

Figure 4.8 shows the estimated probability of suspended sediment concentrations exceeding 1 mg L^{-1}, and the distribution of fine sediment deposits after the one-year simulation. The highest probability for the sediment concentration to exceed 1 mg L^{-1} is predicted along the coastline (Figure 4.8a). The probability in the middle area of the model domain (east from the Rabbit Island) is lower than 0.05. The predicted distribution of fines in bottom sediments (Figure 4.8b), suggests accumulation in sheltered embayments behind Boston Island, along the coastline of Louth Bay, and in Peake Bay. Sediments are eroded from the north-east of Cape Donnington, and from the vicinity of Point Bolingbroke. The model also predicts erosion of the seabed around Rabbit Island and behind Louth Island. The predicted accumulation of fine sediments north and north-west from Cape Donnington is consistent with observations (chapter 3). However the model does not predict enhanced resuspension of fines south from Rabbit Island, as shown by Fernandes et al. (2006, see also chapter 3). The discrepancies between the model and observations are attributed to uncertainties in input data, which were used to initialise and calibrate the model.

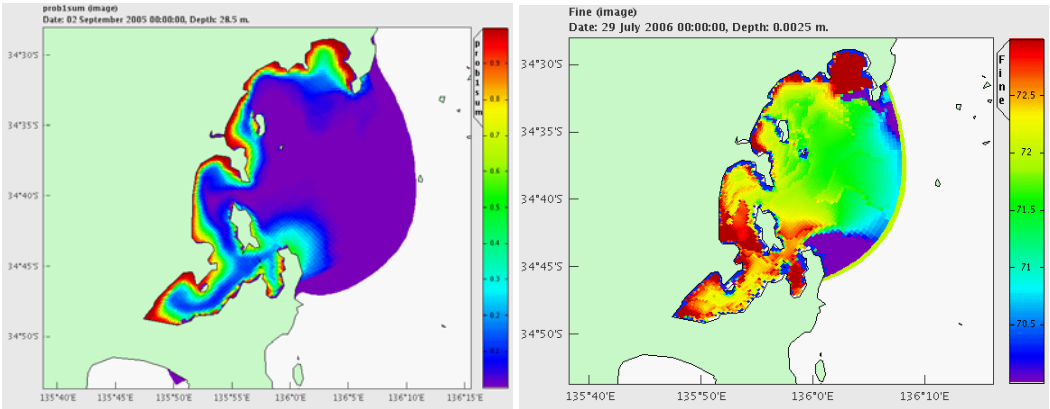

Figure 4.8. Simulated (a) probability of TSS exceeding 1 mg L^{-1} and (b) distribution of fine sediment deposits at the surface of the benthic layer (concentrations are given in kg m^{-3}; initial concentration was 72 kg m^{-3}).

4.4. Discussion

Simulation of sediment transport in the Port Lincoln region undertaken in this study involved a number of simplifying assumptions. In particular, we assumed that the bottom physical roughness associated with the near bottom features and the median grain size of sediments –

two key parameters influencing bottom friction estimates - are evenly distributed throughout the modelling domain. The data available on the sediment grain size distribution and seagrass cover in the region suggests that the physical roughness of the seabed is likely to vary over the study area. However, since the available data cover only part of the model domain, representative values of bottom roughness and sediment grain size were used during the simulation. A comparison of Figure 4.7a with the measured grain size distribution (Figure 3.5), for example, suggests that to a large extent, the areas predicted to have a high probability of resuspension for fine sediments are in fact dominated by coarse sediments. Similarly, many of the areas of high TSS (Figure 4.8a) are actually dominated by seagrasses (Figure 4.9), so may have lower TSS than predicted as seagrasses reduce sediment resuspension.

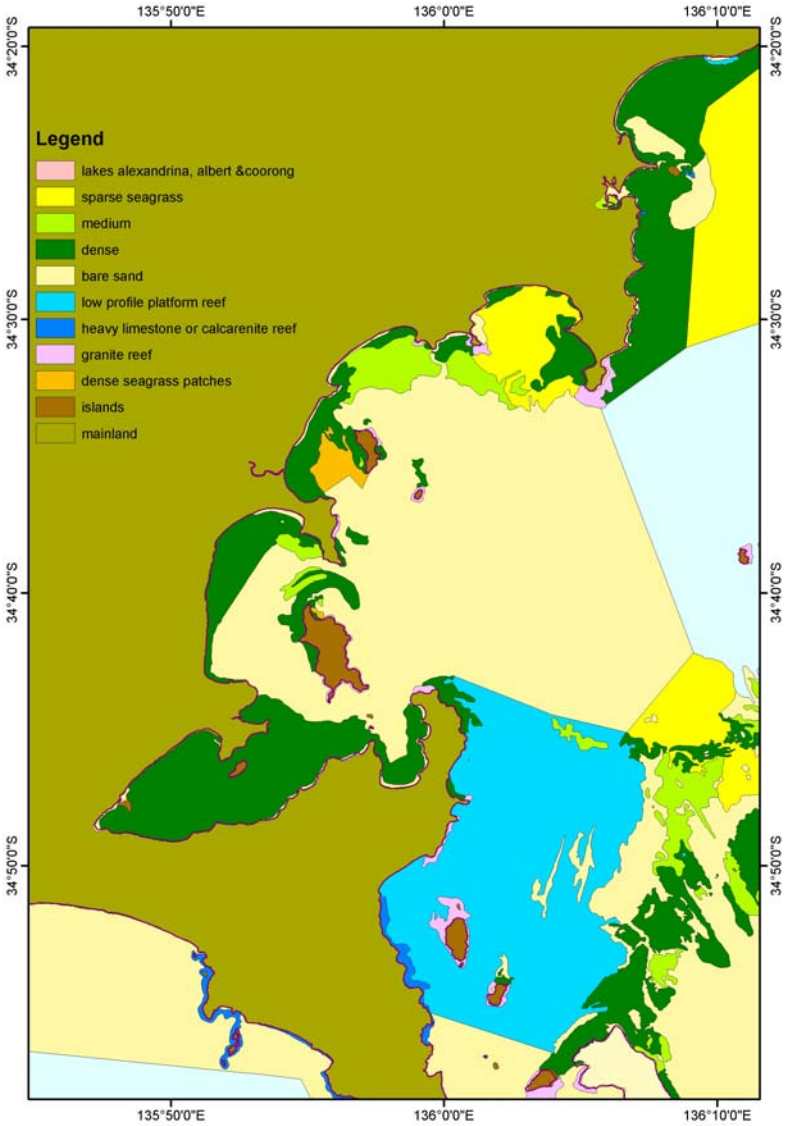

Figure 4.9. Map of the Port Lincoln region showing seagrass distribution (after Edyvane 1999).

Another important simplification was the assumption of constant critical friction of erosion. To assess the impact of these simplified assumptions on the modelled friction and sediment concentrations, a number of test scenarios with altered model parameters have been simulated. Most of the test simulations were limited to a few weeks of September 2005, and

included a period of moderately elevated waves, when the wave height reached 0.95 m near the sea boundary. The results are shown for site R24, which was considered representative of the SBT farming zone.

As illustrated in Figure 4.10, the probability of resuspension of fine cohesive consolidated sediments, under a scenario with ripple height increased from 1 to 3 cm (the bottom roughnes increased from 0.00033 to 0.0033 m) and a scenario having the grain size increased from 0.2 mm to 1 mm, remains low over the greater part of the model domain. The predicted distributions of the erosion zones resemble that simulated under the baseline scenario (compare Figure 4.10 and Figure 4.7b).

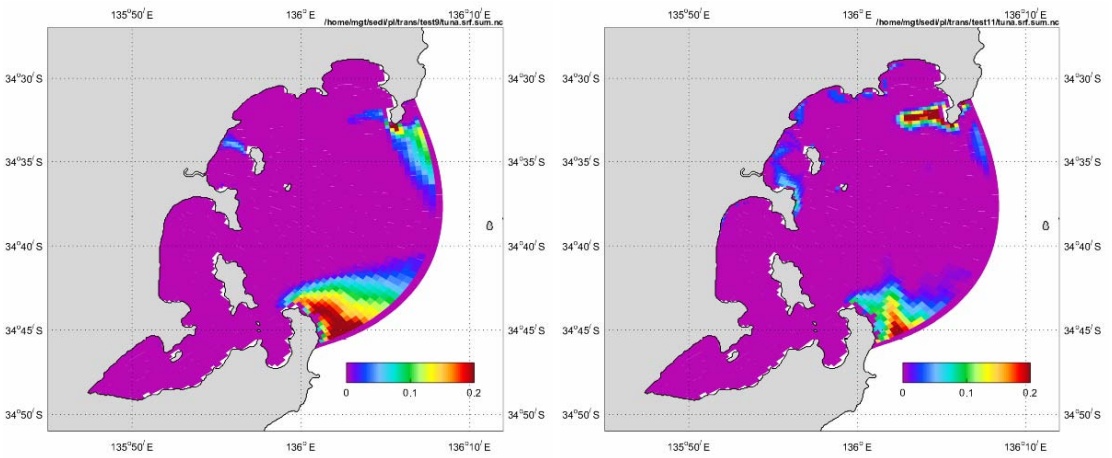

Figure 4.10 Simulated probability of resuspension of consolidated sediments for scenarios having (a) physical roughnes due to ripples increased from the baseline of 0.00033 m to 0.0033 m (b) the sediment grain size increased from the baseline of 0.2 mm to 1 mm.

Increasing the physical roughness by an order of magnitude (from 0.00033 to 0.0033 m), increased the peak values of TSS at site R24 by a factor of ~3 (Figure 4.11), while increasing the grain size from 0.2 mm to 1 mm, had a minor impact on the suspended sediment levels (results not shown). Reducing the critical friction of resuspension from 0.014 to 0.010 m s^{-1} resulted in a higher concentration of suspended sediments at site R24 (Figure 4.12), attributed to the enhanced resuspension of fines in shallow areas followed by the subsequent advection of particles to deeper waters.

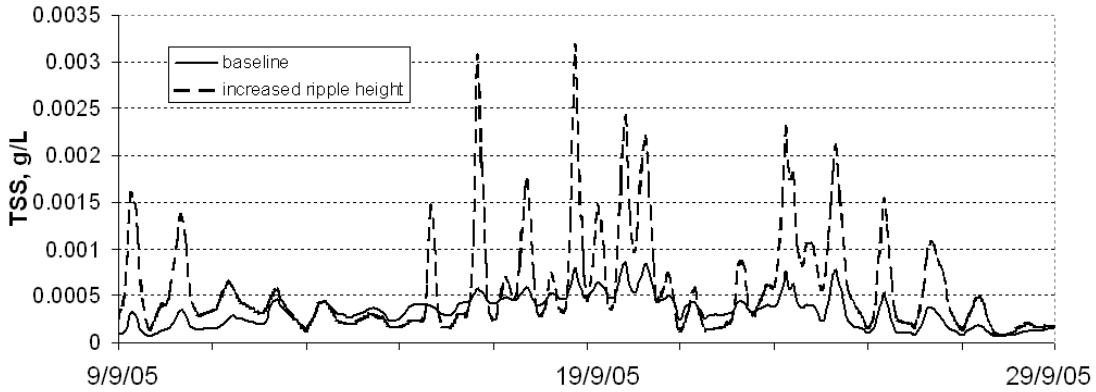

Figure 4.11. TSS at site R24 under the baseline scenario and a scenario with increased ripple height (from 1 to 3 cm).

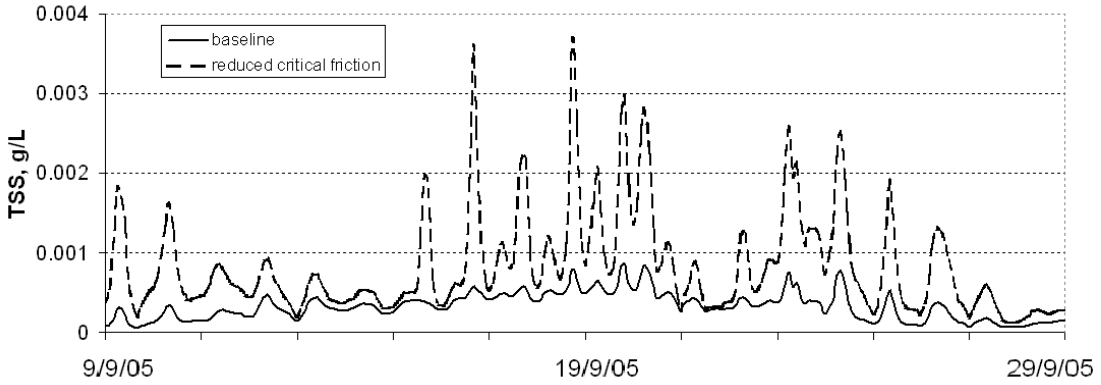

Figure 4.12. Simulated TSS at site R24 under the baseline scenario and a scenario with the reduced critical resuspension friction (from 0.014 to 0.010 m s^{-1})

The study area is characterised by relatively low energy waves and currents, due to the sheltering effect of the coastline and islands in Spencer Gulf (chapter 2). For the simulation period, the significant wave height in the study area predicted by the wave model never exceeded 1.2 m. However, although not observed in this study, extremely high waves could develop in the region during rare weather events, particularly those accompanied by persistent north easterly winds, resulting in large fetch distances for the incident waves (e.g. the April 1996 event). To assess the impact of increased wave energy on the suspended sediment levels at site R24, a numerical experiment has been carried out with the wave height doubled.

Figure 4.13 shows the model response to varying wave height. Increasing the wave height by a factor of 2 resulted in about a 3-fold increase in the maximum levels of suspended solids, with elevated levels maintained for up to 10 days. The model response to varying waves is highly nonlinear. Reducing the wave height to zero had only a minor impact on the sediment concentrations at site R24 (results not shown).

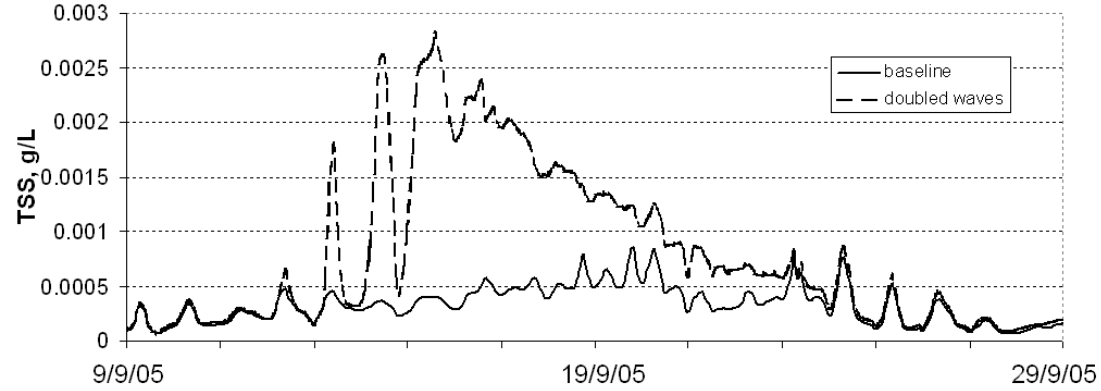

Figure 4.13. Simulated TSS at site R24 under the baseline scenario and a scenario with doubled wave height.

Despite significant uncertainties associated with the sediment model predictions, the modelling results enable us to generate plausible hypotheses pertaining to fine sediment dynamics in the study area. In a low energy environment such as the Port Lincoln region, fine sediments accumulating on the seabed are likely to develop a cohesive consolidating

network, having resistance to resuspension greatly exceeding the resistance of individual particles. Field studies show the existence of extensive areas, in particular northward from Cape Donnington, with a high content of fines (silt and fine sands make up more than half of the sediments close to Cape Donnington (Fernandes et al., 2006)). The shear stresses predicted by the model suggest that cohesive consolidated sediments are likely to be undisturbed over most of the modelling domain unless an exceptionally large storm event happens. For the simulation period, comprising one year, only fresh sediment deposits and microflocs, which do not create a cohesive network in the sediments, were regularly resuspended and mobilised into the water column. These fine particles are likely to make up the low levels of the suspended sediment concentrations typically observed throughout the year in the Port Lincoln region. The bulk mass of the cohesive consolidating sediments remains undisturbed over the years until a major storm event breaks the cohesiveness and releases vast amount of fines into the water column. This scenario may have occurred in April 1996, when persistent north-easterly winds generated large waves due to an exceptionally long fetch, causing extremely high turbidity levels in the region. To quantify the risk of extremely high suspended sediment concentrations, numerical experiments with the sediment resuspension driven by persistent north-easterly winds are needed.

4.5. Conclusions

A 3-D fine resolution model of fine sediment transport in the Port Lincoln region has been developed. The model is driven by simulated waves and currents, and predicts bottom friction and suspended sediment concentrations. The model was calibrated against monthly monitoring data and applied to the study area to simulate transport of fine sediments over a one year period (September 2005 – August 2006).

The analysis of the predicted bottom friction maps suggests regular resuspension of fine sediment fractions, having low critical shear velocity of resuspension (0.005 m s^{-1}) typical of fresh sediment deposits or fluff layer sediments. These fine particles do not create cohesive networks in sediments and can be easily resuspended by waves and currents. The lowest probability of resuspension is predicted around Boston Island and in Proper Bay. Eastward from Rabbit Island, in the middle section of the modelling domain, the simulated sediments are resuspended about 30 % of the time. The probability of resuspension of the bulk mass of cohesive consolidated sediments having higher critical shear velocity of resuspension (0.014 m s^{-1}) does not exceed 20 %, and erosion zones for these sediments are limited to a few isolated areas north-east from Cape Donnington and around Point Bolingbroke.

The sediment transport model predicts accumulation of fines in sheltered coastal embayments and north-west from Cape Donnington, consistent with the field measurements. The model does not reproduce winnowing of fines south from Rabbit Island. Sensitivity tests with varying model parameters suggest that uncertainties in the sea-bed roughness and critical shear stress distribution translate into uncertainty of the predicted suspended sediment concentrations scaled by a factor of 3 Numerical experiments with doubled wave height predict elevated levels of TSS in the SBT farming zone for up to 10 days.

Based on these findings we conclude that while the deeper, exposed to open sea, waters east of Boston Island have better flushing characteristics compared to the sheltered coastal embayments, the energy of the prevailing waves and currents over the greater part of this region is not sufficient to resuspend and disperse consolidated sediments. When waves and currents are sufficiently strong to break the cohesive network of sediments, these sediments can provide an abundant source of fines suspended into the water column. Given large

amount of fine sediment deposits in the Port Lincoln region, the risk of extremely high turbidity levels is acute if another extreme weather event, such as that in April 1996, was to occur. To quantify this risk, numerical experiments on sediment resuspension during persistent north-easterly winds (which have the potential to bring extremely energetic waves into the region) are needed.

4.6. References

Ariathurai, R., Krone, R. B., 1976. Finite element model for cohesive sediment transport. J. Hydraul. Div. ASCE, 104, HY2, pp. 323-328.

Berg, P., Rysgaard, S., Funch, P., Sejr, M., 2001. Effects of bioturbation on solutes and solids in marine sediments. Aquatic Microbial Ecology, vol. 26, pp. 81-94.

Clarke, S.M., 1996. Tuna mortalities: April-May 1996. South Australian Research and Development Institute, Adelaide 20pp.

Condie, S., Sherwood C., 2006. Sediment distribution and transport across the continental shelf and slope under idealized wind forcing. Progress in Oceanography, 70, pp. 255-270.

Edyvane, K. S., 1999. Conserving marine Biodiversity in South Australia. Part 2 - Identification of areas of high conservation value in South Australia. SARDI Aquatic Sciences, Adelaide.

Fernandes, M., Cheshire, A. and Doonan, A. (2006). Sediment geochemistry in lower Spencer Gulf, South Australia: implications for southern bluefin tuna farming. Australian Journal of Earth Sciences, 53, pp. 421-432.

Ganaoui, O., Schaaff, E., Boyer, P., Amielh, M., Anselmet, F., Grenz, C. 2004 The deposition and erosion of cohesive sediments determined by multi-class model. Estuarine, Coastal and Shelf Sciences, 60, pp. 457-475.

Graf G., Rosenberg R. (1997) Bioresuspension and biodeposition: a review. Journal of Marine Systems, 11, pp. 269-278

Grant, D., Madsen, O., 1982. Movable bed roughness in unsteady oscillatory flow. Journal of Geophysical Research, V. 87, N C1, pp. 469-481.

Grant, D., Madsen, O., 1986. The continental shelf bottom boundary layer. Annual Review of Fluid Mechanics, 18, pp. 265-305.

Grzechnik M.P. (2000) Three dimensional tide and surge modelling and layered particle tracking techniques applied to southern australian coastal seas. PhD Thesis, the University of Adelaide, 207 pp.

Herzfeld, M., 2006. An alternative coordinate system for solving finite difference ocean models. Ocean Modelling, 14, pp. 174-196.

Herzfeld, M., Middleton, J.F., Andrewartha, J.R., Luick, J. and Wu, L. (2008) Numerical Hydrodynamic Modelling of the tuna farming zone, Spencer Gulf. Technical report, Aquafin CRC Project 4.6, FRDC Project 2005/059. Aquafin CRC, Fisheries Research & Development Corporation and South Australian Research & Development Institute (Aquatic Sciences), Adelaide. SARDI Publication No F2008/000745-1, SARDI Research Report Series No 342, 100 pp.

Maa, J., Sanford, L., Halka, J. 1998 Sediment resuspension characteristics in Baltimore Harbour, Maryland. Marine Geology, 146, pp. 137-145.

Madsen, O.S., 1994. Spectral wave-current bottom boundary layer flows, in Coastal Engineering 1994 Proceedings, 24th International Conference Coastal Engineering Research Council/ASCE, pp. 384-398.

Margvelashvili N., Saint-Cast F., Condie S. (2008) Numerical modelling of the suspended sediment transport in Torres Strait. Continental Shelf Research. In press.

Mitchener, H., Torfs, H., 1996. Erosion of mud sand mixtures. Coastal engineering, 29, pp. 1-25.

Noye J., 1997. Great Australian Bight surge and suspended particle transport in Boston Bay during the tuna mortalities April 1996. April 1997. Prepared for the Tuna Boat Owners Association of Australia. Adelaide University.

Porter-Smith, R., Harris, P.T., Andersen O.B., Coleman, R., Greenslade D., Jenkins C.J., 2004. Classification of the Australian continental shelf based on predicted seabed threshold exceedance from tidal currents and swell waves. Marine Geology, 211, pp. 1-20.

Van Leussen W. 1998. The variability of settling velocities of suspended fine-grained sediment in the Ems estuary. Journal of Sea Research, 41, pp. 109-118.

Van Rijn L., 1993. Principles of sediment transport in rivers, estuaries and coastal seas. Amsterdam: Aqua Publications.

Chapter 5: Nutrients

Peter Thompson[1,4*], Milena Fernandes[2,4], Jason Tanner[2,4], John Volkman[1,4], Karen Wild-Allen[1,4], Emlyn Jones[3,4], Paul van Ruth[2,4]

[1]CSIRO Division of Marine and Atmospheric Research, GPO Box 1538, Hobart, Tas, 7001
[2] SARDI Aquatic Sciences, PO Box 120, Henley Beach SA 5022
[3]Flinders University of South Australia, GPO Box 2100, Adelaide SA 5001
[4]Aquafin CRC

*corresponding author. Phone +61 (3) 6232 5222, E-mail: peter.a.thompson@csiro.au

Abstract

In this chapter we look at the various sources of, and background levels of, nutrients into the tuna farming zone (TFZ), as well as the broader model domain. Monthly sampling for water column nutrients was conducted along a transect through the TFZ, with some sampling across the mouth of Spencer Gulf. In addition, nutrient data collected by the SA EPA from a range of inshore sites were examined, along with remotely sensed data on chlorophyll from a broader region around the farming zone. There were no differences in nutrient concentrations between surface and bottom samples, and few spatial differences within the farming zone. There was substantial temporal variability, however, and as a consequence of this, different nutrients became limiting at different times of year. Nitrogen tended to be limiting through most of the farming season (February- August), while silica was limiting in December and phosphorus in September. These patterns suggest a regular injection of dissolved inorganic nitrogen into the area in autumn, probably from offshore waters as the scale of this phenomenon is too large to be due to anthropogenic activities. However, tuna farming is likely to provide an important augmentation to this natural nitrogen source. The inshore data from the EPA showed that nutrient levels were relatively low in Boston Bay when compared to other inshore sites in Spencer Gulf and on the west coast of SA. The remotely sensed data showed a strong and consistent peak in chlorophyll-*a* in May, with a low in December.

5.1. Introduction

Dissolved inorganic nutrients in the waters of Spencer Gulf tend to be low in concentration relative to many coastal environments around the globe at similar latitudes. A range of factors contribute to this low nutrient environment including a relatively wide continental shelf, weak currents, weak and sporadic upwelling plus low nutrient concentrations in the Great Australian Bight. For these reasons the region is largely oligotrophic and has a phytoplankton ecology more similar to more tropical areas of Australia than to other temperate areas. For example, many of the diatom genera, and the large annual bloom of *Trichodesmium* in Spencer Gulf are also typical of the Gulf of Carpentaria (Rothlisberg et al. 1994, Burford et al. 1995).

Relative to many regions around Australia, there is a paucity of pelagic measurements of the biological oceanography of Spencer Gulf and the nearby shelf waters. Previous studies have indicated nutrient concentrations in the area varied between <0.4 and 8.0 μM for nitrate, <0.4 and 8.9 μM for ammonia, and <0.2 and 0.9 μM for filterable reactive phosphorus (Clarke et al., 1999, 2000). Long term EPA data, however, suggests concentrations may generally be toward the lower end of these ranges (as indicated in results below). Measurements of offshore nutrient concentrations and other oceanographic conditions such as temperature and salinity are relatively scarce. This lack of regional data makes it more difficult to put our local observations into a broader temporal and spatial perspective, and to determine the underlying dynamics of the system.

In this chapter, we examine monthly nutrient levels within the tuna farming zone (TFZ) east of Port Lincoln over a 1 year period. We also examine the limited other data available, and place the observed nutrient levels into the context of the known (and inferred) nutrient inputs to the region. It is important to understand temporal fluctuations in nutrient levels within the farming zone and its surrounds as nutrients are a major driver of phytoplankton dynamics, and phytoplankton blooms have the potential to have a major detrimental effect on the tuna farming industry. By understanding the major sources of nutrients, we can also begin to assess what impacts human activities, including tuna farming itself, are having on the pelagic ecosystem of the region, and how these effects relate to natural fluctuations in the system.

5.2. Materials and Methods

5.2.1. Sampling

Monthly sampling of nutrients was undertaken at a series of sites in and around the TFZ that were selected from the grid of sites (Figure 5.1) sampled in 2005 as a part of FRDC 2001/104 – the Regional Environmental Sustainability project (Bierman et al. 2007). Previously, this grid had been sampled twice, mostly for water column properties. It was hypothesized that considerable temporal variability in water column properties would be present on shorter time scales, so for the purpose of understanding nutrient and phytoplankton dynamics we sampled monthly. It was further hypothesized that a significant fraction of the spatial variability in nutrient levels, and phytoplankton abundance and species composition, in this region would be associated with an onshore-offshore gradient, so the sampling regime was designed to allow for this variability to be quantified. It was also considered that exchange with inner Boston Bay may have an influence on the water column, so one site at the southern entrance to the Bay (#39) was positioned to assess this.

Sampling of nutrients commenced on August 30th 2005 and continued ~ monthly until 14th September 2006. A range of sites (22, 24, 25, 26, 44, 43, 39, all located on the above-mentioned grid, as well as M1, M2, M3, M4, M5, which are the mooring sites at which instrumentation was deployed for extended periods) and two depths (surface and ~ 1 m above bottom) were sampled (Figure 5.1), but not every site was sampled on every occasion. Monthly samples along the main transect were taken from the RV Breakwater Bay, while some of the mooring sites were sampled from the RV Ngerin. Using latex gloves, surface water samples were collected into a designated water bucket and 1 m above-bottom samples were collected using a water sampler on a measured line. The collected sample was then put into a plastic beaker, which was rinsed with the sample 3 times before filling. A small portion of the sample was then used to rinse a 20 ml syringe 3 times; the sample was also rinsed 3 times through a 0.45 µm filter and into a 50 ml sample bottle and cap. Fifty millilitres of filtrate was then collected into the bottle, immediately placed on ice, and frozen as soon as possible. The sample was then sent frozen to the Monash University Water Studies Centre and analysed for silicate (SiO_2), total nitrogen (TN), total phosphorus (TP), ammonium + ammonia (reported here as NH_4^+), phosphate (PO_4^{3-}), nitrite (NO_2^-) and nitrate (NO_3^-).

Statistical analysis for each nutrient was by 3-way ANOVA followed by Bonferroni t-tests for individual differences relative to controls: January, surface and site 22. Where possible, data from the mooring sites are included in the analyses presented here, but in some cases were excluded due to the need to have balanced observations for some of the more complex statistical analyses.

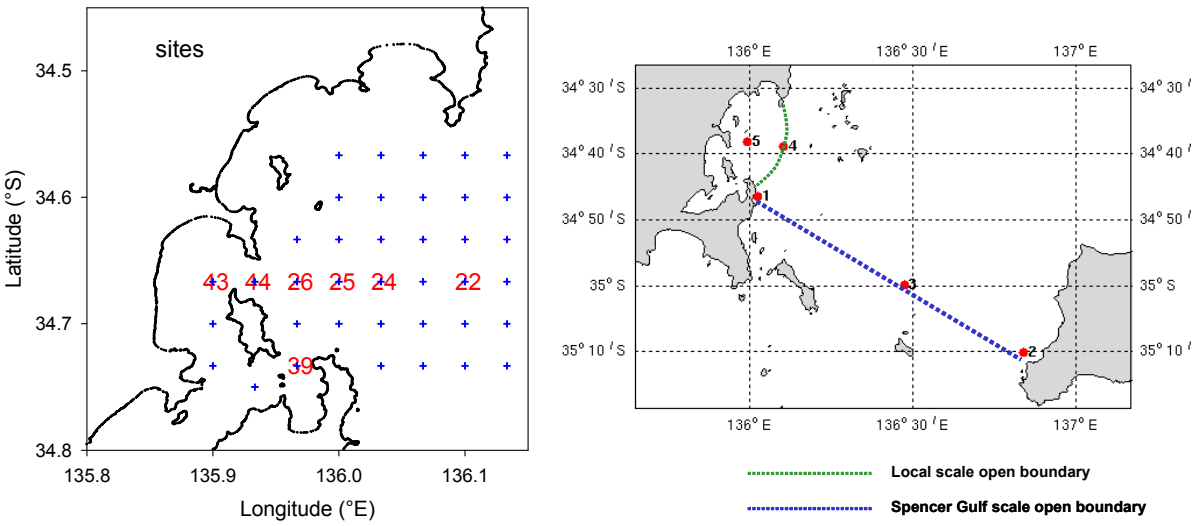

Figure 5.1. Left panel is a map of sites sampled previously by SARDI (+) and sites sampled from August or October 2005 to September 2006 for phytoplankton and water column characteristics. In this report this area is referred to as the TFZ. Right panel shows the locations of moorings deployed in Spencer Gulf – these sites are referred to as M1-M5.

5.2.2. Chemical Analysis

Phosphate (PO_4^{3-})

Flow injection analysis (FIA) was used to determine soluble-reactive phosphorus in a QuickChem 8000 Automated Ion Analyser (method 4500-P G pg 4-149, APHA-AWWA-WPCF 1998). The sample was mixed with ammonium molybdate and antimony potassium tartrate to form phosphomolybdic acid, which is reduced by the addition of ascorbic acid to

form a blue complex, the intensity of the colour being proportional to the concentration of the soluble-reactive phosphorus. The absorbance was measured at 880 nm.

Nitrite (NO_2^-) & Nitrate (NO_3^-) (NO_3^-+NO_2^- = NO_x)

Nitrite/nitrate nitrogen was determined using FIA in a QuickChem 8000 Automated Ion Analyser (method 4500-NO_3-I, pg 4-121, APHA-AWWA-WPCF 1998). The sample is mixed with an acidic sulphanilamide and a diazo compound is formed, which is then mixed with N-(1-naphtyl)-ethylene diamine dihydrochloride to form a purple azo dye, the intensity of which is proportional to the nitrite concentration. The absorbance was measured at 520 nm. To measure nitrate, the sample is passed through a column containing copper-coated cadmium granules. Nitrate in the sample is reduced to nitrite in the presence of cadmium and, then total nitrite is measured as above. Nitrate is then calculated via subtraction.

Ammonium (NH_4^+)

The automated phenate method of analysis was used to determine ammonium levels, except FIA was used rather than an autoanalyser, in a QuickChem 8000 Automated Ion Analyser (method 4500-NH_3 I, pg 4-111, APHA-AWWA-WPCF 1998). Ammonia in the sample reacts with hypochlorite to form monochloramine which, in the presence of phenol, nitroprusside and excess hypochlorite, gives indophenol blue. This results in the formation of indophenol blue, which is proportional to the concentration of ammonia, and can be measured spectrophotometrically at 630 nm.

Silicate (SiO_2)

In the method, β-molybdosilicic acid is formed by reaction of the silicate contained in the sample with molybdate in acidic solution. The β-molybdosilicic acid is then reduced by ascorbic acid to form molybdenum blue. The absorbance of the molybdenum blue, measured at 660 nm, is linearly proportional to the concentration of silicate in the sample. The automated method was first reported by Armstrong (1951), updated and adapted for automation by Armstrong et al. (1967) and Atlas et al. (1971) and undertaken on a FIA in a QuickChem 8000 Automated Ion Analyser rather than an autoanalyser (method 4500-Si-F, APHA-AWWA-WPCF 1998).

5.3. Results and Discussion

5.3.1. Spatial and Temporal Nutrient Dynamics in the TFZ

There were no differences in any nutrient between the depths sampled in the TFZ, and nitrate was the only one that showed any detectable spatial variation (Table 5.1). Differences between months were detectable for most nutrients, however (Table 5.1, Figure 5.2).

Nitrite

Only 4 of 267 measurements of NO_2^- were above detection limits and the estimated mean value for NO_2^-, which is based only on the values above the detection limit, is therefore too high. Fortunately, NO_2^- was a small component (<5%) of dissolved inorganic N (DIN), and thus the overestimation of DIN is small, so this error has little ecological significance.

Nitrate

NO_3^- concentrations in January were significantly lower than those in August, October and November of 2005, and March and September of 2006. Nitrate concentrations at site 22 were significantly lower than those at site 26.

Table 5.1. A summary of the statistical analyses of nutrient data from the TFZ (see map, Figure 5.1). Statistical analysis was by 3 way ANOVA followed by Bonferroni t-tests for individual differences relative to controls: January, surface and site 22.

Nutrient	Average concentration	temporal variation (month)	spatial variability	
	μM	Probability of a significant difference between January and other months (listed if significantly different)	**Horizontal** (site) Probability of a significant difference between site 22 and other sites	**Vertical** (surface vs. bottom) Probability of a significant difference between surface and bottom
NO_3^-	0.45	P < 0.001; March, Aug, Oct, Nov.	P = 0.029	P = 0.34
NO_2	0.036	NA	NA	NA
NH_4^+	0.39	P < 0.001; April	P = 0.28	P = 0.20
PO_4	0.12	P = 0.25	P = 0.47	P = 0.55
SiO_2	0.81	P = 0.001; Feb, Apr, May, June, Aug, Oct, Nov, Dec.	P = 0.12	P = 0.99

Table 5.2. Monthly mean nutrient concentrations at sites 22, 24, 25, 26, 44, 43, 39 at 2 depths for all sampling from August 2005 to September 2006.

Date	SiO_2 μM	NH_4^+ μM	PO_4^{3-} μM	NO_2^- μM	NO_3^- μM
31-August-2005	0.385	0.857	0.045	0.036	0.832
21-October-2005	0.464	0.276	0.045	0.036	0.781
16-November-2005	0.417	0.219	0.062	0.036	0.730
07-December-2005	0.148	0.403	0.526	0.036	0.112
17-January-2006	1.629	0.135	0.065	0.036	0.122
09-February-2006	2.454	0.408	0.064	0.039	0.209
15-March-2006	1.451	0.207	0.138	0.038	0.398
20-April-2006	0.272	0.508	0.081	0.036	0.159
16-May-2006	0.221	0.254	0.089	0.036	0.056
19-June-2006	0.739	0.146	0.166	0.036	0.088
18-July-2006	1.353	0.226	0.108	0.037	0.060
09-August-2006	0.464	0.393	0.101	0.031	0.059
12-September-2006	0.577	0.457	0.118	0.036	2.176
mean	***0.81***	***0.35***	***0.12***	***0.04***	***0.44***
standard deviation	0.69	0.20	0.13	0.00	0.60

Phosphate

PO_4^{3-} showed no significant variability with time (monthly) or spatially; either horizontally (site) or vertically (surface or ~ 1 m above the bottom).

Ammonium

NH_4^+ concentrations were significantly greater in April than January (Table 5.2). No significant spatial variation was detected. Overall the concentrations of NH_4^+ seem unusually high for such an oligotrophic ecosystem. This may represent a real and unusual feature of this ecosystem or a systematic error in measurement.

Silicate

SiO_2 in February was significantly greater than in January while SiO_2 concentrations in Aug, Oct, Nov and Dec of 2005, and April, May, June, Aug and Sept of 2006 (Figure 5.2) were all significantly less than January. No significant spatial variability was detected.

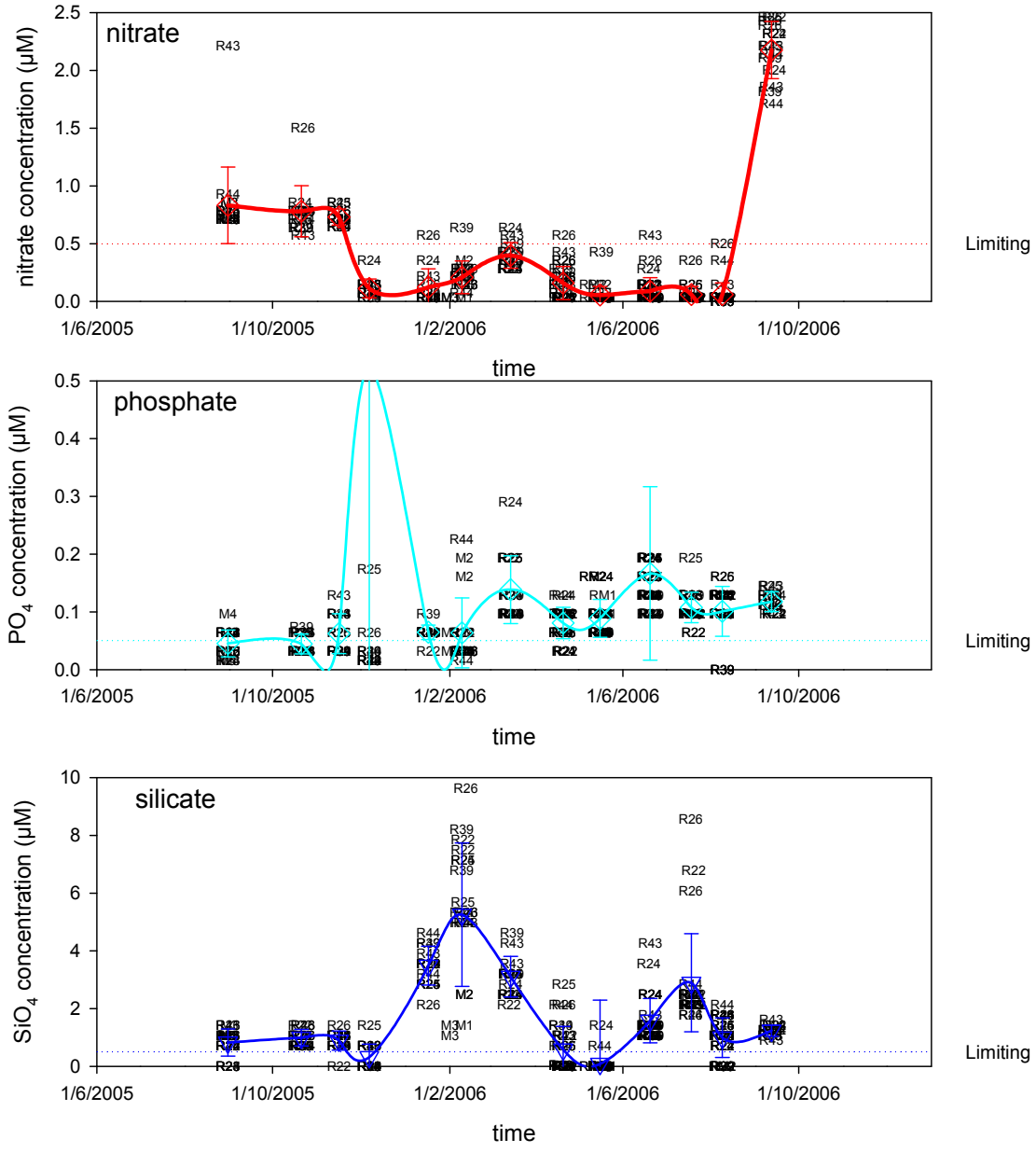

Figure 5.2. The temporal dynamics of nutrients measured at locations in the TFZ and/or further afield. Figure 5.1 indicates locations. Error bars are ± 1 standard deviation.

As the seasonal nutrient dynamics were relatively weak and spatial variation was generally not statistically significant (Table 5.1), the mean annual concentrations (Table 5.2) based on monthly means from all sites and all depths are a good representation of the average condition in the TFZ. From the available data on DIN (Table 5.2) and the estimated volume of the model domain ($9.5x10^9$ m^3, covering an arc from Cape Donnington to Point Bolingbroke and all waters inshore) the average DIN pool of the model domain would be ~ 56 tonnes of N. Using a similar approach and based on the average total nitrogen (TN) concentration of 0.11 mg N L^{-1} (n = 309), the TN pool of the model domain would average 1090 tonnes.

5.3.2. Potentially limiting nutrients

To determine which nutrient might limit phytoplankton growth it is necessary to consider both the nutrient ratios and the nutrient concentrations. For the purpose of this assessment, nutrient concentrations of < 0.5 µM SiO_2, or DIN (NO_3^-+ NO_2^-+NH_4^+), and 0.05 µM PO_4^{3-} were considered potentially limiting. Similarly, based upon Redfield ratios (Redfield 1963), N versus P limitation was judged to be possible when N:P varied from 16:1 and for Si or N when the Si:N ratio varied from 1:1. Only in situations where both criteria (low concentration + ratio outside Redfield) were present was potential nutrient limitation deemed likely (Elser et al. 1990). The results suggest that N limitation was likely from January to August (Figure 5.3). It was also likely that P became limiting in September and Si in December (Figure 5.3).

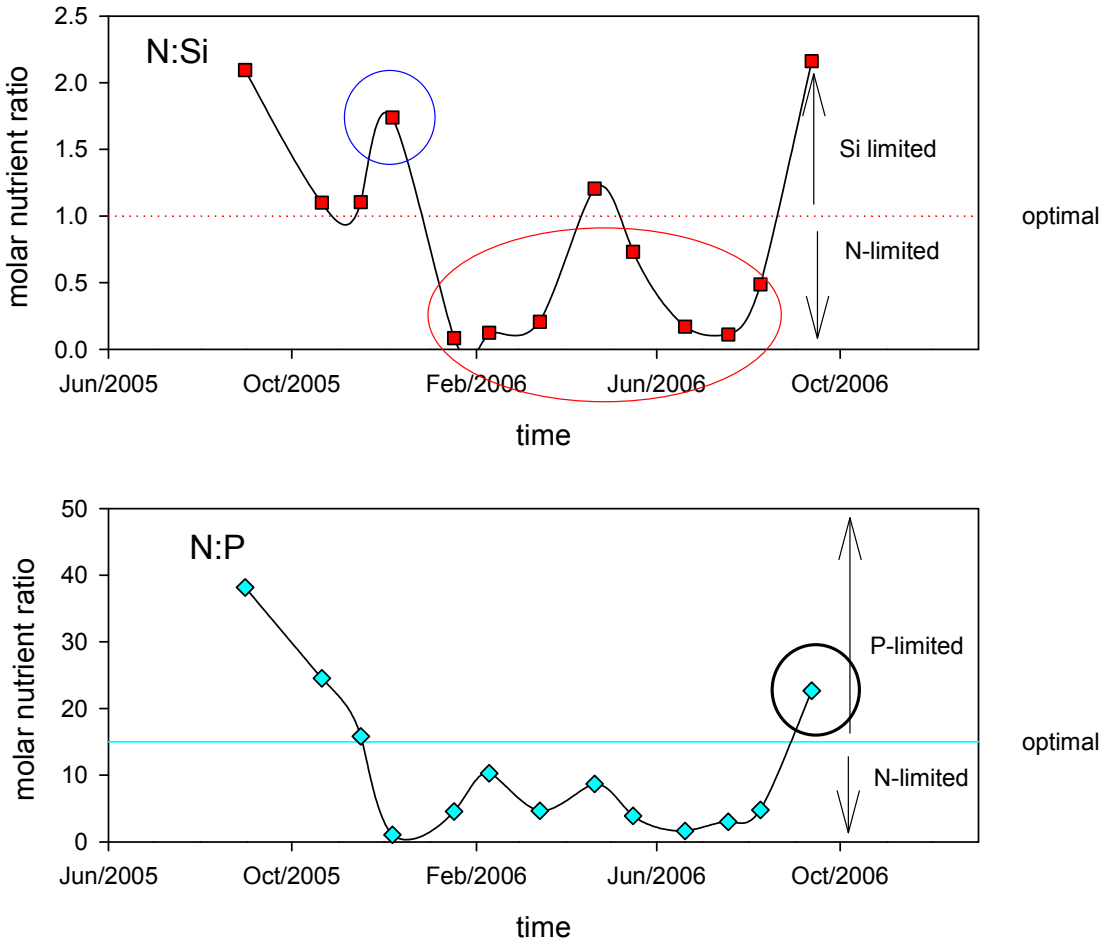

Figure 5.3. Nutrient ratios from Aquafin CRC sampling of DIN (NO_3^-, NO_2^-, NH_4^+), PO_4^{3-} and SiO_2 (see Figure 5.1 for site locations, Figure 5.2 for original data). Circles indicate dates when the combination of nutrient concentrations (Figure 5.2.) and ratios suggest potential limitation by a particular nutrient (blue = Si; red = N; black =P).

Thus, of the major phytoplankton macronutrients (C, N, P and Si), the availability of N appears to have the most potential to limit growth. Sources of N are therefore more important to the phytoplankton ecology of this region than any other nutrient, but the overall picture appears to be quite complex and variable throughout the year. Limitation of algal growth by micronutrients such as iron is highly unlikely in these nearshore, shallow waters.

5.3.3. Assessing spatial and temporal nutrient dynamics: including other data sources.

Given the rather sporadic nature of the nutrient rises evident in the ~ 13 months of data collected for this project, several other sources of relevant data were included in the assessment of a general temporal pattern. The SA EPA data for 6 locations (North Shields, Point Boston, Boston Island, Town Jetty, Billy Lights Point and Proper Bay) in Boston Bay (http://www.epa.sa.gov.au/boston.html) were examined (Gaylard, in prep). Sampling was ~ bimonthly. Unfortunately the majority of observations had concentrations below their detection limit, and in spite of a large number of observations from a range of locations, the useful data were a small subset of the possible data. Still for NO_3^- and NH_4^+ it was possible to add some more observations of elevated concentrations (Figure 5.4, assuming on the basis of the results above that all oxidised N is nitrate). Both NO_3^- and NH_4^+ concentrations were somewhat elevated within Boston Bay as compared to the TFZ, probably due to the shallower waters and enclosed nature of the bay.

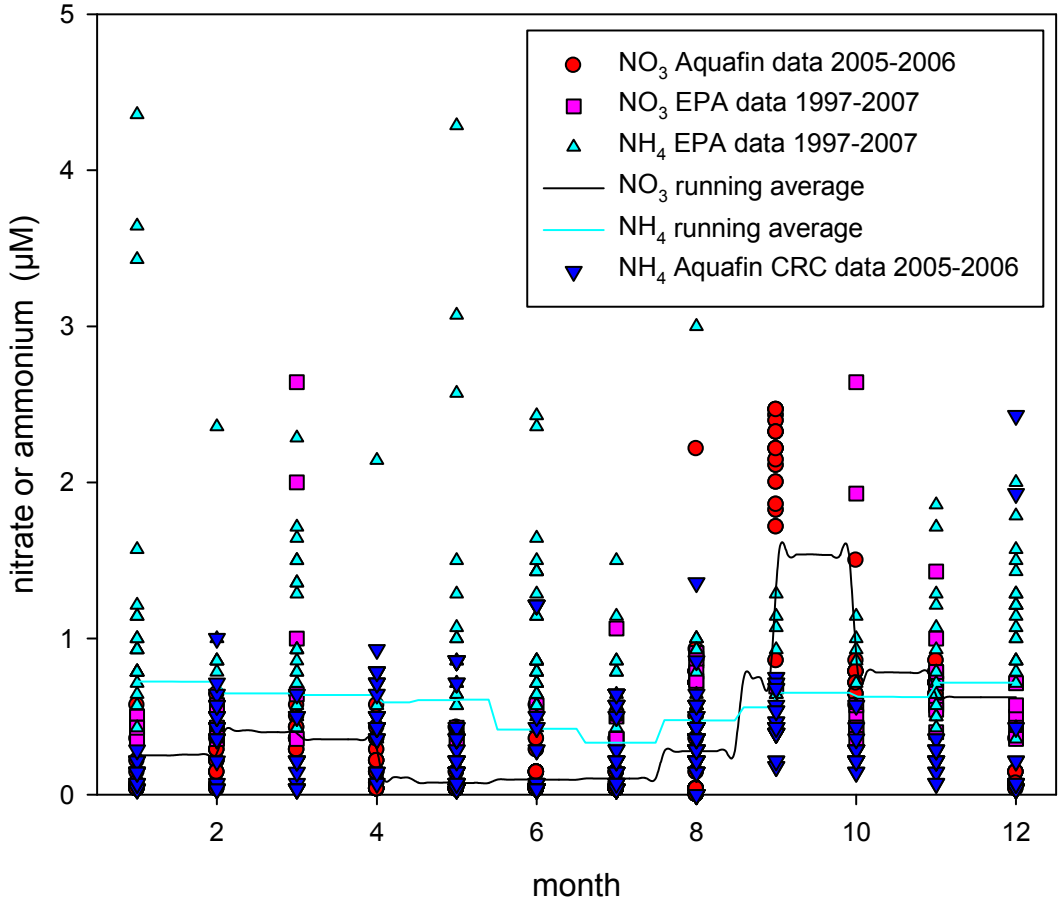

Figure 5.4. Nitrate and ammonium concentrations from this project (detailed above) and SA EPA sampling (details at http://www.epa.sa.gov.au/nrm_map.html). Solid lines are running means.

The combined Aquafin and EPA data sets were analysed for seasonal patterns by fitting a running mean to data binned by month. The Sigmaplot™ running mean function used the nearest 10% of available data to smooth each point. The results support the hypothesis that seasonally elevated NO_3^- concentrations could be found in March and between September and December. Sporadic 'high' concentrations of nitrate (> 0.1 mg L^{-1} of total oxidised nitrogen) in Boston Bay (Figure 5.4) were observed during:

August 1997

October-December 1997,

August 2000,

July 2001,

November 2005, and

March 2006.

Based upon the available data these increases were not detected every year, but this may be an artefact of the bimonthly sampling, which was designed to detect long-term changes. It is

possible that the greater concentrations are short lived or very localised, both factors which would make them difficult to detect with the existing sampling strategy.

Using the SA EPA water quality data from Boston Bay, Venus Bay, Coffin Bay and Port Hughes (http://www.epa.sa.gov.au/nrm_map.html), it was possible to make some regional comparisons. Sampling was variable with from 1 to 6 sites sampled in each location. The temporal period for which data were available varied from 4 years (Coffin Bay, Venus Bay, on the Western Eyre Peninsula) to 11 (Port Hughes, Boston Bay, inside Spencer Gulf), and the total number of observations varied:

Coffin Bay	~ 4 years	3 sites	~ 114 observations
Boston Bay	~ 10 years	6 sites	~ 403 observations
Venus Bay	~ 4 years	3 sites	~ 102 observations
Port Hughes	~ 11 years	1 site	~ 116 observations

A simple statistical analysis of the pooled (combined sites within locations, all years) data sets was used. There were no significant differences between locations for concentrations of NO_x (NO_3^- + NO_2^-). Boston Bay had significantly lower concentrations of total P, NH_4^+ and lower turbidity than any of these other inshore sites (Kruskal-Wallis One Way Analysis of Variance on Ranks, $P < 0.001$, Table 5.3).

Table 5.3. Median values for water quality parameters derived from SA EPA data sets for locations near Boston Bay, Eyre Peninsula.

Location	NO_x (mg L^{-1})	Total P (mg L^{-1})	NH_4 (mg L^{-1})	Turbidity (NTU)
Coffin Bay	0.00800	0.0215	0.0200	0.686
Boston Bay	*0.00760*	*0.0180*	*0.0120*	*0.357*
Venus Bay	0.00750	0.0190	0.0200	0.431
Port Hughes	0.00900	0.0265	0.0220	0.712

There are no indications in the SA EPA data that Boston Bay experiences greater nutrient concentrations, either natural or anthropogenic, than other similar locations in this region. Indeed, nutrient concentrations in Boston Bay tend to be lower than those measured in the other three regions.

5.3.4. Using other data including remotely sensed data to infer nutrient dynamics

Several types of related data have been successfully used to make inferences about nutrient supply. In general there is a strong relationship between DIN inputs and chlorophyll-*a* biomass in Australian coastal ecosystems including the sites from the TFZ off Port Lincoln (Figure 5.5). The corollary of this relationship is that variation in chlorophyll-*a* can be used to indicate a source or supply of DIN. Again it is possible to use the SA EPA data to compare chlorophyll-*a* concentrations for locations around the Eyre Peninsula and Spencer Gulf with those from Boston Bay. Analysis of the SA EPA data from the sites of Boston Bay, Venus Bay, Coffin Bay and Port Hughes (Table 5.4) show that Boston Bay had significantly less chlorophyll-*a* than Coffin Bay and Venus Bay (Kruskal-Wallis One Way Analysis of Variance on Ranks, $P < 0.001$), but about 0.1 μg L^{-1} more than the opposite side of Spencer Gulf (Port Hughes).

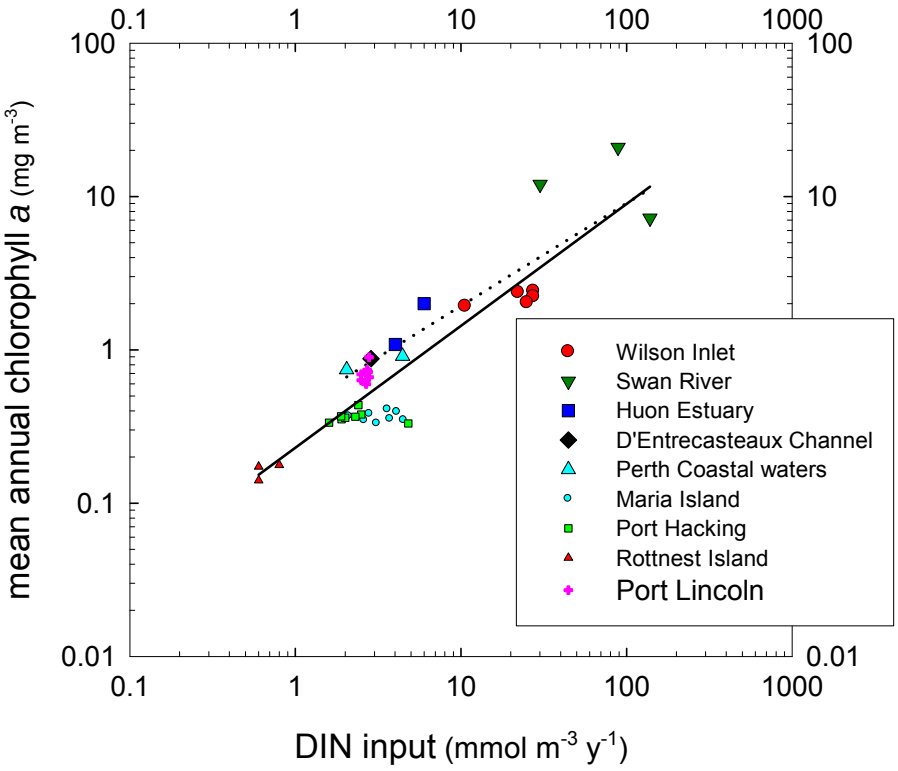

Figure 5.5. Relationships between DIN inputs (calculated as winter maximum DIN concentration minus summer minimum DIN concentration) and annual mean chlorophyll-*a* concentrations. The dotted regression line refers to water bodies where *in situ* measurements of both nutrients and chlorophyll-*a* were obtained (larger symbols), the continuous regression line is from deeper more offshore water bodies where remote sensing was used to estimate mean annual chlorophyll-*a* (smaller symbols). The closely clustered pink crosses are sites 22, 24, 25, 26, 39, 43, 44 from this study (Thompson, unpublished data).

Table 5.4. Chlorophyll-*a* concentrations (μg L^{-1}) in Spencer Gulf and around the Eyre Peninsula (median and 25th & 75th percentiles) from SA EPA over the period from 1996-2007.

Location	N	Median	25%	75%
Coffin Bay	114	1.355	0.790	2.220
Boston Bay	403	0.630	0.433	0.985
Venus Bay	102	0.800	0.560	1.900
Port Hughes	116	0.520	0.330	0.760

Locations on the western side of the Eyre Peninsula had ~ 2 times more chlorophyll-*a* than Boston Bay, possibly reflecting the more direct effects of upwelling along this coast. Boston Bay and Port Hughes varied only slightly in median chlorophyll-*a* concentration. This suggests that, if N is limiting algal biomass, then the average annual availability of DIN in Port Hughes and Boston Bay must be similar. Conversely, chapter 6 suggests that chlorophyll levels in the TFZ are around double those found on the opposite side of the gulf, although ground-truthing of this data is not yet complete.

The remotely sensed chlorophyll-*a* data from a region covering 34 to 36°S x 135 to 137°E (120 x 120 nautical miles centred on the mouth of Spencer Gulf) was obtained from NASA (using GES-DISC Interactive Online Visualization ANd aNalysis Infrastructure from NASA's Goddard Earth Sciences (GES) Data and Information Services Center (DISC), http://reason.gsfc.nasa.gov/Giovanni/). The data show a strong and consistent annual cycle in chlorophyll-*a* (Figure 5.6 and 5.7), with a peak in May and a low during December. The presence of such a consistent chlorophyll-*a* peak in May must require the increase in availability of DIN throughout this region during the preceding weeks or months.

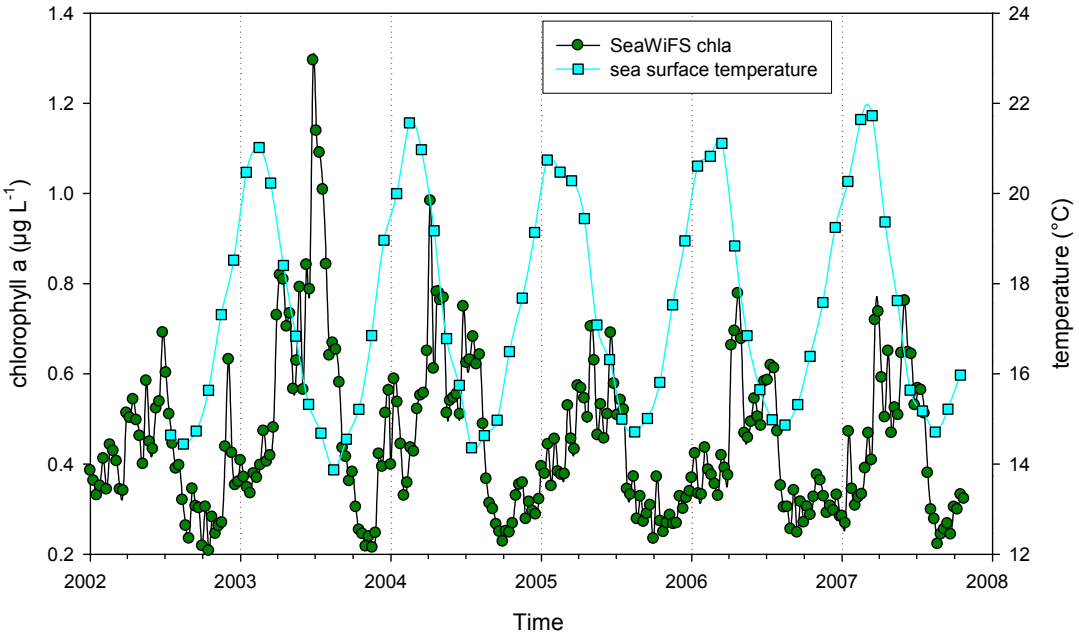

Figure 5.6. Temporal dynamics of remotely sensed chlorophyll-*a* and sea surface temperature for the region around the TFZ (34 to 36°S x 135 to 137°E -120 x 120 nautical miles) obtained from NASA (http://reason.gsfc.nasa.gov/Giovanni/).

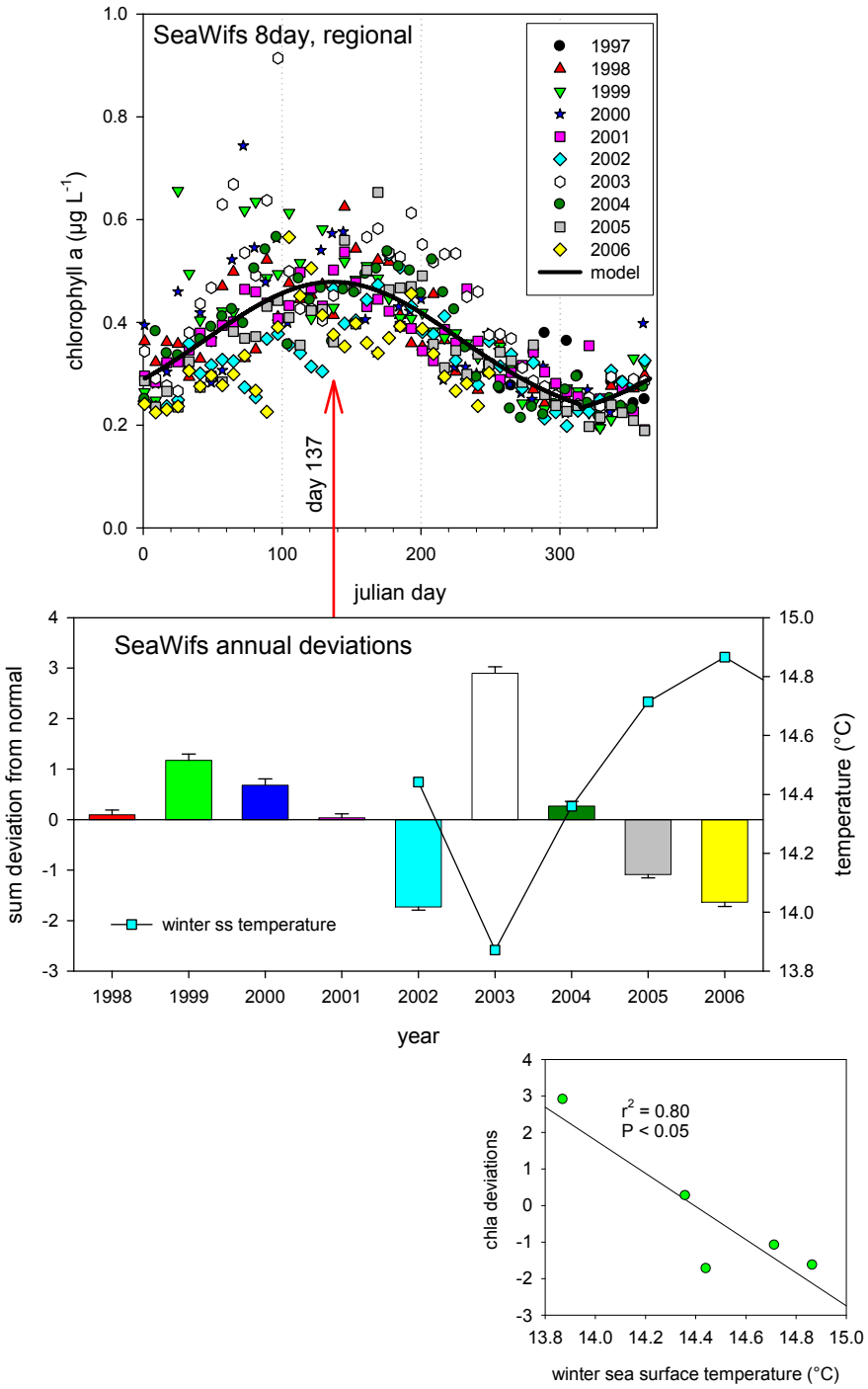

Figure 5.7. Temporal dynamics of remotely sensed chlorophyll-*a* and sea surface temperature for the region around the TFZ (34 to 36°S x 135 to 137°E -120 x 120 nautical miles), obtained from NASA (http://reason.gsfc.nasa.gov/Giovanni/). Annual anomalies in chlorophyll-*a* were summed and plotted versus year. Years with positive anomalies (e.g. 2003) had more chlorophyll-*a* than other years (e.g. 2002 & 2006). These anomalies were significantly correlated with sea surface temperature (bottom panel).

Similar to the relationship between DIN and chlorophyll-*a*, there is often a relationship between sea surface temperature and NO_3^- concentration. Off the continental shelf it is possible to exploit the strong relationship between surface temperature and nitrate concentrations (Goes et al. 1999, Kamykowski and Zentara 1986) to augment sparse data sets. Unfortunately, this approach has not been successfully transferred onto the continental

shelf or into relatively shallow coastal waters. While there are no suitable data sets in the vicinity of the Eyre Peninsula, there are a number of coastal sites in other Australian locations where extensive sea surface temperature and nitrate concentration data are available. These suggest an overall relationship between sea surface temperature and nitrate that may be generic to much of temperate Australia (Figure 5.8). It should, however, be noted that the local data from Boston Bay gave no significant relationship between nitrate and temperature. It would seem that in regions this far inshore, the coldest temperatures arise in the shallowest waters due to rapid heat loss to the atmosphere during winter, but these waters are still low in nitrate. Further offshore, the sea surface temperature signal is likely to be correlated with high nitrate at the surface, and we exploit this here to make inferences about the supply of nitrate into the gulf. We view this approach as useful, but speculative, and caution that a more thorough validation is needed before it can be used reliably.

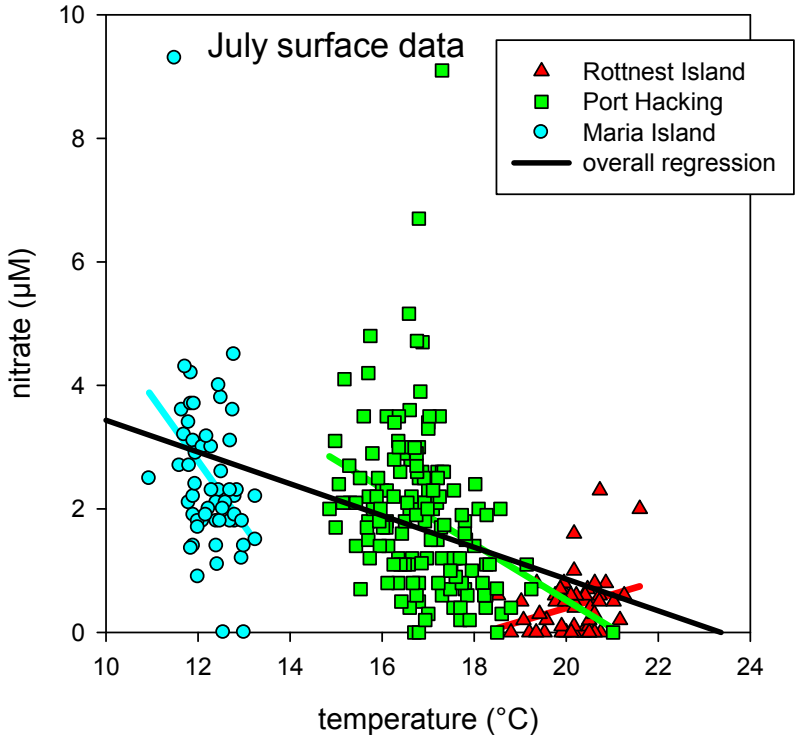

Figure 5.8. Relationships between sea surface temperature in winter and surface nitrate concentrations from the 50 m coastal sites at Rottnest Island (WA), Maria Island (Tas) and Port Hacking (NSW). Lines are linear regressions through data from specific sites or overall (black). Data are available at: http://www.marine.csiro.au/warehouse/servlet/HTMLManager.

Regional sea surface temperature shows a strong seasonal progression with annual highs occurring in January, February or March and lows in July or August (Figure 5.6), depending upon the year (2002-2007). It is evident that the increases in chlorophyll-*a* regularly occurred during the period of falling surface temperatures (Figure 5.6). This will also be a period of declining stratification. It is hypothesized that the decline in stratification is associated with increased vertical mixing resulting in more NO_3^- being injected into the euphotic zone. The rise in NO_3^- concentrations from a low in December 2005 to a high in March 2006, we suggest, was not a dramatic exchange of water from the gulf with nutrient-enriched waters from offshore, but a form of cryptic upwelling (nutrients pushed up into the euphotic zone from offshore (> 1% surface irradiance, which encompasses the entire water column in the TFZ) but not to the surface and not fully visible to satellites measuring sea surface

temperature). Based on the relatively large scale (~ 120 x 120 nautical miles) and regular (every year since 1997) seasonal fall in sea surface temperature in April and the rise in May chlorophyll-*a*, we suggest that there must be a similar autumn increase in the availability of DIN possibly as NO_3^-.

Thus we conclude that the observed autumn peaks in NO_3^- may be related to seasonal cooling and to a greater degree of vertical mixing on a relatively large scale. During April much of Spencer Gulf suddenly cools with water temperatures falling ~5°C in the TFZ (chapter 1). Salinities also fall. This combination suggests increased exchange of water between the TFZ, Spencer Gulf, and further offshore. At the mouth of Spencer Gulf during April, the deeper waters are warmer and less saline than the shallower waters in the gulf (chapter 1), creating the potential for strong convective mixing. The extent of deep mixing is not readily evident from the available data, but the May peak of diatoms suggests that vertical mixing is sufficiently deep to raise nutrient concentrations and produce a low mean irradiance - conditions known to favour the growth of diatoms.

The fact that the timing and magnitude of the autumn rise in chlorophyll-*a* is not consistent throughout the entire gulf and further offshore (chapter 6) suggests that different mechanisms may be responsible for the injection of DIN into the euphotic zone in different regions. In the TFZ, the timing of the observed autumn rise in NO_3^- is coincidental with the seasonal progression of the warm oceanographic front moving northwards (chapter 6) up Spencer Gulf. This movement and weakening of the front may contribute to the rise in DIN and the autumn phytoplankton peaks in the lower Spencer Gulf region.

Whatever the mechanism for the observed rise in NO_3^-, it is likely to be an important component of the nitrogen pool supporting the annual chlorophyll-*a* peak. The annual and regional rise in chlorophyll-*a* during May-June suggests this is a regular event occurring over a relatively wide scale. Based upon the remotely sensed data for chlorophyll-*a* and sea surface temperature, years with lower winter temperatures produce more chlorophyll-*a* in the TFZ (Figure 5.7). The strength of this correlation over a number of years provides strong evidence of the links between the phytoplankton biology of the TFZ and the regional environmental conditions.

Why no Spring bloom?

The late winter-spring (August to October) increases in NO_3^- would seem to be sporadic, possibly representing upwelling of deeper, offshore waters into the TFZ. In other temperate locations around Australia there is a rise in NO_3^- concentrations during autumn, which typically persists through winter and into spring (Thompson et al. 2008). During spring the increasing insolation and stratification combine to produce a strong seasonal increase in chlorophyll-*a* (i.e. a spring bloom). The increased concentrations of NO_3^- observed in spring 2005 did not correlate with increased concentrations of PO_4^{3-} and Si. Normally the cold, deep water from off the continental shelf would be expected to resupply all three nutrients simultaneously (Mann and Lazier 1996; van Ruth unpublished data), but the high NO_3^- concentrations during August-October 2005 had no corresponding rise in phosphate or silicate. The source of this relatively high-nitrate, low-silicate, low-phosphate waters could be the Great Australian Bight, where waters impoverished in silicate are common (Figure 5.9).

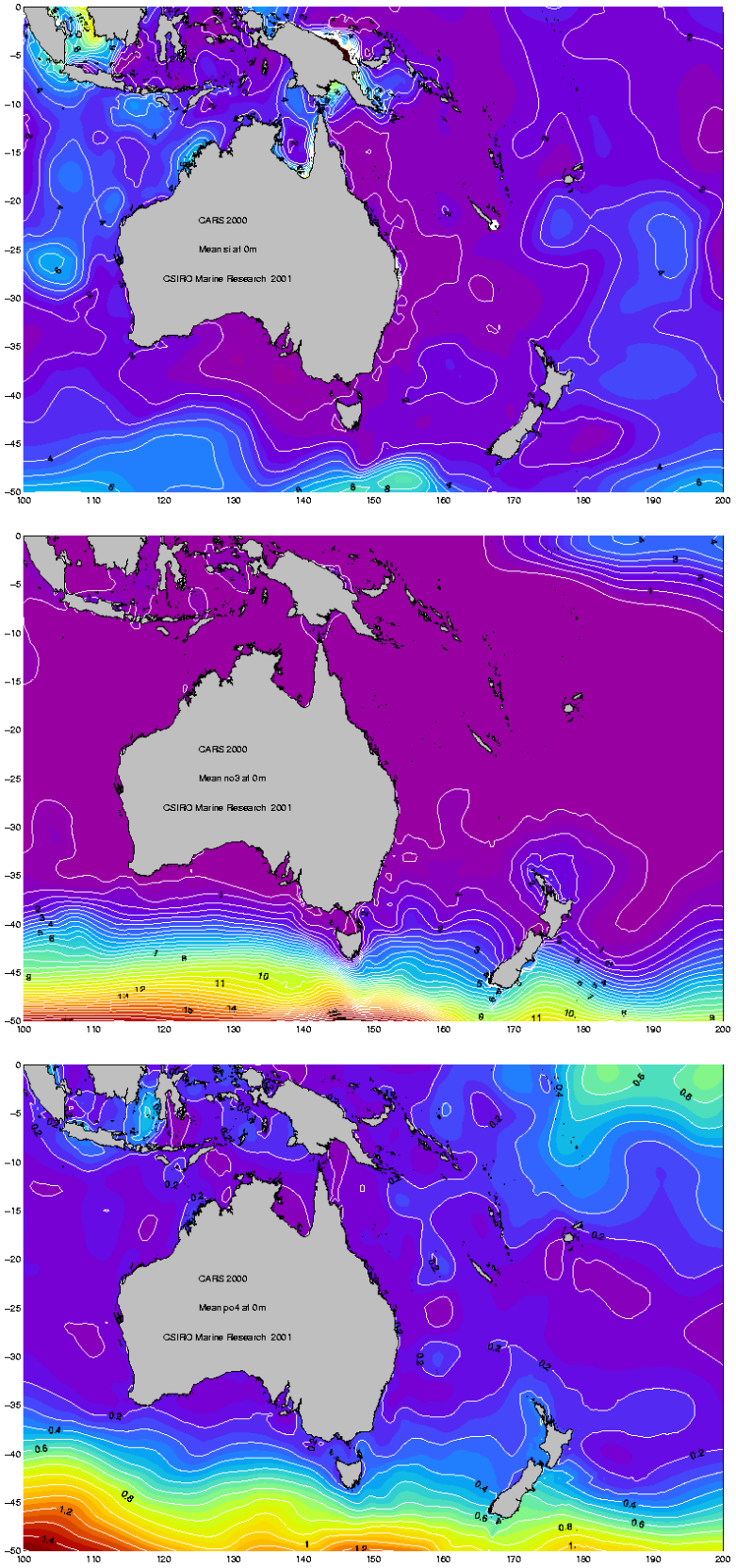

Figure 5.9. Regional nutrients: Pictorial analysis of all CSIRO data for surface silicate (top panel), nitrate (middle panel) and phosphate (bottom panel) showing concentrations contours (μM); data available at: http://www.marine.csiro.au/~dunn/cars2006/. Purple indicates low concentrations, through to red which indicates high concentrations.

The lack of a spring bloom or any detectable biological response could have several explanations:

1. strong top-down control of biomass by zooplankton
2. nutrients are advected into the region and out again rapidly
3. the chlorophyll-*a* biomass that does grow is found at depth and not visible to satellites.

We have little capacity to discriminate between these possible fates of any sporadic increases in NO_3^- during spring although the benthic microalgae are more abundant during spring-summer (chapter 8) and the grazing pressure is certainly high at this time of year (chapter 9). Phytoplankton cell counts from bottom waters (chapter 7), also do not indicate that there is a deeper phytoplankton bloom in spring.

5.3.5. Other sources of nutrients

The continental shelf is relatively wide across the GAB and across most of SA, and, although it narrows considerably towards the Victorian coast, Spencer Gulf is thus largely isolated from water that is sufficiently deep to contain high concentrations of nutrients. Surface concentrations of the macronutrients N, P and Si are relatively low on the continental shelf around most of Australia (Figure 5.9). Furthermore, the residence time of Boston Bay is relatively long, averaging ~ 8 days (chapter 1). Proper Bay, Louth Bay and inside Boston Island are all areas of relatively slow exchange. Therefore, local inputs and recycling of N will have greater significance to these zones than in many coastal ecosystems around Australia. Certainly local supplies of N are likely to determine the extent and magnitude of any phytoplankton blooms outside of those associated with upwelling events. The resupply of nutrients from sediments into the water column has been demonstrated to be a significant local source of nutrients in Australia and around the world (Table 5.5).

Nitrogen from baitfish provided to tuna

The input of nitrogen into the ecosystem from the food provided to the farmed tuna was estimated from the reported quantity of baitfish fed in 2006. It was assumed that baitfish were 3.25% N and that N retention by tuna averaged 9.5% (Fernandes et al. 2007). The nitrogen inputs showed a strong seasonal progression from ~ 40 tonnes N in January to ~ 409 tonnes in April, declining to zero by November (Figure 5.10). Summed over the year the inputs were 1946 tonnes of N. As the largest identified net source of nutrients in the model domain they must provide considerable augmentation to the seasonal phytoplankton peak.

Recycled N from the sediments

Benthic fluxes of NH_4^+ reported by Lauer et al. (2007) were ~ 2.2 mmol m^{-2} d^{-1} for control sites > 1 km from any lease. These are definitely at the high end of values reported for Port Philip Bay (Nicholson and Longmore 1999) and greater than those reported from similar sediments in Cockburn Sound, W.A. (Forehead 2006). They are, however, lower than some values reported from other locations around the world including those from Port Adelaide (Table 5.5).

Assuming that 2.2 mmol m^{-2} d^{-1} (Lauer et al. in prep.) is a robust estimate of the spatial and temporal variation in benthic DIN efflux, then over the model domain of ~ 644 km^2 the total efflux of N into the water column would be 7241 tonnes per year (Table 5.6).

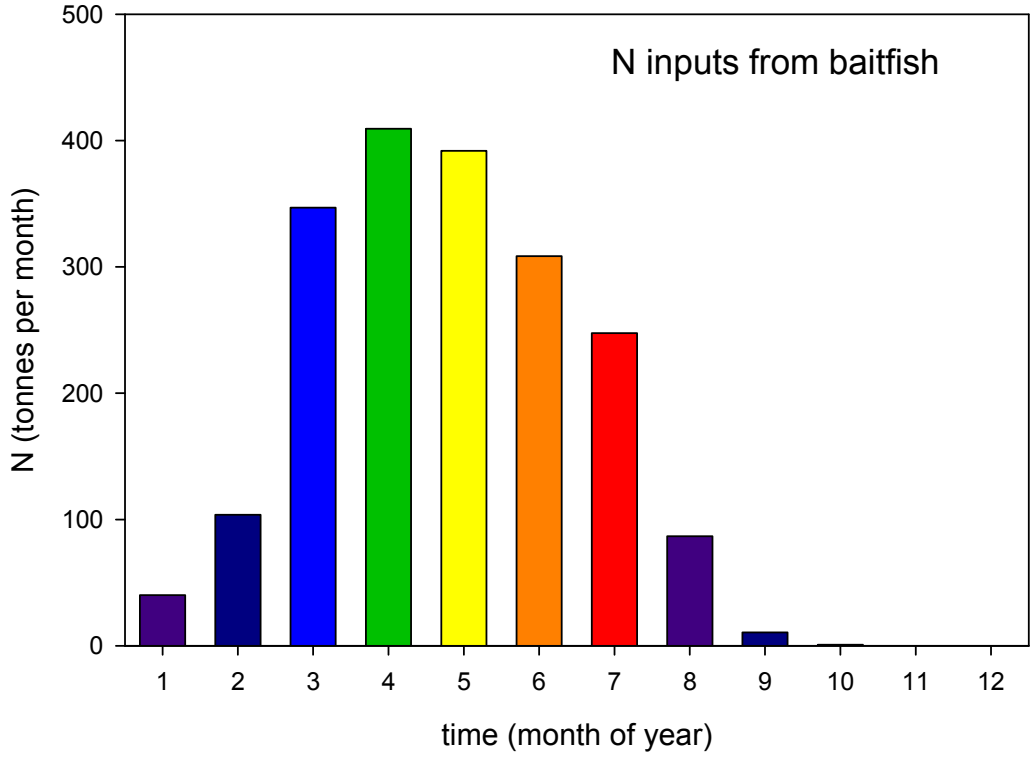

Figure 5.10. Data for nitrogen inputs into the ecosystem from the food provided to the farmed tuna as estimated from the reported quantity of baitfish fed in 2006. Baitfish were assumed to be 3.25% N and N retention by tuna was assumed to average 9.5% (Fernandes et al. 2007).

Table 5.5. Benthic nutrient fluxes reported in other estuarine or marine studies

Location	NH_4^+ (mmol m^{-2} h^{-1})	NO_x (mmol m^{-2} h^{-1})	PO_4^{3-} (mmol m^{-2} h^{-1})	Source
Humber Estuary	–0.28 to 1.1	–1.8 to 0.63	–0.046 to 0.092	Mortimer et al.1998
Tamar Estuary	–0.028 to 0.171	–0.283 to 0.37	0 to 0.033	Watson et al. 1995
North Carolina estuaries	0 to 0.45	0 to 0.006	–0.008 to 0.046	Fisher et al. 1982
Port Phillip Bay, Victoria	0.004 to 0.5	–0.05 to 1	0.002 to 0.079	Nicholson et al. 1996
Lake Illawarra, NSW	0.458 to 2.63	0.04 to 0.31	–0.04 to 0	Qu et al. 2003
Port River Day	–0.67 to 2.75	–1.46 to 0.133	–0.386 to 0.203	Jenkins 2005
Port River Night	0 to 3.21	–1.46 to 0.089	–0.383 to 0.241	Jenkins 2005

Table 5.6. A summary of known nitrogen pools or inputs to the Boston Bay region (model domain is specified in chapters 1 & 10).

		Pools	**Fluxes**	
Reference	**Source**	tonnes	tonnes N/year	tonnes/ha/y
Section 5.3.1	Water column dissolved inorganic N in model domain	56		
Section 5.3.1	Water column particulate N in model domain	1090		
1	Mariculture		926	
3	Mariculture		1137-2200	
Section 5.3.5	Mariculture (2006)		1946	
1	Waste water treatment plant		6.96	
4	Waste water treatment plant		9.2	
1	Proper Bay fish processors		23.8 [a]	
1	Port Lincoln storm water		3.61	
1	Tod River		232[b]	
	Groundwater		Unknown	
6	Sediments (flux into model domain ~ 644 km^2.)		7241	0.1124
Chapter 10	Water column net flux ([+= into], [-=from] model domain		-1789	
2	Atmospheric deposition (into model domain ~ 644 km^2)		792	0.0123
7	Abalone waste		~ 1	

References for Table 5.6.

1	Sinclair Knight Merz (2001). Technical Investigations Report For the Plan Amendment Report Relating to Marine Aquaculture in Lower Eyre Peninsula.
2	Wilkinson, J., Bestland, E., Smyth, L., and White, N. (2006). The loads of particulate matter and atmospheric nitrogen deposited from wet and dryfall to Adelaide metropolitan coastal waters. ACWS Technical Report No. 17 prepared for the Adelaide Coastal Waters Study Steering Committee, March 2006. Flinders University of South Australia.
3	Fernandes, M., Lauer, P., Cheshire, A. and Angove, M. (2007) Preliminary model of nitrogen loads from southern bluefin tuna aquaculture. Marine Pollution Bulletin 54:1321-1332.
4	Smith, S.V. and Veeh, H.H. (1989). Mass balance of biogeochemically active materials (C, N, P) in a hypersaline Gulf. Estuarine, Coastal and Shelf Science 29:195-215.
5	SA Water 2003. Sustainability report. Water, for growth, development and quality of life for all South Australians. SA Water, Adelaide.
6	Lauer, P. R., Fernandes, M., Fairweather, P.G., Tanner, J. and Cheshire, A. (2008). Benthic fluxes of nitrogen and phosphorus at southern bluefin tuna (*Thunnus maccoyii*) sea-cages in South Australia. (in preparation).
7	Tanner, Jason E. & Bryars, Simon (2007) Innovative Solutions for Aquaculture Planning and Management – Project 5, Environmental Audit of Marine Aquaculture Developments in South Australia. FRDC Project 2003/223. Fisheries Research & Development Corporation and South Australian Research and Development Institute (Aquatic Sciences), Adelaide. SARDI Aquatic Sciences Publication No F2007/000766-1 SARDI Research Report No.190.
a,b	These data may be out of date and should be verified before making any firm conclusions.

Nutrient inputs into the water column from sediments may be the largest identified nutrient input into the water column within the model domain but they are not net inputs. Over relatively long time spans the average flux should be a net export of nutrients from the water column into the sediments. There may, however, be a seasonal peak in the flux of nutrients supplied from sediments to the water column. Such a seasonal dynamic has been hypothesized as a partial explanation for an analogous late autumn-early winter peak of phytoplankton along the continental shelf of Western Australia (Lourey et al. 2006). Various mechanisms have been proposed to explain a seasonal rise in nutrient efflux from sediments including greater wave driven resuspension and changes in oxygen penetration. The phytoplankton ecology of our shallow coastal ecosystems will be more predictable when the mechanism(s) that determine nutrient exchange between the sediment and water are better understood.

If we make a number of simplifying assumptions: that 2.2 mmol m^{-2} d^{-1} (Lauer et al. in prep.) is a robust estimate of the spatial and temporal variation in benthic DIN efflux, that the average water depth in the model domain (see chapter 1) is 14.8 m then the daily supply of N to the water column would give a mean concentration of N ~

$$\frac{2.2 mmol N d^{-1}}{14.8 m^3} = 0.21 \mu g\ N\ L^{-1} d^{-1}$$

Assuming the average chlorophyll-*a* concentration is 0.73 µg L^{-1} (chapter 9), and that phytoplankton will produce ~ 1 µg chlorophyll-*a* from about 1 µM DIN (Collos 1990) and the flux is at steady state, then the phytoplankton must be growing at a rate ~

$$\frac{0.21 \mu g\ N\ L^{-1} d^{-1}}{0.73 \mu g\ chla\ L^{-1}} \sim 0.3 d^{-1}$$

Thus the turnover time in this ecosystem for nitrogen would be ~ 0.3 d^{-1} as would the approximate phytoplankton growth rate (assuming nitrogen inputs derive solely from the sediments). This estimate of turnover times is consistent with those made using other independent approaches (chapter 10).

In areas in the study domain where there are longer residence times (Proper Bay, Louth Bay and inshore of Boston Island), this resupply of nutrients from the sediments is likely to be the dominant source of DIN supporting phytoplankton growth.

Based on this assessment, the areas in the Port Lincoln region with long residence times and high rates of labile detritus accumulation will be susceptible to localised phytoplankton blooms and associated potential problems if those blooms are icthyotoxic or clog fish gills. Such areas can be identified by a combination of features: sediments with smaller grain sizes, benthic nutrient flux rates, and hydrodynamic, sediment and biogeochemical modelling. Phytoplankton species that grow by using recycled nutrients are more likely to be problematic or toxic (Smayda 1990) and represent an increased risk to aquaculture. The risks associated with potentially toxic phytoplankton are, however, considered to be low (see chapter 7).

Trichodesmium *as a source of N*

Trichodesmium species can dominate the phytoplankton biomass and supply the majority of the nitrogen to the environment in portions of tropical Australia (Furnas et al.1995). Unlike most other species of plankton, it can grow using atmospheric N_2, giving it a virtually unlimited supply of nitrogen. *Trichodesmium* has frequently been observed in the Port Lincoln region between January and March, and on at least one accoassion formed an extensive 'red tide' across much of southern and central Spencer Gulf, but measurements of its abundance are very rare. It is possible that it forms the majority of the phytoplankton biomass in the northern region of Spencer Gulf during summer. The potential of *Trichodesmium* to accumulate at the surface where wind can cause it to form dense patches could cause problems for aquaculture. Decaying *Trichodesmium* has been associated with some mortalities of marine fauna by contributing to low dissolved oxygen (Chacko, 1942). Given the lack of information on *Trichodesmium*, its contribution to N budgets in the region can only be speculated upon.

Other sources of N

A number of other nutrient inputs into the area, mostly into Boston Bay, were identified in this review process including, as examples, fish processing and the Tod River (see Table 5.6). Both are potentially large inputs of nitrogen into this ecosystem, but neither have been rigorously quantified, with only approximate levels of input known. Other minor sources include storm water runoff from Port Lincoln, and discharges from the Billy Light Point waste water treatment plant, although collectively they only account for ~ 10 tonnes of N per year (Table 5.6). Future management of this ecosystem is likely to require better information on the major nutrient inputs. The aquaculture industry might want to consider whether it should act as an advocate for better monitoring of the other users of this water body. They may also wish to compile their own, but preferably publically available, data base on all known nutrient inputs.

Other nutrients - Silicate

Silicate concentrations tend to be low in the Great Australian Bight and across the south east of Australia (Figure 5.9). The observed rise in silicate in late summer (Figure 5.2) has no obvious source. Late summer and autumn is a time of high evaporation relative to exchange, so salinities rise in the GAB, the northern end of Spencer Gulf and along the eastern side of the gulf. We can only speculate that these high-salinity waters may represent the source of silicate that is evident from the sharp rise in concentrations within the TFZ reaching an annual maximum during February. Similar rises in silicate concentrations have been noted along the western side of the Eyre Peninsula (P. van Ruth, unpublished data). However, it seems unlikely that this rise in silicate in the TFZ originates from offshore and upwelled waters as there was little or no nitrate. We speculate that it is derived from a more localised source, potentially silicate recycling of the annual diatom peak that has sedimented out to the bottom and been remineralised.

5.4. Summary

There is evidence of a natural, relatively large scale and regular input of DIN, including a significant fraction as NO_3^-, into the lower Spencer Gulf during autumn (herein and chapter 1) that results in a phytoplankton peak composed predominately of diatoms. A brief review of the local nutrient inputs (Table 5.6) would suggest that local inputs from fish farming and recycling through microbial processes in the sediments significantly augment the nutrients

available to grow phytoplankton. A precise estimate of the increase in phytoplankton biomass due to nutrients from aquaculture activities is provided elsewhere (chapter 10). The relatively high water quality of the region seems to depend upon processes such as advection, phytoplankton grazing and sedimentation to reduce the nutrient concentrations and phytoplankton biomass. The biogeochemical modelling (chapter 10) indicates the local area exports 1789 tonnes of N per year into lower Spencer Gulf. Thus even the limited advection that takes place is very important in maintaining local water quality. Of the processes investigated, grazing (chapter 9) seems to have the greatest potential to remove phytoplankton biomass from the water column, thus the local ecosystem is susceptible to blooms of grazing-resistant species and mixotrophic or heterotrophic flagellates such as *Dinophysis*.

5.4.1. Risks

There are several risks associated with nutrient inputs into the region. Almost any input of nitrogen (labile organic or inorganic particulates containing N, most dissolved organics containing N, dissolved inorganic N as NO_3^-, NO_2^-, NH_4^+) is likely to cause an increase in phytoplankton growth. Phytoplankton growth produces several types of risk, perhaps the greatest risk is the loss of oxygen when the phytoplankton biomass decays. This has caused extremely large fish kills in such places as Florida (5.5 million dead fish, Cubbison 1973). Risks associated with low dissolved oxygen are exacerbated by high water temperatures (low solubility of O_2) and weak tides (reduced mixing and exchange). Fortunately the major seasonal peak inphytoplankton in the TFZ occurs in May, when water temperatures are falling and oxygen solubility is rising, but, nonetheless, tuna growers should be wary during the decline of this peak (June-August). It would also seem to be true that most of these late autumn-winter peaks are dominated by diatoms. Very few diatoms produce toxins that are a direct risk and very few are toxic to fish (ichthyotoxic), though problems can arise by other means (e.g. gill damage). There was significant interannual variability in phytoplankton biomass, so some years are potentially more risky than others, but there is not (yet) a detectable long-term trend. Climate change is likely to make the problems with O_2 solubility worse.

Similarly, any localised N input into a region of low exchange is likely to produce additional phytoplankton growth. Areas of high risk for this include any areas of low exchange and/or high nutrient input, with the combination being particularly dangerous. Generally the species of phytoplankton that are toxic to fish or humans bloom late in the annual cycle when the water column is well stratified. For the Port Lincoln area this would be from October to March. During this time, localised nutrient inputs are likely to have their greatest influence on phytoplankton ecology, community composition and species abundance. Localised blooms of ichthyotoxic species in response to localised N inputs are a particular risk at this time. Fortunately, inputs from tuna farming do not peak until April/May, when stratification is likely to have broken down, and thus they might not pose as large a risk as they would if peak inputs occurred a few months earlier.

Increased agriculture, finfish aquaculture and human populations are major contributors to the increased load of nutrients to the coastal zone. They need to be managed so as to minimize the risk to the environment. The amount of nutrients disposed of into the ocean as runoff, from sewage or from industries including aquaculture, all need to be measured and their consequences assessed. Further problems can only be avoided if appropriate assessments are conducted and monitoring is ongoing. A further discussion of risks associated with phytoplankton can be found in chapter 7.

Acknowledgements

We thank all the field staff and crew of the vessels used to collect data. We thank Sam Gaylard of the SA EPA for assistance in accessing their nutrient data.

5.5. References

Armstrong, F.A.J. 1951. The determination of silicate in sea water. J. mar. biol. Ass. U.K., 30: 149-60.

Armstrong, F.A.J., Stearns, C.R. and Strickland, J.D.H. 1967. The measurement of upwelling and subsequent biological processes by means of the Technicon_ AutoAnalyzer and associated equipment. Deep-Sea Res. 14: 381-389.

Atlas, E.L., Hager, S.W., Gordon, L.I. and Park, P.K. 1971. A practical manual for use of the Technicon Autoanalyzer in seawater nutrient analyses; revised. Technical Report 215. Oregon State University, Dept of Oceanography, Ref. No. 71-22. 48 pp.

APHA-AWWA-WEF. 1998. Standard Methods for the Examination of Water and Wastewater, 20th. Edition. American Public Health Association, Washington.

Bierman P., Kaempf J., Fernandes M. 2007. Oceanographic conditions in the offshore Southern Bluefin Tuna farming zone, near Pt Lincoln SA. In: Tanner J (ed) Aquafin CRC - Southern Bluefin Tuna Aquaculture Subprogram: Tuna environment subproject - Development of regional environmental sustainability assessments for tuna sea-cage aquaculture (final report for Aquafin CRC Project 4.3.3 and FRDC Project 2001/104). Aquafin CRC, SARDI Aquatic Sciences and FRDC, Adelaide, pp 207-237

Burford, M.A., Rothlisberg, P.C. and Wang, Y.G. 1995. Spatial and temporal distribution of tropical phytoplankton species and biomass in the Gulf of Carpentaria, Australia. Marine Ecology Progress Series, 118: 255-266.

Chacko P. I. 1942. An unusual incidence of mortality of marine fauna. Current Science India, 11:402

Clarke, S., Cartwright, C., Smith, B., Madigan, S., and Haskard, K. 1999. Southern Bluefin Tuna (*Thunnus maccoyii*) Aquaculture Environmental Monitoring Report 1996 to 1998. South Australian Research and Development Institute, Adelaide, 38pp.

Clarke, S., Madigan, S., Edwards, J., Mathews, C., Preece, P., and Haskard, K. 2000. Southern Bluefin Tuna (*Thunnus maccoyii*) Aquaculture Environmental Monitoring Report 1999 to 2000. South Australian Research and Development Institute, Adelaide, 43pp.

Cubbison, C. 1973. Florida wins Dubious Title: Nation's No. 1 Fish Killer. St. Petersburg Times. Feb 21, 1973.

Elser, J.J., Marzolf, E.R. and Goldman, C.R. 1990. Phosphorus and nitrogen limitation of phytoplankton growth in the freshwaters of North America: A review and critique of experimental enrichments. Canadian Journal of Fisheries and Aquatic Sciences 47:1468-77.

Fernandes, M., Lauer, P., Cheshire, A. and Angove, M. 2007. Preliminary model of nitrogen loads from southern bluefin tuna aquaculture. Marine Pollution Bulletin 54:1321-1332.

Fisher, T.R., Carlson, P.R. and Barber, R.T. 1982, Sediment-nutrient regeneration in three North Carolina estuaries. Estuarine, Coastal and Shelf Science 14:101–116.

Forehead, H.I. 2006. The ecology and biogeochemistry of sandy sediments in the warm temperate coastal waters of Western Australia. Doctor of Philosophy Thesis. University of Western Australia, 131 pp.

Furnas, F. Mitchell, A.W. and Skuza M. 1995. Nitrogen and phosphorus budgets for the central Great Barrier Reef shelf. Great Barrier Marine Park Authority #36

Gaylard, S. Ambient Water Quality of Boston & Proper Bays, Port Lincoln:1997-2006. Environment Protection Authority, GPO Box 2607, Adelaide SA 5001 (in prep.).

Goes, I.G., Saino, T., Oaku, H. and Jiang D.L. 1999 A Method for Estimating Sea Surface Nitrate Concentrations from Remotely Sensed SST and Chlorophyll —A Case Study for the North Pacific Ocean Using OCTS/ADEOS Data. IEEE Transactions of Geoscience and Remote Sensing. 37:1633-1644.

Jenkins, C. 2005. Nutrient flux assessment in the Port waterways. South Australia Environmental Protection Agency Report. ISBN 1 876562 87 0

Kamykowski, D. 1987. A preliminary biophysical model of the relationship between temperature and plant nutrients in the upper ocean. Deep-Sea Res. 34: 1067–1079.

Kamykowski, D. and Zentara, S.J. 1986. Predicting plant nutrient concentrations from temperature and sigma-t in the upper kilometer of the world ocean. Deep-Sea Res. 33: 89–105.

Lauer P.R., Fernandes, M., Fairweather, P.G., Tanner, J. and Cheshire, A.. 2007. Benthic fluxes of nitrogen and phosphorus at southern bluefin tuna (Thunnus maccoyii) sea-cages in South Australia. (in prep).

Lourey, M.J., Dunn, J.R. and Waring. J. 2006. A mixed-layer nutrient climatology of Leeuwin Current and Western Australian shelf waters: Seasonal nutrient dynamics and biomass. Journal of Marine Systems 59: 25-51.

Mann, K. H. and Lazier, J. R. N. (1996). Dynamics of marine ecosystems. London, Blackwell Science.

Mortimer, R.J.G., Krom, M.D. and Watson, P.G. 1998, Sediment-water exchange of nutrients in the intertidal zone of the Humber Estuary, UK, Marine Pollution Bulletin 37: 261–279.

Nicholson, G.J, Longmore, A.R. and Cowdell, R.A. 1996. Nutrient status of the sediments of Port Phillip Bay, part of the Port Phillip Bay Environmental Study, CSIRO Projects Office, The Marine and Freshwater Research Institute, Queenscliff; Technical Report No. 26.

Nicholson, G.J. and Longmore, A.R. 1999. Causes of observed temporal variability of nutrient fluxes from a southern Australian marine embayment. Mar. Freshwater Res. 50:581-588.

Qu, W., Morrison, R.J. and West, R.J. 2003. Inorganic nutrient and oxygen flux across the sediment-water interface in the inshore macrophyte areas of a shallow estuary (Lake Illawarra, Australia), Hydrobiologia 492:119–127.

Redfield, A.C., Ketchum, B.H. and Richards, F.A. 1963. The influence of organisms on the composition of sea-water. In: M.N. Hill, Editor, The Sea: Ideas and Observations on Progress in the Study of the Seas, Wiley, New York, pp. 26–77.

Rothlisberg, P.C., Pollard, P.C., Nichols, P.D., Moriarty, J.W., Forbes, A.M.G., Jackson, J. and Vaudrey, D. 1994. Phytoplankton Community Structure and Productivity in Relation to the Hydrological Regime of the Gulf of Carpentaria, Australia, in Summer Aust. J. Mar. Freshwater Res., 45: 265-282.

Smayda, T.J. (1990). Novel and nuisance phytoplankton blooms in the sea; evidence for a global epidemic. In, 'Toxic marine phytoplankton' (Eds. E. Granelli, B. Sundstrom and L. Edler.) pp. 29-40. (Elsevier: New York.)

Thompson, P.A., Bonham, P. I. and Swadling, K.M. In press. Phytoplankton blooms in the Huon Estuary, Tasmania: top down or bottom up control? Journal of Plankton Research.

Watson, P.G., Frickers, P.E. and Howland, R.J.M. 1993. Benthic fluxes of nutrients and some trace metals in the Tamar Estuary, S.W. England. Netherlands Journal of Aquatic Science 27, 135–146

Other relevant literature

The recently completed Adelaide Coastal Waters Study provides a wealth of relevant literature as technical reports. Technical Reports #13 and #17 were used in the preparation of this CRC final report.

ACWS Technical Report No. 1 July 2005 (PDF, 2.4 MB) Audit of the quality and quantity of treated wastewater discharging from Wastewater Treatment Plants (WWTPs) into the marine environment. By Jeremy Wilkinson, Meryl Pearce, Nancy Cromar and Howard Fallowfield

ACWS Technical Report No. 2 2004 (PDF, 2.6 MB) A review of seagrass loss on the Adelaide metropolitan coastline. By Westphalen, G., Collings, G., Wear, R., Fernandes, M., Bryars, S. and Cheshire, A. Publication No. RD04/0073, Adelaide.

ACWS Technical Report No. 3 June 2004 (PDF, 3.3 MB) Audit of contemporary and historical quality and quantity data of stormwater discharging into the marine environment, and field work programme. By Wilkinson, J., Hutson, J., Bestland, E. and H. Fallowfield

ACWS Technical Report No. 4 September 2005 (PDF, 2.5 MB) Estimation of groundwater and groundwater N discharge to the Adelaide Coastal Waters Study area. By Lamontagne, S., Le Gal La Salle, C., Simmons, C., James-Smith, J., Harrington, N., Love, A., Smith, A., Hancock, G. and H. Fallowfield

ACWS Technical Report No. 5 August 2005 (PDF, 1.7 MB) Distribution of Suspended Matter Using SeaWiFS Data. By Peter Petrusevics

ACWS Technical Report No. 6 September 2005 (PDF, 12.5 MB) Remote sensing study of marine and coastal features and interpretation of changes in relation to natural and anthropogenic processes. By David Blackburn and Arnold Dekker

ACWS Technical Report No. 7 May 2006 (PDF, 3.7 MB) In-situ field measurements for Adelaide Coastal Waters Study. By Jochen Kaempf

ACWS Technical Report No. 8 July 2005 (PDF, 3.7 MB) Physical oceanographic studies of Adelaide coastal waters using high resolution modeling, in-situ observations and satellite techniques. By Charitha Pattiaratchi and Rhys Jones

ACWS Technical Report No. 9 August 2005 (PDF, 1.6 MB) Responses to reduced salinities of the meadow forming seagrasses Amphibolis and Posidonia from the Adelaide metropolitan coast. By Westphalen, G., O'Loughlin, E., Collings, G., Tanner, J., Eglinton, Y., and Bryars, S.

ACWS Technical Report No. 10 August 2005 (PDF, 638 kB) Reconstruction of historical stormwater flows in the Adelaide metropolitan area. By Wilkinson, J.

ACWS Technical Report No. 11 August 2006 (PDF, 2.1 MB) Elevated nutrient responses of the meadow forming seagrasses, Amphibolis and Posidonia, from the Adelaide metropolitan coastline. By Greg Collings, Simon Bryars, Sasi Nayar, David Miller, Jodi Lill and Emma O'Loughlin

ACWS Technical Report No. 12 July 2006 (PDF, 721 kB) Turbidity and reduced light responses of the meadow forming seagrasses Amphibolis and Posidonia, from the Adelaide metropolitan coastline. By Collings, G., Miller, D., O'Loughlin, E., Cheshire, A., and Bryars, S.

ACWS Technical Report No. 13 August 2006 (PDF, 2 MB) Nutrient fluxes in the meadow forming seagrasses Posidonia and Amphibolis from the Adelaide metropolitan coast. By Sasi Nayar, Greg Collings, David Miller and Simon Bryars

ACWS Technical Report No. 14 August 2006 (PDF, 2.7 MB) Field surveys 2003-2005: Assessment of the quality of Adelaide's coastal waters, sediments and seagrasses. By Simon Bryars, David Miller, Greg Collings, Milena Fernandes, Gen Mount and Rachel Wear.

ACWS Technical Report No. 15 August 2006 (PDF, 1.4 MB) Assessment of the effects of inputs to the Adelaide coastal waters on the meadow forming seagrasses, Amphibolis and Posidonia. By Simon Bryars, Greg Collings, Sasi Nayar, Grant Westphalen, David Miller, Emma O'Loughlin, Milena Fernandes, Gen Mount, Jason Tanner, Rachel Wear, Yvette Eglinton, and Anthony Cheshire.

ACWS Technical Report No. 16 March 2007 (PDF, 5.1 MB) Adelaide Coastal Waters Study Coastal Sediment Budget. By Yvonne Bone, Linda Deer , Sally Edwards and Elizabeth Campbell

ACWS Technical Report No. 17 March 2006 (PDF, 2.4 MB) The loads of particulate matter and atmospheric nitrogen deposited from wet and dryfall to Adelaide metropolitan coastal waters. By Jeremy Wilkinson, Erick Bestland, Lynn Smythe, Nicholas White.

ACWS Technical Report No. 18 July 2006 (PDF, 1.1 MB) Volumes of inputs, their concentrations and loads received by Adelaide metropolitan coastal waters. By Jeremy Wilkinson, Nicholas White, Lynn Smythe, John Hutson, Erick Bestland, Craig Simmons, Sebastien Lamontagne and Howard Fallowfield.

ACWS Technical Report No. 19 June 2006 (PDF, 2.8 MB) An Integrated Environmental Monitoring Program for Adelaide's Coastal Waters. By Brent Henderson, Melissa Dobbie and Bronwyn Harch.

ACWS Technical Report No. 20 May 2007 (PDF, 5.5 MB) Physical oceanographic studies of Adelaide coastal waters using high resolution modelling, in-situ observations and satellite techniques. By Charitha Pattiaratchi, John Newgard and Ben Hollings.